UNIVERSITA' DEGLI STUDI DI PADOVA

Sede Amministrativa: Università degli Studi di Padova

Dipartimento di Scienze Chimiche

SCUOLA DI DOTTORATO DI RICERCA IN SCIENZE MOLECOLARI

INDIRIZZO SCIENZE CHIMICHE

CICLO XX

ADVANCED PEROVSKITE MATERIALS FOR INTERMEDIATE TEMPERATURE SOLID OXIDE FUEL CELLS

Direttore della Scuola: Ch.mo Prof. Maurizio Casarin

Supervisore: Dott.ssa. Antonella Glisenti

Dottorando: Alessandro Galenda

31 gennaio 2008

To my family

Content

Abstract

The research program developed during the Ph.D. School is focussed on the study of advanced materials for applications in the intermediate temperature solid oxide fuel cells (IT-SOFCs).

Fuel cells (FCs) are often considered as the best solution to produce clean energy starting from various primary resources. FCs are employed for the direct production of electric power by electrochemical conversion of the potential energy of a fuel. Fuel cells work as a common galvanic cell: the fuel is oxidised at the anode and the combustive (usually air) is reduced at the cathode.

Among the various kind of fuel cells, solid oxide fuel cells are very interesting thanks to their singular properties, such as the high output powers (reaching megawatts) and the excellent efficiency (until about 70% with the co-generation). Another interesting characteristic is the ability to work with different type of fuels. Beyond hydrogen (whose usage involves the well know difficulties concerning production, transportation and storage), SOFCs can operate with alcohols (such as methanol and ethanol) or hydrocarbons. This can offer significant opportunity in renewable energy field taking into consideration fuels derived from bio-masses and urban or industrial rubbish.

A common SOFC usually works at very high temperature (800÷1100°C). Anyway, many studies have been carried out to develop new materials able to guarantee the best performances at lower temperatures (500÷700°C) and build the new generation of SOFCs: the so-called Intermediate Temperature Solid Oxide Fuel Cells (IT-SOFCs). Nevertheless it is, necessary to develop new electrolyte materials characterized by high anionic conduction at lower temperatures and new electrodes with electronic, or better mixed ionic-electronic conductivity (MIEC) and a suitable activity toward fuel oxidation and combustive reduction.

In the present study, several perovskite based oxide materials have been considered. These particular compounds show a wide range of interesting chemical and physical properties. Moreover, these characteristics can be tuned employing different constituting elements and different kinds and amounts of dopant elements.

Taking into account the literature research outcomes, two kinds of perovskites have been studied: gallates and cuprates. The first ones are lanthanum gallate doped with strontium and iron and with strontium and copper ($La_{0.8}Sr_{0.2}Ga_{0.8}Fe_{0.2}O_{3-\delta}$, named LSGF,

$La_{0.8}Sr_{0.2}Ga_{0.8}Cu_{0.2}O_{3-\delta}$, LSGC), while the second types derive from lanthanum cuprate ($LaCu_{0.8}Co_{0.2}O_{3-\delta}$, LCC1, and $La_2Cu_{0.8}Co_{0.2}O_{4-\delta}$, LCC2).

The samples have been prepared by means of two wet-chemistry procedure (Pechini process and the Polyacrylamide Gel method) to avoid using the high temperature ceramic route and to study the influence of the preparation procedure.

The obtained catalysts were characterized by means of X–Ray Diffraction (XRD), X–ray Photoelectron Spectroscopy (XPS), and Diffuse Reflectance Infrared spectroscopy Fourier Transform (DRIFT) Spectroscopy.

In general, XRD revealed the presence, beside the desired one, of minor phases whose amount and typology is influenced by the composition and doping. In the case of LCC1, in contrast, a mixture of $La_2Cu_{0.8}Co_{0.2}O_{4-\delta}$ and CuO, was obtained instead of $LaCu_{0.8}Co_{0.2}O_{3-\delta}$. XPS investigation testifies the surface segregation of strontium as carbonate and of lanthanum as oxide and hydroxide. Copper is present as copper oxide both in LCC1 and LCC2. As a general consideration, the presence of carbonate species and hydroxyl groups is mainly a surface phenomenon.

Interesting information have been obtained from the catalytic tests. The reactivity of the materials has been investigated toward methanol and ethanol under several conditions: tests with pure alcohol vapours, under oxidising atmosphere (enriching the carrier gas with O_2) and in steam reforming conditions, have been carried out at several temperatures between RT and 400°C. The experiments were performed employing a home made continuous flow reactor monitoring the exit stream by IR and QMS.

Significant differences have been observed between the samples obtained by means of the two different preparation procedures: the results, as a whole, indicate that the samples obtained by Gel procedure show a higher activity.

Both in alcohol oxidation (carried out with oxygen) and in alcohol steam reforming the higher activity of cuprate based materials is evident. LSGF and LSGC, in contrast, exhibit lower reactivity. It has also to be considered that a certain poisoning of the catalysts surfaces was observed as a consequence of the interaction with the reaction products (carbon dioxide, as an example). This is particularly true when the reaction is carried out with the only alcohols or under steam reforming conditions.

The cathodic activity was investigated by measuring the oxygen permeability throughout the materials pressed as a pellet. The permeation mechanism is specific for O_2 and provides useful information concerning both redox and transport properties (for oxide anions) for the investigated material. Permeability measurements were carried out

employing a home made reactor. This is expressly conceived, realized and optimized during the PhD term. A detailed study concerning the materials (ceramic macor) and fittings has been done (paying particular attention to the pasting of the samples on the ceramic support). The tests have been monitored by means of QMS and show particularly interesting results for the cuprates.

Riassunto

Il programma di ricerca sviluppato durante il triennio della Scuola di Dottorato si focalizza sullo studio di materiali avanzati per applicazioni nel settore delle celle a combustibile ad ossidi solidi operanti a temperatura intermedia (*Intermediate Temperature – Solid Oxide Fuel Cells* o IT-SOFCs).

Le celle a combustibile (Fuel Cells o FCs) sono considerate tra le soluzioni migliori per la produzione di energia elettrica grazie al basso impatto ambientale, alla versatilità (potendo impiegare diversi combustibili e fornire potenza entro un ampio intervallo di valori) e alle elevate efficienze di conversione. Le FCs operano come una classica cella galvanica, dove il combustibile è ossidato all'anodo, mentre il comburente (normalmente aria) è ridotto al catodo.

Tra le varie tipologie di FCs, le celle ad ossidi solidi sono le più interessanti grazie alle loro singolari proprietà, come ad esempio, le alte potenze raggiungibili (nell'ordine dei MW) e la straordinaria efficienza (fino al 70% con la co-generazione). Un'altra interessante caratteristica è la capacità di lavorare con differenti tipi di combustibili. Oltre all'idrogeno (per il quale sono noti i problemi di produzione e utilizzo), le SOFCs possono usare alcoli (es. metanolo o etanolo) o idrocarburi. Questo offre una significativa opportunità nell'uso di fonti di energia rinnovabili, ad esempio considerando i combustibili ottenibili da bio-masse.

Una classica SOFC opera ad altissime temperature (800÷1100°C). Tuttavia, molti studi sono orientati allo sviluppo di nuovi materiali capaci di garantire ottime prestazioni a temperature più basse (500÷700°C), e costruire, così, una nuova generazione di celle: le cosiddette celle a combustibile ad ossidi solidi operanti a temperatura intermedia (IT-SOFCs). A questo scopo, tuttavia, è necessario sviluppare nuovi elettroliti dotati di buona conducibilità ionica a basse T, ed elettrodi, con conducibilità elettronica o meglio mista ionico-elettronica (Mixed Ionic-Electronic Conductor o MIEC) oltre che un'adeguata attività ossido-riduttiva rispetto al combustibile ed all'ossidante.

Nel presente studio, sono stati considerati alcuni materiali appartenenti alla categoria delle perovskiti. Questi composti mostrano interessanti proprietà chimiche e fisiche. Inoltre, queste caratteristiche possono essere modulate impiegando differenti composizioni e differenti tipi e quantità di droganti.

I risultati della ricerca bibliografica hanno suggerito di prendere in considerazioni due tipi di composti: gallati e cuprati. I primi sono stati ottenuti modificando il gallato di

lantanio, rispettivamente, con stronzio e ferro e con stronzio e rame ($La_{0.8}Sr_{0.2}Ga_{0.8}Fe_{0.2}O_{3-\delta}$, chiamato LSGF, $La_{0.8}Sr_{0.2}Ga_{0.8}Cu_{0.2}O_{3-\delta}$, LSGC); della seconda tipologia, invece, sono stati considerati due derivati del cuprato di lantanio ($LaCu_{0.8}Co_{0.2}O_{3-\delta}$, LCC1, and $La_2Cu_{0.8}Co_{0.2}O_{4-\delta}$, LCC2).

I campioni sono stati preparati secondo due procedure per via umida (processo Pechini e metodo del gel di polyacrylamide) per ovviare alle alte temperature necessarie nella classica "via ceramica". I catalizzatori ottenuti sono stati caratterizzati per mezzo della diffrazione dei raggi X (X-Ray Diffraction, XRD), della spettroscopia fotoelettronica a raggi X (X-ray Photoelectron Spectroscopy, XPS)e la spettroscopia IR.

Le analisi XRD mostrano la presenza, accanto alla fase voluta, di fasi minoritarie la cui quantità e natura è influenzata dalla composizione e dal drogaggio. La sintesi della fase $LaCu_{0.8}Co_{0.2}O_{3-\delta}$, invece, non ha dato gli esiti desiderati, ottenendosi, invece, una miscela di CuO e $La_2Cu_{0.8}Co_{0.2}O_{4-\delta}$. I dati XPS indicano che lo stronzio si segrega in superficie principalmente come $SrCO_3$ in LSGF e LSGC mentre il lantanio come ossido e idrossido. Nei campioni in cui è presente il rame, tale elemento è presente in superficie come CuO. In generale, la presenza di specie carbonato, ossido ed idrossido, è un fenomeno principalmente di superficie.

Interessanti risultati sono stati ottenuti nei test catalitici. La reattività dei materiali è stata indagata rispetto al metanolo ed etanolo in diverse condizioni. Sono stati condotti test con i soli alcoli, in condizioni ossidanti e in condizioni di *steam-reforming* a varie temperature tra RT e 400°C. La reattività nei confronti di metanolo ed etanolo è stata studiata mediante spettroscopia IR e spettrometria di massa a quadrupolo (Quadrupolar Mass Spectrometry, QMS), impiegando un reattore a flusso.

Interessanti differenze sono state notate tra i composti ottenuti con differenti procedure sintetiche. I risultati indicano che i composti ottenuti con il metodo del gel presentano, usualmente la maggiore attività.

In condizioni ossidanti e di *steam-reforming* è evidente la maggior reattività delle perovskiti a base di cuprati rispetto a quelle derivate dal gallato di lantanio. Nell'ambito di questi ultimi, tra l'altro, il composto drogato con rame presenta, dal punto di vista dell'attività catalitica, caratteristiche migliori rispetto a quello drogato ferro. Altro aspetto significativo è costituito dalla tendenza, particolarmente evidente quando la reattività è studiata nei confronti degli alcoli puri ed in condizioni di *steam-reforming*, ad un avvelenamento dei siti attivi presenti sulla superficie dei catalizzatori a causa dell'interazione con i prodotti di reazione (ed in particolare con l'anidride carbonica).

L’attività catodica è stata misurata prendendo in considerazione la permeabilità dell’ossigeno attraverso una membrana costituita dal materiale indagato. Il meccanismo di permeazione è specifico per O_2 e fornisce utili informazioni sia riguardo alle proprietà ossido-riduttive sia di trasporto (degli anioni ossido). Le misure di permeabilità sono state sono state eseguite per mezzo di una camera di permeazione costruita in casa. Il congegno è stato appositamente concepito, realizzato ed ottimizzato durante il triennio di dottorato. A tale scopo, sono stati studiati i migliori materiali, le modalità di giunzione e di fissaggio della pastiglia analita alla camera. I test sono stati seguiti via QMS fornendo risultati particolarmente incoraggianti soprattutto per quanto concerne i cuprati.

Introduction

Energy availability always influences people life's. Nowadays, energy is required in most of the human activities and it is considered as an irremissible means to maintain high life standards.

Energy demand daily increases and the development of important countries, such as India and China, speed up the consumptions. Moreover, it is essential to improve the status of poorest countries and face the environmental problems concerning the world greenhouse effect.

As a matter of fact, most of consumed energy is obtained by the combustion of fossil fuels such as oil, coal or natural gas and only a low percentage is produced by means of renewable sources. Moreover, the devices employed for the conversion of the raw sources (fossil, renewable and nuclear) potential energy into electrical energy, are characterized by a very low efficiency.

In order to improve the overall procedures for a better energy production, new devices and technologies must be developed. From this point of view, the fuel cells (FCs) are considered as a suitable solution.

Fuel cells represent one of the cleanest power generating technologies available today. They are electrochemical devices which provide the electro-oxidation of a fuel directly obtaining electrical power. In other words, they work as the common galvanic cells: the fuel oxidation half-reaction occurs at the anode site, while the comburent reduction takes place at the cathode site. The electrons exchanged in the redox reaction (from the anode to the cathode site) are conducted by an external circuit to the users; because of their operating principle, fuel cells guarantee very high efficiencies.

To be true, FCs are not new devices, since they were invented in 1839 by Sir William Grove and are one of the oldest electrical energy conversion technologies known to man. Nevertheless, their technological development has lagged behind the more well known steam engine and internal combustion engine. The reasons for the late evolution of fuel cells can be reduced to mainly economic factors, material problems, and certain inadequacies in the operation of electrochemical devices.

It is worth to point out that a fuel cell is a rather complicated system since each component (both electrodes and electrolyte) requires specific chemical and physical properties.

From the first generation of fuel cells, many technological improvements have been achieved and several typologies of cells have been developed. The main differences involve the operating temperature (and thus the adopted materials, the long-time stability and the device performance) and the fuels.

The first most successful application of the fuel cells was achieved with the space technologies in the Apollo program from 1960 to 1965. The great obtained results started a new era for the FCs development and allowing new applications and improvements. Nowadays, FCs have been tested in portable devices, vehicle propulsion and distributed electrical power generation. Nevertheless, FCs still need deeper investigation (concerning both FCs and fuels) to achieve a wider commercial diffusion.

As mentioned above, the various kinds of FCs differ with respect to the operating temperature and for the employed materials. Furthermore, the choice of the most suitable fuel is also an important question.

From this point of view, hydrogen is often considered as the best fuel thanks to its environmental compatibility. Anyway, H_2 has some disadvantages concerning its production (actually mainly from hydrocarbons) and the storage. In other words, the wide use of H_2 appears so far away and others available fuels are required.

Waiting for hydrogen availability, light alcohols (such as methanol or ethanol) or light hydrocarbons (mainly methane or ethane) can be used.

The present research project is focussed on the study of new materials for application in solid oxide fuel cells.

Among the various kinds of FCs, the solid oxide fuel cells (SOFCs) are a special type of high temperature (typically 800÷1100°C) FCs, often considered as the most suitable devices for large stationary power plant applications. They are characterized by several

singular properties, such as the high output powers (reaching megawatts) and the excellent efficiency (until about 70% with the co-generation). Another interesting characteristic is the ability to work with different type of fuels. Beyond hydrogen, SOFCs can operate with alcohols (such as methanol and ethanol) or hydrocarbons. This can offer significant opportunity in renewable energy field taking into consideration fuels derived from bio-masses and urban or industrial rubbish.

A common SOFC usually works at very high temperature (800÷1100°C). These extreme conditions are required to achieve good performances but can cause undesired interface reactions and force to use advanced materials specifically designed at this purpose.

Nowadays, many studies have been carried out to develop new materials able to guarantee the best performances at lower temperatures (500÷700°C) and build the new generation of SOFCs: the so-called Intermediate Temperature Solid Oxide Fuel Cells (IT-SOFCs). Scientists agree that a significant breakthrough could be warranted by the reduction of the working temperature at about 500÷600°C and this means the development of apposite materials.

A brief hint at fuel cell principle and functioning and to the related problems is reported in Chapter 1.

Literature data suggest that the perovskite-based materials can advantageously adopted in the IT-SOFCs. Perovskite are a wide class of oxide based materials characterized by very interesting chemical and physical properties. Moreover, these properties can be tuned in order to achieve the best performances for the cells, by employing different constituting elements and different kinds and amounts of dopant elements.

In this work, two types of perovskites are considered. In particular, the study focuses on two doped lanthanum gallate-based systems ($La_{0.8}Sr_{0.2}Ga_{0.8}Fe_{0.2}O_{3-\delta}$, named LSGF and $La_{0.8}Sr_{0.2}Ga_{0.8}Cu_{0.2}O_{3-\delta}$, named LSGC) and two doped lanthanum cuprate-based compounds ($LaCu_{0.8}Co_{0.2}O_{3-\delta}$, named LCC1 and $La_2Cu_{0.8}Co_{0.2}O_{4-\delta}$, named LCC2). This choice should also allow comparing the influence of dopants on chemical properties. Dopants are required for conductivity improvement but their effect on reactivity still need to be investigated.

The samples have been prepared by means of two wet-chemistry procedure (Pechini process and the Polyacrylamide Gel method) to avoid using the high temperature ceramic route and to study the influence of the preparation procedure. As a matter of fact, this is another important point still not adequately considered.

After a deep characterization by means of X–Ray Diffraction (for the crystallographic structures), X–ray Photoelectron Spectroscopy (for surface investigation) and Diffuse Reflectance Infrared Fourier Transform spectroscopy (to study the functional groups), the reactivity of the samples was investigated. At first, the interaction with methanol and ethanol was considered. These alcohols have been chosen both for their significance as probe molecules and for the possible use as fuels in SOFCs. Because of this reason the catalytic activity of the perovskites was also studied under oxidising atmosphere and in steam reforming conditions. The joint use of IR Spectroscopy and Quadrupolar Mass Spectrometry allowed accomplishing this purpose.

The synthesis of the samples and their characterization are illustrated in Chapter 2, while the reactivity of the four compounds is reported in Chapter 3 to 6.

The catalytic activity in oxygen reduction was also explored by making use of another important property of perovskites: their oxygen permeability. A new permeation chamber was specifically conceived and realized at this purpose. All points concerned with oxygen reduction and the obtained results are explained in Chapter 7.

Chapter 1

Fuel cells

Nowadays, peoples base their comfort on the energy availability. New energy sources are continuously pursued to improve life standards, but most of the required energy is still obtained by fossil fuels such as coal, natural gas and oil. Moreover, the world economy is now deeply influenced by the developing countries, such as China and India, and the energy demand daily grows and oil quotations reach new records day by day. Taking into account the trend for the energy demand, the consumption could reach about $130 \cdot 10^{12}$ kWh/year in 2010 (in 1995 it was about $95 \cdot 10^{12}$ kWh). [1]

It is interesting to point out that oil is not only a strategic energy source, but also an essential pseudo-commodity for the chemical industry. It is worth to underline that about 90% of the crude oil is employed as energy source, while only 10% is dedicated to chemical industry. From this small percentage, about 90% of the chemical commodities are obtained. [2]

The increasing price of oil and the uncertainty about the real supplies suggest that a more rational use of this important source must be done.

Fuel cells (FCs) can be considered as the most suitable device for a better and more sustainable use of energy stocks. [3]

A fuel cell can be described as a device which carries out the electrochemical oxidation of a fuel. In this way, the potential energy of the fuel is directly converted in electrical energy without further transformations which reduce the overall yield.

Thermodynamics of fuel cells

A fuel cell is an electrochemical device which works as a common galvanic cell: the oxidation and reduction half-reactions occur at the anode and the cathode site respectively. The exchanged electrons pass through an external circuit and reach the user, while the electrodes are connected by an ionic conductor (electrolyte). Figure 1.1 shows a simplified representation of a solid oxide fuel cell.

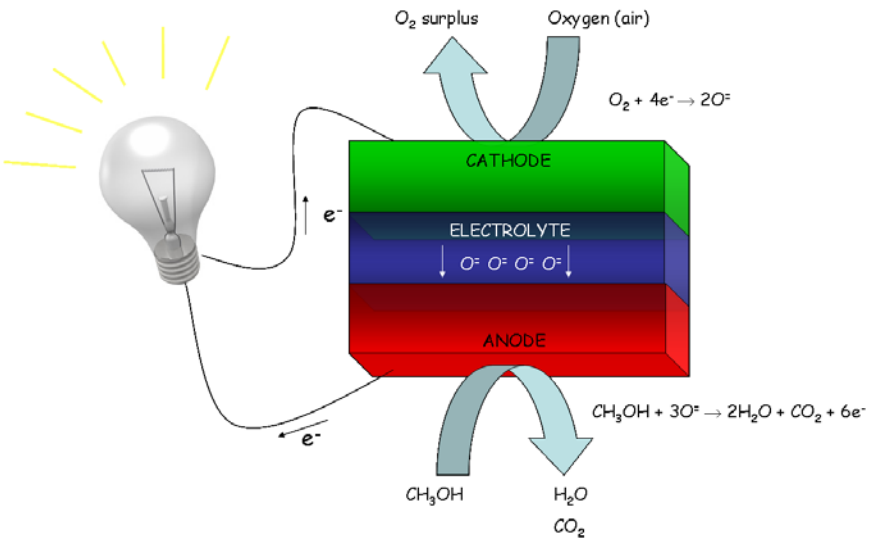

Figure 1.1. Schematic representation of a solid oxide fuel cell.

The given description does not point out the high complexity of the operations in a fuel cell. It is worth to underline that the electrodes work as electrons collector but also act as catalysts for oxidation and reduction reactions. The electrolyte material must be an ionic conductor to avoid short-circuits in the cell. The studies on the FCs have allowed the development of several systems differing in relation to many significant aspects. Nevertheless, all the fuel cells are subject to the same principles.

The overall generic combustion reaction (1) can be considered as the sum of the fuel (compound "*A*") oxidation (2), and the reduction of the comburent (compound "*B*", (3)). During the reaction, *n* electrons are transferred.

$$aA_{red} + bB_{ox} \rightarrow cC_{ox} + dD_{red} \quad (1)$$

$$aA_{red} \rightarrow cC_{ox} + ne^{-} \quad (2)$$

$$bB_{ox} + ne^{-} \rightarrow dD_{red} \quad (3)$$

The electrode potential can be easily obtained by means of the Nernst law (4):

$$E = E° - \frac{RT}{nF} \ln \frac{(red)^{\nu_{red}}}{(ox)^{\nu_{ox}}} \quad (4)$$

Where E is the actual potential at the electrode, $E°$ is the potential under standard conditions, R the universal gas constant, T the absolute temperature, n the number of exchanged electrons, F the Faraday constant and "*red*" and "*ox*" the activities of the reduced and oxidised compounds. ν_{ox} and ν_{red} are the stoichiometric coefficients of the oxidised and reduced compound.
Since the cell potential is given by (5):

$$\Delta E_{cell} = E_{cathode} - E_{anode} = E_{+} - E_{-} \quad (5)$$

The cell potential is (6):

$$\Delta E_{cell} = \Delta E° - \frac{RT}{nF} \ln Q \quad (6)$$

With Q reaction quotient.

For a closed or an open electrochemical system under steady state conditions, with constants temperature and pressure (7):

$$\Delta G = -(w_{el})_{rev} \quad (7)$$

Where ΔG is the free Gibbs energy variation and $(w_{el})_{rev}$ is the reversible electric work.

Since the electric work is defined as the product between charge and potential, it is easy to obtain (8):

$$\Delta G = -nF\Delta E \qquad (8)$$

And (9):

$$\Delta E = -\frac{\Delta G}{nF} \qquad (9)$$

By the obtained equations, it can be seen that the open circuit voltage (OCV, measured at zero current) for a fuel cell only depends on the thermodynamics parameters of the reaction.

When the circuit is closed, and current starts to flow, the cell voltage decreases as a consequence of polarization phenomena. The main causes are related to overvoltage for charge transfer at the electrodes, diffusion (matter transfer), absorption and desorption of the reactants and from ohmic resistance of the electrolyte (figure 1.2).

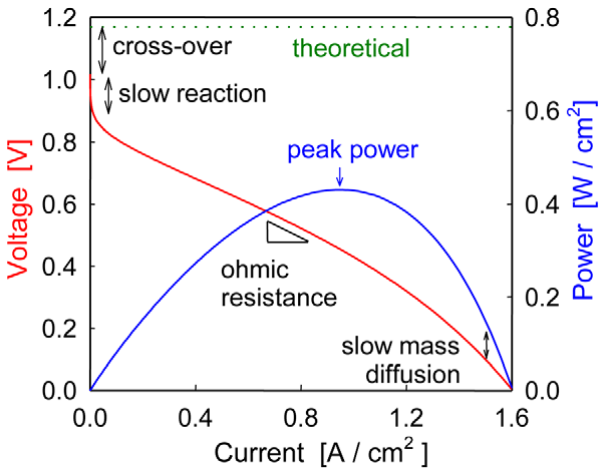

Figure 1.2. Schematic fuel cell polarization and power density curves. [4]

All these phenomena lower the electrochemical work. A suitable parameter for the quantification of a fuel cell performance is the "voltage efficiency", ε_V (10):

$$\varepsilon_V = \frac{\Delta E}{\Delta E_{rev}} \qquad (10)$$

Equation (10) for cell efficiency may be not so useful since free Gibbs energy changes as a function of the operating conditions (for example, pressure and temperature). Taking into account that a fuel cell uses materials that are usually burnt to release their energy, it would make sense to compare the electrical energy produced with the heat that would be produced by burning the fuel. The efficiency obtained is often called "thermodynamics efficiency" (ε_T, equation 11):

$$\varepsilon_T = \frac{\Delta G}{\Delta H} = 1 - \frac{T\Delta S}{\Delta H} \tag{11}$$

The last way to quantify the cell efficiency is related to the "current efficiency" (ε_I). The maximum current produced by each cell is described by the Faraday law (12):

$$I_{\max} = nF\frac{df}{dt} \tag{12}$$

With *df/dt* reaction rate for fuel consuming. In the operating conditions, the current (I) is less than I_{max} and is related to the real *df/dt*. ε_I is than defined as (13):

$$\varepsilon_I = \frac{I}{I_{\max}} \tag{13}$$

Types of fuel cells

As mentioned before, the study on the fuel cell technologies allowed the development of different cells. They are usually classified with respect to the operating temperatures or the employed fuel. With regard to the temperatures, two types of fuel cells can be identified:

1) *low temperature FCs* (with operating temperature 80÷200°C)

The low temperature FCs are considered as the best solution for the applications requiring a quick start-up procedure, such as portable devices or automotive applications.

Alkaline fuel cells (AFCs) are the first type of cells developed by NASA, in early Fifties in relation to the space missions. The AFCs use a KOH aqueous solution as electrolyte, and Ni- or Pt-based electrodes. They offer a very high thermodynamics efficiency but it quickly drop down if not very high purity H_2 is employed as fuel (because of the formation of carbonate species in the electrolyte).

Proton Exchange Membrane (or Polymer Electrolyte Membrane) fuel cells (PEMFCs) are a useful low temperature FCs. They employ a polymeric protonic conductor as electrolyte. The development of the polymer has required the main efforts, since different aspects have been optimized. The studies have improved its stability and the proton conductivity. At this purpose, the water management is a very important point: a low hydration causes low proton conduction, while an excessive water content causes the electrodes flooding. Nevertheless, the PEMFCs are probably the most widely studied FCs.

The *Direct Methanol Fuel Cells* (DMFCs) are low temperature FCs which are classified in relation to the employed fuel: methanol. They directly derive from the PEMFCs technology and employ almost the same electrodes (Pt or Pt-Ru, Re, Rh, Os, alloys) and electrolytes. Moreover an important problem for the DMFCs is related to the so-called "methanol crossover", in other words, the permeation of the fuel through the electrolyte from the anode to the cathode. This phenomenon originates a short circuit which lowers the cell efficiency.

Phosphoric Acid Fuel Cells (PAFCs) are a widespread kind of cells. Their main advantages are the simple realization, and management and the stability in the operating conditions (150÷200°C). The electrolyte is a concentrated phosphoric acid aqueous solution (~85%) which guarantees good proton conduction. The electrolyte solution is embedded in a very stable silicon carbide matrix. The electro-combustion of the fuel (H_2) occurs at the Pt/C-based electrodes.

2) *high temperature FCs* (with operating temperature 600÷1100°C)

Opposite to the low temperature FCs, the cells operating at high temperature are suitable for a stationary use. In fact, they can run for very long time periods producing high output powers (form kilowatts to megawatts), feeding various kinds of users (from houses to hospitals, airports, etc.). Another very important advantages of the high temperature FCs is the possibility of recycling the heat produced during the cell

operations (energy co-generation) thus allowing the yield of the cell to reach high values (about 70 %).

Molten Carbonate Fuel Cells (MCFCs) employ molten lithium, sodium or potassium carbonate in a $LiAlO_2$ matrix, as electrolytes. In these particular devices, the oxide ions are carried from cathode to anode as $CO_3^{=}$. The carbonate anions derive from the interaction between $O^{=}$ and CO_2 (which is obtained as oxidation product at the anode site and is partially recycled at the cathode).

MCFCs usually operate at about 600÷900°C. These conditions allow the use of hydrocarbons as fuel, since their reforming can be obtained directly at the anode site.

The high operating temperature guarantees good reaction rate with less expensive catalysts than Pt: NiO and Ni/Al or Ni/Cr are usually used as cathode and anode electrodes respectively.

Solid Oxide Fuel Cells (SOFCs)

Solid oxide fuel cells (SOFCs) are a very interesting class of high temperature fuel cells since they are probably the most suitable devices for large stationary power plant applications. A SOFC employs a solid electrolyte as oxide ion conductor (figure 1.1). The absence of liquid phases allows to avoid all the questions concerning the liquid management, such as leakages, evaporation, corrosion, diffusion, etc.

The high temperature of SOFCs is advantageous for the processing of common fuels (H_2 but also hydrocarbons and alcohols) and for combined SOFCs/gas turbine power plants. On the other hand, significant disadvantages derive from the long-term stability and the costs of the materials and components. Finally the demanding long start-up time, has to be considered. SOFCs usually operate at about 800÷1100°C; the high temperature is required by the thermally activated transport processes and the electrochemical reactions such as the oxide ion conductivity of the solid electrolyte and different reactions at the electrodes, respectively. Moreover, SOFCs show very high efficiency (up to 50% for the simplest SOFCs, up to 70% for the large pressurized SOFCs-gas turbine systems) and extraordinary overall yields (up to 70÷90%) with the co-generation (heat and power generation). [5]

A decrease in the operation temperatures generally results in decreased of power density and efficiency. Nevertheless, the long-term stability can be improved. The overall costs

may also be reduced using less costly metal alloys for interconnections and external components. Because of these reasons, one of the aims in SOFCs' research is to develop a new generation of SOFCs, the so-called *intermediate temperature solid oxide* FCs (IT-SOFCs), operating at temperatures between 500 and 600°C. [5, 6]

Figure 1.3 well summarizes the advantages and disadvantages for the use of different operating temperatures SOFCs.

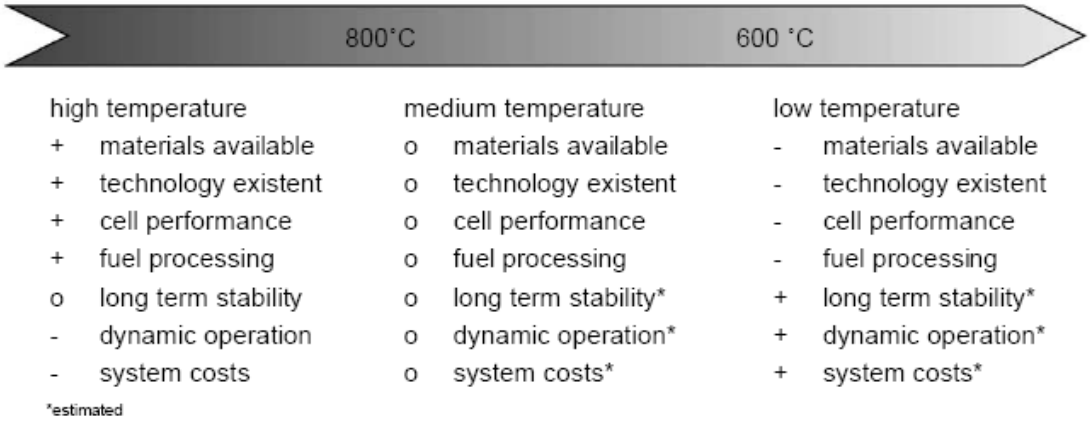

Figure 1.3. Advantages (+) and disadvantages (-) of SOFCs for different temperature ranges (o represent states between + and -).

It is well evident that the new IT-SOFCs achievement needs the detailed investigation of advanced materials for electrode and electrolyte applications, as well as the development of new production and operation technologies.

Moreover, the design of SOFCs has received great relevance in order to optimize the fluid-dynamics and the interconnections in the cell stacks and to improve, therefore, the overall efficiency. The most common SOFCs designs use tubular cell stacks with Siemens-Westinghouse design (figure 1.4a) or Sulzer-Hexis design (figure 1.4b) or planar design (figure 1.5). [3]

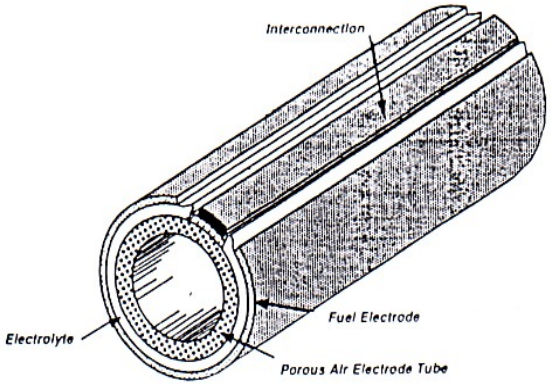

Figure 1.4a. SOFC cell design: Siemens-Westinghouse tubular design.

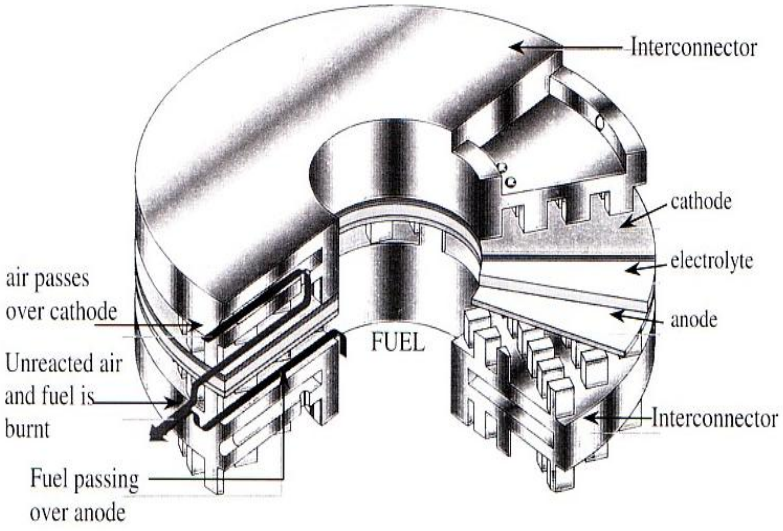

Figure 1.4b. SOFC cell design: Sulzer-Hexis tubular design.

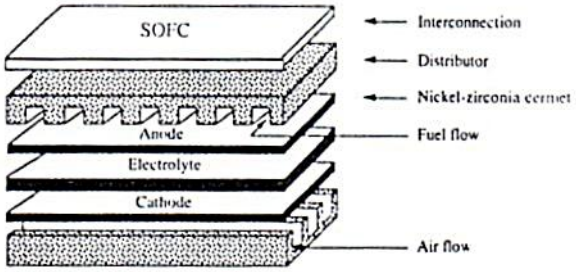

Figure 1.5. SOFC cell design: planar design.

These different designs offer advantages as well as disadvantages but it is always evident that a SOFC is a very complex device whose realization requires advanced materials characterized by well defined chemical, physical and mechanical properties.

Fuels

The choice of the most suitable fuel for FCs is a very important point because the fuel choice influences the required FCs characteristics and vice versa.
Alkaline fuel cells, as an example, need high purity hydrogen (in other words the absence of hydrocarbons) to avoid the absorption of carbon dioxide in the electrolyte and the formation of carbonate species which lower the ionic conductivity. Furthermore the Pt-based electrodes, commonly used for low temperature fuel cells, are deeply poisoned by carbon monoxide absorption, and Pt-Ru alloys have to be employed to improve the resistance.
Another point to be considered concerns the problems connected with hydrogen production and storage. [3] Since no significant H_2 natural resources are present on Earth, it must be produced from other hydrogen-containing compounds. Hydrogen compounds, in fact, are largely diffuses and water represents the more interesting one.
The catalytic water splitting reaction (14) is actually an important challenge for many Researchers. This “simple” reaction allows to obtain high quality hydrogen (carbon free and with a high purity) starting from a very cheap and widely diffused raw reactant.

$$H_2O \rightleftharpoons H_2 + 1/2O_2 \qquad (14)$$

Equation (14) needs, however, an energy source since the water splitting is an endothermic process. Many researcher agree that the photo-catalytic splitting (using solar radiations as primary, clean and free energy source) of water is the best solution for H_2 production. [7, 8, 9]
Other Authors are studying biological ways to obtain bacteria which convert biomasses into hydrogen. [10, 11]
Summarizing, the general ideas involve the H_2 production starting from renewable, clean and cheap sources.

Nevertheless, these interesting environmental-friendly ways need to be improved and H_2 is actually produced mainly starting from hydrocarbon (HCs), alcohols or coal. Small amounts are also obtained from the decomposition of chemical species such as ammonia, hydrazine, metal hydrides or by electrochemical methods.
Hydrogen is produced from HCs or alcohols mainly by steam reforming (15) or by partial oxidation (16) reactions:

$$C_nH_m + nH_2O \rightleftharpoons nCO + (n+1/2m)H_2 \quad (15)$$

$$C_nH_m + n/2O_2 \rightleftharpoons nCO + m/2H_2 \quad (16)$$

Since equation (15) is endothermic, and equation (16) is an exothermic process, they can be coupled into the so-called autothermal reforming.
Finally, H_2 can be obtained by coal gasification (17):

$$C + H_2O \rightleftharpoons CO + H_2 \quad (17)$$

It is worth to point out that carbon containing by-products (CO, CO_2…) will be always produced if hydrocarbons are employed as raw materials.
Beyond the H_2 production, further problems concern its storage. Hydrogen can by liquefied (~20K), pressurized, adsorbed on carbon nanotubes or fibres or chemically converted into suitable chemical compounds such as metal hydrides (for example the so-called “powerballs”: NaH). All these methods have advantages and disadvantages but no one represent the best solution.
Summarizing, hydrogen is certainly the best fuel but its real wide employment is still quite far away. For these reasons alternative fuels have been investigated for fuel cells applications. High temperature FCs, thanks to their operating conditions, can often work directly with hydrocarbons or alcohols.
Alcohols, such as methanol and ethanol, are considered as a suitable answer for the fuels demand. In fact, they are characterized by a high energy density and require a simple management. As a liquid fuel, they can be handled as the common gasoline and the same distribution network can be employed. Furthermore, methanol and ethanol are already widely available.
Methanol was firstly obtained in 1830 by the destructive distillation of wood, while the first methanol plant was realized in 1923 by BASF. Nowadays, methanol is an

important commodity and it is widely produced (about $33 \cdot 10^6$ tons/year) employing $CuO/ZnO/Al_2O_3$-based catalysts starting from CO/CO_2 and H_2. [12]

On the other hand, ethanol can be obtained by fermentation processes, using fully renewable resources such as biomasses and this involves the possibility for a huge reduction of the CO_2 emissions (and so avoid greenhouse effect).

Chapter 2

Perovskite-based oxide materials: a suitable choice for solid oxide fuel cells

In the Chapter 1, the basic operating principles of the fuel cells were explained. The main cell typologies were also briefly described in relation to the operating conditions and the constituent materials. Among them, solid oxide fuel cells (SOFCs) were widely dealt with respect to their characteristics, their advantages, disadvantages and the possible ways to improve them.
In this chapter, innovative materials for SOFCs are described and compared to the classical ones. Moreover, the most suitable synthetic procedures are also treated.

SOFCs: the materials

The primary components of a solid oxide fuel cell are an oxide ion conducting electrolyte, a cathode and an anode as shown in figure 2.1. As mentioned in Chapter 1, a SOFC works at very high temperature, typically 800÷1100°C. These extreme conditions are imposed by thermally activated transport processes in the electrolyte.

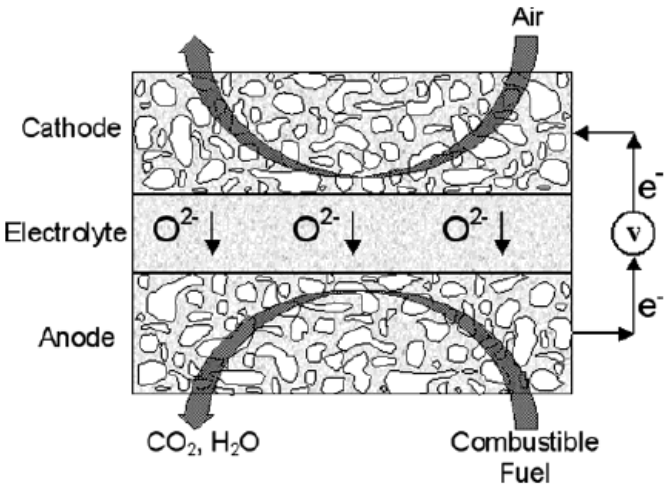

Figure 2.1. Schematic view of solid oxide fuel cell operating principle. [13]

The classic oxide ion conductor is the Yttria Stabilized Zirconia (YSZ, typically 8% Y_2O_3-92% ZrO_2). The yttria addition is required to stabilize the cubic structure of ZrO_2 (otherwise, pure cubic ZrO_2 is stable from 2370°C until the melting point, 2680°C) [14] and to guarantee a sufficient conductivity; nevertheless, YSZ shows a remarkable ionic conductivity only at very high temperature. On the other hand, YSZ is also used for its good mechanical stability under the operating conditions.

The anode is usually a composite ceramic-metallic material (called cermet) made of nickel and YSZ. Metallic nickel provides the catalytic activity for the fuel oxidation and the electronic conductivity, while YSZ guarantees the continuity with the electrolyte (both with respect to the thermal expansion coefficient and chemical composition) and avoids the nickel sintering. Nickel is widely employed thanks to its low cost, mechanical and electrical properties and because it is a good steam reforming catalyst. [13] The last important feature allows to feed the cell directly with hydrocarbons, which are in-situ reformed and used (an external reformer is thus not necessary and the overall system appears more simple). These systems operate near to 96% of thermodynamic efficiency and are tolerant to most impurities. [15]

Nevertheless, the major limitation to Ni-based anodes is that nickel catalyzes carbon deposition at low $H_2O/C_{(fuel)}$ ratios. Concerning this aspect, some Authors investigated the best operating conditions to limit the carbon formation in the direct hydrocarbon fuel cells. [16, 17, 18]

The outcomes suggest that there is a narrow temperature window (550÷650°C) in which carbon is not stable when methane is used as fuel. In fact, the equilibrium constant for

methane dissociation into C and H_2 is strongly shifted toward methane under 650°C and the equilibrium for the Boudouard reaction (disproportion of CO into C and CO_2) is shifted toward CO above 550°C. Moreover, the same opportunity does not exist when ethane is used.

Transition-metal oxides were originally investigated as SOFCs cathode due to their good electrical conductivity and as a relatively low cost alternative to platinum (Pt was firstly considered as cathode before 1965). Since about 1973, the cathode is generally a strontium-doped lanthanum-manganite. The Sr doping provides for oxygen transfer to the cathode-electrolyte interface. Nevertheless, Sr-doped $LaMnO_3$ compounds show a poor ionic conductivity. [19]

It is also interesting to point out that the classical electrodes materials are pure (or almost pure) electronic conductors, while the electrolyte material is a pure ionic conductor. Under these conditions and taking into consideration the cell operations, the fuel oxidation and the oxygen reduction occur in a restrict zone where the electronic conductor, the ionic conductor and the gas phase (which carries the reactants) are very close: the so-called three phase boundary (TPB) region. Figure 2.2a shows the required condition at the anode side, while figure 2.2b schematizes the cathode one (for pure electronic on the left, and composite on the right, cathode).

These limitations strongly reduce the active areas for the electrochemical reactions and contribute to increase the over-potential phenomena.

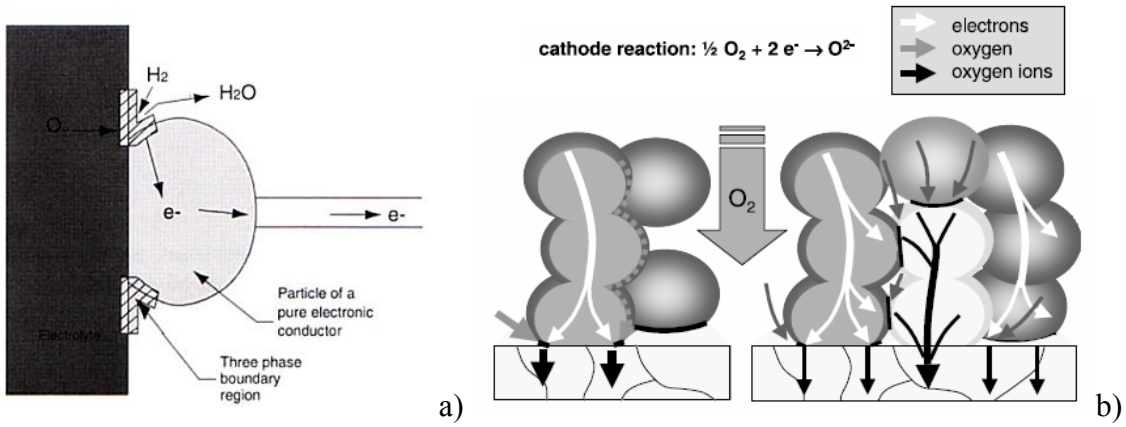

Figure 2.2. Schematization of the three phase boundary (TPB) region for the anode (a) and the cathode (b) sides for pure electronic (electrodes) and ionic (electrolyte) compounds.
The electrodes are symbolized as gray spheres, while the electrolytes are represented as black (a) and white rectangles and spheres (b).

A much better result can be obtained if mixed ionic-electronic conductors (the so-called MIECs) are used as electrodes. A MIEC shows electronic and ionic conductivity at the same time. This important property allows a remarkable enhancement of the active area, since the oxide ions can diffuse into the electrode materials. Figures 2.3a and 2.3b show the improvements at the anode and cathode sides respectively.

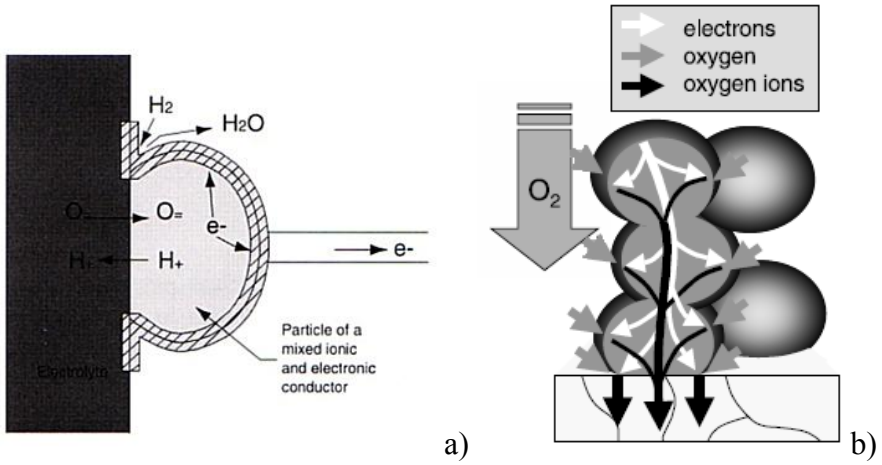

Figure 2.3. Schematization of the active areas at the anode (a) and the cathode (b) sides for mixed electronic-ionic conductor electrodes.
The electrodes are symbolized as gray spheres, while the electrolytes are represented as black (a) and white rectangles (b).

Summarizing, from a physical point of view, the innovative electrode materials should be mixed ionic-electronic conductors, while the electrolyte material must be a pure ionic conductor.

Another important requirement is that, obviously, the components must be characterized by very similar thermal expansion coefficients. This is another critical aspect, since mechanical fractures can occur during the thermal cycles (start-up and turning off).

Moreover, to improve the diffusion of the reactants and promote a better contact between the gas phase and the electrodes, the last ones should be porous (to avoid reagents mixing the electrolytes, in contrast, are required not to be porous).

Figure 2.4. well summarizes the overall characteristics for the fuel cell components.

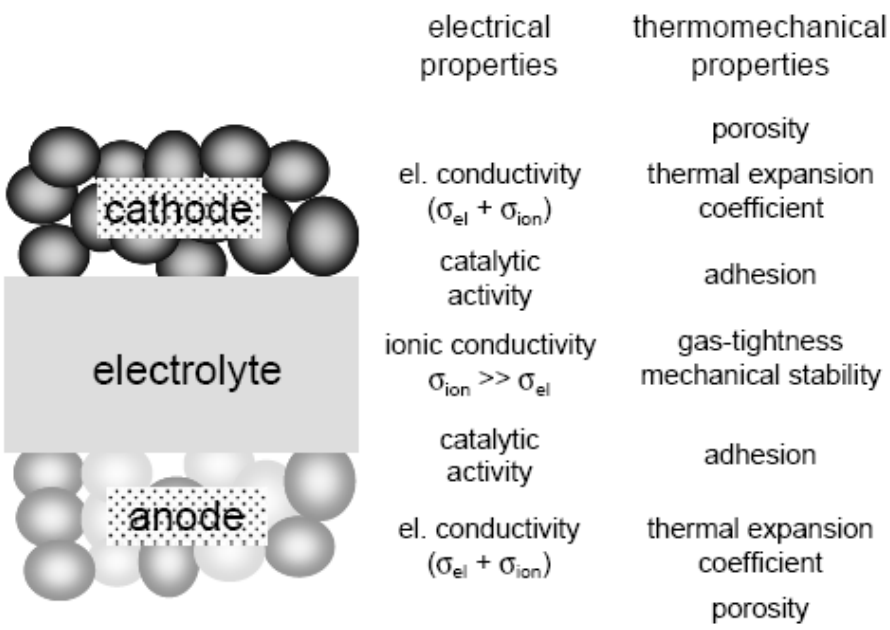

Figure 2.4. Overview for the principal electrical and thermo-mechanical properties required to the fuel cell materials. [5]

Figure 2.4 also specifies another important property required to the electrode materials: they must be good catalysts for the fuel oxidation and for the oxygen reduction. Finally, with respect to the chemical properties, the electrode materials must be compatible with the electrolyte one. In other words, no chemical reactions should occur between the components to avoid the formation of dangerous intermediate phases which can modify the interfacial properties and lower the cell performance.

As specified in Chapter 1, a large number of studies are focussed on the reduction of the operating temperature of the solid oxide fuel cells: a lower temperature allows an improvement in the long-term stability. Furthermore, cheaper materials and procedures for the material processing can be adopted.

In order to reduce the operating temperature, new suitable materials should be prepared. A lower temperature, in fact, causes a worsening in the thermally activated catalytic reactions (at the electrodes) and transport processes (in the electrolyte). The overall result appears as a decrease in the cell performances (output power).
Since the main reason for the high temperature is the achievement of a suitable ionic conductivity through the electrolyte, new electrolyte materials with a better conductivity at lower temperature must be prepared. Figure 2.5 shows the conductivity as a function of temperature for a wide set of electrolytes.

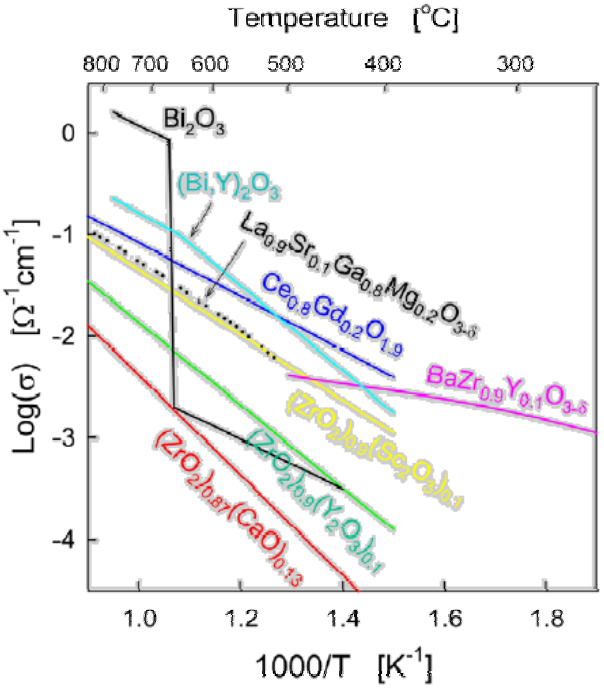

Figure 2.5. Conductivities of selected electrolytes for solid oxide fuel cell applications. [4]

As can be seen from the figure 2.5, the ionic conductivity of the classical zirconia-based compounds is not high enough at the lower temperatures (500÷600°C). Another interesting behaviour is observed for Bi_2O_3. The ionic transport properties of Bi_2O_3 has received a significant academic attention as a consequence of a phase transition at ~700°C which leads to an increase in conductivity by almost three orders of magnitude. In order to stabilize the conducting cubic phase, various kinds of doped compounds were obtained; however, the key limitations of bismuth-based compounds are their very high electronic conductivities and the tendencies to be reduced to metallic bismuth under reducing atmospheres. [4]

CeO_2-based electrolytes also show a good ionic conductivity at low temperature. Nevertheless, they are scarcely resistant at temperatures higher than 600/700°C and in reducing environments, because of the loss of lattice oxygen and the partial reduction of Ce^{4+} to Ce^{3+}. This behaviour modifies the conductivity properties changing the compound into a MIEC. [6, 20, 21, 22, 23, 24]

Another very interesting electrolyte material is a Sr- and Mg-doped $LaGaO_3$-based compound. Since the ionic properties of the material change as a function of the composition, many studies have been accomplished to find out the best one. Beyond

that shown in figure 2.5 ($La_{0.9}Sr_{0.1}Ga_{0.8}Mg_{0.2}O_{3-\delta}$), many Authors agree that a suitable composition is $La_{0.8}Sr_{0.2}Ga_{0.8}Mg_{0.2}O_{3-\delta}$. [25, 26]

Perovskite-based oxide materials [27]

The hint to Sr- and Mg-doped lanthanum gallate allows introducing a new category of substances: the perovskite-based materials.

Perovskite-based compounds are studied since Seventies, in relation to their use as catalysts for worn-out gases. Nowadays, perovskite materials are widely used in catalysis (for example for CO or HCs oxidation or in reduction reactions) and in the preparation of special membranes for oxygen separation, or gas detection.

The name "perovskite" comes from the Russian mineralogist Lev Aleksevich von Perovski and identify the $CaTiO_3$. Beside the first perovskite-type mineral, $CaTiO_3$, many others similar compounds were discovered; all these ones can be generally summarized with an ABX_3-type stoichiometry. A and B are metallic cations, while X is the anion. Most of the perovskite-type materials are oxides, but carbides, nitrides and halides are also known; oxide-based perovskites are widely diffused minerals since about 90% of the metallic elements are stable in the perovskite structure.

The structure of an ideal perovskite is schematized in figure 2.6: in a cubic lattice, the A-type cation stays in the centre of the cube (12-folds coordinated by oxide ions), while the B-type cations occupy the apexes (6-folds coordinated). The oxygen anions are at the middle of each edge.

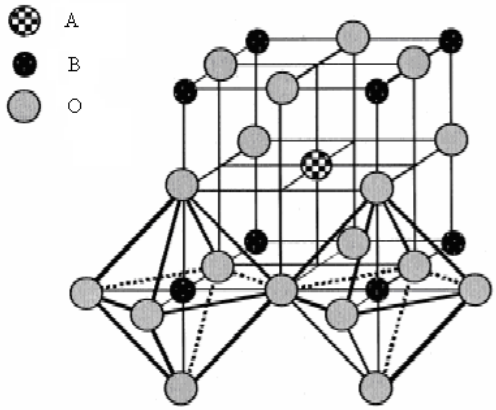

Figure 2.6. Schematization of the ideal perovskite structure.

In order to realize the described structure, it is necessary to satisfy some geometrical characteristics. In particular, for an ideal cubic structure is (1):

$$r_A + r_O = \sqrt{2}(r_B + r_O) \quad (1)$$

Where r_A, r_B and r_O are the ionic radii of the elements.
Nevertheless, the ideal structure is rarely realized and various kinds of distortions are observed. The most common structures are tetragonal, orthorhombic or rhombohedral. Since many metallic elements (with different geometric characteristics) can crystallize as oxides in perovskite structure, the tolerance factor, *t*, is introduced as follow (2):

$$t = \frac{r_A + r_O}{\sqrt{2}(r_B + r_O)} \quad (2)$$

The perovskite structure is retained for $0.75 \leq t \leq 1$.
The perovskite structure ABO_3 belongs to the wide category of the Ruddelsden-Popper's structures: $(AO)_m[ABO_3]_n$. The scripture indicates the regular periodicity of *m* rock-salt planes and *n* perovskite-like planes. In the case of $m = n = 1$ the A_2BO_4-type compounds can be found.
A very interesting feature of the perovskite-based materials concerns the possibility of modifying their basic properties by introducing suitable dopant elements, on the *A*- or *B*-type cations. A doped compound can be written as: $A_{(1-x)}A'_xB_{(1-y)}B'_yO_{3-\delta}$, where the dopant elements are identified as *A'* and *B'* and their amounts *x* and *y* substitute an equal amount of the main elements, *A* and *B*. Finally, the oxygen amount is labelled as "3-δ". Since the doping may be aliovalent, the real amount of oxygen can slightly differ from the ideal value; the oxygen non-stoichiometry is generally summarized in the term "δ" (which can be positive or negative). It is interesting to point out that the doping can generate a large number of vacancies to balance the different valence states. Moreover, the electro-neutrality can also be obtained with the partial oxidation or reduction of the cations, achieving unusual valence states, such as Fe(IV), Co(IV) or Cu(III).
Oxygen excess non-stoichiometry in perovskite oxides is not as common as anion-deficient non-stoichiometry probably because introduction of interstitial oxygen in perovskite structure is thermodynamically un-favourable.

The ABO_3 perovskites display several interesting physical properties such as ferroelectricity ($BaTiO_3$), ferromagnetism ($SrRuO_3$), weak ferromagnetism ($LaFeO_3$), superconductivity ($YBa_2Cu_3O_7$), insulator-to-metallic transitions of interest for thermistor applications ($LaCoO_3$), fluorescence compatible with laser action ($LaAlO_3$: Nd), and transport properties of interest for high temperature thermoelectric power (La_2CuO_4).

In particular, perovskites show wide variations in the electrical conductivity. Several compounds have been used for their dielectric properties, while others show metallic conductivity, although most are semiconductors. As for other compounds, the electrical behaviour in perovskites depends on the outermost electrons, which may be localized at specific atomic sites or may be collective.

Concerning the catalytic application of perovskites, the identification of the nature and structure of the exposed sites on the surfaces as well as the possible involvement of these sites in catalytic reactions have frequently been studied by the adsorption of suitable probe molecules. Both the equilibrium and the kinetics of adsorption and, in some cases, the desorption of molecules from the surface were analyzed.

As widely shown in Chapter 1 and above, the materials for fuel cell applications need particular electrical (type of conductivity), chemical (catalytic activity) and physical (thermal expansion coefficient) properties. In a perovskite-type compound, these characteristics can be adjusted by doping.

Concerning the electrolyte compounds, as an example, the electric insulator $LaGaO_3$ [28] is converted into the oxide ions conductor by doping with strontium and magnesium. The obtained material (often named LSGM) shows very interesting electrical properties at low temperature (500÷600°C) and can be adopted in a solid oxide fuel cell.

Ionic conduction is not yet fully understood but a “jumping” mechanism such as the one shown in figure 2.7 has been hypothesized; however mechanisms involving grain boundaries have also to be considered.

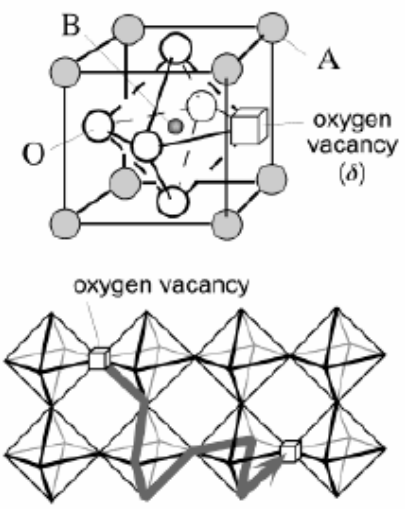

Figure 2.7. Schematization of the oxide transfer through oxygen vacancies ("jumping" mechanism).

Starting from this important outcome and taking into account the literature data concerning the new trends for the SOFCs technology, several perovskite-based compounds are here considered.

Investigated compounds

In this research project, four types of perovskite-based oxide materials have been considered:

1. $La_{0.8}Sr_{0.2}Ga_{0.8}Fe_{0.2}O_{3-\delta}$ (LSGF)
2. $La_{0.8}Sr_{0.2}Ga_{0.8}Cu_{0.2}O_{3-\delta}$ (LSGC)
3. $LaCu_{0.8}Co_{0.2}O_{3-\delta}$ (LCC1)
4. $La_2Cu_{0.8}Co_{0.2}O_{4-\delta}$ (LCC2)

Ishihara et al. [29] observed a good chemical stability for the LSGF-based systems in reducing atmosphere. Moreover, these materials show a significant activity as redox catalyst.

The investigated LSGC-based compound ($La_{0.8}Sr_{0.2}Ga_{0.8}Cu_2O_{3-\delta}$) has no references in literature and its composition was planned in relation to the LSGM stoichiometry and the properties of the copper-containing catalysts in the methanol oxidation. In fact,

many Authors agree that copper ions are very interesting active sites in the methanol oxidation. [30, 31, 32]

Finally, it is worth to underline that LCC1 and LCC2 differ with respect to their crystallographic structure: LCC1 has the ABO_3 stoichiometry, while LCC2 is an A_2BO_4-type compound. This difference could significantly affect the sample properties and behaviour and particularly the reactivity.

Synthetic procedures

The synthetic procedures play a key role in the preparation of the catalysts and for a heterogeneous catalyst, in particular, the surface properties are of primary importance. In relation to the specific application, a catalyst can be employed in different allotropic states, with different surface terminations (chemical groups) or, even more, with specific exposed faces.

Because of these reasons, the choice of the more suitable synthetic route can significantly affect the catalytic activity. The preparation of a complicated compound such as a multi-element perovskite, often requires special procedures to avoid phase segregations or the sintering of the catalyst.

The synthesis of a mixed oxide is classically carried out by means of the so-called "ceramic route". [33] It involves intimate mechanical mixing of oxides, carbonates, acetates or nitrates and repeated grinding and heating cycles to achieve the complete reaction between all reactants. However, despite the advantage of its simplicity, this technique has clear disadvantages since it produces large grains (1÷10 μm) and requires multiple repetitions of thermal treatments (typically at 1300÷1700°C) and grinding. As a consequence, uncontrolled crystallites growth can occur, which could induce chemical and grain-size non uniformity.

Synthesis using wet chemistry, often called the "chemical route", can overcome many of these disadvantages. The homogeneity of the product is expected to increase because the mixing of the reagents occurs at the molecular level, in solution. The resulting oxide powders have a high specific surface area and, consequently, a high reactivity, which decreases the final temperature treatment and time of synthesis.

Unfortunately, these methods are time consuming if large quantities of fine powders are required. Moreover, achieving high homogeneity for complex compositions (involving

a large number of cations) might become very difficult owing to the generally different chemical behaviour of each cation.

Different chemical routes are known to produce fine ceramic powders. The most common are the co-precipitation, the citrate method and the Pechini method; the polyacrylamide gel method is also very interesting. In the first cited process, the precipitation of the cations as hydroxide is induced by basification of the raw solution. The solid mixture is then calcined to achieve the ceramic powder. This procedure appears very simple, but unhelpful if sequential precipitation occurs thus originating highly heterogeneous precursors. The others three methods involve the formation of stable metal-ligand complexes and their dispersion into a homogeneous means such as a polymer. The following thermal treatments (typically at temperature ≤1000°C) allow to decompose the polymer network and to obtain the ceramic powder.

In this work the investigated substances are produced by means of Pechini process and polyacrylamide gel method starting from the oxides of the elements as raw precursors. Table 2.1 summarizes the characteristics of the employed chemicals. [33, 34, 35, 36, 37]

In the Pechini process, citric acid and ethylene glycol (each one with molar ratio 1:1 with respect to the total amount of cations) are added to a clear solution obtained by the mineralization of the precursors with HNO_3; the obtained solution is then heated at 70÷80°C to evaporate the aqueous solvent and obtain the gel. The mixture is then slowly heated at 110°C for 1 h (to complete the solvent evaporation) and at 400°C for 2 h to remove the polymeric network.

In the polyacrylamide gel method, the metal cations solution (obtained by mineralization of the precursors with HNO_3) is basified with an ammonia solution until pH 7 is achieved. A stoichiometric amount of EDTA (with respect to the total amount of cations), acrylamide (6 g) and N, N' methylenebisacrylamide (1 g, as cross-linker) are then added to the solution. At this purpose, particular attention has to be paid to the complexing agent choice, because only a quantitative complexation can guarantees an adequate polymerization of acrylamide.

The mixture is heated at 80°C and H_2O_2 is added as the polymerization starter. After the polymerization reaction, the gel is slowly dehydrated at 110°C and calcined at 400°C. The decomposition of the polyacrylamide gel is a dangerous step since it tends to auto-ignite and explode. To avoid these phenomena it is necessary to treat small portions and slowly warm up the material.

The powders obtained after the treatment at 400°C need further calcination in order to achieve the desired crystallographic phase. Previous works on very similar compounds ($La_{0.6}Sr_{0.4}Co_{0.8}Fe_{0.2}O_{3-\delta}$) [38] suggest that a thermal treatment at 900°C can be sufficient.

It is worth to underline that the powders obtained from the polyacrylamide gel appear "less compact" (in other words, characterized by a lower density) with respect to the correspondent sample obtained by means of the Pechini method. This can be an important consideration with respect to the surface specific area, and then to the catalytic activity.

Table 2.1. Specifics of the used reactants.

Reactant	Purity (%)	Supplier
Lanthanum oxide	99.9	Aldrich
Strontium carbonate	99.9+	Aldrich
Cobalt (II) oxide		Aldrich
Iron powder -325 mesh	99.9+	Aldrich
Gallium (III) acetylacetonate	99.99+ (Ga)	Strem Chemicals
Copper (II) oxide	99.999	Strem Chemicals
Citric acid anhydrous reagent ACS	99.5	Acros Organics
EDTA	99	Acros Organics
Ethylene Glycol	99+	Acros Organics
Acrylamide	98.5	Acros Organics
N, N' methylenebisacrylamide	96	Acros Organics
Ammonia solution 30%		Carlo Erba
Nitric acid 65%		Carlo Erba
Hydrogen peroxide 35%		Aldrich

Chapter 3

$LaCu_{0.8}Co_{0.2}O_{3-\delta}$ (LCC1)

Synthesis

The perovskite-type $LaCu_{0.8}Co_{0.2}O_{3-\delta}$ was prepared by Pechini process (the corresponding compound is named “LCC1 Pec”), and Polyacrylamide Gel method (compound named LCC1 Gel). The procedures are widely described in Chapter 2. In both cases, the obtained powders were heated at 900°C for 5 h in air.

Characterization

XRD

The obtained products were characterized firstly by X Ray Diffraction; the figure 3.1 shows the XRD patterns for LCC1 Pec and LCC1 Gel.

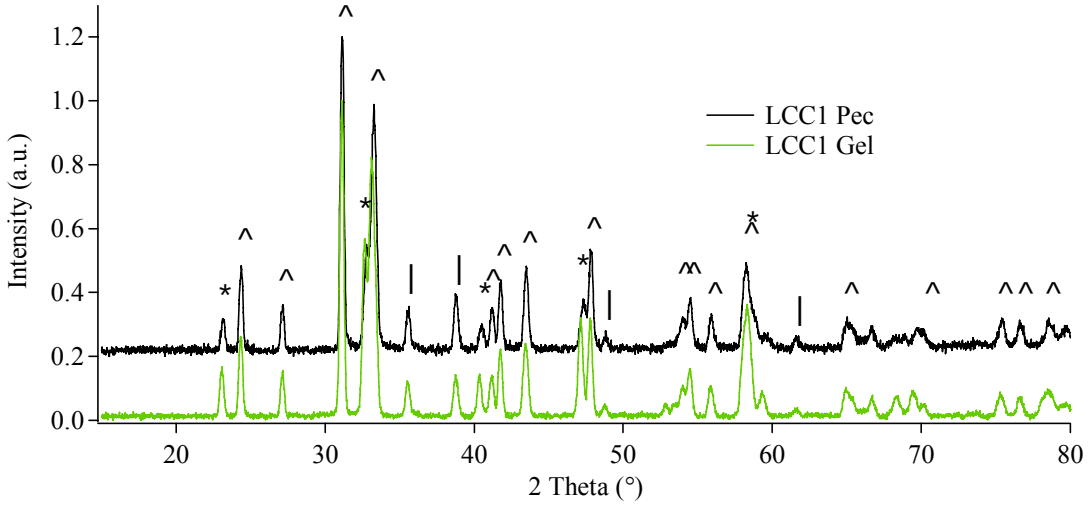

Figure 3.1 XRD patterns for LCC1 Pec (—) and LCC1 Gel (—). The markers stand for: $La_2Cu_{0.8}Co_{0.2}O_4$ (^), CuO (|) and $LaCoO_3$ (*). The spectra are shifted for a better comprehension.

By comparing the obtained data with the JCPDS database, several crystallographic phases can be identified; table 3.1 summarizes the observed ones. Regardless the synthetic procedure, the most evident outcome is the absence of the desired phase, $LaCu_{0.8}Co_{0.2}O_3$, and the presence of another kind of perovskite structure: $La_2Cu_{0.8}Co_{0.2}O_4$. Reflections characteristic of CuO and $LaCoO_3$ phases are also present.

Table 3.1. XRD compositions obtained for LCC1 Pec and LCC1 Gel.

sample	*main phase*	*minor phases*	*crystallographic lattice*	*JCPDS number*
LCC1 Gel and LCC1 Pec	$La_2Cu_{0.8}Co_{0.2}O_4$		orthorhombic	79-0453
		CuO	monoclinic	45-0937
		$LaCoO_3$	rhombohedral	86-1663

Literature data suggest that the highly oxidised $LaCuO_3$ structure can be more easily obtained under very high oxygen partial pressure. Furthermore, it has to be considered that $LaCuO_3$ loses oxygen when heated in air (or inert gas) changing into more stable La_2CuO_4. [39, 40, 41]

Consistently, the presence of CuO can be explained: the starting amounts of the precursors materials were calculated for $LaCu_{0.8}Co_{0.2}O_3$ stoichiometry and the overabundance of copper segregates as CuO.

The behaviour observed for the sample LCC2 confirms this hypothesis: in this case, the starting amounts of precursors were set for the phase $La_2Cu_{0.8}Co_{0.2}O_4$ and the segregation of CuO was never observed (see Chapter 4).

Finally, the evidence for $LaCoO_3$ phase, induces to think that the main perovskite $La_2Cu_{0.8}Co_{0.2}O_4$ has a slight deficiency in cobalt with respect to the nominal value.

It is interesting to note that the ABO_3 phase can be obtained by adding strong oxidising compounds in the precursors mixture. Karppinen et al., [39] for example, add a large excess of $KClO_4$ as external oxygen generator. Nevertheless, the decomposition of these oxidising agents leave some undesired by-products (for example KCl from $KClO_4$).

It is worth to underline that the synthesis of a compound like lanthanum cuprate with ABO_3 structure, was tried with Pechini and polyacrylamide gel methods for the first time: the activity of nitrates (introduced in large amount with HNO_3 in the mineralization step), as clean oxidising agent in helping the formation of the desired phase, was tested and revealed to be insufficient.

XPS

The samples LCC1 Gel and LCC1 Pec were analyzed by X-ray Photoelectron Spectroscopy. The obtained outcomes are shown in figure 3.2 (extended spectra) and 3.3 (detailed spectra). The following tables 3.2 and 3.3 summarize the peaks positions (binding energies, eV) and the surface compositions (atomic %) respectively. All BEs values are corrected for the charging effects by assuming C1s at 285.0 eV.

By observing the extended spectra, it can be seen that there are no pollutants elements except for adventitious carbon.

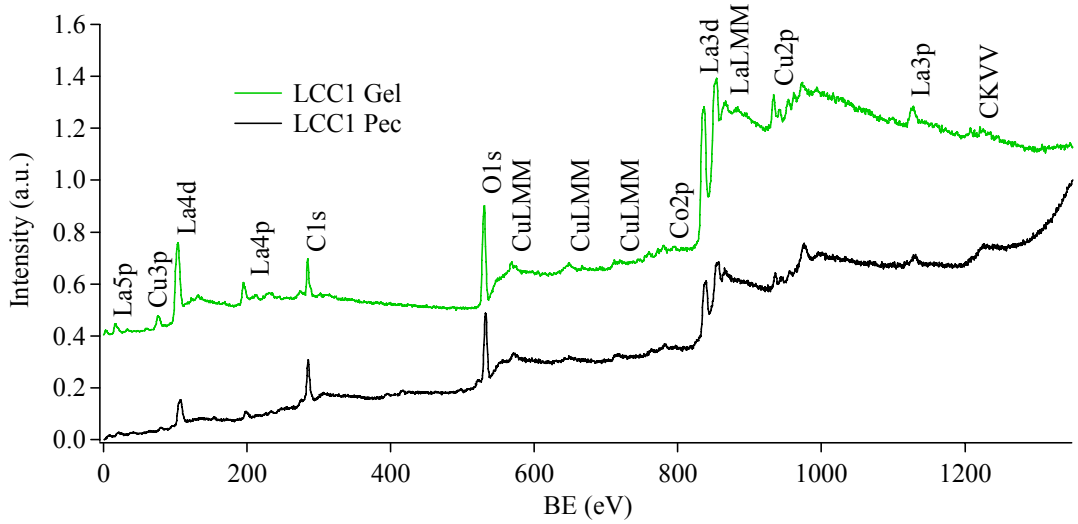

Figure 3.2. Extended XP spectra (surveys) obtained for LCC1 Gel and Pec. The spectra are shifted for a better comprehension.

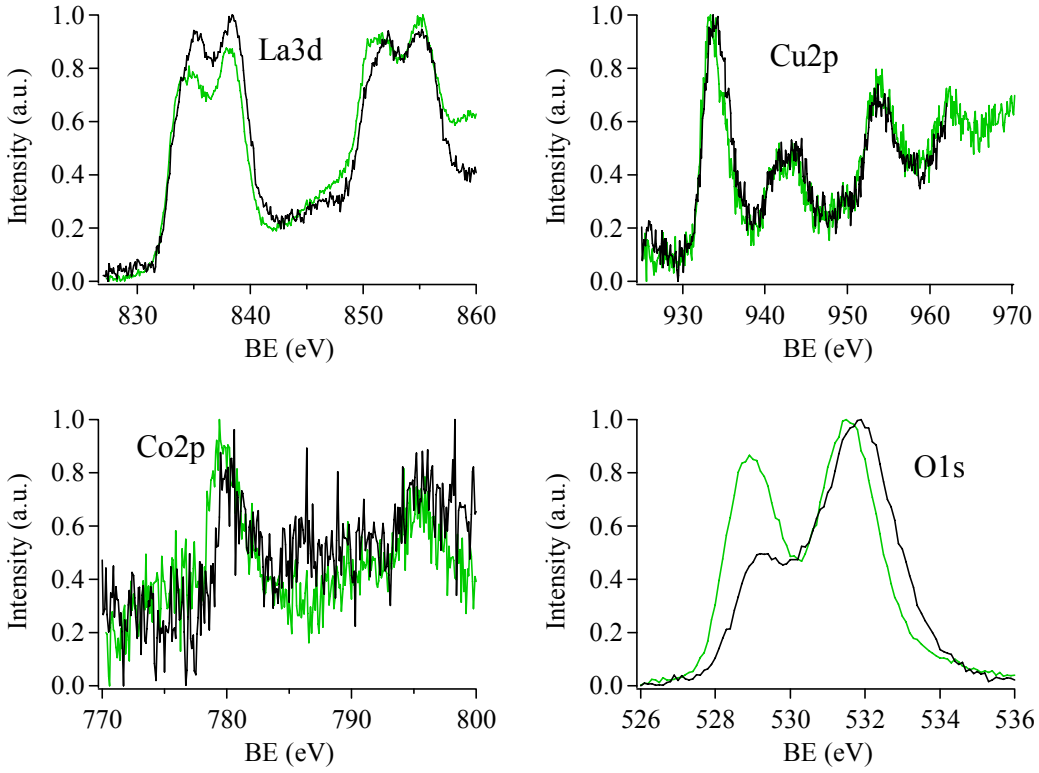

Figure 3.3. XP spectra for La3d, Cu2p, Co2p and O1s for LCC1 Pec (—) and Gel (—). All spectra are normalized with respect to their maximum value. [1]

Table 3.2. XPS peak positions (binding energy, eV) obtained for LCC1 Gel and Pec. Literature data are also reported for comparison.

sample	*ref*	*BE (eV)*						
		$La3d_{5/2}$ and $_{3/2}$		$Cu2p_{3/2}$ and $_{1/2}$		$Co2p_{3/2}$	$O1s_{(lattice)}$	$O1s_{(OH, CO3)}$
LCC1 Pec		835.1	852.0	933.9	953.9	780.1	529.3	531.8
LCC1 Gel		834.5	851.5	933.7	954.1	779.6	529.0	531.5
$La_{1.8}Sr_{0.2}CuO_4$	30			933.2	952.8			
$La_{0.8}Sr_{0.2}Co_{0.8}Fe_{0.2}O_3$	38	834.4					529.7	531.4
$LaCuO_3$	39			933.2				
La_2O_3	42	833.7					530.1	
Co_2O_3	42					780.7	529.9	
CuO	42			933.6				
Co_2O_3	43					779.9		
$La(OH)_3$	44	835.0						
CuO	45			933.6			529.6	
La_2CuO_4	45	833.6		932.6				
La_2CuO_4	46			933				
$La_{0.6}Sr_{0.4}CoO_3$	47	833.4						
$La_{0.7}Sr_{0.3}MnO_3$	48	833.7						

[1] XP spectra are obtained with Al monochromatic source for LCC1 Gel and Mg standard source for LCC1 Pec.

Table 3.3. XPS and nominal compositions (atomic %) for LCC1 Gel and Pec.

sample	*LCC1 Pec*		*LCC1 Gel*		*nominal composition*	
					oxide	cations
element						
La	20	65	12	66	22	50
Cu	8	27	5	27	18	40
Co	2	8	1	7	4	10
O	70		82		56	

The lanthanum 3d peak positions and shape agree with the presence of La(III) compounds: the well evident shake-up contributions at ~838 eV and ~855 eV confirm the observation. In particular, looking at LCC1 Gel, the BE appears similar to that reported for perovskite-type materials. In LCC1 Pec, otherwise, the higher value for BE suggests the presence of a contribution arising from $La(OH)_3$. Concerning Cu2p, the peak shape, and the well pronounced shake-up peaks at about 943 and 962 eV, show that Cu is present as Cu(II). Furthermore, the comparison with literature data suggests that Cu is present as CuO. The Co2p XP spectra appear with a low signal to noise ratio (because of the very low amount). This feature does not allow to prove the valence state of Co.

O1s photoelectronic peak consists of two contributions. The one at lower BE is related to lattice oxide in the perovskite phase while the second one, at about 531.5 – 531.8 eV, refer to hydroxyl and carbonate groups. Looking at the $O_{lattice}/O_{OH\text{-}CO3}$ ratio, LCC1 Gel shows a higher value.

Table 3.3 shows the XPS and the nominal compositions obtained for LCC1 Gel and Pec. The nominal values are calculated taking into account the amounts of the metal precursors introduced during the synthesis. The oxygen amount is determined considering the charge balance. It is worth to underline that the calculation do not take into account the formation of A_2BO_4 phase, but only the real amounts of the precursors.

Concerning the compositional data, table 3.3 always shows a high oxygen amounts. This is not surprising and can be related to surface terminations such as hydroxyl and carbonate groups. Taking into consideration the only cations, the compositions are quite similar in LCC1 Gel and LCC1 Pec (thus suggesting that the preparative procedure does not affect the surface composition). Furthermore, the surfaces are lanthanum enriched (probably due to the reactivity of this element toward atmosphere [49]) while copper tends to diffuse into the bulk. It is now convenient to underline that the perovskite compounds often tend to be poor in the B-site cations. [50] Finally, cobalt shows only a slight decrease with respect to the nominal value.

DRIFT

Diffuse reflectance infrared spectra were recorded for LCC1 Gel and Pec and figure 3.4 summarizes the results.

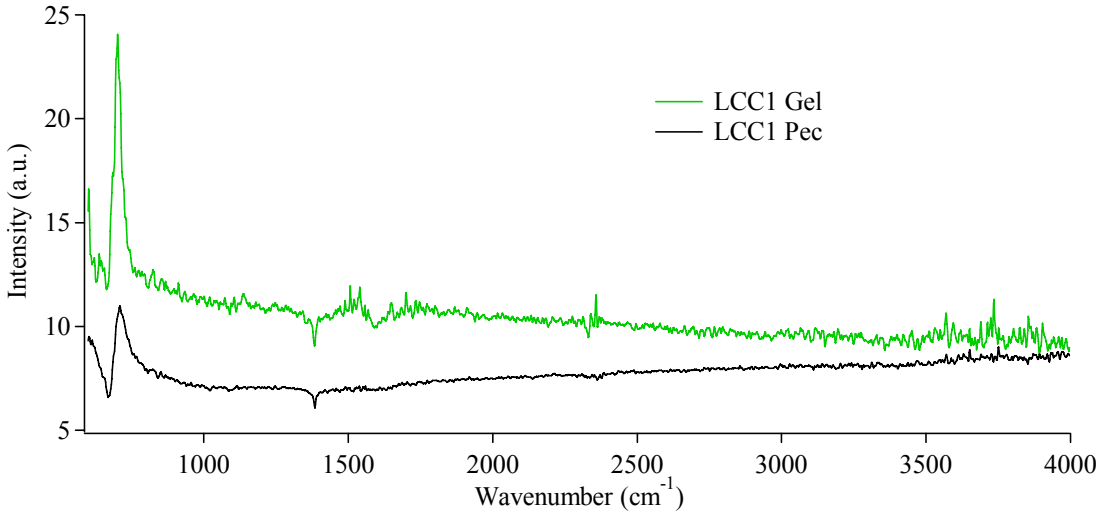

Figure 3.4. DRIFT spectra obtained at RT for LCC1 Gel and Pec. Region between 600 and 4000 cm^{-1}.

As can be seen, both spectra appear poor of signals and the only remarkable peaks are assignable to lattice vibration modes (about 702 cm^{-1}). No changes were detected rising up the temperature and only a slight background increase was observed.

Reactivity toward methanol and ethanol: chemisorption tests

After the characterization, LCC1 Pec and LCC1 Gel were investigated in relation to their use as anodic materials in solid oxide fuel cells.

As mentioned in Chapter 1, methanol and ethanol are considered suitable fuels instead of hydrogen. Because of this reason, the reactivity of the prepared compounds was investigated by means of FTIR and QMS between RT and 400°C under different conditions: in presence of pure alcohol vapours, under oxidizing atmosphere (by enriching the carrier gas with O_2) and in steam reforming conditions (see appendix B).

To better investigate the interactions between the samples and the alcohols, chemisorption experiments (investigated by DRIFT) were carried out for the samples LCC1 Gel and Pec prior to the activity investigations. Figure 3.5 and 3.6 show the DRIFT spectra obtained after exposing the LCC1 Gel sample to methanol and ethanol

vapours at temperatures between RT and 200°C. The spectra obtained after Argon evacuation for 5 minutes (80 $cm^3 \cdot min^{-1}$) are also shown.

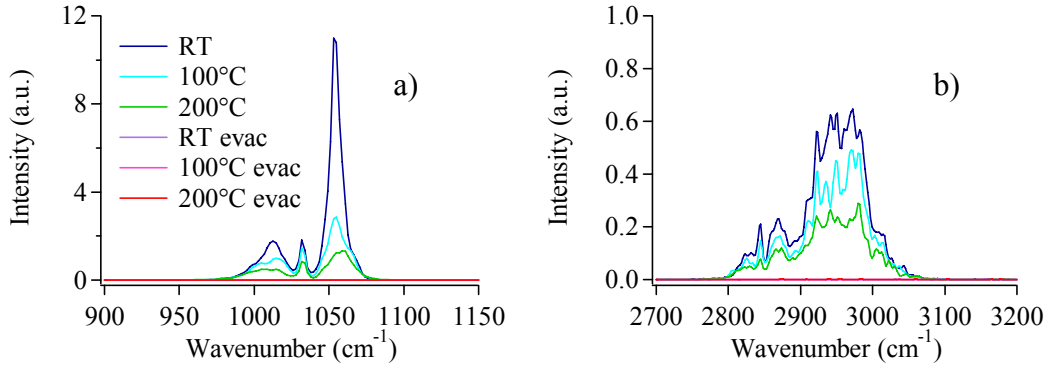

Figure 3.5. DRIFT spectra obtained after exposing the LCC1 Gel sample to methanol vapours at different temperatures and after evacuation with Argon; a) region between 900 and 1150 cm^{-1}, b) region between 2700 and 3200 cm^{-1}.

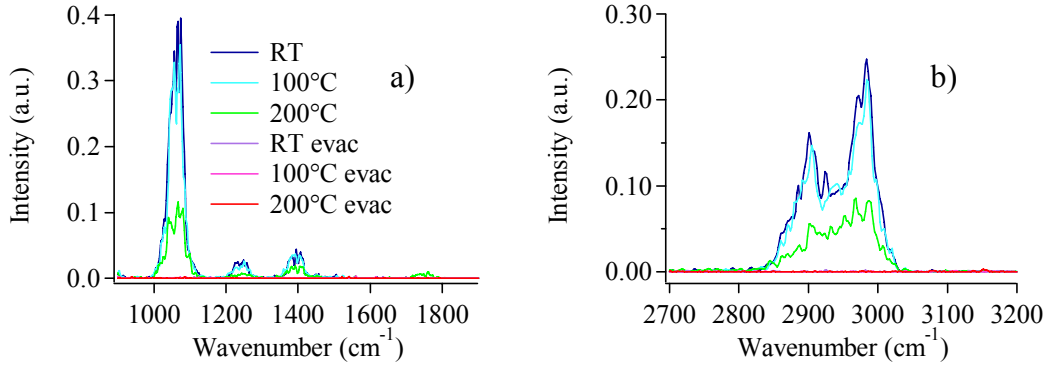

Figure 3.6. DRIFT spectra obtained after exposing the LCC1 Gel sample to ethanol vapours at different temperatures and after evacuation with Argon; a) region between 950 and 1900 cm^{-1}, b) region between 2700 and 3200 cm^{-1}.

The performed measurements are always consistent with the presence of pure methanol, as testified by the characteristics bands due to C-O stretching (1034 cm^{-1}) and C-H stretching (2850 and 2950 cm^{-1}) modes (figures 3.5 a and 3.5 b, respectively). No reactions occur between RT and 200°C since no reaction products have been observed. The spectra recorded after evacuation never show residual signals arising from chemisorbed species.

The outcomes of the ethanol chemisorption test are similar to those obtained for methanol. The bands in figure 3.6 a are assigned to C-O stretching (1066 cm^{-1}) and C-H bending modes (1240 and 1394 cm^{-1}) in gaseous ethanol, while in figure 3.6 b, the C-H stretching modes (2900 and 2980 cm^{-1}) are evident. Nonetheless, at 200°C a weak band

at about 1750 cm^{-1} is evident. This type of signal is consistent with the C-O stretching modes for gaseous acetaldehyde (probably arising from the dehydrogenation of ethanol). The spectra recorded after the evacuation confirm the absence of chemisorbed species. The results of the chemisorption tests performed on LCC1 Pec are very similar to those shown for LCC1 Gel.

Activity toward methanol and ethanol: catalytic tests

Methanol and ethanol vapours

The catalytic tests performed on LCC1 Gel and Pec toward pure methanol vapours show interesting features. In figure 3.7 QMS intensities obtained for methanol, hydrogen, carbon monoxide and carbon dioxide are displayed as a function of temperature. To facilitate the comparison, QMS data are always normalized with respect to the intensities of the fuels (set to 1 for methanol or ethanol). Because of this reason, these results can only give a qualitative idea of the activity of each catalyst, while quantitative data concerning conversions and yields will be given beyond. As it can be seen, the catalytic activity starts at about 200°C.

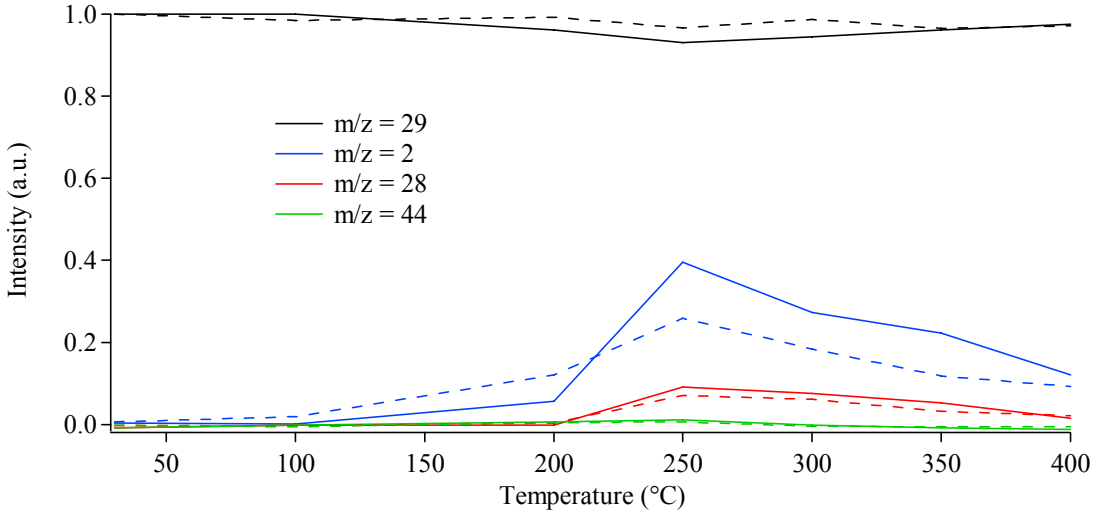

Figure 3.7. QMS data obtained for m/z = 29 (methanol), m/z = 2 (hydrogen), m/z = 28 (carbon monoxide) and m/z = 44 (carbon dioxide) at the investigated temperatures in the test with pure CH_3OH. The intensities of m/z = 2, 28 and 44 are magnified 3 folds. Solid lines stand for LCC1 Gel, dashed lines for LCC1 Pec.

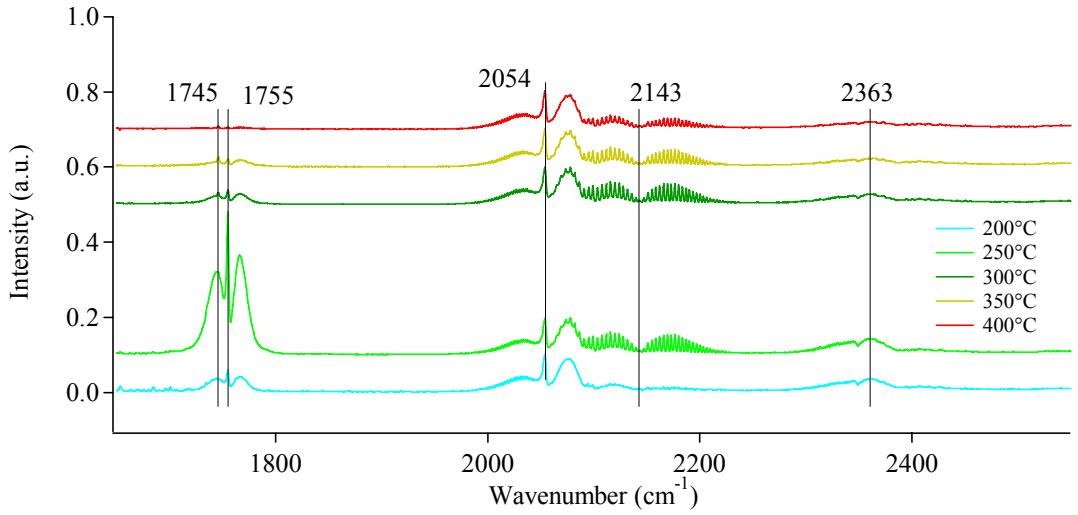

Figure 3.8. FTIR spectra obtained after exposing LCC1 Gel to CH_3OH vapours (gas mixture from the reactor). Region between 1650 and 2550 cm^{-1}. The spectra are shifted for a better comprehension.

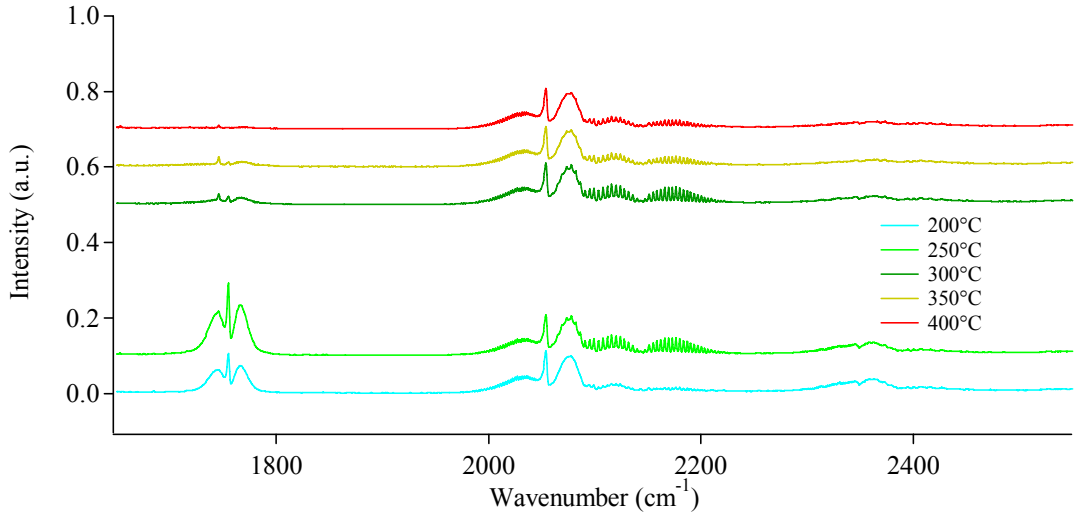

Figure 3.9. FTIR spectra obtained after exposing LCC1 Pec to CH_3OH vapours (gas mixture from the reactor). Region between 1650 and 2550 cm^{-1}. The spectra are shifted for a better comprehension.

QMS and IR data (figure 3.7 and figure 3.8 for LCC1 Gel and 3.9 for LCC1 Pec) suggest that the catalytic activity starts at about 200°C. At this temperature, the only detected products are hydrogen and methyl formate (band at 1755 cm^{-1}); the band centred at 2054 cm^{-1} is the overtone of C-O stretching of methanol. As the temperature grows up, new contributions from carbon monoxide (band centred at 2143 cm^{-1}), carbon dioxide (2363 cm^{-1}) and formic acid (small peak at 1745 cm^{-1} overlapped to methyl formate band) are evident.

Reactivity slightly changes as a function of temperature. Both catalysts reach the highest activity at 250°C then, the signals from hydrogen and CO decrease; those from

methyl formate, formic acid and CO_2 decrease and disappear at the highest temperature (400°C). A similar behaviour can be observed for LCC1 Gel and LCC1 Pec; the only distinctions concern the amounts of the products: LCC1 Gel always guarantees a better activity than LCC1 Pec.

Literature data suggest that methyl formate is an important intermediate in reactions involving methanol when Cu-based catalysts are employed. It can be found both in methanol synthesis and decomposition. [51, 52] Rodriguez-Ramos et al. indicate that methyl formate is formed in methanol dehydrogenation at about 200÷240°C and at higher temperatures it rapidly decomposes toward carbon monoxide and hydrogen (reactions 1 and 2).

$$2CH_3OH \rightleftharpoons HCOOCH_3 + 2H_2 \quad (1)$$

$$HCOOCH_3 \rightleftharpoons 2CO + 2H_2 \quad (2)$$

Methyl formate can also decompose in carbon dioxide and methane (3):

$$HCOOCH_3 \rightleftharpoons CO_2 + CH_4 \quad (3)$$

Anyway, there are no evidences for CH_4, and the observed carbon dioxide can better be explained with the Boudouard reaction (4): [53]

$$2CO \rightleftharpoons C + CO_2 \quad (4)$$

or taking into account reactions involving oxygen from perovskite (5):

$$CO + O_P \rightleftharpoons CO_2 + O_V \quad (5)$$

(with O_P = perovskite oxygen and O_V = oxygen vacancy). While reaction (4) should be favored at high temperature, equation (5) can play an important role in different conditions. Two different reaction mechanisms have been proposed for perovskites oxidation reactions involving two different oxygen species: [54, 55] at low temperature the interaction between adsorbed oxygen and reactants has been assumed. At high temperature, when the coverage of molecular O_2 strongly decreases, lattice oxygen becomes active.

Resuming, the outcomes suggest that methanol undergoes decomposition to hydrogen and carbon monoxide (equation 6), and the latest one can react again to give carbon dioxide.

$$CH_3OH \rightleftharpoons 2H_2 + CO \qquad (6)$$

The activity of the catalysts also changes as a function of time. Figure 3.10 shows the trend of m/z = 2 (hydrogen) with respect to the reaction time, while figure 3.11 displays the IR spectra taken at 400°C at increasing time. From these data is it possible to observe that the activity is maximum at the beginning of the test at each temperature. The intensities of the products rapidly decrease for about 5 minutes, than seems to reach a steady state (or a less relevant decrease).

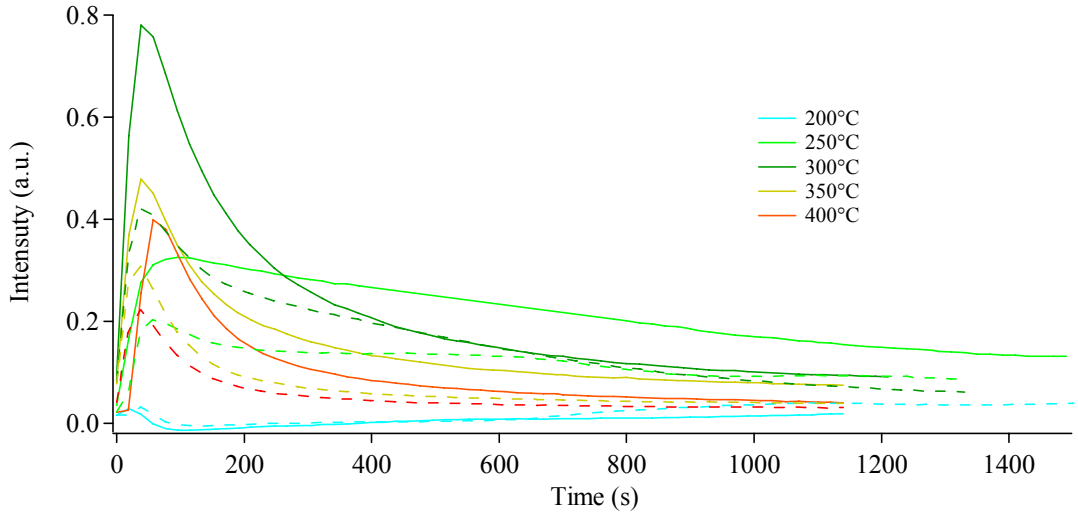

Figure 3.10. QMS data obtained for m/z = 2 (hydrogen) as a function of time for LCC1 Gel (solid line) and LCC1 Pec (dashed line) in the test with CH_3OH vapours.

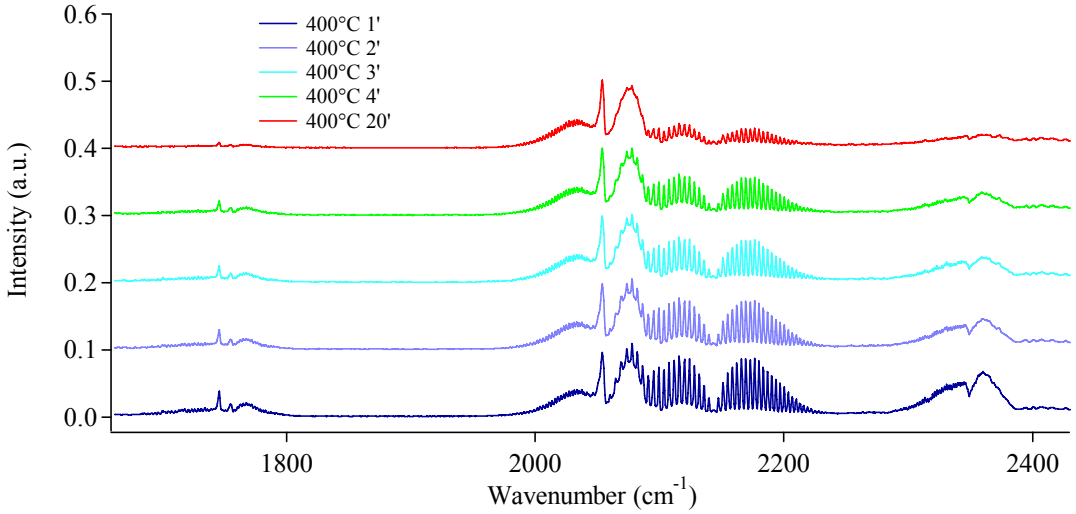

Figure 3.11. FTIR spectra obtained for LCC1 Gel after 1, 2, 3, 4 minutes exposure to CH_3OH vapours and at the end of the test (20 minutes) at 400°C (gas mixture from the reactor). Region between 1650 and 2450 cm^{-1}. The spectra are shifted for a better comprehension.

The observed features suggest that the catalysts undergo partial deactivation caused by poisoning of active sites. Furthermore the particular trend observed as a function of time indicates that the poisoning occurs at every tested temperature and the high reactivity measured at the beginning of the exposure (excluding 250°C) is due to partial desorption of products caused by the heating process. In fact, it is reasonable to think that the less bound species can desorb as a consequence of the heating steps (from 250 to 300°C, from 300 to 350°C…) freeing some active sites.

To check this hypothesis, the same test was performed on fresh LCC1 Gel starting from 400°C and proceeding then at decreasing temperature. Figure 3.12 shows the IR spectra obtained at 400°C at increasing time. Signals assignable to HCOOH, CO and CO_2 are well evident at the beginning and rapidly decrease with time. Furthermore, it is interesting to point out that the catalyst loses totally its activity (figure 3.13) when the reactor is cooled down to 350°C (300 and 250°C) and the activity trend observed in the previous test (fig 3.8) is not repeated. The behaviour clearly indicates that the sample is poisoned by un-desorbed species.

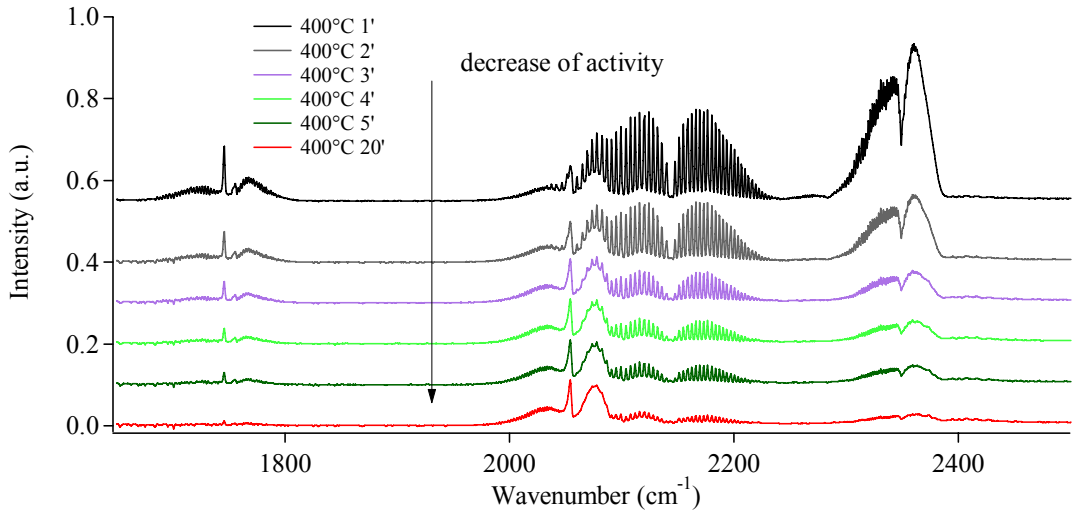

Figure 3.12. FTIR spectra obtained for LCC1 Gel after1, 2, 3, 4, 5, and 20 minutes exposure to CH_3OH vapours at 400°C (gas mixture from the reactor). Test at decreasing temperature. Region between 1650 and 2500 cm^{-1}. The spectra are shifted for a better comprehension.

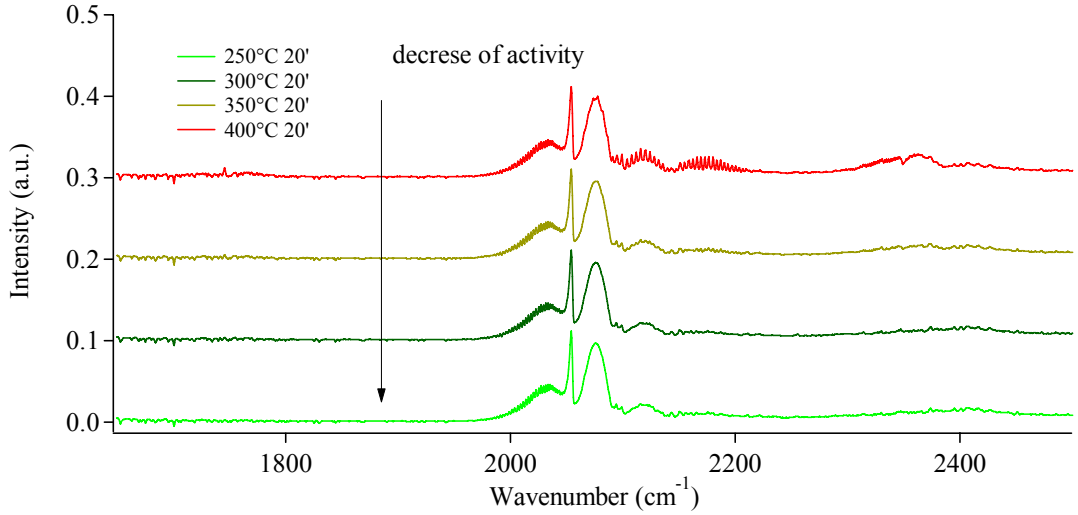

Figure 3.13. FTIR spectra obtained exposing LCC1 Gel to CH_3OH vapours (gas mixture from the reactor). Test at decreasing temperature. Region between 1650 and 2500 cm^{-1}. The spectra are shifted for a better comprehension.

In figure 3.14 the DRIFT spectra of LCC1 Gel as prepared and the worn-out LCC1 Gel after the test with methanol at decreasing temperatures are compared. A new band at 1300÷1500 cm^{-1} appears. In detail, it is possible that carbon dioxide interacts with the surface basic sites (such as La-sites) to give carbonate species. [49] For example, De Asha et al., [56] studying the interaction between CO_2 and oxidised La/Cu(111), found that various type of carbonates are formed on LaO_x.

As a general consideration different surface species can result from the CO_2 adsorption accordingly to the acid/basic character of the surface. [57, 58, 59, 60]

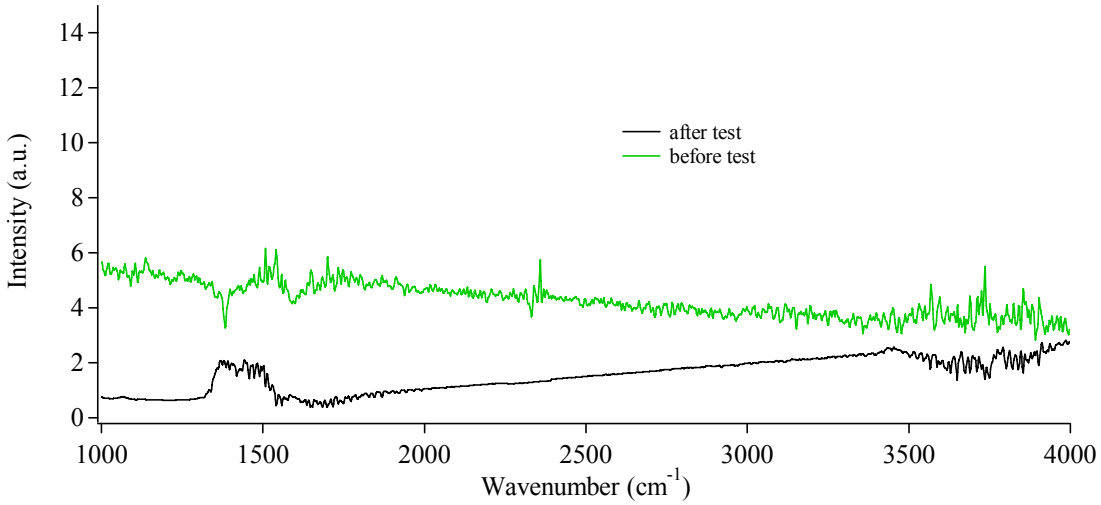

Figure 3.14. DRIFT spectra obtained for LCC1 Gel at RT before (as prepared catalyst) and after (worn-out catalyst) test with CH_3OH at decreasing temperature. Region between 1000 and 4000 cm^{-1}.

The adsorption on an OH group give rise to the formation of bicarbonate species while the interaction with a surface Lewis acidic sites causes the formation of superficial carbonyl groups. The adsorption on basic sites (co-ordinatively unsaturated oxygen anions) originates monodentate carbonates while the interaction with an acid metal ion and the neighboring basic oxygen or with two acid metal ions, originate a bidentate or bridge carbonate.

Exhaust LCC1 Gel was also investigated by XPS and compared with fresh LCC1 Gel. XP spectra for La3d, Cu2p, O1s and C1s and Auger peak for Cu LMM are shown in figure 3.15. Tables 3.4 and 3.5 show the peak positions (BE, eV) and the atomic compositions (%) respectively.

Looking at the La3d peak position, the shift toward slightly higher BE suggests the presence of $La(OH)_3$, LaO(OH) or $La_2(CO_3)_3$ [39, 50, 61] Concerning the Cu2p peaks, the shift toward lower BE and the absence of shake up peaks indicate the reduction of copper from Cu(II) to Cu(I). The comparison between the Cu LMM peak position (916.5 eV) and literature data (916.2÷916.6 eV) confirm the hypothesis. [62]

The observed reduction suggests a significant role played by copper in the oxidation products formation.

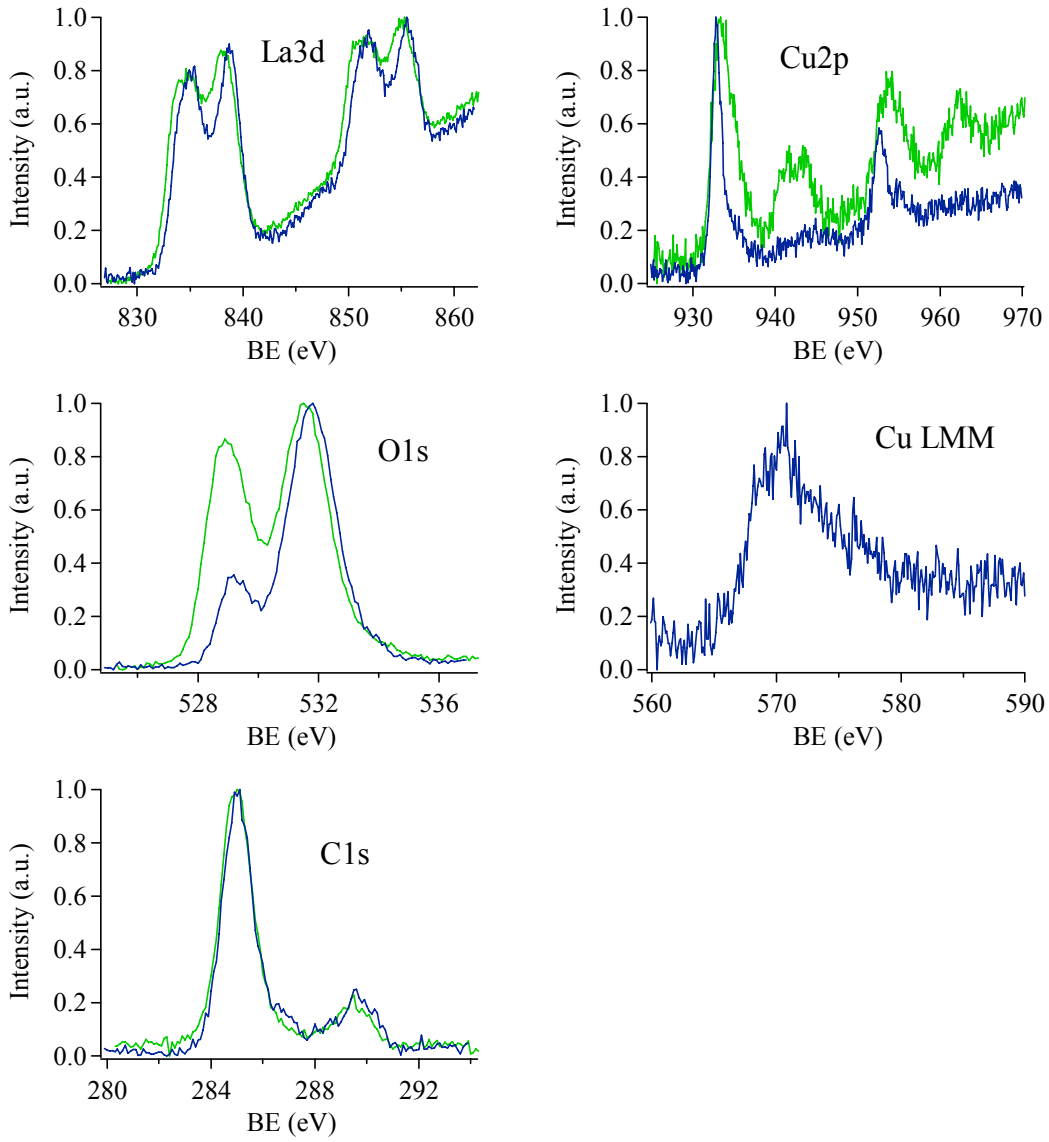

Figure 3.15. XP spectra obtained for LCC1 Gel before (as prepared sample —) and after (worn-out sample —) test with CH_3OH at decreasing temperature. All spectra are normalized with respect to their maximum value.

Table 3.4. XPS peak positions (binding energy, eV) obtained for LCC1 Gel before (as prepared) and after the reaction with methanol. The kinetic energies (KE, eV) obtained for CuLMM are also reported.

XP peak	LCC1 Gel as prepared	LCC1 Gel after reaction
$La3d_{5/2}$ and $_{3/2}$	834.5 – 851.5	835.1 – 851.8
$Cu2p_{3/2}$ and shake up	933.7 – 942.7	932.9 – ND
$Cu2p_{1/2}$ and shake up	954.1 – 962.7	952.7 – ND
O1s lattice and OH/CO_3	529.0 – 531.5	529.2 – 531.8
C1s HC and CO_3	285.0 – 289.4	285.0 – 289.6
Auger peak		
Cu LMM	NA	916.5

ND = not detectable
NA = not available

Table 3.5. XPS and nominal compositions (atomic %) for LCC1 Gel before (as prepared) and after (exhaust) the reaction with methanol.

sample	LCC1 Gel as prepared			LCC1 Gel after reaction			nominal composition	
							oxide	cations
element								
La	13	20	66	10	18	65	22	50
Cu	5	8	27	5	8	30	17	40
Co	2	2	7	< 1	1	5	4	10
O	46	70		42	73		57	
C	34			43				

For O1s is well evident an increase in high BE contribution, assignable to a more relevant presence of hydroxyl and carbonate species. Finally, it is evident that the C1s peak shape and position do not change significantly after the reaction; however, the atomic percentage increases from 34 to 43%. Moreover, a weak shoulder at about 286.5÷287.0 eV is consistent with the presence of C in alcohol species. [63]
Surface atomic composition agrees thus with an increase in carbonaceous species after the reaction with CH_3OH. Taking into consideration the oxide and cations compositions (2^{nd} and 3^{rd} columns for each sample), no remarkable differences are evident between LCC1 Gel and Pec.

The interaction between LCC1 Gel and Pec and pure ethanol vapours was also investigated. QMS and IR results are displayed in the figures 3.16, 3.17 and 3.18. Both samples become active at 200°C producing hydrogen (fig 3.16) and acetaldehyde (band at 1745 cm^{-1} in fig 3.17 and 3.18). QMS and IR data do not show any other kind of products. The obtained products suggest that the dehydrogenation of alcohol is the main reaction (7).

$$CH_3CH_2OH \rightleftharpoons H_2 + CH_3CHO \qquad (7)$$

The reactivity reaches its maximum degree toward dehydrogenation at 250°C for both samples (250 and 300°C for LCC1 Gel), decreasing at higher temperatures. Anyway, at 400°C small amounts of ethylene (coming form ethanol dehydration) are evident from IR data (insert in fig 3.17 and 3.18, peak at 950 cm^{-1}).
The observed dehydration product suggests the possible formation of surface active acidic sites [64]

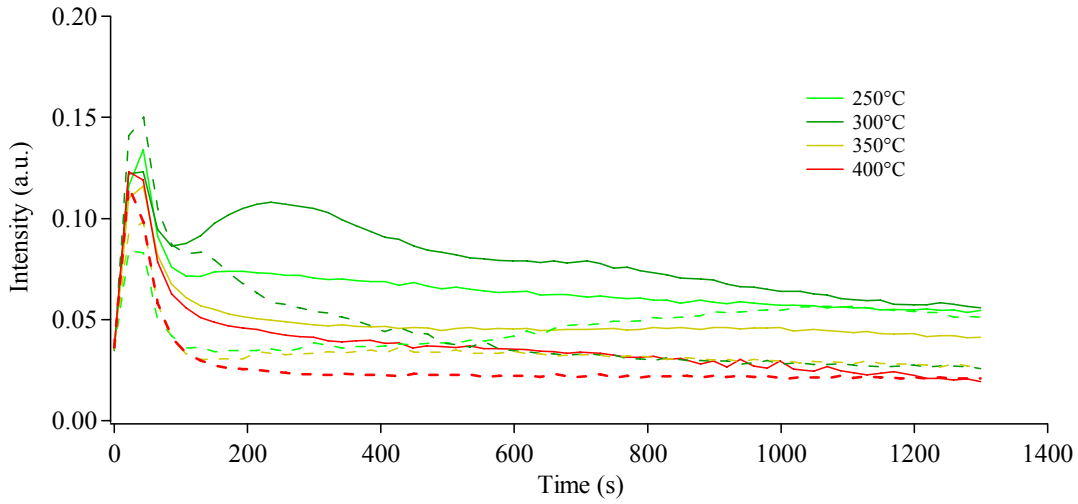

Figure 3.16. QMS data obtained for m/z = 2 (hydrogen) as a function of time for LCC1 Gel (solid lines) and LCC1 Pec (dashed lines) at increasing temperatures in the test with CH_3CH_2OH vapours.

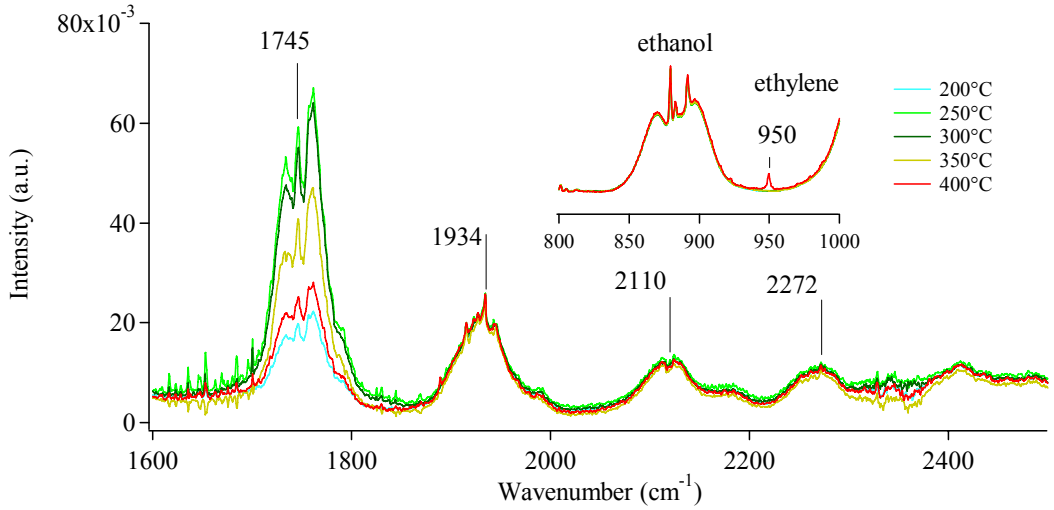

Figure 3.17. FTIR spectra obtained after exposing LCC1 Gel to CH_3CH_2OH vapours (gas mixture from the reactor). Region between 1600 and 2500 cm^{-1}. Insert: region between 800 and 1000 cm^{-1}.

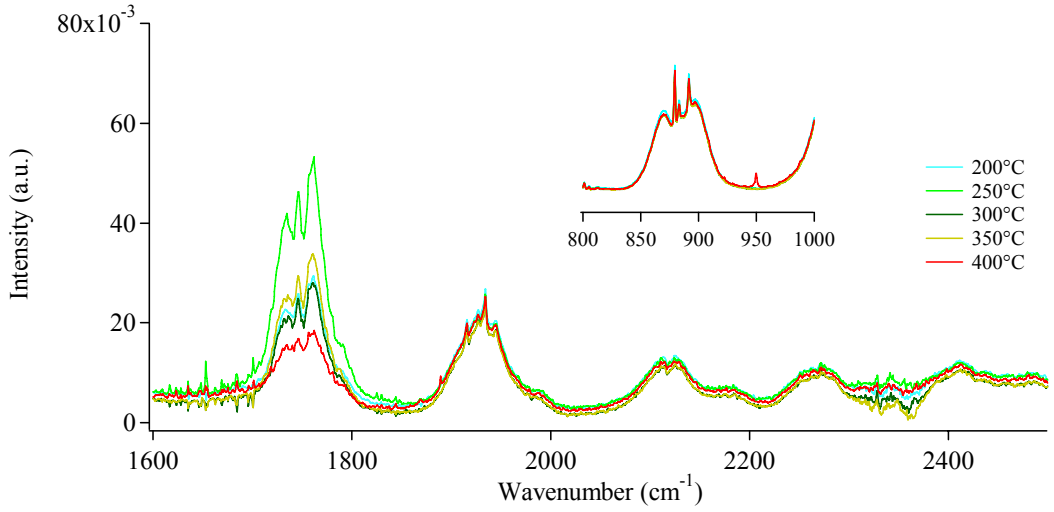

Figure 3.18. FTIR spectra obtained after exposing LCC1 Pec to CH_3CH_2OH vapours (gas mixture from the reactor). Region between 1600 and 2500 cm^{-1}. Insert: region between 800 and 1000 cm^{-1}.

As already seen for methanol, the activity is higher at the beginning of each experiment, at every temperature; figure 3.16 and 3.19 show the obtained trends. As for CH_3OH, it seems that catalysts undergo a deactivation process. However, in this instance, the poisoning could be slightly different, since no CO or CO_2 are detected. Domok et al. [65] found various kinds of carbonaceous species adsorbed on Pt/Al_2O_3, stable until 450°C. These by-products (regarding C_1 and C_2 species) are released only at higher temperature and cause the deactivation of the catalysts. Others studies concerning the interaction between transition metal oxides and metals or noble metals supported by transition metal oxides [66, 67, 68, 69, 70] indicate that ethanol reacts with the catalysts in several modes. Anyway, it seems that the first step consist in the formation of ethoxy species.
As in the case of pure methanol vapours, LCC1 Gel shows a better activity than LCC1 Pec.

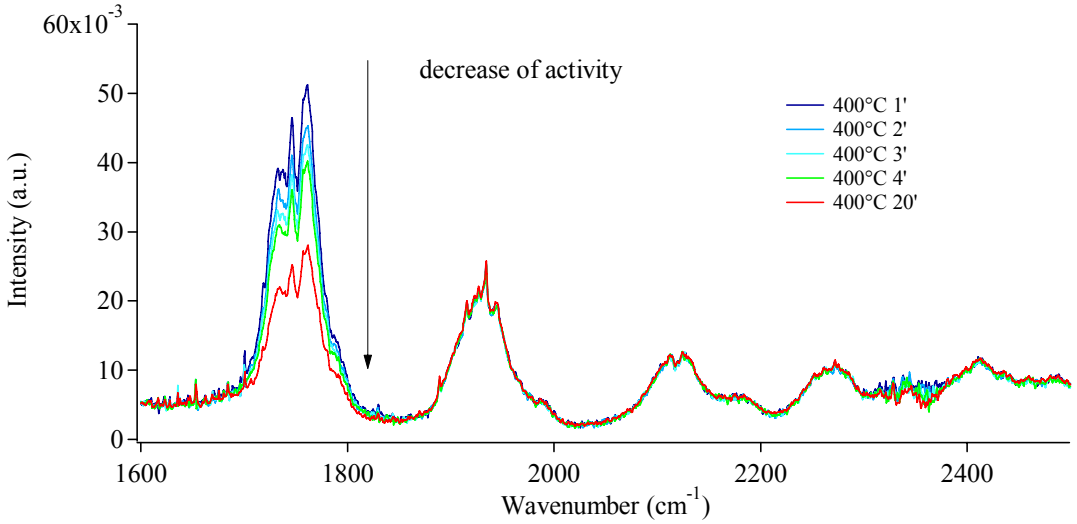

Figure 3.19. FTIR spectra obtained for LCC1 Gel after1, 2, 3, 4 and 20 minutes exposure to CH_3CH_2OH vapours at 400°C (gas mixture from the reactor). Region between 1600 and 2500 cm^{-1}.

Table 3.6. Conversions of fuels and yields for products obtained for LCC1 Gel and LCC1 Pec with respect to the reaction with pure methanol and ethanol vapours.

	CH_3OH			CH_3CH_2OH		
sample	T max react (°C)	conv (%)[a]	yield H_2 (%)[b]	T max react (°C)	conv (%)[a]	yield H_2 (%)[b]
LCC1 Gel	250	7	1	250	ND[c]	1
LCC1 Pec	250	4	< 1	250	3	1

Note:
[a] conversions determined by QMS (see appendixes A, B)
[b] yield by QMS (see appendixes A, B)
[c] not detectable

Table 3.6 summarizes the obtained data for conversion of fuels (methanol and ethanol) and the yields for hydrogen at the temperature of maximum activity. As a general consideration, the activity toward pure alcohols vapours is quite low, and both catalysts better react with methanol than ethanol. Hydrogen is always the main product; it derives from methanol decomposition and from dehydrogenation of ethyl alcohol. LCC1 Gel and Pec show their maximum activity at 250°C, after this, the catalytic potential decrease because of the poisoning from adsorbed species.

The low activity and the different kind of reactions that occur do not permit an accurate evaluation of the yields for hydrogen.

Methanol and Ethanol oxidation

A second type of experiments was performed on LCC1 Gel and Pec. In these new tests, the carrier gas (Argon) was enriched with an over stoichiometric amount of oxygen (with respect to fuel). In this way, it was possible to evaluate the activity toward fuel total oxidation.

Figures 3.20, 3.21 and 3.22 show the QMS and IR outcomes for LCC1 Gel and Pec with respect to CH_3OH oxidation at the investigated temperatures. Both catalysts become active since 250°C with the formation of small amounts of formic acid (band at 1745 cm^{-1}) and methyl formate (band at 1755 cm^{-1}), while at 300°C, traces of carbon dioxide (2363 cm^{-1}) are also evident. Anyway, only at 350 and 400°C both LCC1 Gel and Pec show a great activity toward total oxidation of methanol, with a larger production of water and carbon dioxide. In these conditions, some by-products such as CO and H_2 are also detected.

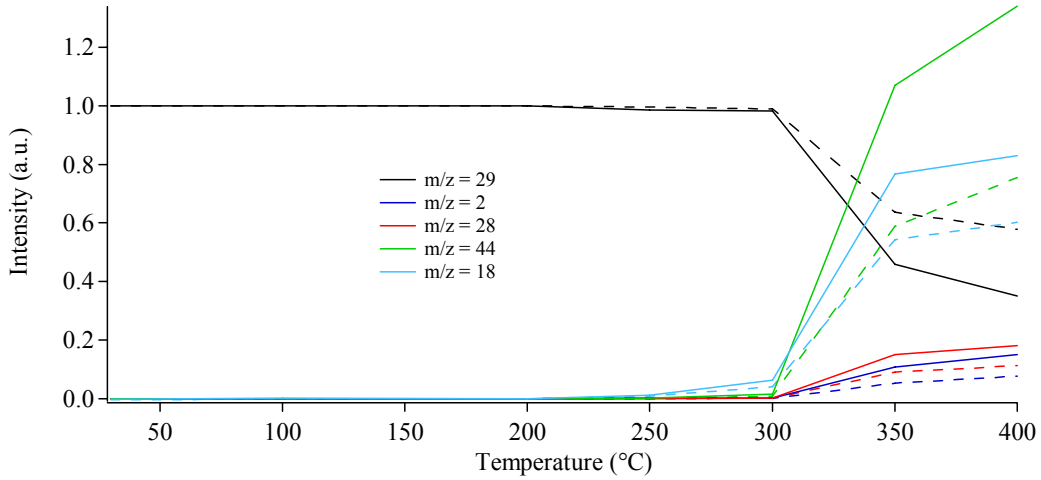

Figure 3.20. QMS data obtained for m/z = 29 (methanol), m/z = 2 (hydrogen), m/z = 28 (carbon monoxide), m/z = 44 (carbon dioxide) and m/z = 18 (water) in oxidizing conditions at the investigated temperatures. Solid lines stand for LCC1 Gel, dashed lines for LCC1 Pec.

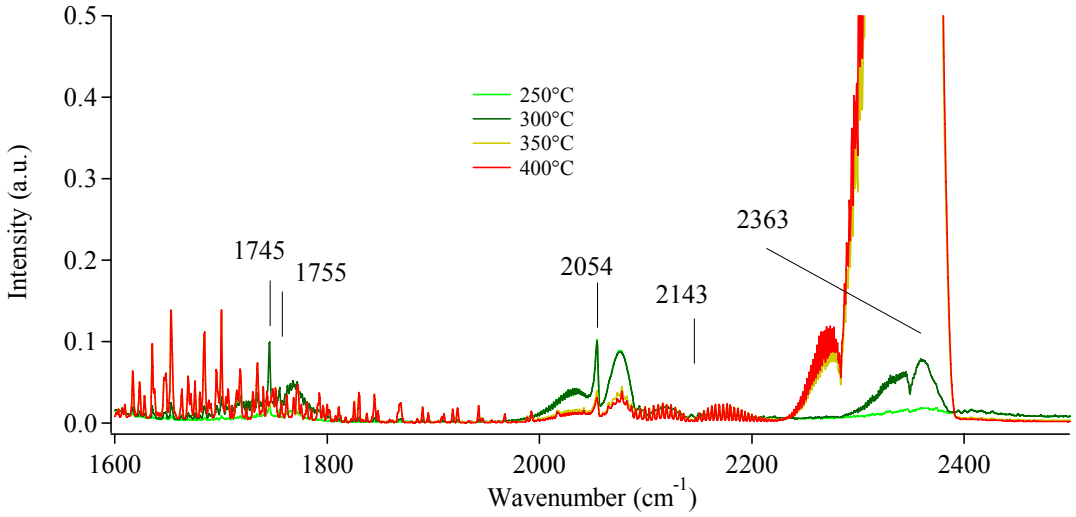

Figure 3.21. FTIR spectra obtained after exposing LCC1 Gel to CH_3OH vapours O_2 enriched (gas mixture from the reactor). Region between 1600 and 2500 cm^{-1}.

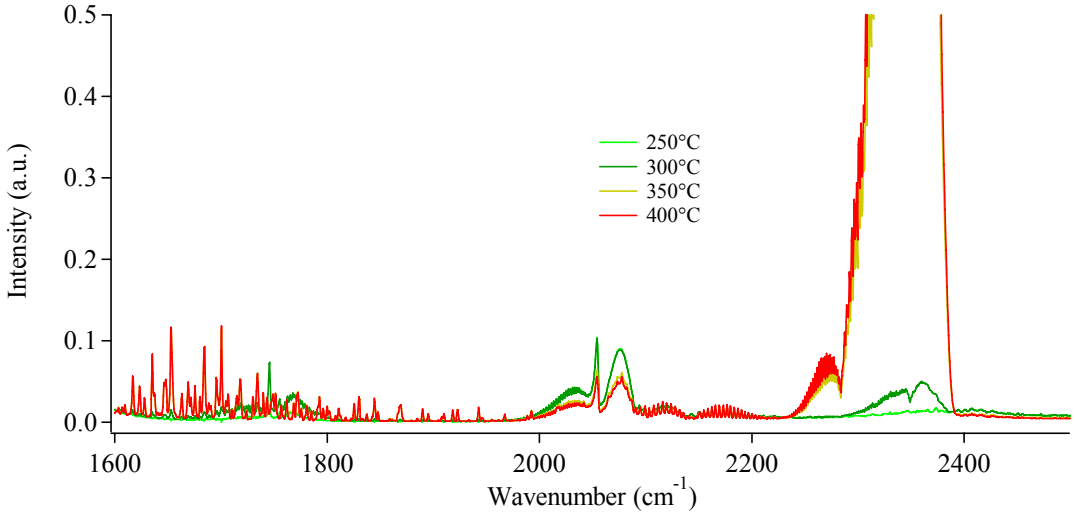

Figure 3.22. FTIR spectra obtained after exposing LCC1 Pec to CH_3OH vapours O_2 enriched (gas mixture from the reactor). Region between 1600 and 2500 cm^{-1}.

Unlike the case of pure methanol, no deactivation or decrease in activity are evident for LCC1 Gel and Pec at increasing temperatures.

It's interesting to underline that at high temperatures, when total oxidation take place, the catalysts showed incandescence. The position of the thermocouple (at the outer wall of the reactor) does not allow to exactly know the temperature; anyway, judging by the colour of the catalysts, it is reasonable to think that it was about 550÷600°C. This feature can be explained considering that heat coming from the combustion reaction was not removed fast enough by the Argon flow. Nevertheless, this behaviour needs to be further investigated.

Furthermore, the obtained IR and QMS data suggest that in the described conditions, the reaction is still catalyzed by LCC1 Gel and Pec, because the amounts of the products increase from 350 to 400°C.

To support the hypothesis, it is worth to take into account the outcomes obtained for barium-doped lanthanum manganites sample ($La_{0.6}Ba_{0.4}MnO_3$). [71] The Author investigated the compound toward ethanol oxidation in the same conditions here employed. Figure 3.23 shows the obtained IR spectra. The catalytic activity started at 200°C with the formation of acetaldehyde (band at 1745 cm^{-1}). Starting from 250°C, the sample became incandescent and produced considerable amounts of CO_2 (2363 cm^{-1}) and H_2O (1595 cm^{-1}); CO (2143 cm^{-1}) was also produced in low amount as partial oxidised by-product. The calculated conversions for ethanol vary between 34% (at 250°C) and 46% (at 400°C) and these values can be conveniently compared to those shown in table 3.7 for the LCC2 samples.

It's reasonable to suppose that the conversion rate of ethanol should be about the same if the oxidation is un-catalyzed.

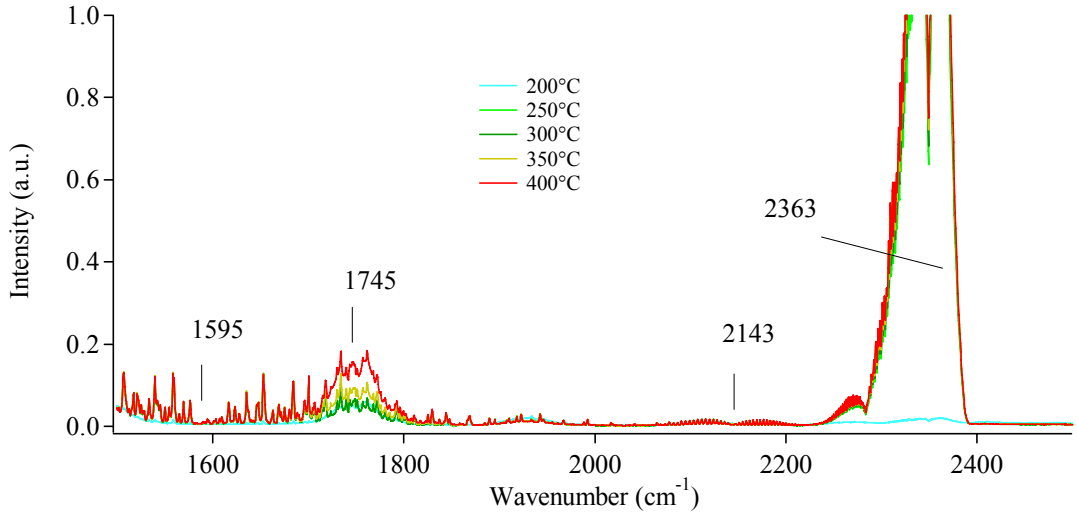

Figure 3.23. FTIR spectra obtained after exposing $La_{0.6}Ba_{0.4}MnO_3$ to CH_3CH_2OH vapours O_2 enriched (gas mixture from the reactor). Region between 1500 and 2500 cm^{-1}.

The activity toward ethanol oxidation was also investigated. LCC1 Gel and Pec start to convert ethanol at about 300°C producing small amounts of acetaldehyde and hydrogen.

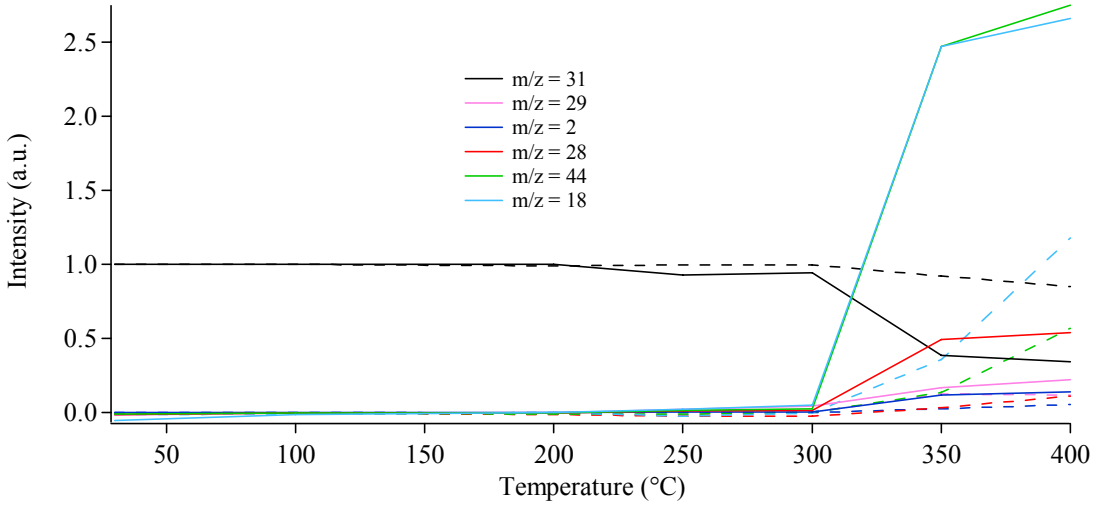

Figure 3.24. QMS data obtained for m/z = 31 (ethanol), m/z = 29 (acetaldehyde), m/z = 2 (hydrogen), m/z = 28 (carbon monoxide), m/z = 44 (carbon dioxide) and m/z = 18 (water) in oxidizing conditions at the investigated temperatures. Solid lines stand for LCC1 Gel, dashed lines for LCC1 Pec.

As shown in figures 3.24÷3.26, the oxidation of ethyl alcohol begins only at 350°C with the formation of larger amounts of water (vibro-rotation signals centred at 1595 cm^{-1}) and carbon dioxide (peak at 2363 cm^{-1}); while CO, as intermediate oxidation product (band at 2143 cm^{-1}), is also present. In figure 3.25, the wide band at 1643 cm^{-1} is due to liquid water condensed in IR cell. Less intense signals due to acetaldehyde and hydrogen (fig 3.24) are still evident. From the comparison between figure 3.25 and 3.26, is clear that LCC1 Pec is a less efficient catalyst toward ethanol oxidation.

The formation of partial oxidation products (formic acid, methyl formate, acetaldehyde), particularly at low temperatures and in small amounts, is consistent with a mechanism in agreement with how observed in literature for oxide-catalyzed alcohols oxidation. [72] The first step is the interaction between the alcohol and the surface active sites of the catalyst. Successively, the coordinated alcohol molecules loose hydrogen to give aldehydes and then carboxilates. These species decompose to originate the final oxidation products.

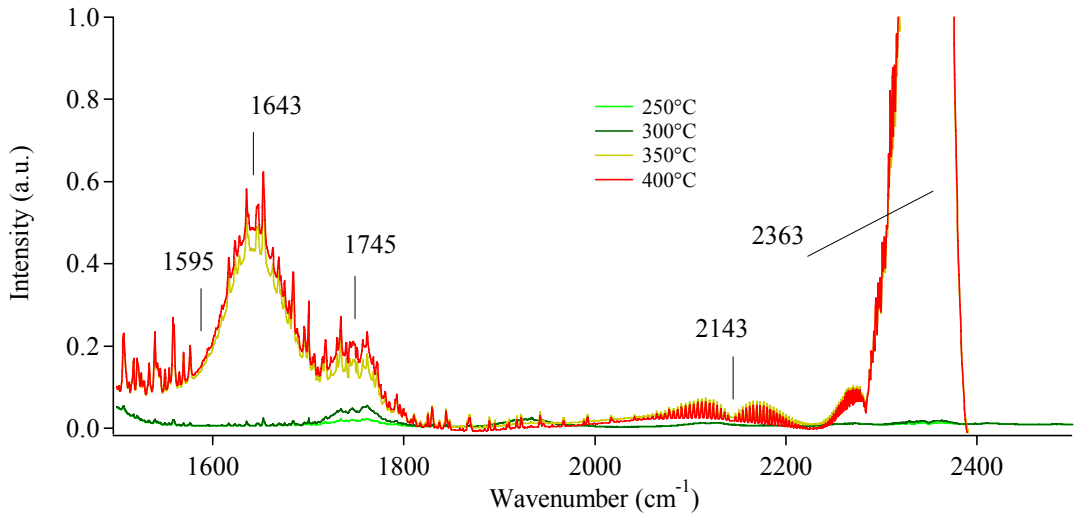

Figure 3.25. FTIR spectra obtained after exposing LCC1 Gel to CH_3CH_2OH vapours O_2 enriched (gas mixture from the reactor). Region between 1500 and 2500 cm^{-1}.

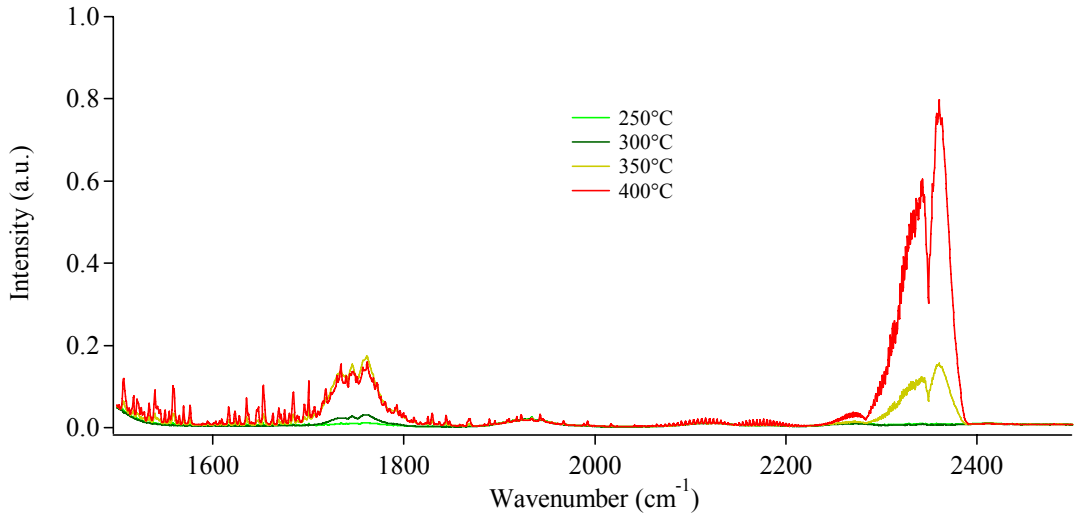

Figure 3.26. FTIR spectra obtained after exposing LCC1 Pec to CH_3CH_2OH vapours O_2 enriched (gas mixture from the reactor). Region between 1500 and 2500 cm^{-1}.

Table 3.7. Conversions of fuels and yields for products at 400°C obtained for LCC1 Gel and LCC1 Pec with respect to methanol and ethanol oxidation.

	CH_3OH/O_2				CH_3CH_2OH/O_2			
sample	conv	yield H_2	yield CO	yield CO_2	conv	yield H_2	yield CO	yield CO_2
LCC1 Gel	65	2	ND[a]	36	66	5	9	57
LCC1 Pec	42	1	2	23	15	1	< 1	12

Note:
[a] not detectable
all data are in % (see appendixes A, B)

Looking at the intensities of QMS data and IR bands, is well evident that LCC1 Gel is more efficient in oxidation of methanol and ethanol than LCC1 Pec. Conversions of reactants and the yields for the main products (table 3.7) confirm this trend. In these kind of tests, both catalysts show good activity toward total oxidation of methanol and ethanol, especially at high temperatures.

Methanol and Ethanol steam reforming

The last type of experiments performed on LCC1 Gel and Pec consist in the steam reforming of the alcohols. To do this, the carrier gas flowed through an aqueous solution (1 mol·l^{-1}) of methanol and ethanol.

Figure 3.27 summarizes the QMS data for steam reforming of methanol; the activity starts at about 300° and increases with temperature. The most evident products are hydrogen and carbon dioxide, but carbon monoxide is also present. IR data, figure 3.28 and 3.29, confirm the QMS outcomes.

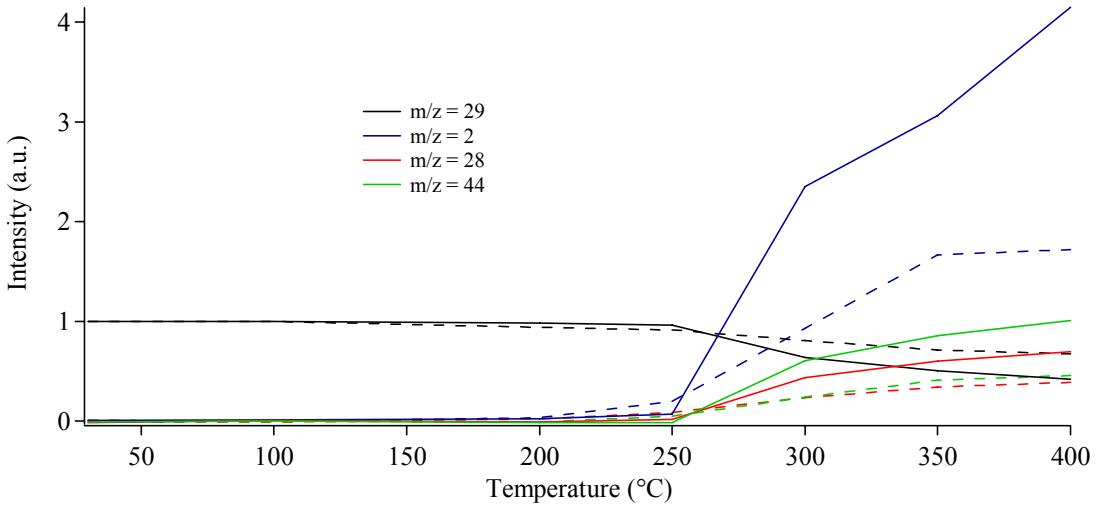

Figure 3.27. QMS data obtained for m/z = 29 (methanol), m/z = 2 (hydrogen), m/z = 28 (carbon monoxide), and m/z = 44 (carbon dioxide) in steam reforming conditions at the investigated temperatures. Solid lines stand for LCC1 Gel, dashed lines for LCC1 Pec.

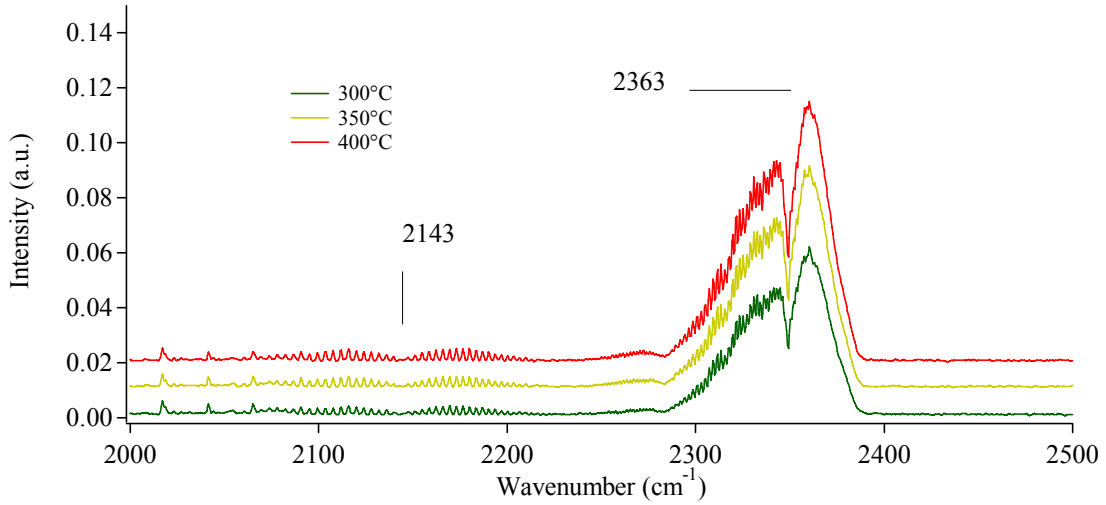

Figure 3.28. FTIR spectra obtained after exposing LCC1 Gel to CH_3OH 1M vapours (gas mixture from the reactor). Region between 2000 and 2500 cm^{-1}. The spectra are shifted for a better comprehension.

All data suggest that the main reaction is just the steam reforming of methanol (8):

$$CH_3OH + H_2O \rightleftharpoons 3H_2 + CO_2 \qquad (8)$$

Equation (8) is often explained as a sum of two consecutive reactions. [53] The first step is the methanol decomposition (6):

$$CH_3OH \rightleftharpoons CO + 2H_2 \qquad (6)$$

While the second one is the water gas shift reaction (9):

$$CO + H_2O \rightleftharpoons CO_2 + H_2 \qquad (9)$$

Looking at the relative intensities for CO and CO_2 in the IR spectra, it is reasonable to think that reaction (9) is faster than (6).

Others reaction paths for the decomposition of methanol toward methyl formate and formic acid are suggested by Jiang et al.: equations (1), (10) and (11) [73] however, the by-products observed by those Authors, were never observed in the present case.

$$2CH_3OH \rightleftharpoons HCOOCH_3 + 2H_2 \qquad (1)$$

$$HCOOCH_3 + H_2O \rightleftharpoons HCOOH + CH_3OH \qquad (10)$$

$$HCOOH \rightleftharpoons CO_2 + H_2 \qquad (11)$$

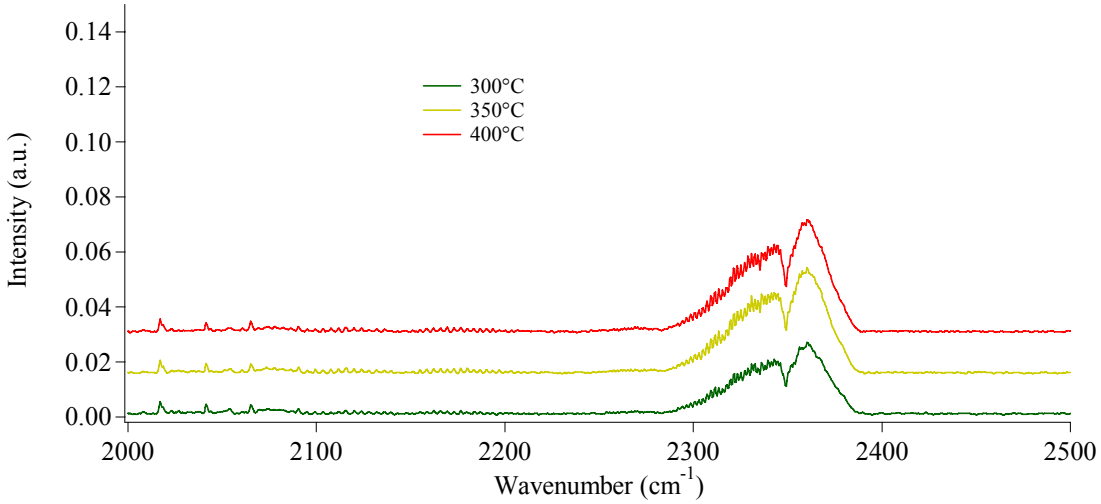

Figure 3.29. FTIR spectra obtained after exposing LCC1 Pec to CH_3OH 1M vapours (gas mixture from the reactor). Region between 2000 and 2500 cm^{-1}. The spectra are shifted for a better comprehension.

Regarding the steam reforming of ethyl alcohol, reactions take place from 250°C with the production of acetaldehyde, hydrogen and minor amounts of carbon dioxide. Signals arising from m/z = 28 are also present (fig 3.30). This signal could be indicative of the carbon monoxide or ethylene. The absence of the corresponding IR peaks (figures 3.31 and 3.32) has probably to be ascribed to the higher sensitivity of QMS with respect to IR spectroscopy.

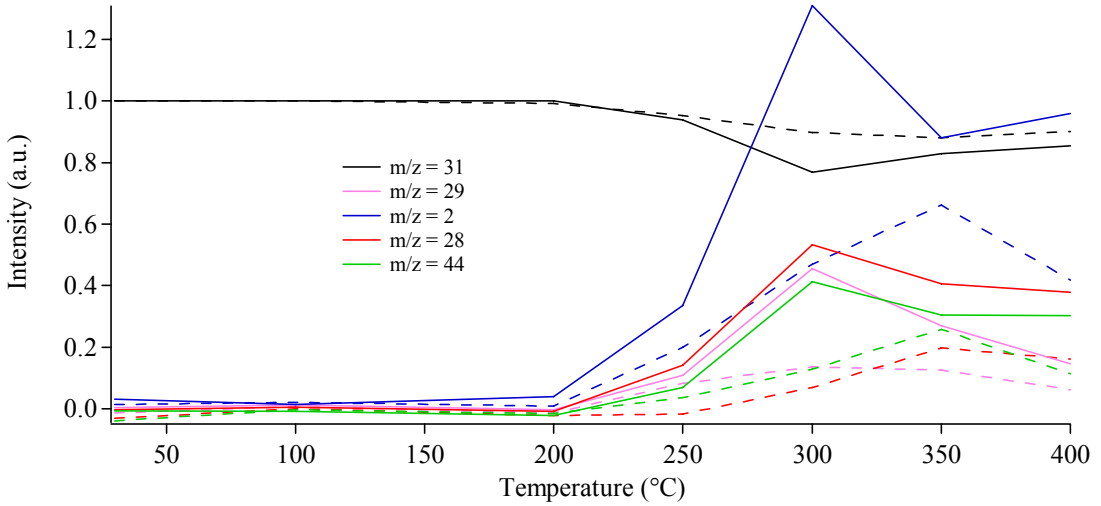

Figure 3.30. QMS data obtained for m/z = 31 (ethanol), m/z = 29 (acetaldehyde) m/z = 2 (hydrogen), m/z = 44 (carbon dioxide) and m/z = 28 (carbon monoxide and ethylene) in steam reforming conditions at the investigated temperatures. Solid lines stand for LCC1 Gel, dashed lines for LCC1 Pec.

The activity increases with temperature and reaches its maximum at 300°C for LCC1 Gel and 350°C for LCC1 Pec (fig 3.30).

Literature data suggest that the stem reforming of ethanol can give a wide range of chemicals. The main products seem to be hydrogen, acetaldehyde and carbon dioxide, but ethylene, carbon monoxide, methane, dimethyl ketone, diethyl ether and acetic acid can also be present. [65, 74, 75]

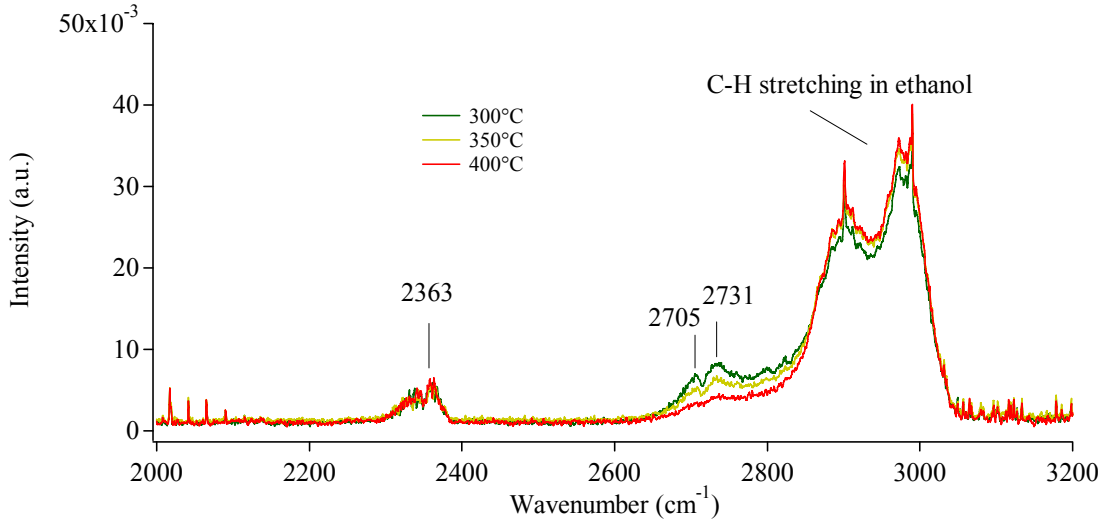

Figure 3.31. FTIR spectra obtained after exposing LCC1 Gel to CH_3CH_2OH 1M vapours (gas mixture from the reactor). Region between 2000 and 3200 cm^{-1}.

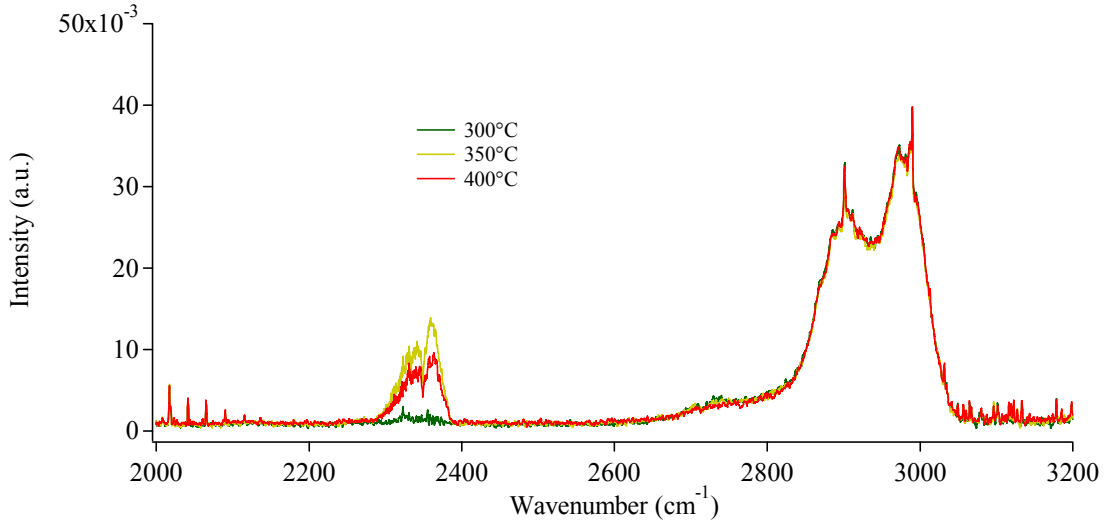

Figure 3.32. FTIR spectra obtained after exposing LCC1 Pec to CH_3CH_2OH 1M vapours (gas mixture from the reactor). Region between 2000 and 3200 cm^{-1}.

The obtained outcomes well agree with literature; however, looking at the data, the dehydrogenation of ethyl alcohol seems to be the first and the fastest step. [74]

Acetaldehyde can be transformed following different reaction paths; it can be oxidized to acetate (12; $_{(a)}$ indicate the adsorbed products):

$$CH_3CHO_{(a)} + OH_{(a)} \rightleftharpoons CH_3COO_{(a)} + H_2 \quad (12)$$

which decomposes into methyl group and carbon dioxide (13):

$$CH_3COO_{(a)} \rightleftharpoons CH_{3(a)} + CO_{2(a)} \quad (13)$$

Methyl groups can react with hydroxyl groups of water molecules to yield CO and H_2.
In contrast acetaldehyde can be decomposed to methane and carbon monoxide that can react with water to give carbon monoxide and hydrogen (14):

$$CH_4 + H_2O \rightleftharpoons CO + 3H_2 \quad (14)$$

In the present case, the last reaction seems not occur, since no traces of methane are evident.
Concerning LCC1 Gel, the reforming of acetaldehyde toward CO_2 is not so fast at temperature lower than 400°C. LCC1 Pec, on the other hand, is less active at 300°C but seems to be a better reformer at 350 and 400°C.
Nevertheless, from figure 3.30, LCC1 Gel appears always more reactive than LCC1 Pec and, as often occur, a more active catalyst is less selective toward a specific product.
Finally, the trend of the catalysts performances, with the decreases of the reactivity at high temperatures, suggests that both LCC1 Gel and Pec undergo a poisoning from surface absorbed products.
Table 3.8 shows the values for conversions of reactants and yields for typical steam reforming products. As seen in the previous conditions, LCC1 Gel and Pec well react with methanol, while they are less active with respect to ethyl alcohol.
As already mentioned above, the amounts of reactants in the feed stream are quite low, so the data for the yields of products could be not very accurate. Nevertheless, is well evident that a relevant amount of carbon-containing species (such as CO and CO_2) are missing. This behaviour suggests that carbonaceous species are retained on catalysts surface. The phenomenon is more evident in ethanol steam reforming, in which the catalytic activity decreases at high temperatures.

Table 3.8. Conversions of fuels and yields for products obtained for LCC1 Gel and LCC1 Pec with respect to methanol (data at 400°C) and ethanol (data at 400°C and at maximum activity) steam reforming.

	CH_3OH 1M				CH_3CH_2OH 1M			
sample	conv	yield H_2	yield CO	yield CO_2	conv	yield H_2	yield CO	yield CO_2
LCC1 Gel	59	17	ND[a]	6	15	< 1	ND	ND
LCC1 Pec	32	6	ND	ND	10	ND	ND	ND
LCC1 Gel			data at 300°C		23	1	ND	ND
LCC1 Pec			data at 350°C		12	ND	ND	ND

Note:
[a] not detectable
all data are in % (see appendixes A, B)

Chapter 4

$La_2Cu_{0.8}Co_{0.2}O_{4-\delta}$ (LCC2)

Synthesis

The perovskite-type $La_2Cu_{0.8}Co_{0.2}O_4$ was prepared by two synthetic routes: Pechini process (the corresponding compound is named “LCC2 Pec”), and Polyacrylamide Gel method (compound named LCC2 Gel). The procedures are widely described in Chapter 2. The gels, obtained as intermediate compounds from Pechini and Polyacrylamide Gel processes, were dehydrated and calcined at 900°C for 5 h in air.

Characterization

XRD

LCC2 Gel and LCC2 Pec were characterized by X-Ray Diffraction to establish the crystallographic composition. By comparison with the JCPDS database, it can be seen that both XRD patterns (figure 4.1) show typical reflections arising from $La_2Cu_{(1-x)}Co_xO_4$ perovskite structure as main phase; minor contributions from $LaCoO_3$ are also

present. In the sample LCC2 Pec, furthermore, little peaks due to traces of lanthanum oxide are evident. Table 4.1 summarizes the XRD outcomes.

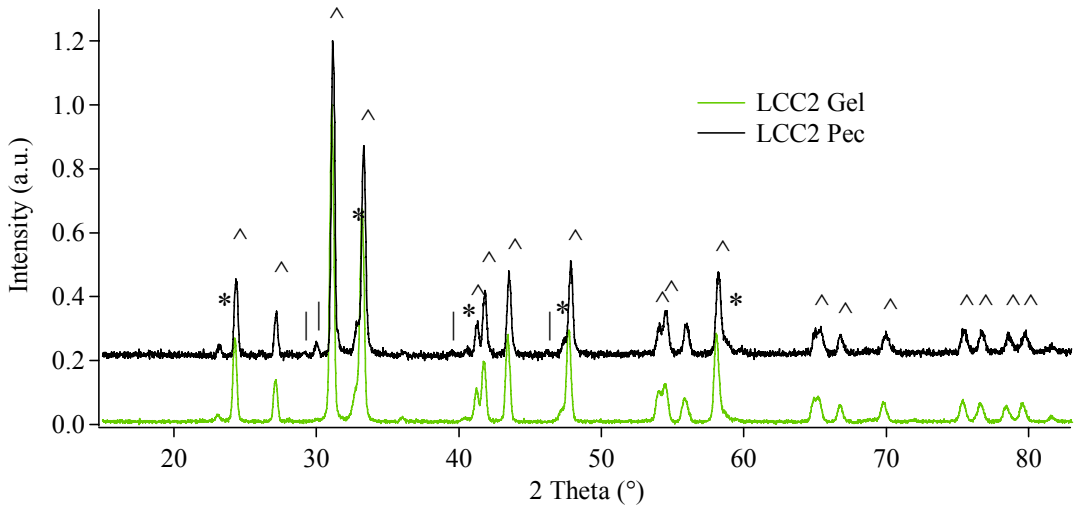

Figure 4.1. XRD patterns obtained for LCC2 Pec (—) and LCC2 Gel (—). The markers stand for: $La_2Cu_{0.8}Co_{0.2}O_4$ (^), $LaCoO_3$ (*) and La_2O_3 (|). The spectra are shifted for a better comprehension.

Table 4.1. XRD compositions obtained for LCC2 Pec and LCC2 Gel.

sample	main phase	minor phases	crystallographic lattice	JCPDS number
LCC1 Gel	$La_2Cu_{0.8}Co_{0.2}O_4$		orthorhombic	79-0453
		$LaCoO_3$	rhombohedral	86-1663
LCC1 Pec	$La_2Cu_{0.8}Co_{0.2}O_4$		orthorhombic	79-0453
		$LaCoO_3$	rhombohedral	86-1663
		La_2O_3	hexagonal	74-1144

It is now convenient to compare XRD outcomes from LCC1 and LCC2 samples. As already reported in Chapter 3 beyond the main phase ($La_2Cu_{0.8}Co_{0.2}O_4$), CuO and $LaCoO_3$ were observed as minor phases in LCC1 Gel and Pec.

In LCC2 samples, the presence of CuO was never evident and this confirms the hypothesis about its formation illustrated in Chapter 3. Consistently with this hypothesis, the formation of CuO in LCC1 is a consequence of the higher Cu amount. Beside this, $LaCoO_3$ has a very good stability since it is present in all analyzed samples.

As a general consideration, LCC1 and LCC2 mainly differ in the relative amounts of the identified phases. From this point of view, LCC2 samples appear to be better from a crystallographic point of view: the desired A_2BO_4 phase is well defined and the other phases are present in very low amounts.

XPS

Figure 4.2 displays the extended XP spectra for LCC2 Gel and Pec. All peaks belong to the elements of LCC2 samples and the only foreigner signals arise from adventitious carbon. Figure 4.3 and table 4.2 summarize the detailed spectra and the positions for La3d, Cu2p, Co2p and O1s photoelectronic peaks. All binding energies are corrected for charging effects by assuming C1s at 285.0 eV.

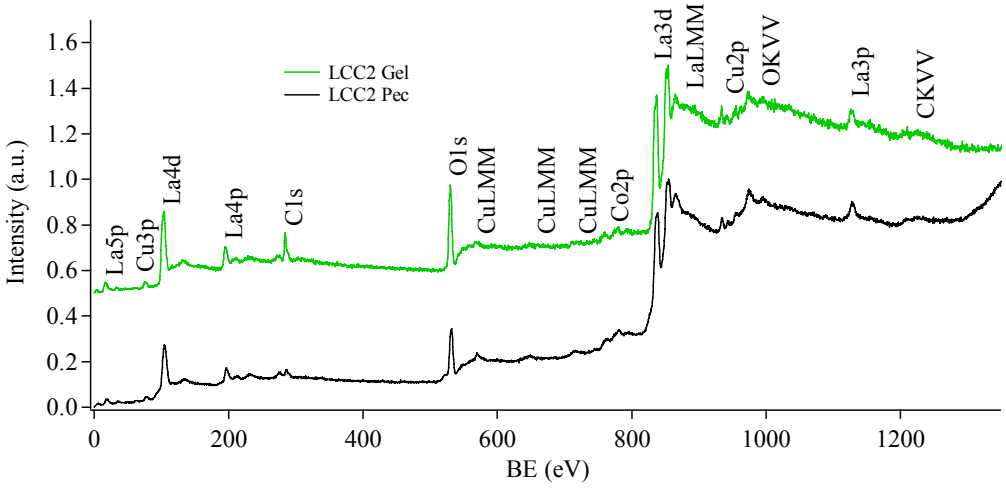

Figure 4.2. Extended XP spectra (surveys) obtained for LCC2 Gel and Pec. The spectra are normalized with respect to their maximum value and shifted for a better comprehension.

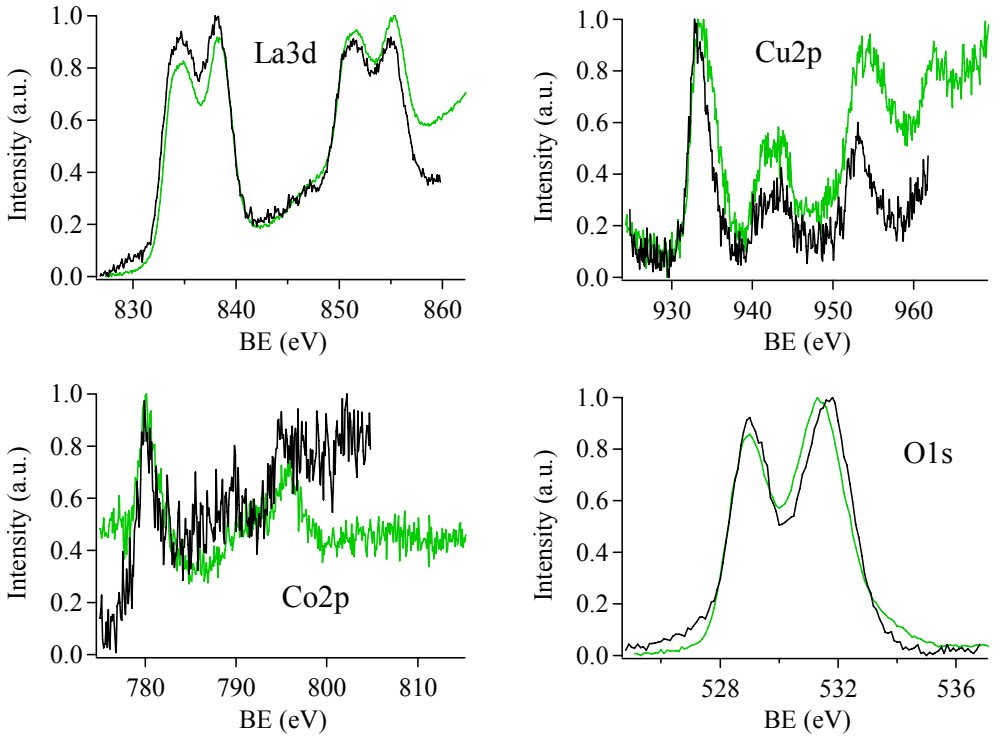

Figure 4.3. XP spectra obtained for La3d, Cu2p, Co2p and O1s for LCC2 Pec (—) and Gel (—).[1] All spectra are normalized with respect to their maximum value.

[1] XP spectra are obtained with Al monochromatic source for LCC2 Gel and Mg standard source for LCC2 Pec.

Lanthanum 3d photoelectronic peak shape (with the spin-orbit coupling and the typical shake-up contributions) and positions are characteristics for La(III) in perovskite-type materials.

Regarding Cu2p, the observed binding energies and the well evident shake-up at 943 and 962 eV, suggest that copper is present as Cu(II). Furthermore, the comparison with the literature data suggests that copper is mainly present as CuO. As already seen for LCC1, Co2p has not a very good signal to noise ratio (especially in LCC2 Pec) because of the low content of this element. Nevertheless, the peak positions and the absence of the shake-up contributions at 787 and 805 eV suggest the presence of Co(III).

Finally, the O1s profile appears very similar for LCC2 Gel and Pec. Both samples show two contributions; the first one, at lower BE (529.0 eV) is due to lattice oxygen, while that at ~531.5 eV is attributed to oxygen in hydroxyl and carbonate species. [42]

Table 4.2. XPS peak positions (binding energy, eV) obtained for LCC2 Gel and Pec. Literature data are also reported for comparison.

sample	ref	BE (eV)						
		$La3d_{5/2}$ and $_{3/2}$		$Cu2p_{3/2}$ and $_{1/2}$		$Co2p_{3/2}$	$O1s_{(lattice)}$	$O1s_{(OH, CO3)}$
LCC2 Pec		834.7	851.3	933.4	953.1	779.9	529.0	531.7
LCC2 Gel		834.6	851.4	933.5	954.0	779.9	529.0	531.4
$La_{1.8}Sr_{0.2}CuO_4$	30			933.2	952.8			
$La_{0.8}Sr_{0.2}Co_{0.8}Fe_{0.2}O_3$	38	834.4					529.7	531.4
$LaCuO_3$	39			933.2				
La_2O_3	42	833.7					530.1	
Co_2O_3	42					780.7	529.9	
CuO	42			933.6				
Co_2O_3	43					779.9		
$La(OH)_3$	44	835.0						
CuO	45			933.6			529.6	
La_2CuO_4	45	833.6		932.6				
La_2CuO_4	46			933				
$La_{0.6}Sr_{0.4}CoO_3$	47	833.4						
$La_{0.7}Sr_{0.3}MnO_3$	48	833.7						

Table 4.3. XPS and nominal compositions (atomic %) obtained for LCC2 Gel and Pec.

sample	LCC2 Pec		LCC2 Gel		nominal composition	
					oxide	cations
element						
La	21	79	22	81	28	66
Cu	4	15	4	14	11	27
Co	1	6	1	5	3	7
O	74		73		58	

Table 4.3 shows the XPS and the nominal (i.e. from the weighted amounts) compositions for LCC2 samples. Noteworthy, the obtained results are very similar for the two samples, suggesting that the preparation procedure does not affect the surface composition. Both samples surfaces are richer in oxygen with respect to the nominal value; this can be explained taking into account the surface termination with hydroxyl or carbonate groups. Focussing on the relative amounts of cations, the trend is the same already observed for LCC1: lanthanum is always overabundant consistently with its surface segregation, while copper is present in lower amount, suggesting its diffusion into the bulk. Finally, the Co concentration agrees with the nominal value.

DRIFT

DRIFT measures (figure 4.4) do not show any appreciable contributions from functional groups such as hydroxyl, carbonate or any others species residual from synthesis procedures. The only remarkable signals appear at about 704 cm^{-1} for both samples, and are assignable to lattice vibration modes. No significant changes are observed at higher temperatures. This result is consistent with the surface specific character of the hydroxyl and carbonate contaminations.

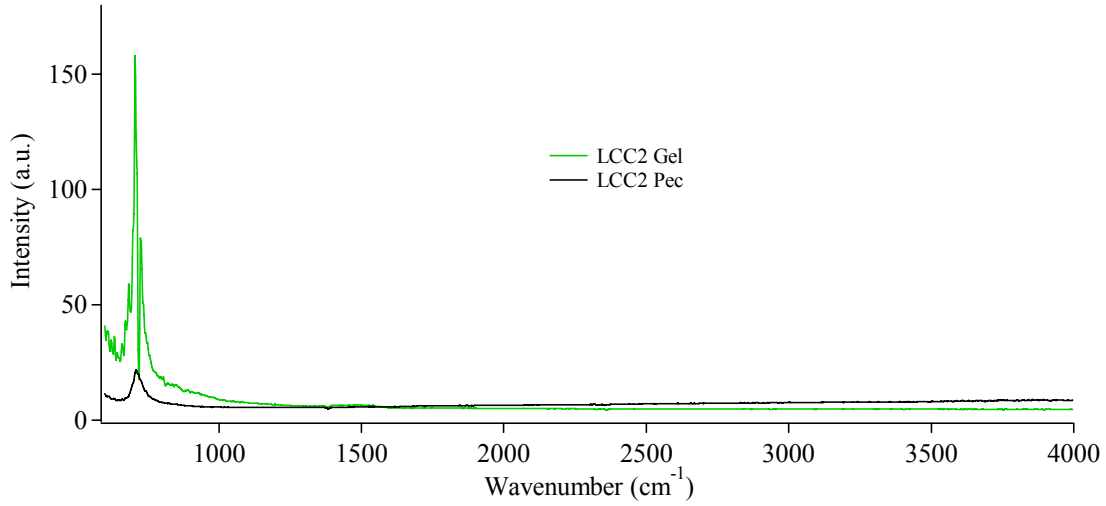

Figure 4.4. DRIFT spectra obtained at RT for LCC2 Gel and Pec. Region between 600 and 4000 cm^{-1}.

Reactivity toward methanol and ethanol: chemisorption tests

The interaction of LCC2 Gel and LCC2 Pec with methanol and ethanol was investigated by means of DRIFT technique. This is the first step to better understand the LCC2 systems reactivity. The spectra obtained for LCC2 Gel are shown in figures 4.5 and 4.6.

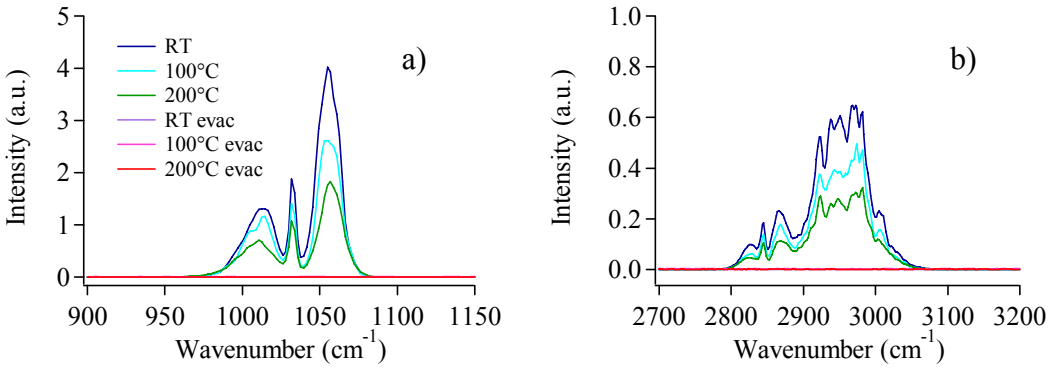

Figure 4.5. DRIFT spectra obtained for LCC2 Gel exposed to methanol, at increasing temperatures, before and after evacuation with Ar flow; a) region between 900 and 1150 cm^{-1}, b) region between 2700 and 3200 cm^{-1}.

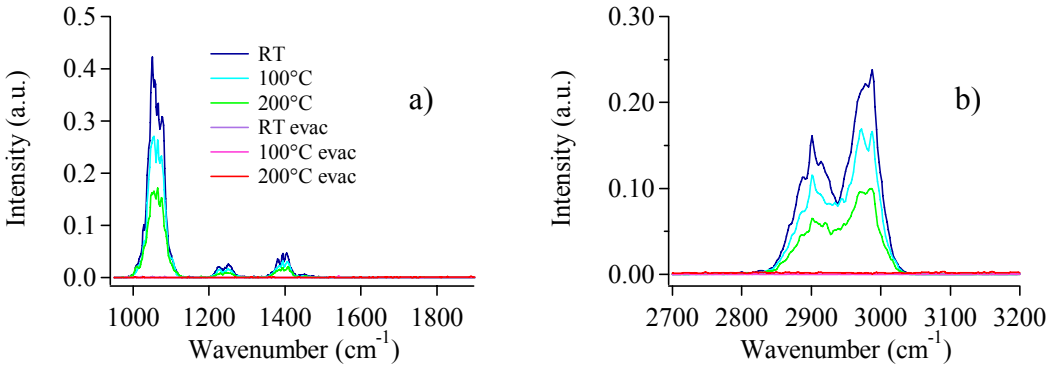

Figure 4.6. DRIFT spectra obtained for LCC2 Gel exposed to ethanol, at increasing temperatures, before and after evacuation with Ar flow; a) region between 950 and 1900 cm^{-1}, b) region between 2700 and 3200 cm^{-1}.

In figure 4.5, the C-O stretching mode (band centred at 1034 cm^{-1}) and the bands due to the stretching of C-H bonds (symmetric stretching at ~2850 cm^{-1}, asymmetric at ~2950 cm^{-1}) from gaseous methanol are well evident at every temperature. The outcomes from the performed test never show any signals arising from reaction products. The spectra obtained after evacuation with Argon (5 minutes at 80 $cm^3 \cdot min^{-1}$) never show clear signals due to adsorbed species; this allows excluding significant interactions between methanol and LCC2 Gel.

The results of the tests performed with ethanol (figure 4.6) show the typical IR spectrum of the alcohol at every temperature. The bands due to C-O stretching (1066 cm^{-1}) and C-

H bending (1240 and 1394 cm^{-1}) are displayed in fig 4.6a, while fig 4.6b shows symmetrical and asymmetrical C-H stretching modes (2900 and 2980 cm^{-1}). As for methanol, no significant signals can be observed after evacuation with Ar. Due to the high noise, however, the residual presence of ethoxy species can not be completely excluded. The outcomes from LCC2 Pec are very similar to those obtained for LCC2 Gel and are not shown for sake of brevity.

Activity toward methanol and ethanol: catalytic tests

Methanol and ethanol vapours

Beside the upon mentioned chemisorption tests, the reactivity of LCC2 Gel and Pec toward pure methanol and ethanol vapours was monitored by QMS and IR techniques (as described in appendix B). For an easier comparison, the QMS data are always normalized setting at 1 the intensity of the fuel signals (methanol and ethanol).

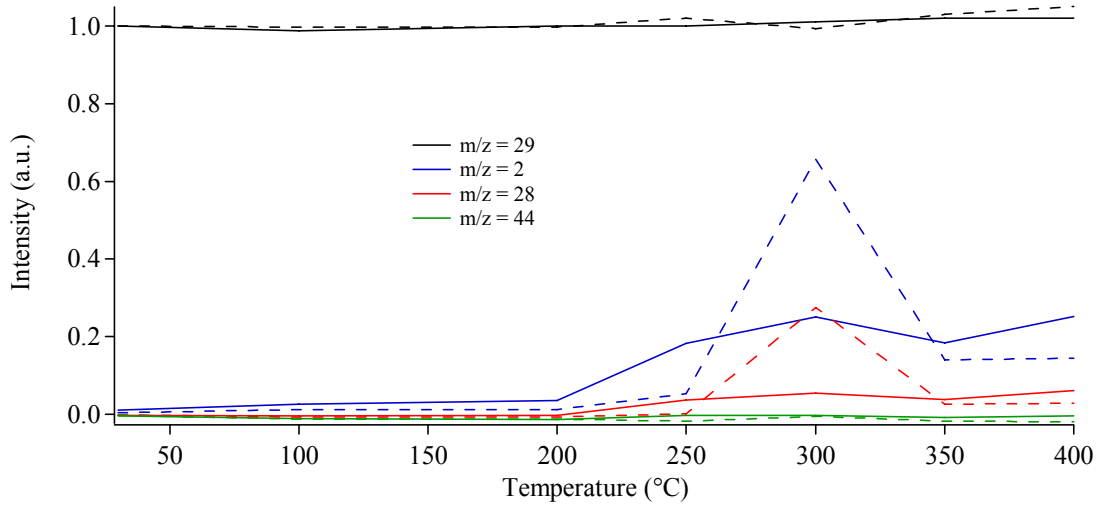

Figure 4.7. QMS data obtained for m/z = 29 (methanol), m/z = 2 (hydrogen), m/z = 28 (carbon monoxide) and m/z = 44 (carbon dioxide) at the investigated temperatures in the test with pure CH_3OH vapours. The intensities of m/z = 2, 28 and 44 are magnified 4 folds. Solid lines stand for LCC2 Gel, dashed lines for LCC2 Pec.

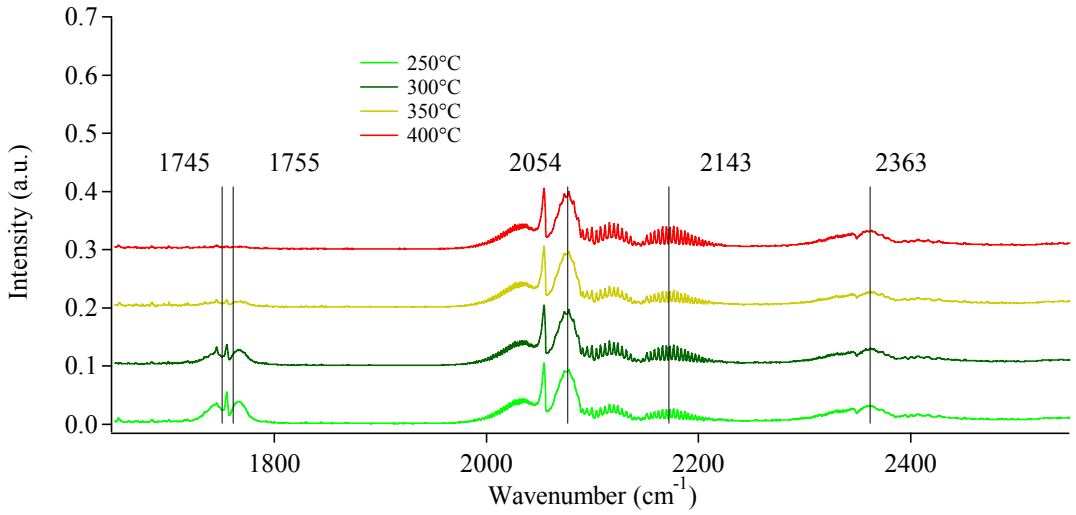

Figure 4.8. FTIR spectra obtained after exposing LCC2 Gel to CH_3OH vapours (gas mixture from the reactor). Region between 1650 and 2550 cm^{-1}. The spectra are shifted for a better comprehension.

Figure 4.7 shows the QMS trend (with respect to temperature) for m/z = 29 (methanol), 2 (hydrogen), 28 (carbon monoxide) and 44 (carbon dioxide). The obtained results clearly indicate that LCC2 Gel becomes active from 250°C and its activity remains approximately constant with increasing temperature. LCC2 Pec, otherwise, becomes active at 300°C and immediately reaches its maximum reactivity, while, at higher temperature it shows worse performances. IR spectra confirm the QMS data. Figures 4.8 and 4.9 indicate that both catalysts produce the same kind of chemicals but in a different amount. LCC2 Gel, at lower temperature, mainly forms methyl formate (band centred at 1755 cm^{-1}), while CO and CO_2 are less evident. As the temperature raises up, the band from methyl formate decreases [52] and the contribution of formic acid (at 1745 cm^{-1}) becomes more relevant. The intensities of the bands of CO and CO_2 (at 2143 and 2363 cm^{-1} respectively) remain almost constants.

LCC2 Pec is still inactive at 250°C, but at 300°C it produces a considerable amount of carbon monoxide; carbon dioxide and traces of methyl formate and formic acid are also present. At higher temperature the activity of LCC2 Pec rapidly decreases.

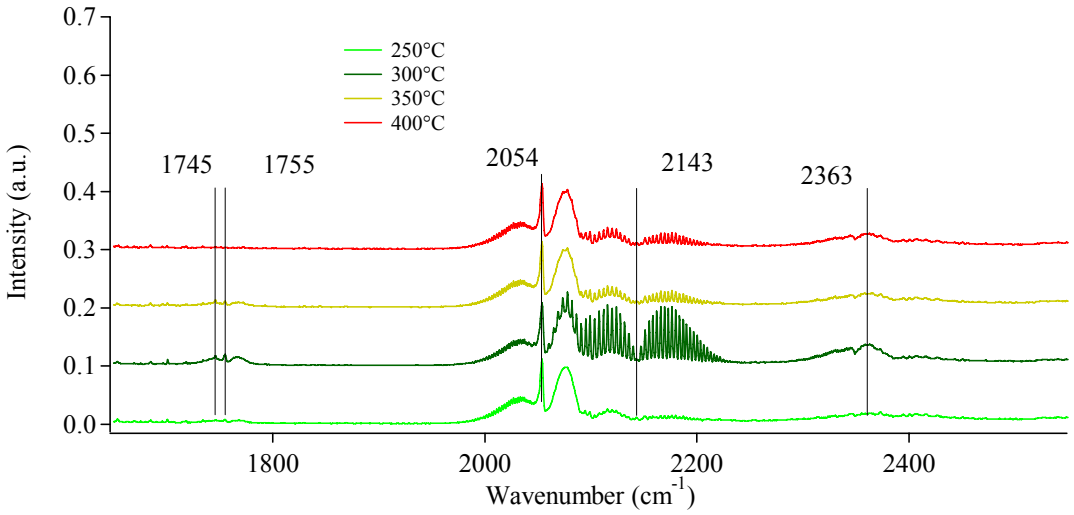

Figure 4.9. FTIR spectra obtained after exposing LCC2 Pec to CH_3OH vapours (gas mixture from the reactor). Region between 1650 and 2550 cm^{-1}. The spectra are shifted for a better comprehension.

An interesting comparison can be carried out between LCC2 and LCC1 samples. The interaction with methanol gives the same products, and the most evident difference concerns their relative amounts. This suggests that the reactions taking place in the two cases are the same; in particular, at lower temperature, CH_3OH reacts to give methyl formate and hydrogen (1): [51, 52]

$$2CH_3OH \rightleftharpoons HCOOCH_3 + 2H_2 \qquad (1)$$

Methyl formate decomposes to CO and H_2 with temperature rising up.
Finally, carbon dioxide can be obtained from the Boudouard reaction (2) [53] or by oxidation of CO employing oxygen from perovskite lattice (3):

$$2CO \rightleftharpoons C + CO_2 \qquad (2)$$

$$CO + O_P \rightleftharpoons CO_2 + O_V \qquad (3)$$

(with O_P = perovskite oxygen and O_V = Oxygen vacancy). As mentioned in Chapter 3, reaction (2) should be favored at high temperature, while reaction (3) can utilize two type of oxygen. At lower temperature adsorbed oxygen is presumably employed, while at higher temperature lattice oxygen becomes active. [54, 55]

The observed behaviour regarding the activity of LCC2 Gel and Pec suggests that both catalysts undergo deactivation caused by poisoning of active sites. This is well evident

for LCC2 Pec but, looking at the very low activity improvement revealed for LCC2 Gel with increasing temperature, a surface poisoning can not be excluded also for this sample.

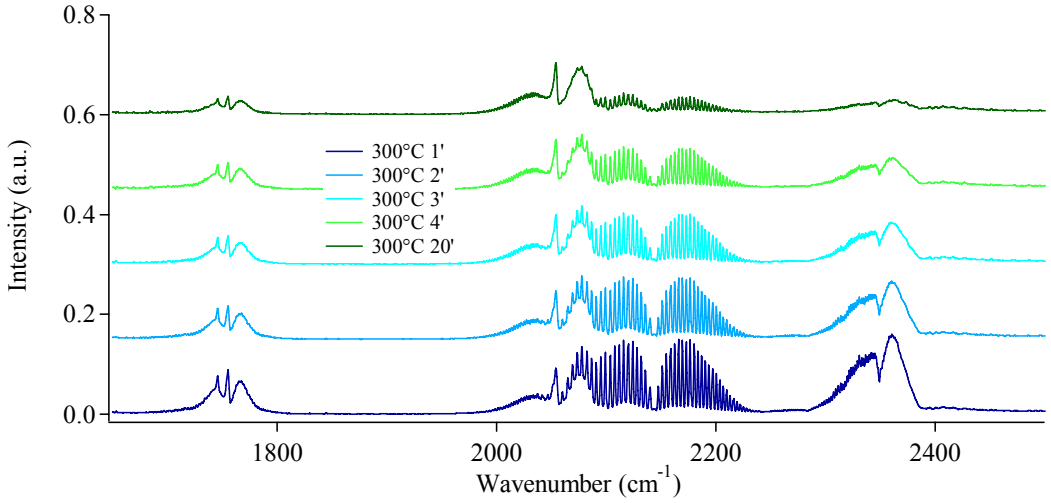

Figure 4.10. FTIR spectra obtained for LCC2 Gel after exposure for 1, 2, 3, 4 minutes to CH_3OH vapours and at the end of the test (20 minutes) at 300°C (gas mixture from the reactor). Region between 1650 and 2450 cm^{-1}. The spectra are shifted for a better comprehension.

Figures 4.10 and 4.11 point out that the reactivity reaches its maximum at the beginning of each measurement and than decreases in a few minutes reaching a steady state (or a less evident decrease) at the end of the experiments. Figure 4.11, in detail, shows that LCC2 Gel is a better catalyst for methanol decomposition (forming major amounts of products) but it undergoes the highest poisoning effect and its activity decreases more markedly than that of LCC2 Pec. The insert confirm the same trends also for m/z = 28 (carbon monoxide) and m/z = 44 (carbon dioxide) at 300°C.

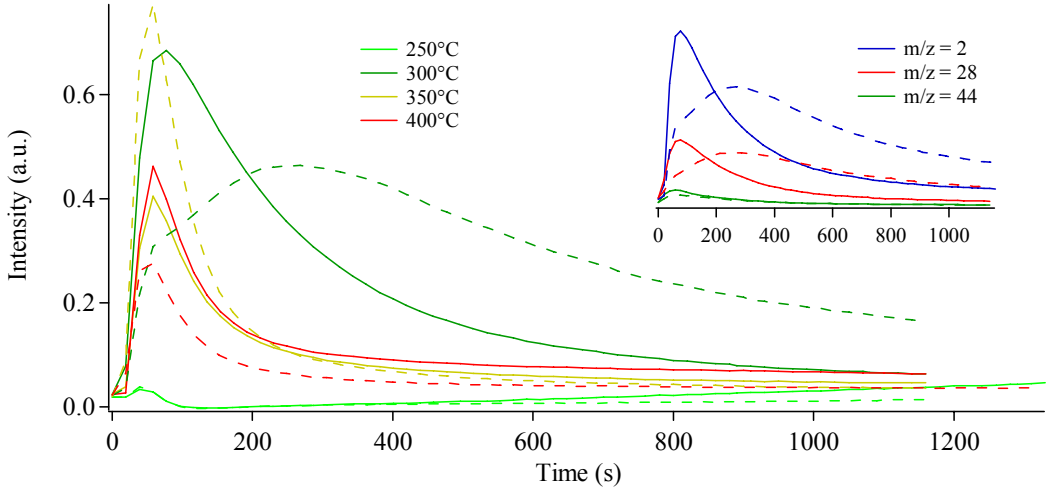

Figure 4.11. QMS data obtained for m/z = 2 (hydrogen) as a function of time for LCC2 Gel (solid lines) and LCC2 Pec (dashed lines) in the test with CH_3OH vapours. The insert shows the trends at 300°C for m/z = 2, 28 (carbon monoxide) and 44 (carbon dioxide).

To better understand the LCC2 poisoning observed during the reaction with methanol, LCC2 Gel reactivity was analyzed with respect to pure methanol vapours at decreasing temperature, starting thus from 400°C.

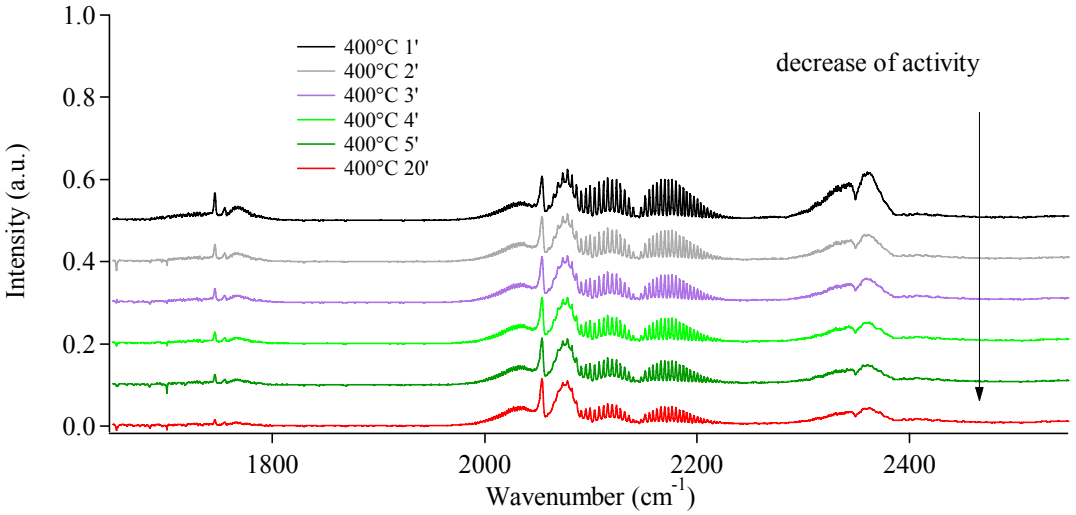

Figure 4.12. FTIR spectra obtained for LCC2 Gel after 1, 2, 3, 4, 5 and 20 minutes exposure to CH_3OH vapours at 400°C (gas mixture from the reactor). Test at decreasing temperature. Region between 1650 and 2500 cm^{-1}. The spectra are shifted for a better comprehension.

Figure 4.12 shows the behaviour observed for LCC2 Gel at 400°C at increasing time. IR spectra indicate that the amount of all products rapidly decreases with time.

Furthermore, from figure 4.13, it can be seen that LCC2 Gel completely loses its catalytic activity when the reactor is cooled down at 350°C (or at 300 and 250°C). It is important to point out that the activity trend observed in the previous test (figure 4.8) is not repeated in this new test (figure 4.13) thus confirming the hypothesized effect of surface active site poisoning on the catalyst activity.

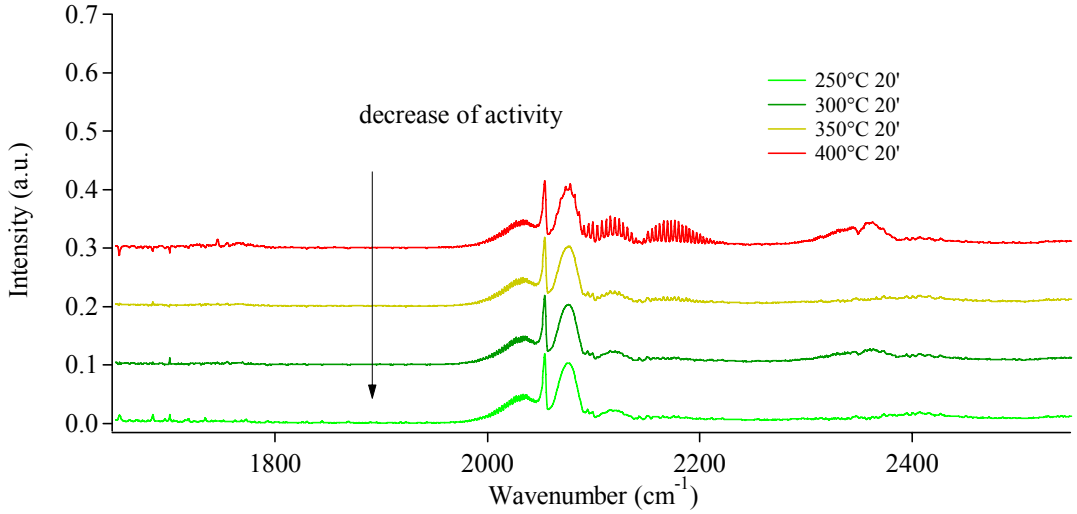

Figure 4.13. FTIR spectra obtained exposing LCC2 Gel to CH_3OH vapours for 20 minutes (gas mixture from the reactor). Test at decreasing temperature. Region between 1650 and 2500 cm^{-1}. The spectra are shifted for a better comprehension.

Worn-out LCC2 Gel was than analyzed by DRIFT to look for traces of pollutants. The obtained spectrum is shown in figure 4.14; the spectrum of fresh catalyst is also reported. The spectra comparison evidences the presence of an intense band in the region from 1300 to 1600 cm^{-1}. This is ascribed to various types of carbonate groups adsorbed on LCC2 Gel surface. Unfortunately, is not possible to understand clearly the nature of absorbed groups, but the bands suggest the presence of variously coordinated carbonate species. [76, 77, 78, 79]

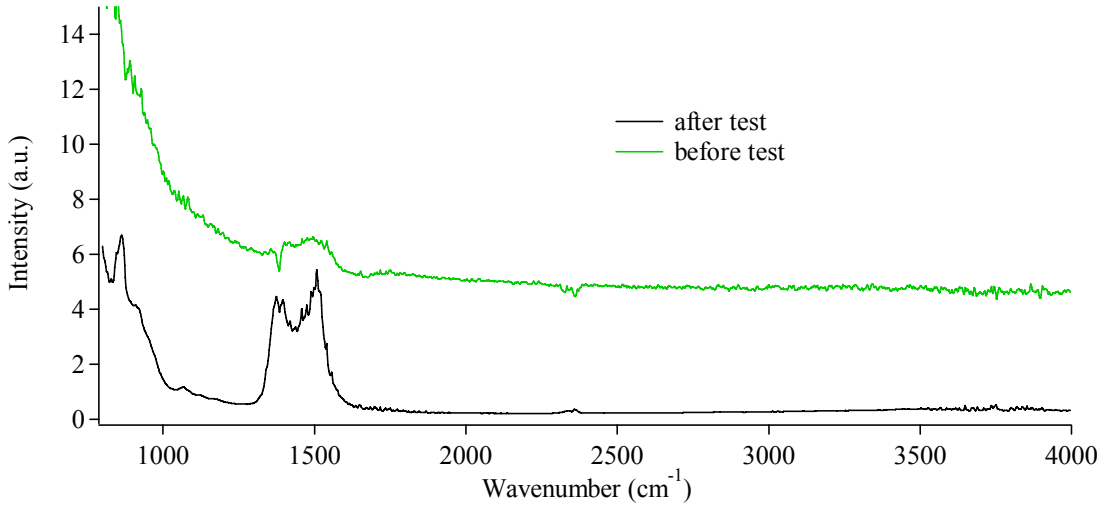

Figure 4.14. DRIFT spectra obtained for LCC2 Gel at RT before (as prepared catalyst) and after (worn-out catalyst) test with CH_3OH at decreasing temperature. Region between 800 and 4000 cm^{-1}.

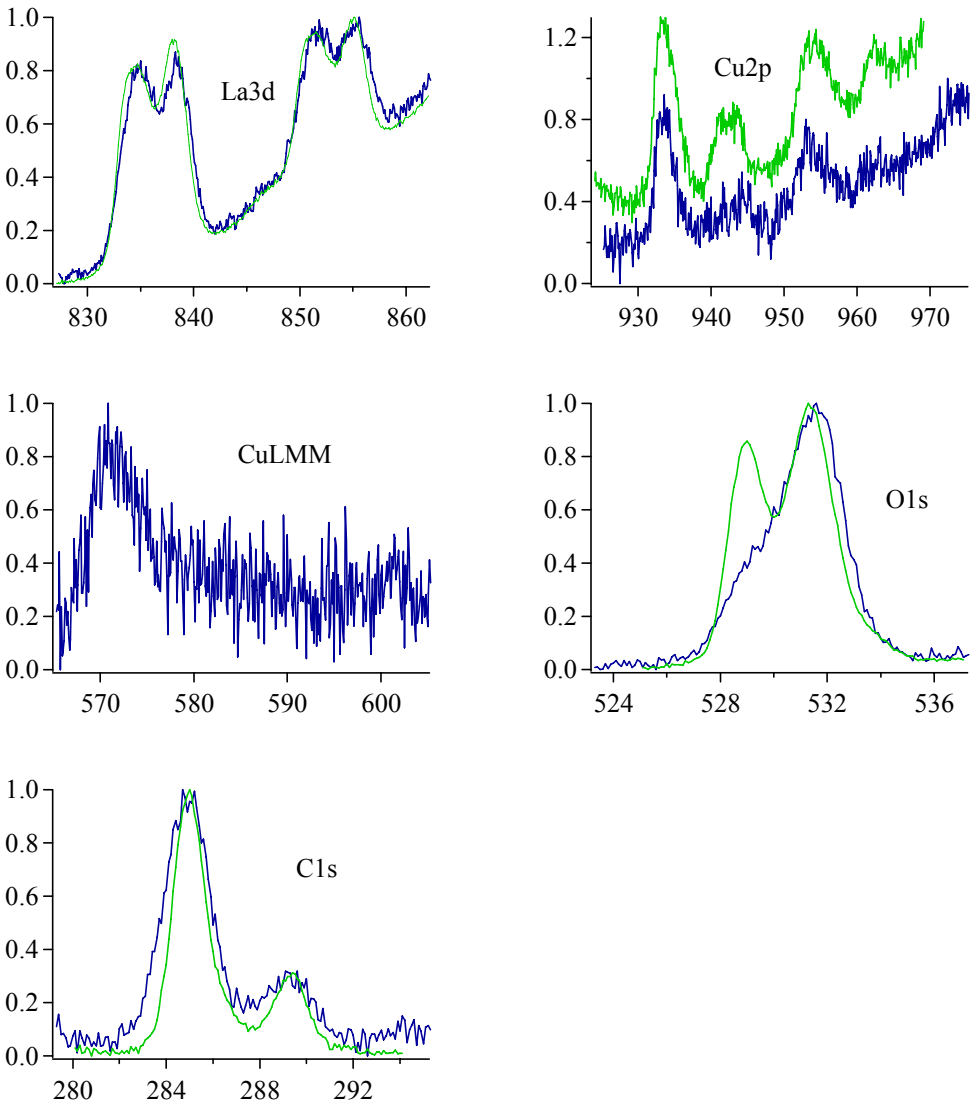

Figure 4.15. XP spectra obtained for LCC2 Gel before (as prepared sample —) and after (worn-out sample —) test with CH_3OH at decreasing temperature. All spectra are normalized with respect to their maximum value.

Table 4.4. XPS peak positions (binding energy, eV) obtained for LCC2 Gel before (as prepared) and after reaction with methanol. The kinetic energies (KE, eV) obtained for CuLMM are also reported.

XP peak	LCC2 Gel as prepared	LCC2 Gel after reaction
$La3d_{5/2}$	834.6	835.0
$Cu2p_{3/2}$ and shake up	933.5 – 942.5	933.5 – ND
$Cu2p_{1/2}$ and shake up	954.0 – 962.8	953.2 – ND
O1s lattice and OH/CO_3	529.0 – 531.4	529.0 – 531.6
C1s HC and CO_3	285.0 – 289.3	285.0 – 289.3
Auger peak		
Cu LMM	NA	915.7

ND = not detectable
NA = not available

Table 4.5. XPS and nominal compositions (atomic %) for LCC2 Gel before (as prepared) and after (worn-out) the reaction with methanol.

sample	LCC2 Gel as prepared			LCC2 Gel after reaction			nominal composition	
							oxide	cations
element								
La	14	22	81	11	19	78	22	50
Cu	2	4	14	2	4	18	17	40
Co	1	1	5	< 1	1	4	4	10
O	45	73		43	76		57	
C	38			43				

Worn-out LCC2 Gel was also investigated by means of XPS; in figure 4.15 the most significant outcomes are compared with those obtained for the fresh catalyst. The absence of the shake-up peaks in the Cu2p photoelectronic peaks clearly indicates that Cu undergoes reduction during the catalytic test. Furthermore, looking at the CuLMM peak, is possible to conclude that Cu has been reduced to Cu(I). In fact, the measured kinetic energy for the CuLMM results to be 915.7 eV, which is consistent with the literature data for Cu(I) compounds (~916 eV). [62]

Focussing on the O1s photoelectronic peak, the contribution due to hydroxyl and carbonate species, at higher binding energies (~531.5 eV), greatly increases with respect to lattice oxygen (~529.0 eV). Moreover, the FWHM of the C1s peak increases, indicating that more carbon-containing species are present.

The XPS compositions obtained for LCC2 Gel as prepared and after the test can be compared in table 4.5. From these data, an enrichment in carbon is evident for worn-out sample, thus confirming the increment of carbonaceous species due to the reaction. The relative amount of the cations and the oxygen content do not change significantly, and only a slight copper increase is observed.

Summarizing, all obtained data suggest that carbonate groups, formed as a consequence of the interaction between CO_2 and the surface, strongly interact with the active sites, and remain adsorbed on the catalyst surface. These pollutants cause the deactivation of LCC2 and a decrease in their activity toward methanol decomposition.

LCC2 Gel and Pec activity was also investigated whit respect to pure ethyl alcohol vapours. Figure 4.16, 4.17 and 4.18 show the QMS and the IR outcomes.

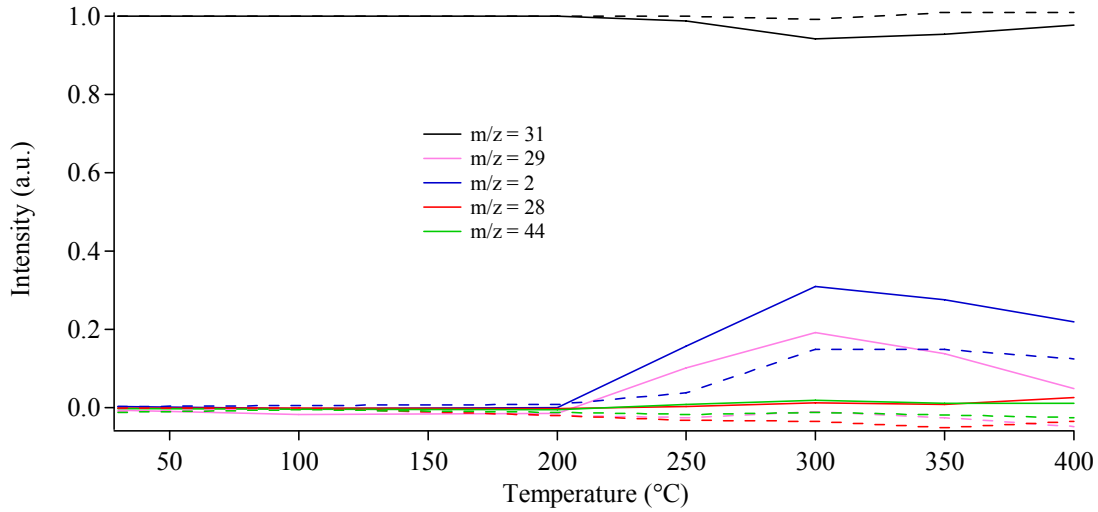

Figure 4.16. QMS data obtained for m/z = 31 (ethanol), m/z = 29 (acetaldehyde) m/z = 2 (hydrogen), m/z = 44 (carbon dioxide) and m/z = 28 (carbon monoxide and ethylene) at the investigated temperatures, in the test with pure CH_3CH_2OH vapours. The intensities of m/z = 2, 28, 29 and 44 are magnified 3 folds. Solid lines stand for LCC2 Gel, dashed lines for LCC2 Pec.

The obtained data indicate that both LCC2 Gel and Pec start to react with ethanol at 250°C and reach the maximum activity at 300÷350°C. At 400°C a decrease of the intensities of the signals due to the different products is observed.

QMS data and IR spectra confirm that the main products are acetaldehyde (band centred at 1745 cm^{-1}) and hydrogen; this kind of chemicals agrees with the dehydrogenation of ethyl alcohol (4):

$$CH_3CH_2OH \rightleftharpoons CH_3CHO + H_2 \qquad (4)$$

No others products are detected until 400°C, when a small amount of ethylene can be seen in the IR spectra (950 cm^{-1}) and from the slight increase of the fragment with m/z = 28 in the QMS measurements.

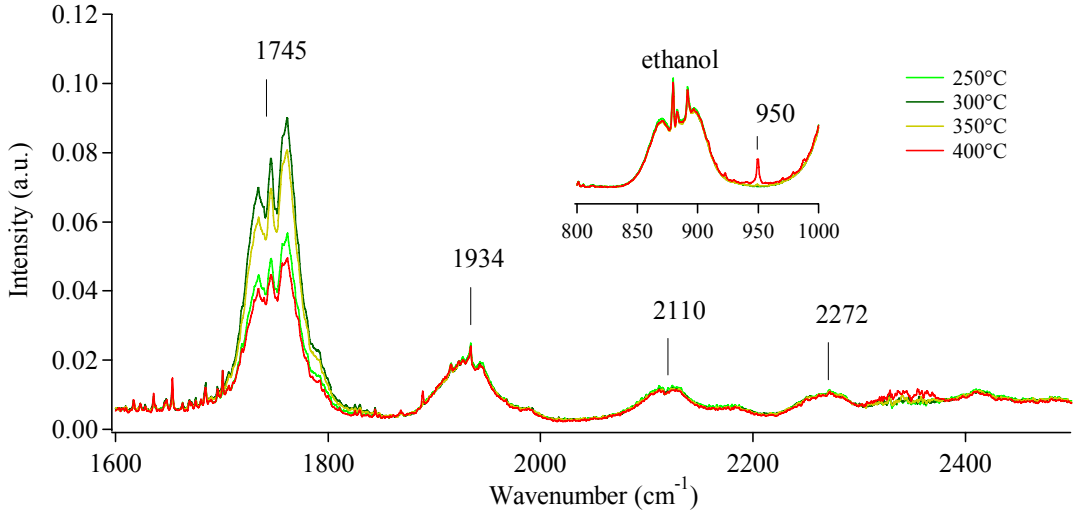

Figure 4.17. FTIR spectra obtained after exposing LCC2 Gel to CH_3CH_2OH vapours at increasing temperatures (gas mixture from the reactor). Region between 1600 and 2500 cm^{-1}. Insert: region between 800 and 1000 cm^{-1}.

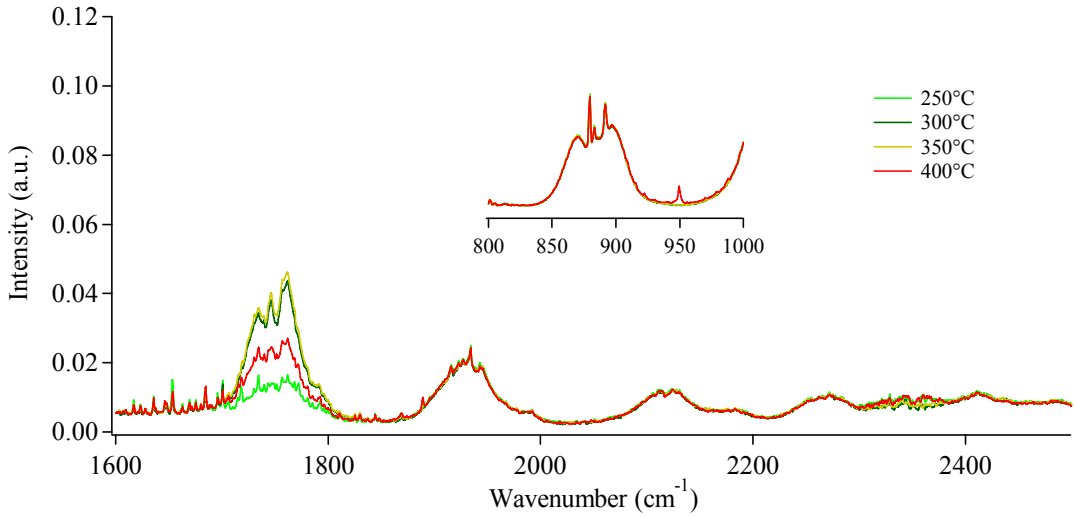

Figure 4.18. FTIR spectra obtained after exposing LCC2 Pec to CH_3CH_2OH vapours at increasing temperatures (gas mixture from the reactor). Region between 1600 and 2500 cm^{-1}. Insert: region between 800 and 1000 cm^{-1}.

Figure 4.19 well illustrates that the activity of LCC2 Gel (the outcomes for LCC2 Pec are very similar) is higher at the beginning of the test and decreases with time. This behaviour, united to the general decrease of the activity revealed at high temperature, suggests that LCC2 sample undergo poisoning as already seen for methanol pure vapours.

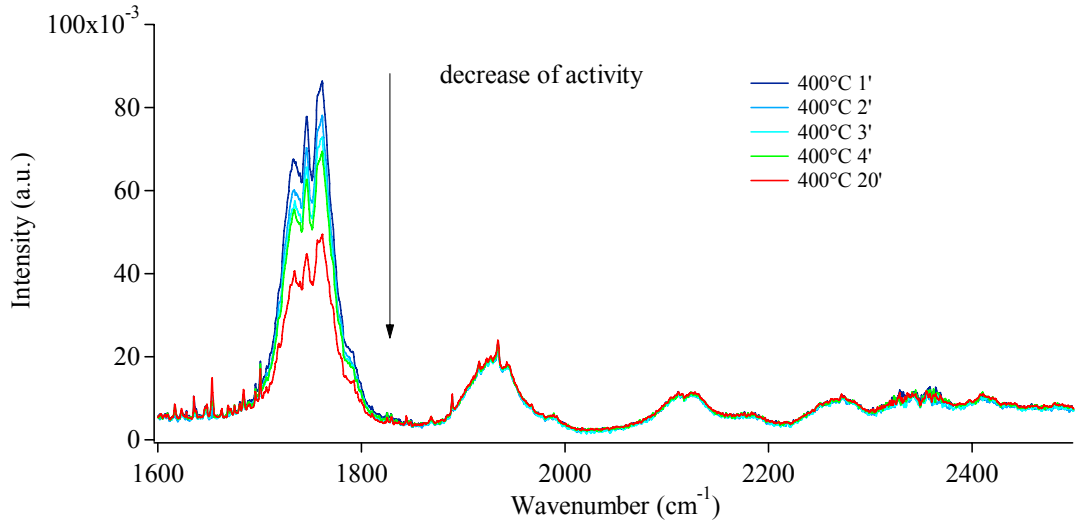

Figure 4.19. FTIR spectra obtained for LCC2 Gel after 1, 2, 3, 4 and 20 minutes exposure to CH_3CH_2OH vapours at 400°C (gas mixture from the reactor). Region between 1600 and 2500 cm^{-1}.

Table 4.6 summarizes the data obtained for the conversions of methanol and ethanol and the yields for the hydrogen. The obtained values indicate a scarce activity toward the analyzed alcohols. In the adopted conditions, the catalysts react better with ethyl alcohol than with methanol. The values, nevertheless, should be judged taking into account the specific parameters for each test; from appendix B it can be seen that the WHSV (weight hourly space velocity) used for methanol is almost twice than the one adopted for ethanol.

Table 4.6. Conversions of fuels and yields for products obtained for LCC2 Gel and LCC2 Pec with respect to the reaction with pure methanol and ethanol vapours.

	CH_3OH			CH_3CH_2OH		
sample	T max react (°C)	conv (%)[a]	yield H_2 (%)[b]	T max react (°C)	conv (%)[a]	yield H_2 (%)[b]
LCC2 Gel	250	ND[c]	< 1	300	3[d]	2
LCC2 Pec	300	1	1	300	< 1	< 1

Note:
[a] conversions determined by QMS (see appendixes A, B)
[b] yield by QMS (see appendixes A, B)
[c] not detectable
[d] medium value between QMS and IR conversions

Methanol and Ethanol oxidation

LCC2 Gel and Pec were analyzed with respect to the oxidation of methanol and ethanol. To do this, the carrier gas (Argon) was enriched with an over stoichiometric amount (with respect to fuels) of oxygen.

Figures 4.20÷4.22 show the QMS data and IR spectra collected for LCC2 Gel and Pec during the methanol oxidation experiment. The outcomes indicate that the activity is unimportant until 250°C; at 300°C small amounts of hydrogen, methyl formate (IR band at 1755 cm^{-1}), formic acid (band at 1745 cm^{-1}) and carbon dioxide (2363 cm^{-1}) are detected. At 350°C (and at 400°C only for LCC2 Pec) the total oxidation of the alcohol becomes well evident: the amount of the characteristic products of this reaction (H_2O and CO_2) greatly increases. It is worth to underline that, when the oxidation get significant, both catalysts become incandescent, as already seen for LCC1-type materials.

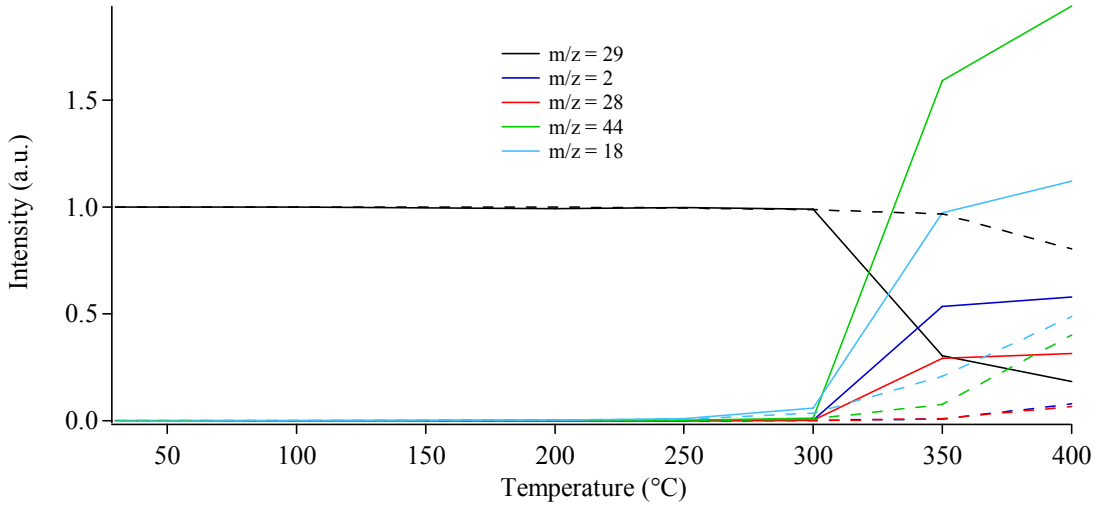

Figure 4.20. QMS data obtained for m/z = 29 (methanol), m/z = 2 (hydrogen), m/z = 28 (carbon monoxide), m/z = 44 (carbon dioxide) and m/z = 18 (water) in oxidizing conditions at the investigated temperatures. Solid lines stand for LCC2 Gel, dashed lines for LCC2 Pec.

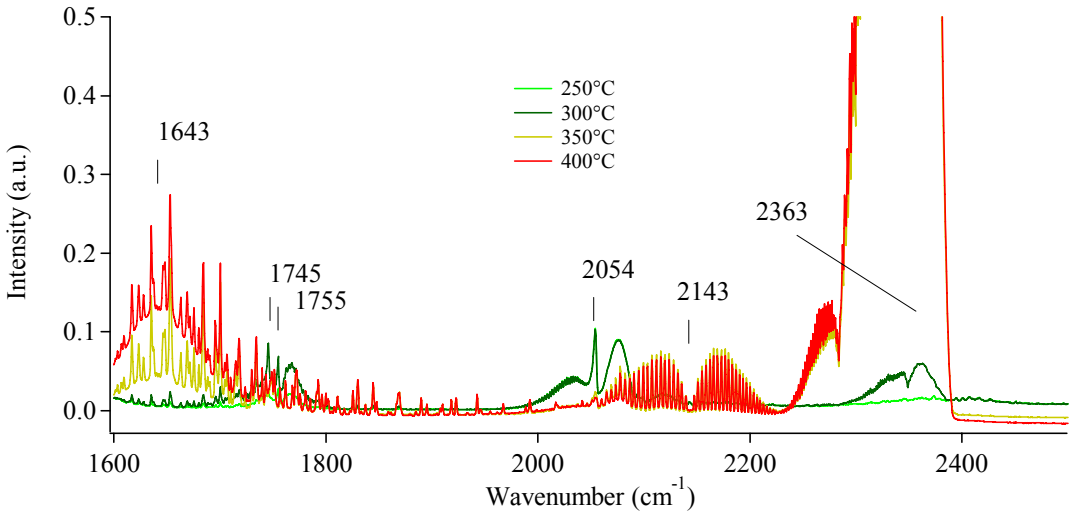

Figure 4.21. FTIR spectra obtained after exposing LCC2 Gel to CH_3OH vapours O_2 enriched (gas mixture from the reactor). Region between 1600 and 2500 cm^{-1}.

By-products such as CO and H_2 are also observed. Their presence can be explained considering partial oxidation reactions. It is well known that carbon monoxide arises from an incomplete oxidation, which can depend on an under-stoichometric amount of O_2 or, more probably from a too short contact time with the catalyst (5). The same considerations hold for hydrogen (6).

$$CH_3OH + 1/2O_2 \rightleftharpoons CO + H_2O \quad (5)$$

$$CH_3OH + 1/2O_2 \rightleftharpoons CO_2 + H_2 \quad (6)$$

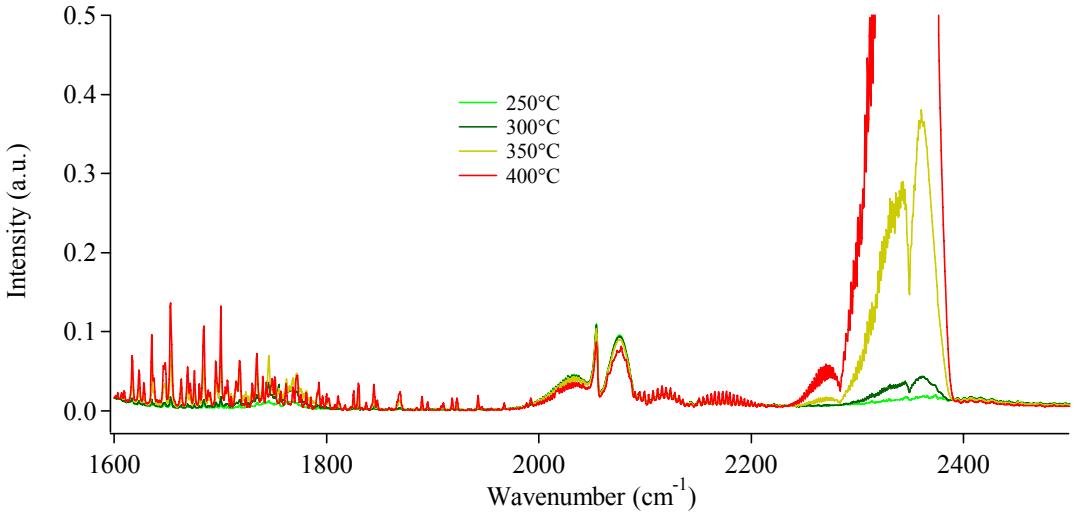

Figure 4.22. FTIR spectra obtained after exposing LCC2 Pec to O_2 enriched CH_3OH vapours (gas mixture from the reactor). Region between 1600 and 2500 cm^{-1}.

The results of the ethanol oxidation tests carried out with LCC2 Gel and Pec are shown in figures 4.23, 4.24 and 4.25. Both QMS and IR data suggest that LCC2 Gel and Pec start to convert ethyl alcohol at 250°C, producing very small amounts of acetaldehyde (IR band at 1745 cm^{-1}) and hydrogen. The reaction of dehydrogenation continues and improves its rate at 300°C. From 350°C a larger amounts of CO_2 (2363 cm^{-1}) and H_2O (vibro-rotational band centred at 1595 cm^{-1}) can be observed. Only at 400°C the total oxidation widely occurs and, as for the test with CH_3OH, both catalysts become incandescent. Nevertheless, acetaldehyde and hydrogen are still present among the products; CO is also detected and probably arises from the partial oxidation of ethanol.

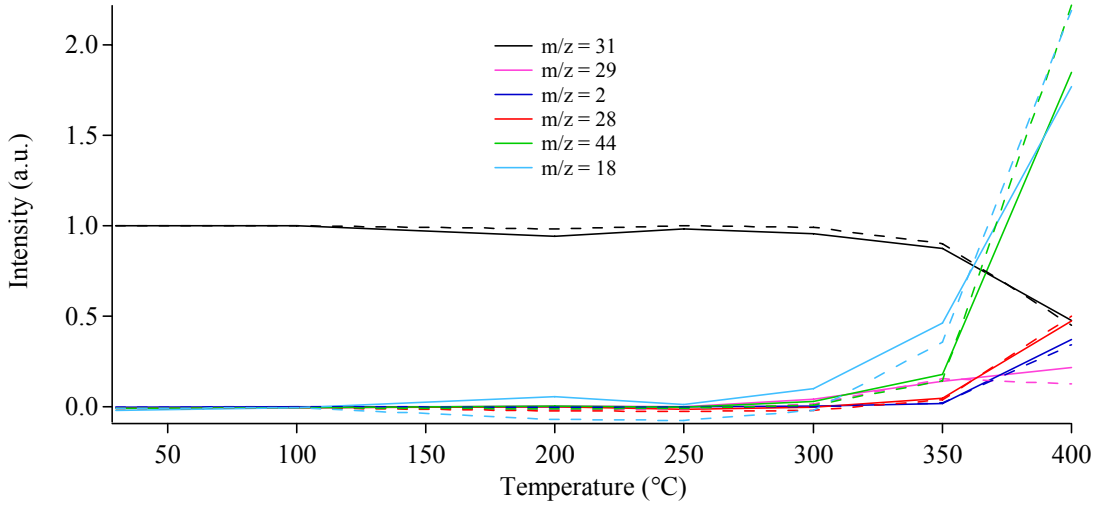

Figure 4.23. QMS data obtained for m/z = 31 (ethanol), m/z = 29 (acetaldehyde), m/z = 2 (hydrogen), m/z = 28 (carbon monoxide), m/z = 44 (carbon dioxide) and m/z = 18 (water) in oxidizing conditions. Solid lines stand for LCC2 Gel, dashed lines for LCC2 Pec.

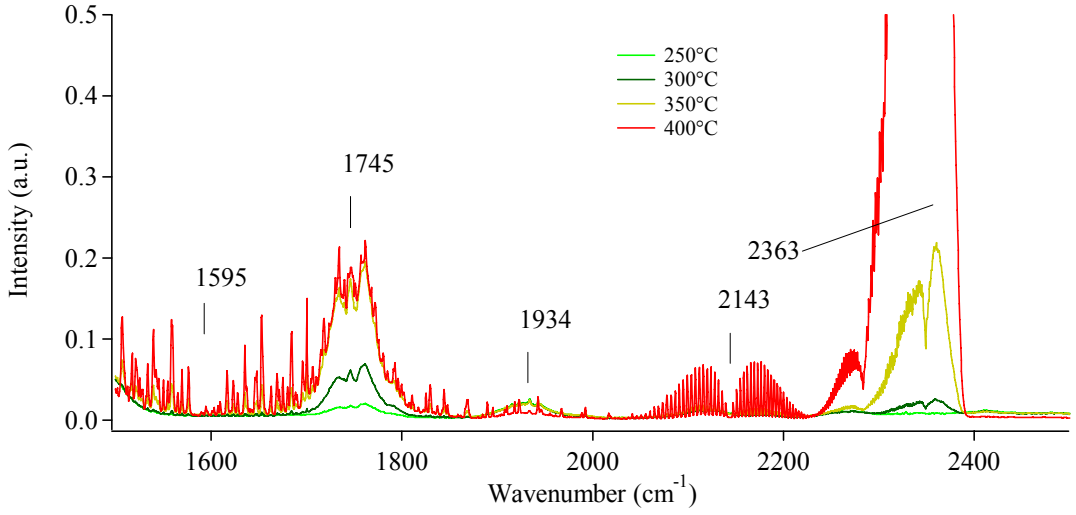

Figure 4.24. FTIR spectra obtained after exposing LCC2 Gel to CH_3CH_2OH vapours O_2 enriched (gas mixture from the reactor). Region between 1500 and 2500 cm^{-1}.

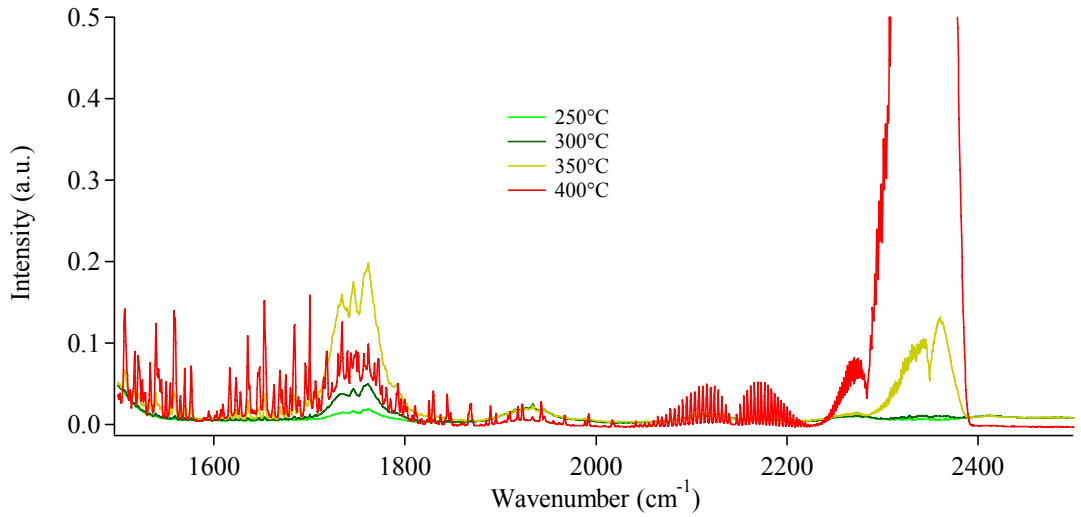

Figure 4.25. FTIR spectra obtained after exposing LCC2 Pec to CH_3CH_2OH vapours O_2 enriched (gas mixture from the reactor). Region between 1500 and 2500 cm^{-1}.

Table 4.7. Conversions of fuels and yields for products at 400°C obtained for LCC2 Gel and LCC2 Pec with respect to methanol and ethanol oxidation.

	CH_3OH/O_2				CH_3CH_2OH/O_2			
sample	conv	yield H_2	yield CO	yield CO_2	conv	yield H_2	yield CO	yield CO_2
LCC2 Gel	82	7	6	45	57	17	8	41
LCC2 Pec	19	1	< 1	13	55	13	ND[a]	42

Note:
[a] not detectable
all data are in % (see appendixes A, B)

From the analysis of the QMS data, the values for methanol and ethanol conversion and the yields for the main products can be calculated. Table 4.7 summarizes the outcomes. [2] LCC2 Gel shows the best performance with both alcohols; in the case of methanol, in particular, a very good conversion value is reached. In contrast, LCC2 Pec appears less active. Considering ethanol, LCC2 Pec seems to promote the total oxidation better than LCC2 Gel, since the intensity of the acetaldehyde IR band appears less intense.

[2] Some mismatches between the conversions and the yields data are evident. This is mainly due to uncalculated products (such as acetaldehyde) and to the uncertainly in the real stoichiometry of the reactions.

Methanol and Ethanol steam reforming

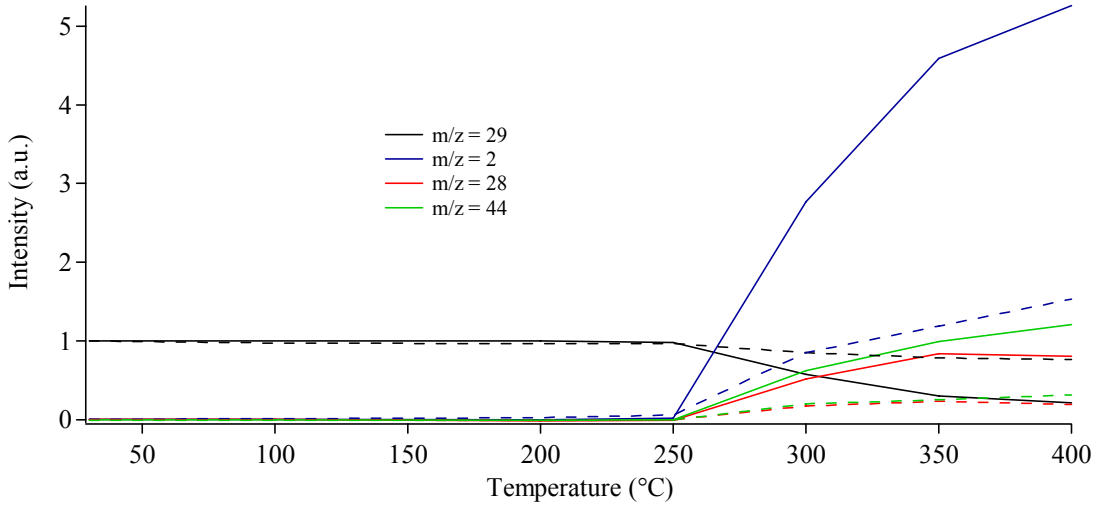

Figure 4.26. QMS data obtained for m/z = 29 (methanol), m/z = 2 (hydrogen), m/z = 28 (carbon monoxide), and m/z = 44 (carbon dioxide) in steam reforming conditions. Solid lines stand for LCC2 Gel, dashed lines for LCC2 Pec.

Outcomes from the methanol steam reforming catalyzed by LCC2 Gel and Pec are shown in figures 4.26÷4.28. From figure 4.26 it can be seen that both catalysts are inactive until 250°C, while at 300°C hydrogen, carbon dioxide and carbon monoxide are detected. At higher temperature LCC2 Gel and Pec improve their performances. IR spectra confirm the observations for CO (2143 cm^{-1}) and CO_2 (2363 cm^{-1}).
H_2 and CO_2 are produced from the overall steam reforming reaction (7):

$$CH_3OH + H_2O \rightleftharpoons 3H_2 + CO_2 \qquad (7)$$

The reaction above is assumed to be the sum of the decomposition of methanol in CO and H_2 (8), followed by the water gas shift reaction (9):

$$CH_3OH \rightleftharpoons 2H_2 + CO \qquad (8)$$

$$CO + H_2O \rightleftharpoons H_2 + CO_2 \qquad (9)$$

This mechanism allows explaining the formation of carbon monoxide as intermediate product.

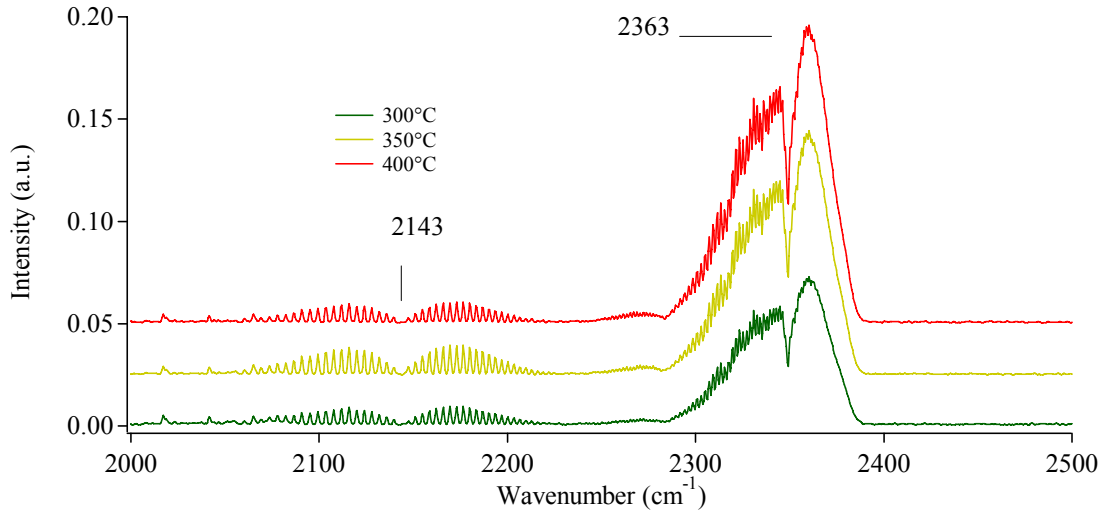

Figure 4.27. FTIR spectra obtained after exposing LCC2 Gel to CH_3OH 1M vapours (gas mixture from the reactor). Region between 2000 and 2500 cm^{-1}. The spectra are shifted for a better comprehension.

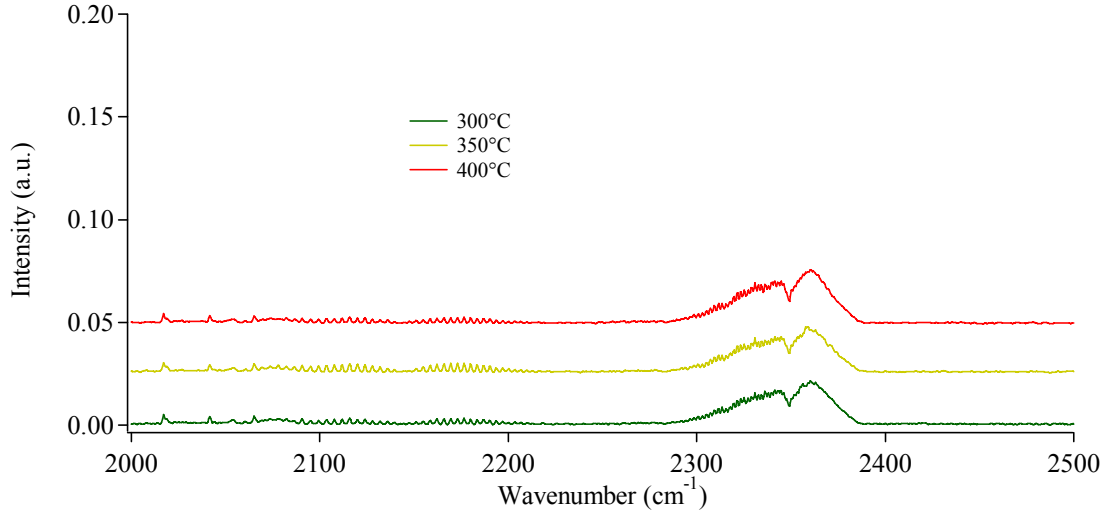

Figure 4.28. FTIR spectra obtained after exposing LCC2 Pec to CH_3OH 1M vapours (gas mixture from the reactor). Region between 2000 and 2500 cm^{-1}. The spectra are shifted for a better comprehension.

IR and QMS data suggest that LCC2 Gel always reacts with the methanol/water mixture better than LCC2 Pec. The values for the conversions of methyl alcohol and the yields in H_2 and CO_2 (table 4.8) confirm this trend. From the same table, a huge mismatch between the conversion of methanol and the yield for the main products can be seen. A possible cause for this behaviour could be a scarce release of the products from the catalyst surface. This phenomenon was already observed in the tests with pure methanol vapours. In this case, anyway, the missing amounts of products induce to think that the catalysts undergo to a deep poisoning, causing worse performances at increasing time. To investigate this, the reactivity of LCC2 Gel was analyzed with respect to methanol steam reforming, but the test was left to run for 6 h at 400°C.

Table 4.8. Conversions of fuels and yields for products at 400° obtained for LCC2 Gel and LCC2 Pec with respect to methanol and ethanol steam reforming.

	CH_3OH 1M				CH_3CH_2OH 1M			
sample	conv	yield H_2	yield CO	yield CO_2	conv	yield H_2	yield CO	yield CO_2
LCC2 Gel	79	24	< 1	22	40	4	ND	ND
LCC2 Pec	23	5	ND[a]	ND	12	ND	ND	ND

Note:
[a] not detectable
all data are in % (see appendixes A, B)

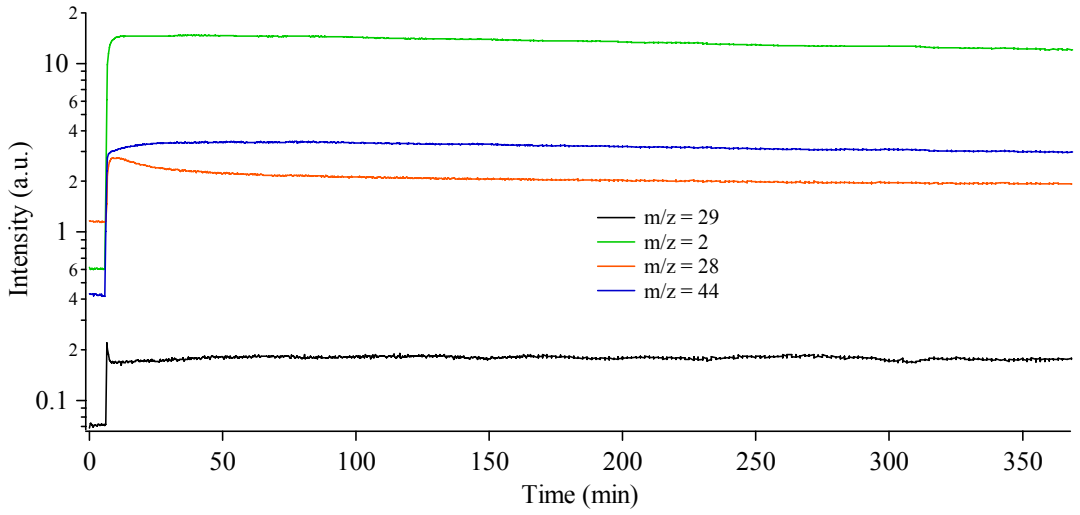

Figure 4.29. QMS data obtained for m/z = 29 (methanol), m/z = 2 (hydrogen), m/z = 28 (carbon monoxide), and m/z = 44 (carbon dioxide) for LCC2 Gel in steam reforming conditions for 6 h at 400°C.

Figure 4.29 shows the trend measured for the fragments characteristic of methanol (31), hydrogen (2), carbon monoxide (28) and carbon dioxide (44); a brief conditioning time before the beginning of the test is also shown. A detailed analysis of the trends for the investigated masses, on the overall experiment, indicates that H_2, CO and CO_2 slightly decrease with time. Nevertheless, looking at the paths for CO and CO_2, it can be seen that the first one shows its maximum production in the first few minutes, and when it decreases, the CO_2 amount, in contrast, increases. This could be interpreted as a variation in the relative rate of methanol decomposition (8) and the water gas shift reaction (9), and also considering a possible retention of CO on the catalyst surface.

$$CH_3OH \rightleftharpoons 2H_2 + CO \quad (8)$$

$$CO + H_2O \rightleftharpoons H_2 + CO_2 \quad (9)$$

The path of the mass 31 (methanol) appears more elaborate. In fact, it is the sum of two opposite trends: a decreasing trend caused by the depletion of methanol in the CH_3OH/ H_2O 1M solution used as feed (caused by the stripping of methanol by Argon flow), and an increasing trend due to a drop in the catalyst reactivity.
Table 4.9 summarizes the conversions and the observed yields.

Table 4.9. Conversions of CH_3OH and yields for products at 400°C obtained for LCC2 Gel with respect to CH_3OH steam reforming for 6 h.

time (min)	CH_3OH conv	yield H_2	yield CO	yield CO_2	total C out	missing C
0	80	21	6	17	23	57
160	76	19	5	16	21	55
360	71	17	4	14	18	53

all data are in % (see appendixes A, B)

The total steam reforming reaction can be considered as the sum of reactions (8) and (9); the relative amounts of CO_2/CO suggest that reaction (9) is faster than (8). Furthermore, the decreasing rate of conversion and yields appear almost constant, so it is possible to hypothesize that the reaction mechanism remains the same during the whole test. Finally, the last column of the table 4.9 (which is obtained by subtracting column 2 – column 6) shows the "missing" carbon, i.e. the amount of carbonaceous products retained on the catalyst surface. This amount decreases with time, suggesting a possible saturation of the adsorbing sites. Figure 4.30 shows the DRIFT spectra for LCC2 Gel catalyst as prepared, after 1 h and at the end of the long-test with CH_3OH 1M. The spectra confirm that the uptake of pollutants is not linear with time, but is faster at the beginning.
Taking into account that the activity of a perovskite material is mainly due to the B-cations [80, 81] (here Cu and Co), and the huge amount of adsorbed species, compared to the high conversions values, is reasonable to think that the poisoning species are adsorbed mainly on the less active sites (lanthanum cations are able to react with CO_2 [49]), and less on the active sites. In other words, the large amount of the unreleased species does not agree with the low activity decrease (and vice versa). In fact, if the poisoning species would adsorbed on the active sites, the catalytic activity should suddenly drop to zero. This suggests that the active sites are only slightly influenced by the poisoning species.

These hypotheses could be verified with further analysis. A possible way is to perform chemisorption tests with CO and CO_2 to investigate the active sites. Another way is to repeat the test for a longer time just to verify if the uptake of carbon species really reaches a steady state, and which is the trend of conversion i.e. if the conversion values decrease consistently or continues to decrease (gradually or with a sudden drop).

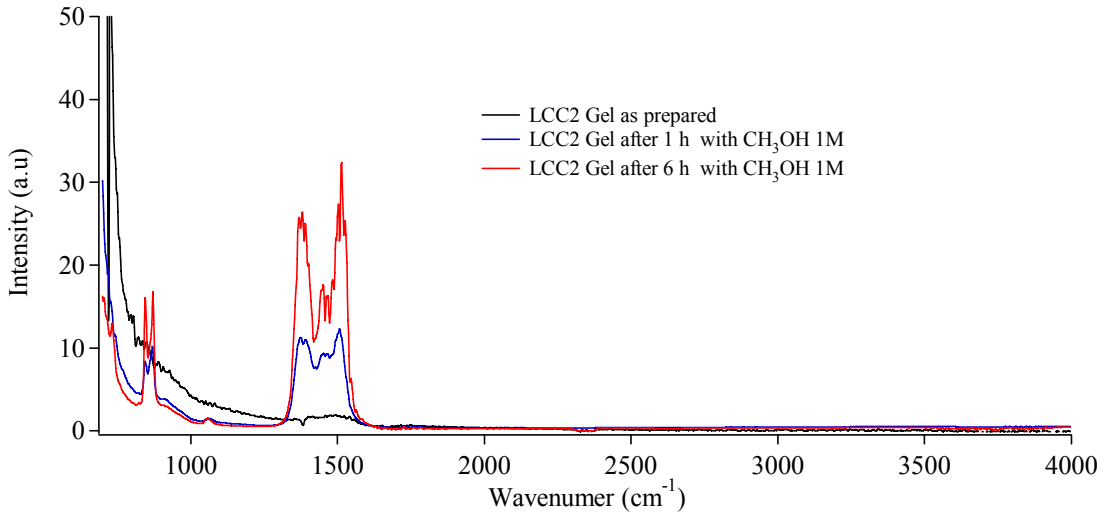

Figure 4.30. DRIFT spectra obtained at RT for LCC2 Gel as prepared, after 1 h and after 6 h of exposure CH_3OH 1M at 400°C. Region between 800 and 4000 cm^{-1}.

Worn-out LCC2 Gel was also investigated by XPS. In figure 4.31 La3d, Cu2p, CuLMM, O1s and C1s peaks obtained for the worn-out catalyst and those for the as prepared LCC2 Gel are compared. La3d photoelectronic peak appears wider in the used sample and the shake-up contributions are less defined. Nevertheless, the peak positions are quite similar to those of the as prepared LCC2 (table 4.10). This behaviour agrees with a more disordered chemical environment and the possible presence of new species such as $La(OH)_3$, La_2O_3 and $La_2(CO_3)_3$ [42, 44, 50, 61]

From Cu2p region, it is well evident the reduction of copper from (II) to (I): the absence of the shake-up contributions (typical for Cu (II)), and the position of CuLMM auger peak (kinetic energy = 916.5 eV [62]) confirms this result.

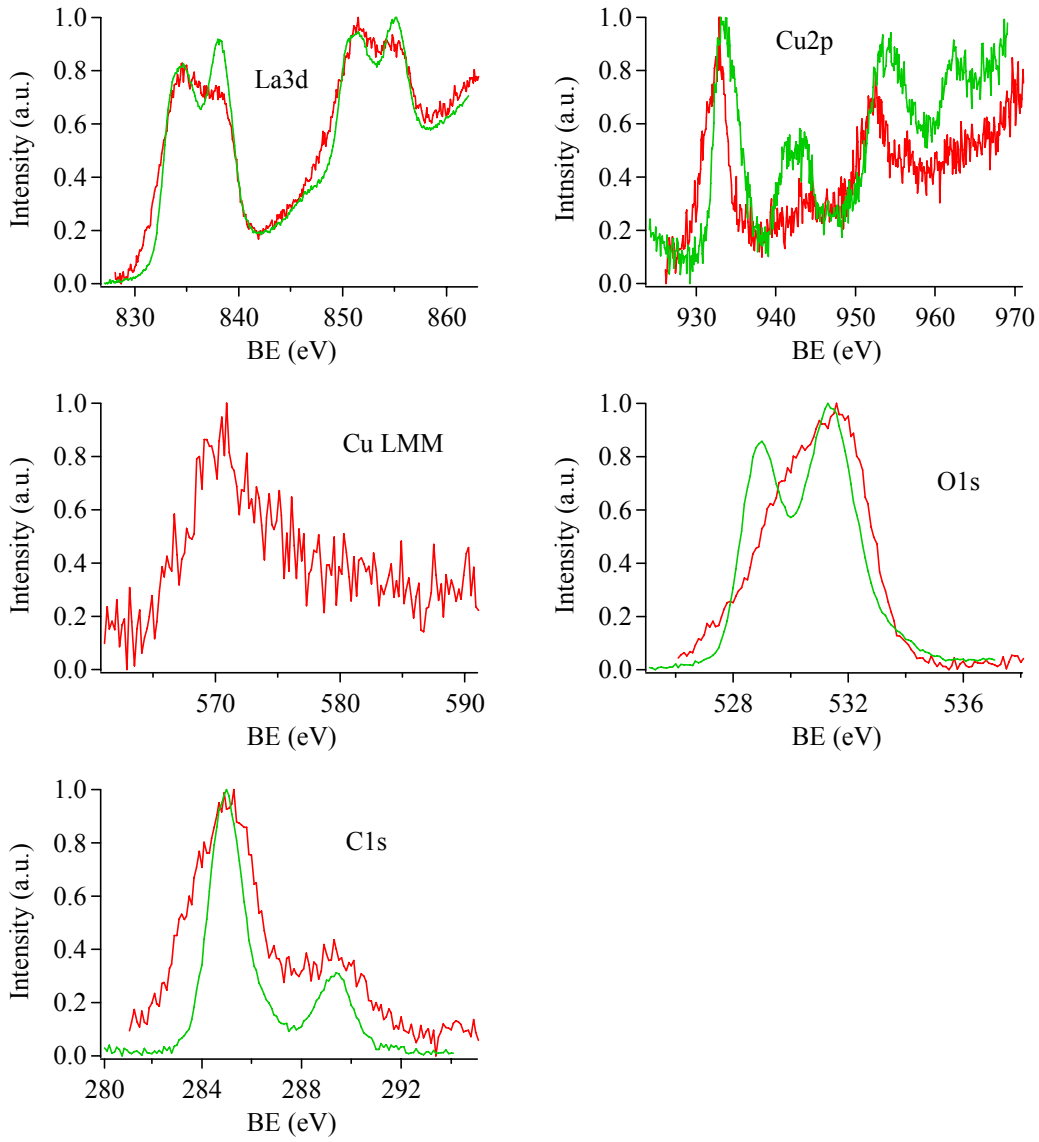

Figure 4.31. XP spectra obtained for LCC2 Gel before (—) and after (—) testing with CH_3OH 1M at 400°C for 6 h. All spectra are normalized with respect to their maximum value.

The surface of the worn-out sample appears enriched in hydroxyl and carbonate species, since the contribution at ~531.5 eV in O1s photoelectronic peak appears very intense with respect to the one ascribed to lattice oxygen (at 529.0 eV). Finally, C1s peak is very broad and, beside the adventitious carbon at 285.0 eV and the carbonate species (289.3 eV), new C-containing species seem to be present. The quantitative analysis (table 4.11) confirms, in the reacted sample, the increased amount of carbon, which is compatible with the hypothesized presence of carbonaceous species.

Concerning the only cations, cobalt is almost undetectable, while lanthanum and copper amounts are, respectively, lower and higher than in the fresh LCC2. The observed behaviour can be a further confirmation of the above hypothesis concerning the

adsorption of the pollutants one the A-sites with the consequent intensity attenuation due to the poisoning layers. [82]

This result is also confirmed by De Asha and Nix. [56] In their paper, a La/Cu(111) system is prepared by oxidation (under UHV environment) of La films deposited on Cu(111); the obtained LaO_x/Cu(111) is then exposed to increasing amounts of CO_2 at RT. The XPS outcomes allowed the Authors to point out that carbon dioxide is only absorbed over the LaO_x overlayers, as confirmed by the $La3d_{5/2}$ binding energy shifts. Carbonate species form as a consequence of the lattice oxygen involvement (testified by the variation of the $O_{lattice}/O_{CO2}$ and by C/O_{CO2} XPS ratios); moreover XPS and UPS data suggest that the main surface species in all observed cases is essentially of a carbonate nature and no distinct surface species (carbon oxygen complexes, peroxides, …) are evident.

Table 4.10. XPS peak positions (binding energy, eV) obtained for LCC2 Gel before (as prepared) and after reaction with CH_3OH 1M at 400°C for 6 h. The kinetic energies (KE, eV) obtained for CuLMM are also reported.

XP peak	LCC2 Gel as prepared	LCC2 Gel after reaction
La3d $_{5/2}$ and $_{3/2}$	834.6 – 851.4	834.9 – 851.5
Cu2p$_{3/2}$ and shake up	933.5 – 942.5	932.9 – ND
Cu2p$_{1/2}$ and shake up	954.0 – 962.8	952.3 – ND
O1s lattice and OH/CO_3	529.0 – 531.4	ND – 531.6
C1s HC and CO_3	285.0 – 289.3	285.0 – 289.3
Auger peak		
Cu LMM	NA	916.5

ND = not detectable
NA = not available

Table 4.11. XPS and nominal compositions (atomic %) obtained for LCC2 Gel before (as prepared) and after the reaction with CH_3OH 1M at 400°C for 6 h.

sample	LCC2 Gel as prepared			LCC2 Gel after reaction			nominal composition	
							oxide	cations
element								
La	14	22	81	12	20	77	22	50
Cu	2	4	14	4	6	23	17	40
Co	1	1	5	< 1	< 1	< 1	4	10
O	45	73		38	74		57	
C	38			46				

LCC2 catalysts were also investigated with respect to ethanol steam reforming. Figures 4.32÷4.34 indicate that LCC2 Gel is active from 300°C with the production of hydrogen, acetaldehyde, (IR band at 2705 and 2731 cm^{-1}), carbon dioxide (2363 cm^{-1}) and a contribution from m/z = 28 probably due to carbon monoxide and ethylene. These last species, probably being produced in very small amounts, are only detected by QMS. LCC2 Pec, appears less active than LCC2 Gel but the observed products are the same.

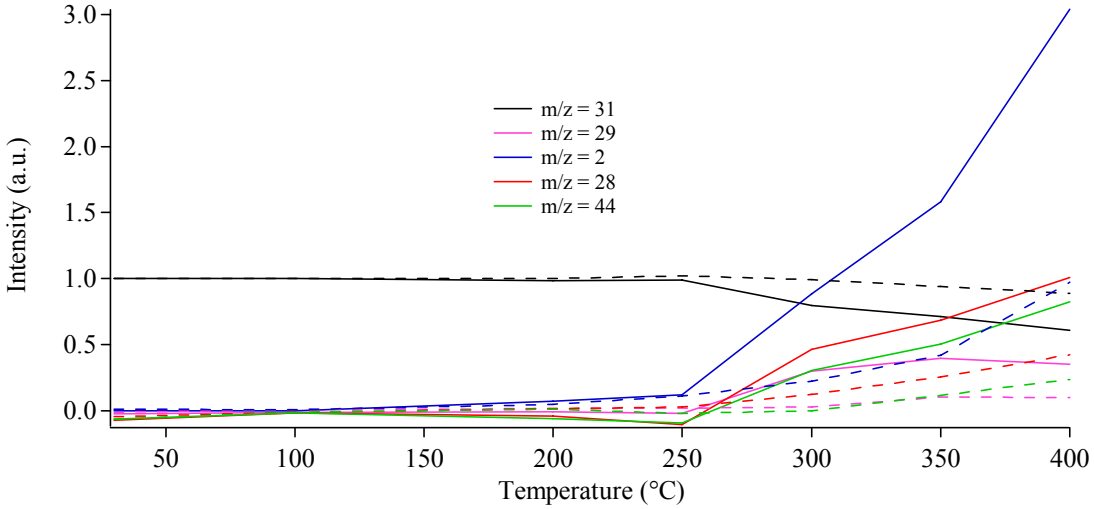

Figure 4.32. QMS data obtained for m/z = 31 (ethanol), m/z = 29 (acetaldehyde) m/z = 2 (hydrogen), m/z = 44 (carbon dioxide) and m/z = 28 (carbon monoxide and ethylene) in steam reforming conditions. Solid lines stand for LCC2 Gel, dashed lines for LCC2 Pec.

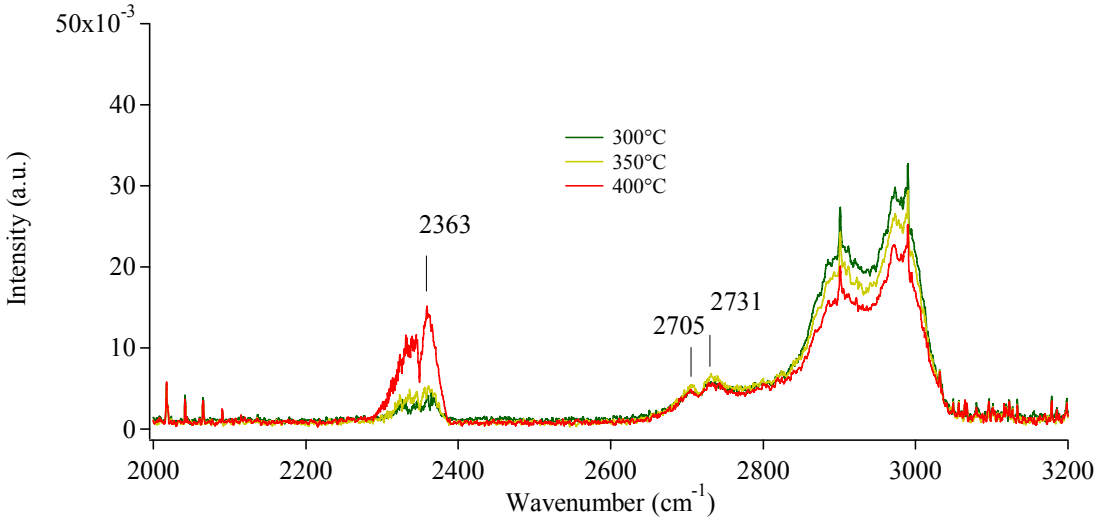

Figure 4.33. FTIR spectra obtained after exposing LCC2 Gel to CH_3CH_2OH 1M vapours (gas mixture from the reactor). Region between 2000 and 3200 cm^{-1}.

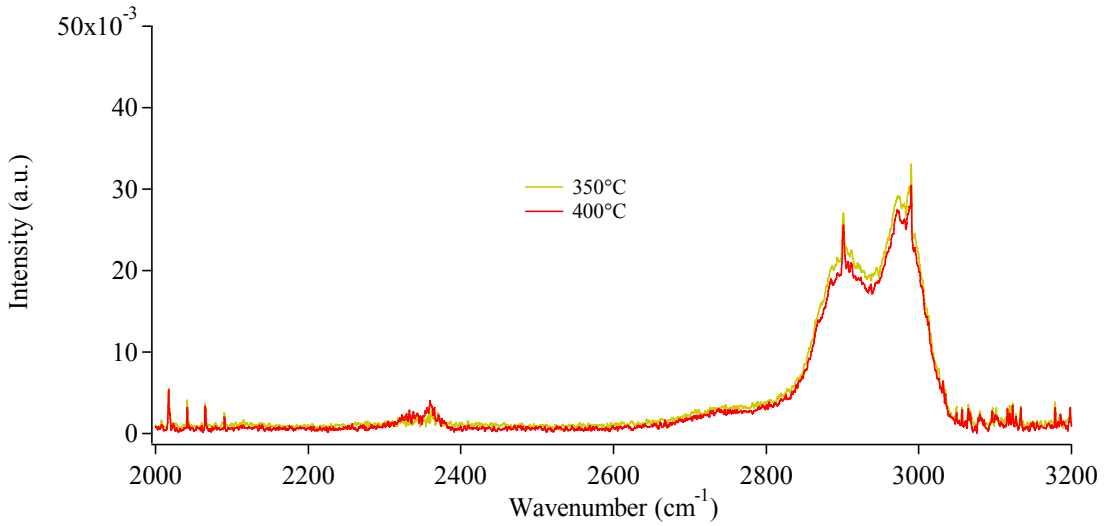

Figure 4.34. FTIR spectra obtained after exposing LCC2 Pec to CH_3CH_2OH 1M vapours (gas mixture from the reactor). Region between 2000 and 3200 cm^{-1}.

The values in table 4.8, concerning the conversion of ethanol and the yields for the steam reforming products, indicate that LCC2 Pec is a less efficient catalyst in the investigated conditions. Anyway, both samples are widely poisoned by un-desorbed reaction products or intermediates.

Considering the tests performed on LCC2 samples, it is possible to state that LCC2 Gel appears as the best catalyst under every condition.

Chapter 5

$La_{0.8}Sr_{0.2}Ga_{0.8}Fe_{0.2}O_{3-\delta}$ (LSGF)

Synthesis

Strontium and iron were added to lanthanum gallate in order to obtain $La_{0.8}Sr_{0.2}Ga_{0.8}Fe_{0.2}O_{3-\delta}$. Sr- and Fe-doped $LaGaO_3$ was synthesized employing Pechini process (sample named "LSGF Pec") and Polyacrylamide Gel method (compound named "LSGF Gel"). The synthetics procedures are widely described in Chapter 2. The intermediate gel-like products, obtained from Pechini and Polyacrylamide Gel route, were dehydrated and successively calcined at 900°C for 5 h to allow the formation of the perovskite phase.

Characterization

XRD

LSGF Gel and LSGF Pec samples were characterized by X-Ray Diffraction to define the crystallographic composition. The obtained XRD patterns are shown in figure 5.1.

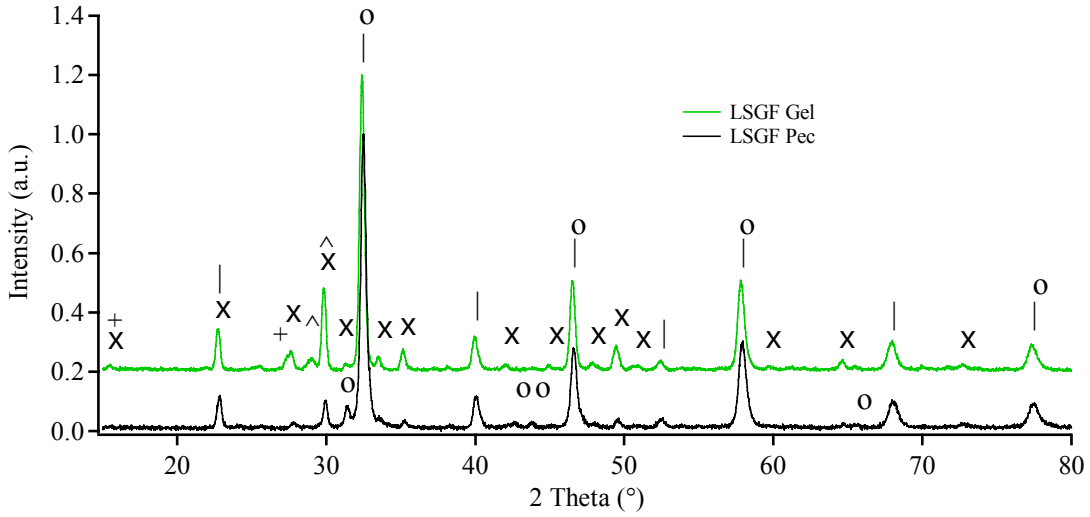

Figure 5.1. XRD patterns for LSGF Pec (—) and LSGF Gel (—). The markers stand for: $La_{0.8}Sr_{0.2}Ga_{0.8}Fe_{0.2}O_3$ (|), $SrLaGaO_4$ (o), $SrLaGa_3O_7$ (x), $La(OH)_3$ (+) and La_2O_3 (^). The spectra are shifted for a better comprehension.

Table 5.1. XRD compositions obtained for LSGF Pec and LSGF Gel. The relative amounts are in wt %.

sample	main phase	(%)	lattice	minor phases	(%)	lattice
LSGF Gel	$La_{0.8}Sr_{0.2}Ga_{0.8}Fe_{0.2}O_3$	67	orthorhombic			
				$SrLaGa_3O_7$	30	tetragonal
				La_2O_3	< 2	hexagonal
				$La(OH)_3$	< 1	hexagonal
LSGF Pec	$La_{0.8}Sr_{0.2}Ga_{0.8}Fe_{0.2}O_3$	79	orthorhombic	$SrLaGa_3O_7$	11	tetragonal
				$SrLaGaO_4$	10	tetragonal

The XRD analysis indicates that $La_{0.8}Sr_{0.2}Ga_{0.8}Fe_{0.2}O_3$ is the main phase in both samples. Reflections of other phases ($SrLaGaO_4$, $SrLaGa_3O_7$, La_2O_3 and $La(OH)_3$) are also present in different amounts as a function of the synthetic procedure. The weight fractions of the different phases were obtained by Rietveld's method (see appendix A) and the results are shown in table 5.1. The $La_{0.8}Sr_{0.2}Ga_{0.8}Fe_{0.2}O_3$ was fitted adapting the $La_{0.99}Sr_{0.01}GaO_3$ phase available on ICSD database, since no Sr- and Fe-doped lanthanum gallate structures are known by literature data.

The results reported by different Authors reveal a great heterogeneity when studying doped- $LaGaO_3$ perovskites. Tsuruta et al. [83] indicate that no secondary phases are observed in $La_{(1-x)}Sr_xGa_{0.6}Fe_{0.4}O_3$ until x = 0.4. Yuenyongchaiwat et al. [84] observe that, for $La_{(1-x)}Sr_xGa_{(1-y)}Fe_yO_3$ system, $SrLaGaO_4$ impurities appear for x > 0.2 and y < 0.8. Furthermore, Leonidov et al. [85] report the formation of $SrLaGa_3O_7$ for gallium contents ≥ 0.3 in $La_{0.3}Sr_{0.7}Fe_{(1-x)}Ga_xO_3$ materials. Finally, Kharton et al. [86] state that for low Sr contents, the amount of $SrLaGa_3O_7$ depends on processing conditions, while, at low Fe

concentrations, it may be partially affected by kinetic factors. Taking into account the literature data, it seems that various amounts of minor phases such as $SrLaGaO_4$ and $SrLaGa_3O_7$ are quite present in Sr-doped $LaGaO_3$ systems. As a general consideration, the presence of minor phases is influenced by the preparation conditions whenever the dopant amount is low; and by dopants whenever they are present in higher concentrations. The obtained outcomes agree with the literature data, furthermore, judging from the relative amounts of minor phases, Pechini process seems to guarantee the higher crystallographic purity. It is important to note that the synthetic procedure also significantly influences the crystallite sizes. The perovskite prepared by Pechini process is characterized by smaller crystallite sizes (64 nm) than the one prepared by Gel method (94 nm).

XPS

LSGF Gel and LSGF Pec were analyzed by XPS; figures 5.2 and 5.3 show the extended and the detailed spectra, respectively.

Both samples show only the XP and Auger peaks distinctive of the constituent elements, and the only impurities come from the adventitious carbon.

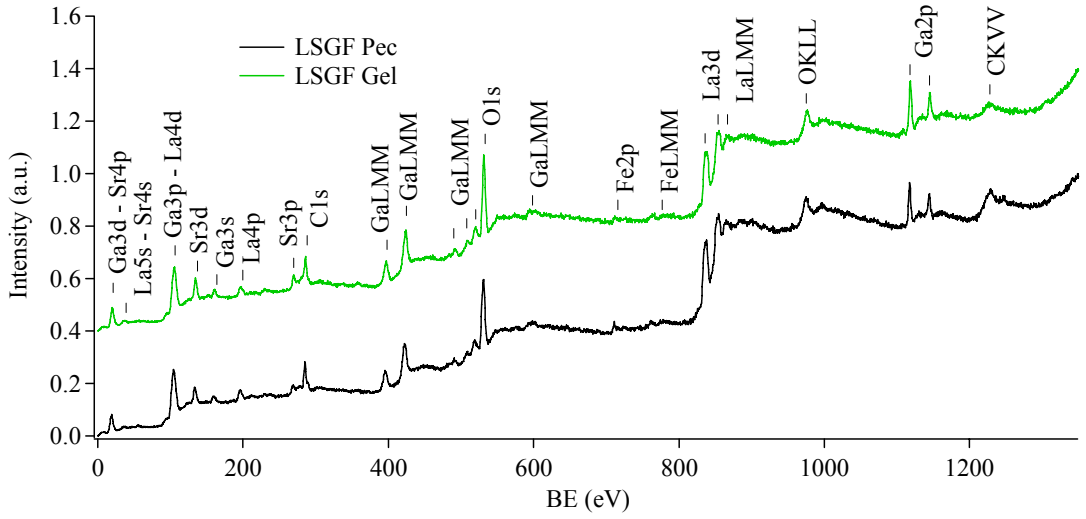

Figure 5.2. Extended XP spectra (surveys) obtained for LSGF Gel and Pec. The spectra are normalized with respect to their maximum value and shifted for a better comprehension.

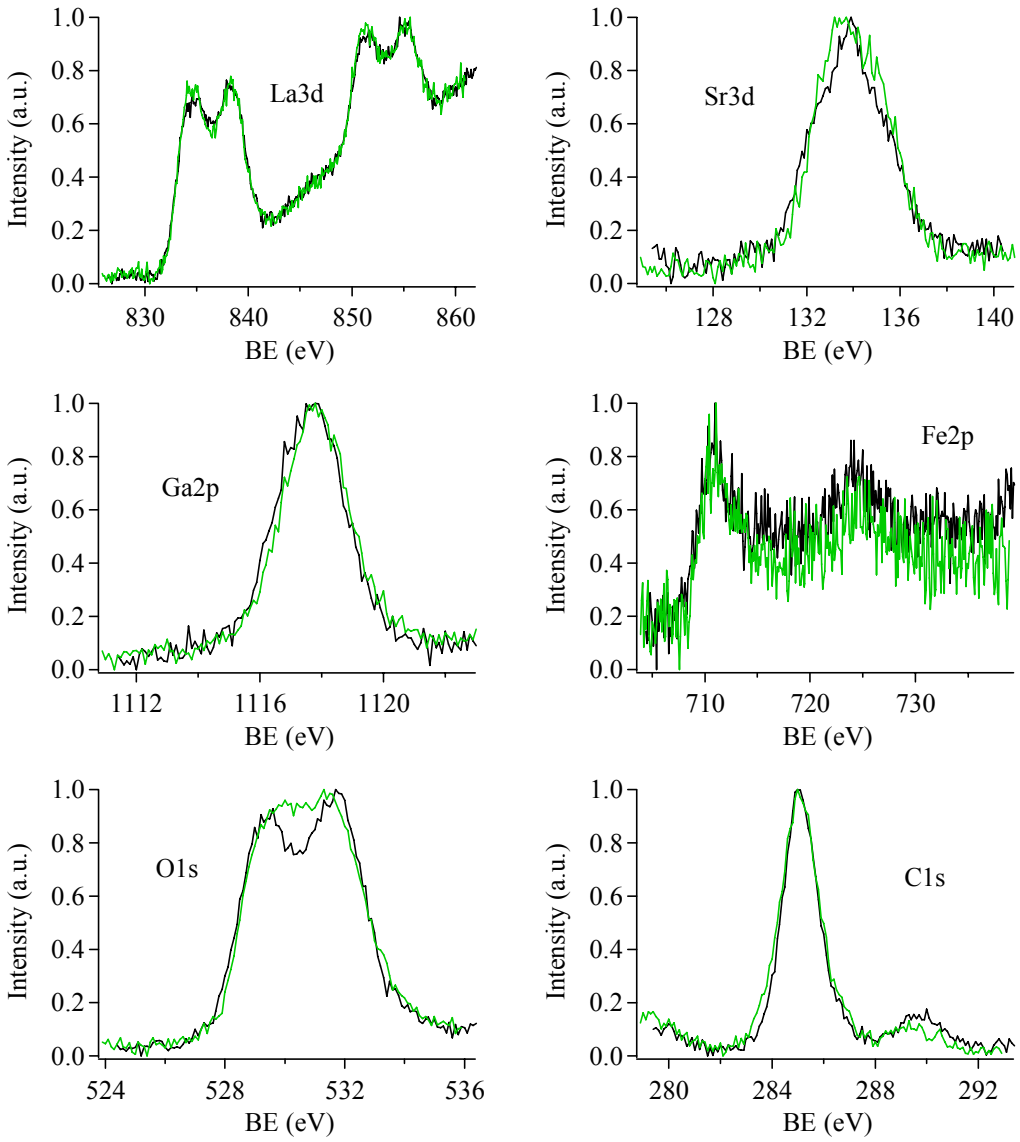

Figure 5.3 XP spectra obtained for La3d, Sr3d, Ga2p Cu2p, O1s and C1s for LSGF Pec (—) and Gel (—). All spectra are normalized with respect to their maximum value.

Lanthanum 3d peak position (table 5.2) and shape agree with the literature data reported for perovskite-type materials; besides the typical spin-orbit coupling ($La3d_{5/2}$ and $La3d_{3/2}$), the shake-up contributions are evident and confirm the presence of La(III). Sr3d photoelectronic peak, instead, shows an unusual shape. The Sr3d peaks appear broadened and the deeper analysis of the data suggests the presence of more overlapping doublets. These are ascribable to different types of strontium compounds. In detail, the first contribution, with the $Sr3d_{5/2}$ centred at about 132.0 eV, is compatible with Sr in the perovskite phase. Kozhukharov et al. and Tabata et al., however, [87, 88] suggest that a strontium sub-oxide (SrO_{1-x}) can contribute to this signal. Even if the presence of this compound can not be excluded, the synthetic conditions (the synthesis is carried out at air) suggest that a reduced valence state for Sr can not be easily

achieved. Therefore, the attribution of this component to a Sr^{2+} ions surrounded by oxygen vacancies in the perovskite structure can be possible. [91] A second contribution at about 133.3 eV is attributable to $SrCO_3$, [90, 92] while the last one at about 134.0 can derive from strontium oxide. [87, 89]

Table 5.2. XPS peak positions (binding energy, eV) obtained for LSGF Gel and Pec. Literature data are also reported for comparison. O1s I indicates the perovskite lattice oxygen, O1s II the SrO lattice oxygen and O1s III the hydroxyl and carbonate contribution.

sample	ref	BE (eV)							
		$La3d_{5/2}$ and $_{3/2}$		Sr3d	$Ga2p_{3/2}$	$Fe2p_{3/2}$	O1s I	O1s II	O1s III
LSGF Pec		834.8	851.6	133.8	1117.6	710.9	529.2	531.0	532.0
LSGF Gel		834.7	851.4	133.6	1117.8	711.1	529.3	531.0	532.2
$La_{0.8}Sr_{0.2}Co_{0.8}Fe_{0.2}O_3$	38	834.4		131.8 133.6 134.8		711.0	529.7		531.4
La_2O_3	42	833.7					530.1		
Fe_2O_3	42					710.8			
$La(OH)_3$	44	835.0							
Ga_2O_3	44				1117.8				
$La_{0.88}Sr_{0.12}Ga_{0.82}Mg_{0.12}O_3$	44	835.2		134.8	1117.8		529.9		531.9
La_2CuO_4	45	833.6							
$La_{0.6}Sr_{0.4}CoO_3$	47	833.4		131.8 134.2					
$La_{0.7}Sr_{0.3}MnO_3$	48	833.7							
$SrCO_3$	63			133.5					
Ga_2O_3	63				1117.5				
$La_{0.3}Sr_{0.7}CoO_3$	87	834.6	851.4	132.3 133.0 134.5					
$La_{0.8}Sr_{0.2}CoO_3$	88			130.5 134.2					
SrO	89			134.0			530.6		
$SrCO_3$	90			133.3					
$La_{0.8}Sr_{0.2}Ga_{0.8}Mg_{0.2-x}Co_xO_3$	91	833.5		132.0 133.9	1116.8		528.9		531.6

Table 5.3. XPS and nominal compositions (atomic %) obtained for LSGF Gel and Pec.

sample	*LSGF Pec*		*LSGF Gel*		*nominal composition*	
					oxide	cations
element						
La	12	41	10	35	16	40
Sr	5	19	7	24	4	10
Ga	7	25	9	33	16	40
Fe	4	15	2	8	4	10
O	72		72		60	

$Ga2p_{3/2}$ peak appears as expected for Ga(III) compounds. In this case, the literature does not give many references for gallium-containing perovskite although the peak position seems to be quite similar to those reported for Ga(III) compounds.

Besides the low signal to noise ratio the observed Fe2p peak positions and shapes agree with how expected for Fe(III) compounds.

Unlike how observed for the others signals, the O1s XP spectra for LSGF Pec and Gel show a different shape. The fitting of the O1s peak in LSGF Pec shows three contributions, the first one, at about 529.2 eV, agrees with oxygen in the perovskite lattice. The second one, at 531.0 eV, is ascribable to oxygen in strontium oxide, [89] while the last one, at 532.0 agrees with the hydroxyl and carbonate species. LSGF Gel, shows, on the other hand, a unique broad peak; this can be again convoluted in three contributions centred at 529.3, 531.0 and 532.2 eV. In particular, the component at 531.0 eV is present in higher amount in the LSGF Gel sample, suggesting a larger amount of SrO.

Finally, C1s photoelectronic peak shows two contributions, the first, at 285.0 eV derives from hydrocarbon contamination, while the one at 289.9 eV arises from carbonate groups.

Table 5.3 summarizes the XPS and nominal compositions for LSGF Pec and Gel. The compounds are always richer in oxygen than the nominal composition; this is not surprising and can be explained taking into account the hydroxyls and carbonates surface terminations. Concerning the metal cations, for both samples, strontium is clearly overabundant, when compared to the nominal amount. This behaviour agrees with how observed for similar compounds [38] and is caused by the basic properties of Sr and its tendency to segregate in surface reacting with atmospheric CO_2 and forming $SrCO_3$. Lanthanum and iron amounts agree with the nominal values and only slight differences can be revealed in LSGF Gel for lanthanum (slight decrease) and in LSGF Pec for iron (slight increase). Finally, gallium tends to diffuse in to the bulk.

DRIFT

LSGF Pec and Gel were analyzed by diffuse reflectance infrared spectroscopy; figure 5.4 displays the spectra obtained at room temperature. Detailed pictures of the regions 1250÷1700 and 3000÷3700 cm^{-1} are also reported.

Both samples show an intense absorption band at wavenumbers lower than 1000 cm^{-1} caused by the lattice vibration modes. A second absorption occurs between 1300 and 1600 cm^{1} assignable to different type of carbonate groups. In detail, for LSGF Gel the peaks at 1410 and 1490 cm^{-1} are consistent with polydentate carbonate. Small amounts

of bidentate carbonate (1335 and 1545 cm^{-1}) are also detectable. In LSGF Pec sample, beside the same species, a more intense peak appears at about 1450 cm^{-1}. This contribution is consistent with monodentate carbonate groups. [76, 77, 78, 79]

Finally, a weak broad band can be observed between 3000 and 3600 cm^{-1}. It agrees with O-H stretching mode in bi- and tri-coordinated hydroxyl groups, and to physisorbed water. [93]

Measurements performed at higher temperatures (until 300°C) show the disappearance of the O-H stretching band, while the one of carbonate groups remain essentially the same.

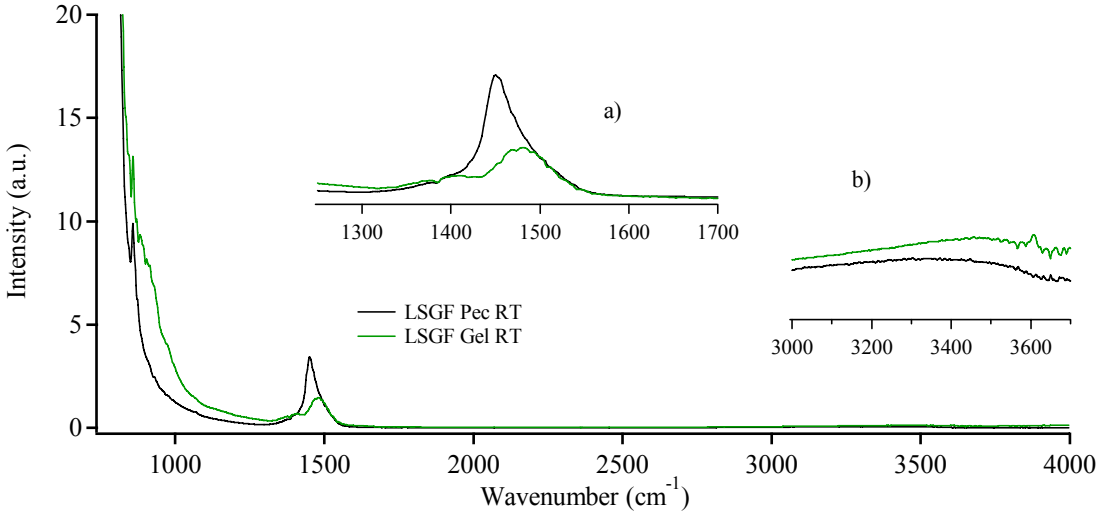

Figure 5.4. DRIFT spectra obtained at RT for LSGF Gel and Pec. Region between 750 and 4000 cm^{-1}. The inserts show the regions between 1250 and 1700 (a) and between 3000 and 3700 cm^{-1} (b).

Reactivity toward methanol and ethanol: chemisorption tests

The interactions between LSGF samples and methyl and ethyl alcohols were firstly investigated by means of DRIFT spectroscopy. In this way, the interaction between the catalyst surfaces and the fuels can be better understood. Figures 5.5 and 5.6 summarize the outcomes for the tests with LSGF Pec. The spectra obtained for LSGF Gel are very similar and are not reported here for sake of brevity.

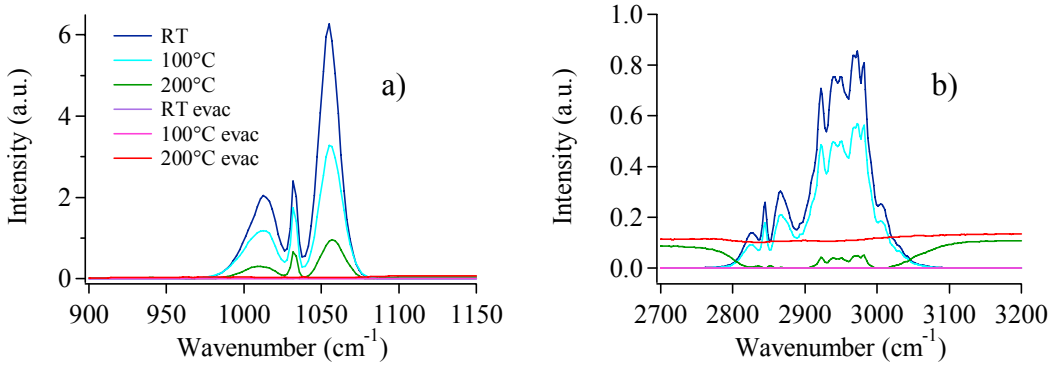

Figure 5.5. DRIFT spectra obtained for LSGF Pec exposed to methanol, at increasing temperatures, before and after evacuation with Ar flow; a) region between 900 and 1150 cm^{-1}, b) region between 2700 and 3200 cm^{-1}.

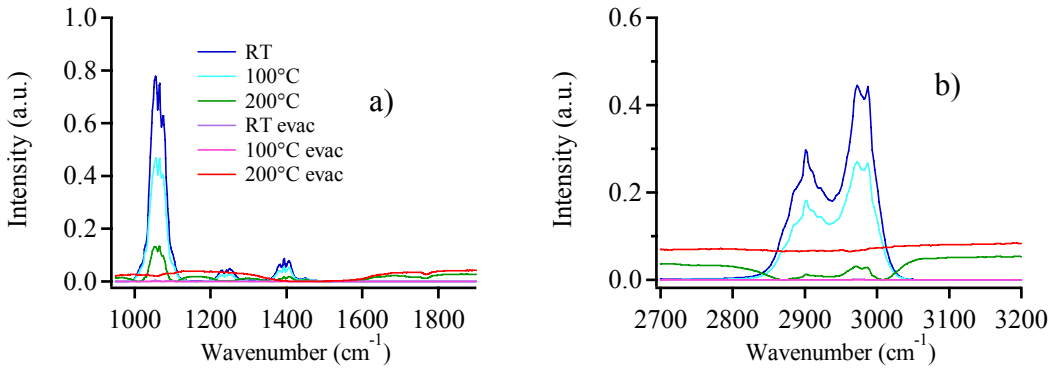

Figure 5.6. DRIFT spectra obtained for LSGF Pec exposed to ethanol, at increasing temperatures, before and after evacuation with Ar flow; a) region between 950 and 1900 cm^{-1}, b) region between 2700 and 3200 cm^{-1}.

The spectra obtained after methanol chemisorption (fig 5.5 a and b) always show the typical contribution of gaseous methanol: the vibro-rotational band centred at 1034 cm^{-1} (C-O stretching) and the bands centred at 2850 and 2950 cm^{-1} (asymmetric and symmetric C-H stretching respectively).

The spectra obtained after evacuation of the chamber with Ar (5 minutes at 80 $cm^3 \cdot min^{-1}$) never show residual signals assignable to methanol dissociation or to chemisorbed products.

It is interesting to observe the shapes of the spectra collected at 200°C before and after evacuation. They show a very abnormal trend because of the variation of the characteristics of the sample.

It is now necessary to recall that the spectra here shown are obtained using the sample as a background. In this way, only the bands characteristics of the adsorbed species are shown. Considering this, the changes in the spectra recorded at 200°C, and even more in that obtained after evacuation, are due to an alteration occurred to the sample.

Chemisorption test carried out with ethyl alcohol never reveals traces of dissociative absorption. The spectra always show the typical signals of gaseous ethanol (both at low and high temperatures). Figures 5.6 a and b show the bands of C-O stretching (1066 cm^{-1}), C-H bending mode (1240 and 1394 cm^{-1}) and C-H stretching (2900 and 2980 cm^{-1}). The spectra recorded at 200°C (both with alcohol and after evacuation) show the same irregular trend already seen in methanol chemisorption.

It has been observed that the alterations in the LSGF Pec and Gel IR spectra, in the measurements at 200°C, are always accompanied by a variation in the colour of the samples. They change the original dark brown-black colour in a light brown-ochre.

LSGF: investigation of the redox behaviour

This unexpected behaviour deserves to be better investigated. Firstly, it has been noted that the alteration occurs in reducing atmosphere (vapour of methanol or ethanol) at 200°C for 1 h of exposure time. This observation allows thinking that a redox phenomenon occurs. Furthermore, the variation is observed also in inert atmosphere but requires higher temperature and longer time. This may suggests that a reducing agent only emphasizes the reaction but it is not fundamental. So, the alteration could depend only on the redox state of the perovskite components. It is well known that most of the perovskite-type materials easily manage oxygen, allowing its oxidation and reduction (see Chapter 2 and 7), thanks to their oxygen vacancies. [27] Furthermore, perovskite materials tend to lose oxygen during heating processes. [94] These considerations suggest that LSGF samples lose oxygen reaching a more reduced state.

Interesting reasoning can derive by LSGF and LSGC ($La_{0.8}Sr_{0.2}Ga_{0.8}Cu_{0.2}O_3$, see Chapter 6) samples comparison. The last compound appears stable both in inert and in reducing atmosphere, and never show changes in its appearance (in its colour in particular). Since the only difference between LSGF and LSGC involve the present of iron instead of copper, it is reasonable to think that iron could be involved in the reduction reaction.

Moreover, the reaction seems to be completely reversible. In fact, the reduced sample goes back to the original conditions when exposed to pure oxygen atmosphere at 200°C for 5 h.

To better investigate the phenomenon, LSGF Pec was analyzed by means of various techniques, both after the reduction and after the re-oxidation in pure O_2 at 200°C for 5h and compared to the as prepared sample. Figure 5.7 summarizes the XP outcomes, while tables 5.4 and 5.5 summarize the XP peak positions and atomic compositions respectively.

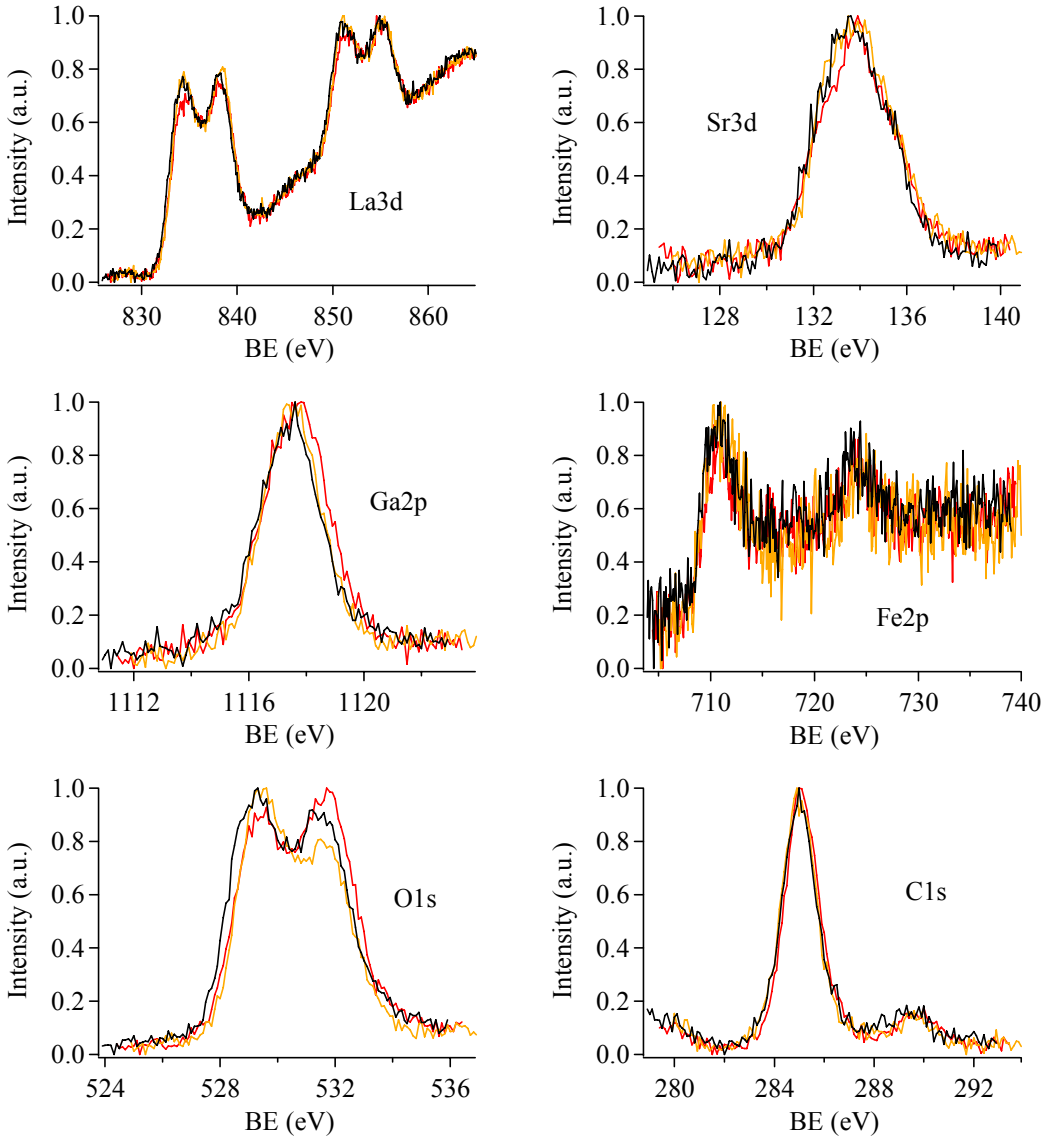

Figure 5.7. XP spectra obtained for La3d, Sr3d, Ga2p Fe2p, O1s and C1s for LSGF Pec as prepared (—), after treatment with methanol vapours at 200°C for 1 h (—) and after re-oxidation in pure O_2 at 200°C for 5 h (—). All spectra are normalized with respect to their maximum value.

Table 5.4. XPS peak positions (binding energy, eV) obtained for LSGF Pec as prepared, after treatment with CH_3OH vapours at 200°C for 1 h and after re-oxidation with pure O_2 at 200°C for 5 h.

Sample LSGF Pec	ref	BE (eV)						
		$La3d_{5/2}$ and $_{3/2}$		Sr3d	$Ga2p_{3/2}$	$Fe2p_{3/2}$	O1s (lattice)	O1s (OH/CO_3)
as prepared		834.8	851.6	133.8	1117.6	710.9	529.2	532.0
after CH_3OH		834.4	851.5	133.7	1117.4	711.0	529.5	531.6
after re-oxidation		834.5	851.5	133.5	1117.5	710.8	529.5	531.4

Table 5.5. XPS and nominal compositions (atomic %) obtained for LSGF Pec as prepared, after treatment with CH_3OH vapours at 200°C for 1 h and after re-oxidation with pure O_2 at 200°C for 5 h.

Sample LSGF	as prepared		after CH_3OH		after re-oxidation		nominal composition
element							
La	7	12	8	13	8	13	16
Sr	3	5	4	6	4	6	4
Ga	4	7	6	8	5	9	16
Fe	3	4	3	4	3	4	4
O	45	72	45	69	44	68	60
C	38		34		36		

XP spectra for La3d, Sr3d, Ga2p, Fe2p and C1s in the reduced and re-oxidized samples show no remarkable differences when compared to the as prepared compound. The slight changes in O1s photoelectronic peaks are not relevant: only the $O1s_{lattice}/O1s_{OH/CO3}$ ratio differs and no "new" types of oxygen are evident. These observations, anyway, do not exclude that the changes in the sample could be so weak that the XPS technique can not detect them.

Concerning the compositional data, they appear pretty much the same for all the samples. This observation confirms that no significant changes occur at the samples surface. In particular no formation of methoxy groups (which can be a consequence of the interaction between methanol and surface) was observed.

The LSGF Pec after the reduction was also analyzed by means of XRD to evaluate possible changes. The obtained XRD pattern (not shown for sake of brevity) is totally identical to the one of the as prepared sample.

To confirm LSGF oxygen losing during the heating process, TPD analysis (thermal programmed desorption) was carried out with a quadrupolar mass detector in an ultra high vacuum chamber. The analysis reveals (figure 5.8) that the sample loses oxygen starting from about 75°C until 200°C, and several peaks can be observed. At the same

time, LSGF desorbs water. The sample appears light brown-ochre at the end of the analysis.

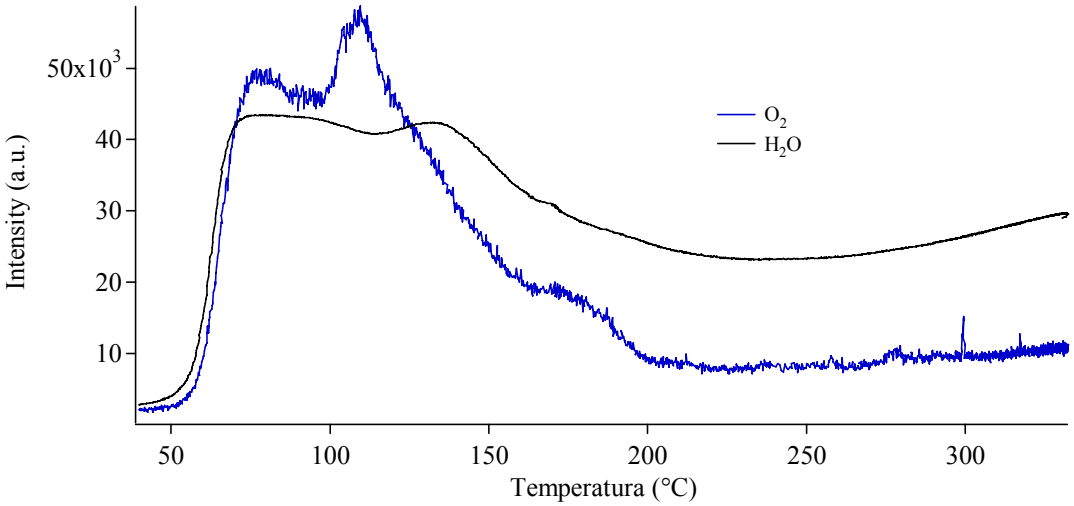

Figure 5.8. MS spectra obtained from the TPD test on LSGF Pec as prepared for m/z = 18 (water) and m/z = 32 (oxygen). The intensity of the signal m/z = 32 is magnified 500 folds.

It has to be underlined that the ultra high vacuum (UHV) environment has to be considered when comparing the TPD results with how observed during the chemisorption experiments. As a matter of fact, oxygen lose is greatly favoured when heating under UHV conditions. Nevertheless, it is unambiguous that LSGF sample desorbs a significant amount of oxygen.

To better investigate the colour change, the LSGF Pec as prepared and in its reduced form were investigated by means of UV-Vis spectroscopy. The obtained spectra are shown in figure 5.9.

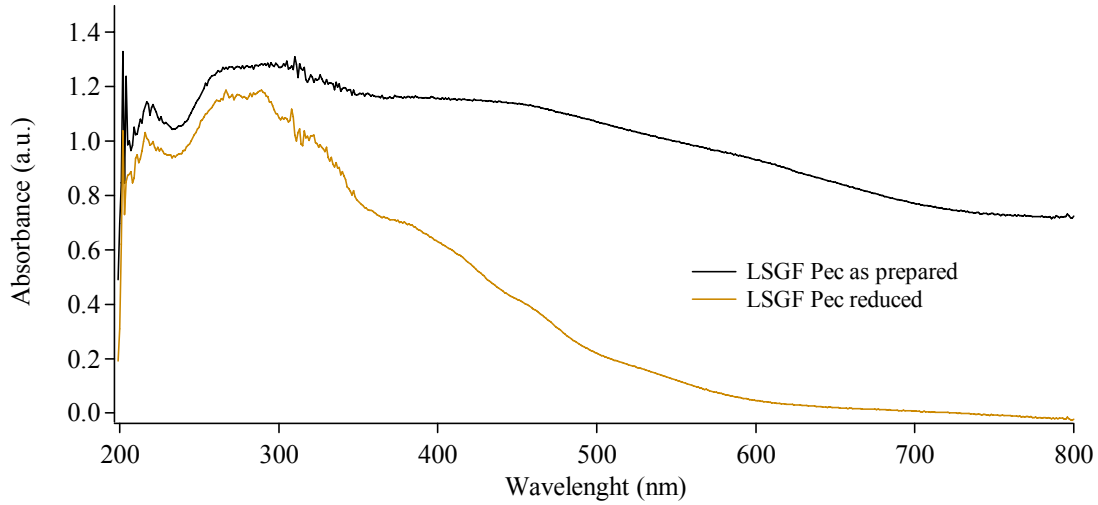

Figure 5.9. Diffuse reflectance UV-Vis spectra obtained for LSGF Pec as prepared and after treatment with CH_3OH at 200°C 1 h.

The UV-Vis spectra appear very similar in the region from 200 to 300 nm, while they differ at higher wavelengths. In the UV region, both the samples show the typical Fe(III) absorption bands at 200, 270 and 290 nm. Characteristics bands assignable to Fe(III) are also detectable in the visible region (450 and 550 nm) for the reduced LSGF. These absorptions are essentially due to ligand to metal charge transfers, since their intensities obscure the lower intensities of the d-d absorptions (406, 411, 540 and 793 nm). [95, 96, 97, 98]

LSGF as prepared, otherwise, shows a continuous trend and no clear bands are evident. In this case, the absorption which gives the brown-black colour to the sample probably covers the absorption bands of Fe(III).

LSGF Pec as prepared and reduced were finally investigated by means of Mössbauer spectroscopy obtaining useful information concerning the iron oxidation and coordination states. The measurements were performed both at room temperature (RT) and 11 K. The first sample, LSGF as prepared, gives a single line spectrum centred near zero velocity and with a broadening towards negative velocity values, as figure 5.10 shows. The best fitting was achieved by using two components: one due to Fe(III) and one due to Fe(IV). Both species occupy high symmetry octahedral sites (Mössbauer parameters are reported in table 5.6). The presence of Fe(IV), quite common in this type of compound [99, 100] is strengthened by low temperature measurement. In fact, the 11 K spectrum has shown the presence of Fe(V) and Fe(III), as consequence of Fe(IV) disproportion. The outcomes suggest that Fe(IV) is about 20% of the total iron amount.

The Mössbauer spectrum of the reduced LSGF shows a broad absorption near zero velocity values. The best fitting was achieved by two Fe(III) sites differing each other by the symmetry. The low temperature measure does not show any significant variations.

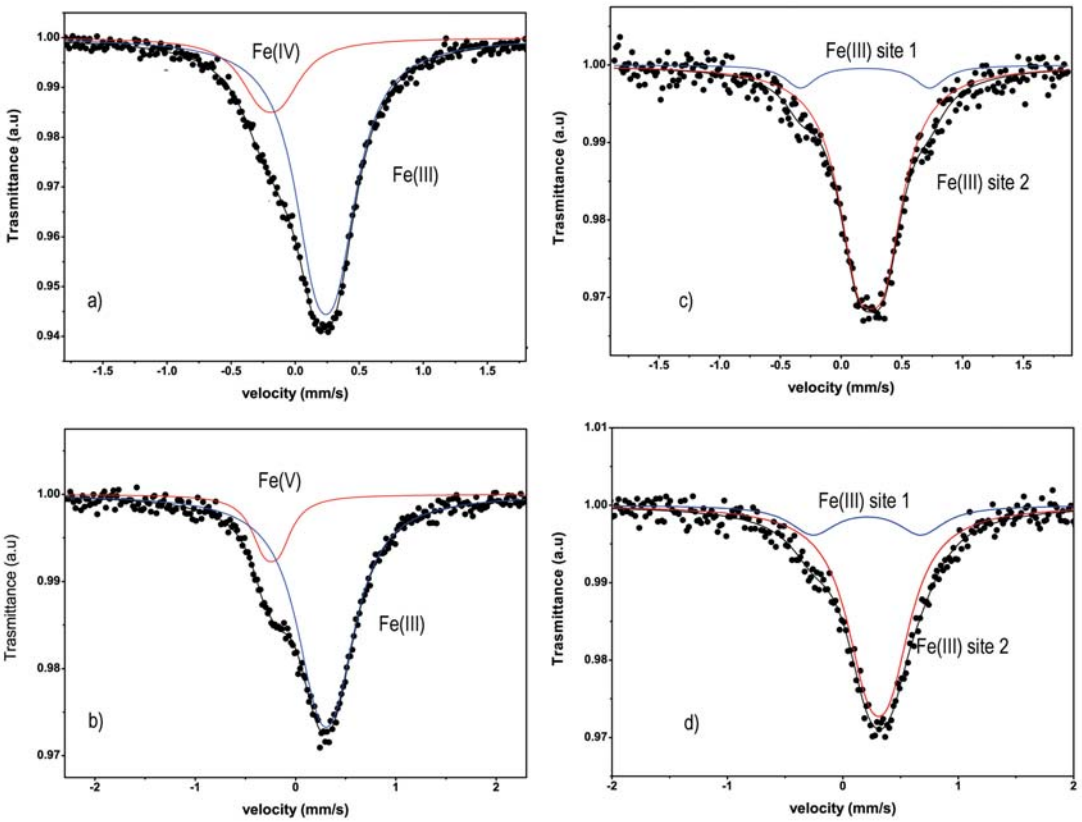

Figure 5.10. Mössbauer spectra obtained for LSGF Pec a) as prepared RT, b) at 11 K; c) after reduction RT, d) at 11 K.

Table 5.6. Mössbauer parameters for room-temperature (RT) and low-temperature (11K) measurements on LSGF Pec. δ: isomeric shift; Δ: quadrupole splitting; Γ: full-width at half-height; A: relative area; δ is quoted to metallic α-iron

Sample	T (K)	δ (mm/s)	Δ (mm/s)	Γ (mm/s)	A (%)	Attribution
LSGF Pec as prepared	RT	-0.07±0.03	0.17±0.03	0.40±0.03	21±5	Fe(IV)
		0.36±0.03	0.18±0.03	0.41±0.03	79±5	Fe(III)
	11	-0.13±0.03	0.14±0.03	0.32±0.03	15±5	Fe(V)
		0.42±0.03	0.19±0.03	0.56±0.03	85±5	Fe(III)
LSGF Pec after reduction	RT	0.36±0.03	0.22±0.03	0.39±0.03	90±5	Fe(III)
		0.32±0.03	1.06±0.03	0.31±0.03	10±5	Fe(III)
	11	0.42±0.03	0.20±0.03	0.48±0.03	82	Fe(III)
		0.33±0.03	0.90±0.03	0.48±0.03	18	Fe(III)

An additional study was conducted on a series of $La_{(1-x)}Sr_xGa_{(1-y)}Fe_yO_3$ systems with x = 0, 0.2, 0.4 and y = 0, 0.2 and 0.6 (table 5.7). [101] Beyond the extended outcomes deriving from the characterization of the samples, it is worth to underline the colours of the compounds. $LaGaO_3$ appears white, as the two Sr-doped samples; the Fe-doped compounds are pale yellow, for y = 0.2, or yellow for y = 0.6. It's interesting to note that only the Sr- and Fe-doped $LaGaO_3$ appears with the brown-black coloration.

Table 5.7. Compositions and colours for $La_{(1-x)}Sr_xGa_{(1-y)}Fe_yO_{3-\delta}$ samples.

x	*y*	**colour**
0	0	white
0.2	0	white
0.4	0	white
0	0.2	pale yellow
0	0.6	yellow
0.2	0.2	brown-black

As known, the substitution of La(III) with Sr(II) creates a deficiency in the positive charges which can be balanced by oxygen vacancies. Another way to balance the charge mismatch is to change the valence state of some elements; no other stable states are allowed for La and Sr cations, while iron can adopt several valence states such as (II), (III) and the less common (IV). Literature often contemplates unusual valence states for transition metals in the perovskite compounds. [27]

It is reasonable to think that iron reaches a higher oxidation state, (IV), to compensate the excess of negative charges due to Sr(II) in LSGF sample; the changes observed when heating under reducing conditions cloud then be ascribed to the reduction of Fe(IV) to Fe(III).

Activity toward methanol and ethanol: catalytic tests

Methanol and ethanol vapours

The activities of LSGF Pec and Gel toward pure methanol vapours were investigated by means of IR spectroscopy and QMS. Figures 5.11÷5.13 summarize the obtained outcomes.

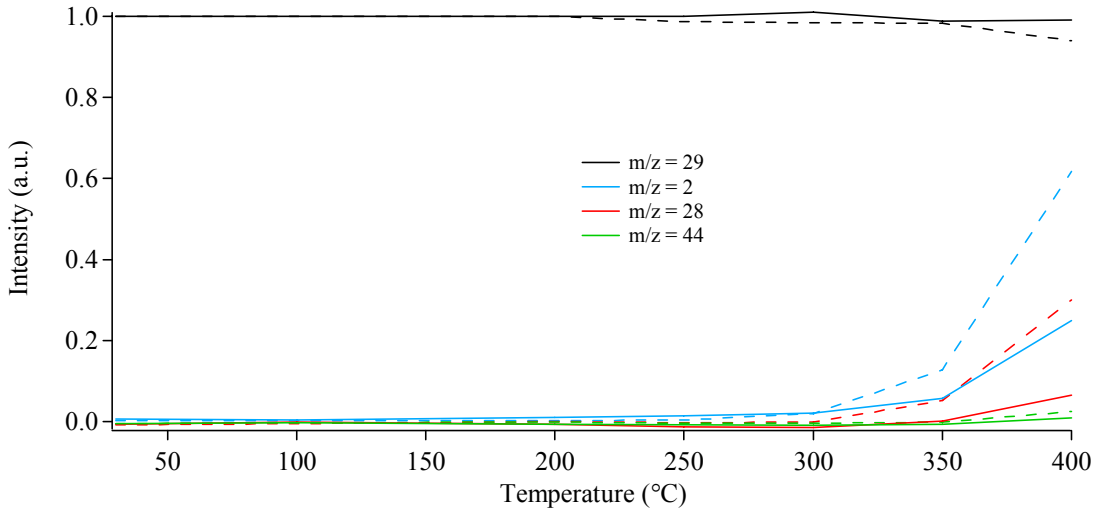

Figure 5.11. QMS data obtained for m/z = 29 (methanol), m/z = 2 (hydrogen), m/z = 28 (carbon monoxide) and m/z = 44 (carbon dioxide) at the investigated temperatures in the test with pure CH_3OH vapours. The intensities of m/z = 2, 28 and 44 are magnified 3 folds. Solid lines stand for LSGF Gel, dashed lines for LSGF Pec.

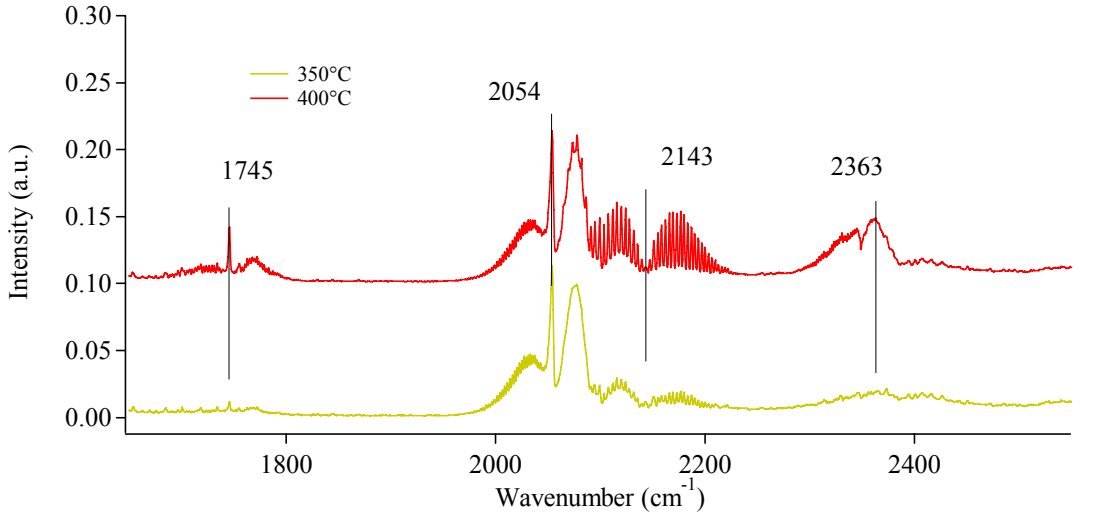

Figure 5.12. FTIR spectra obtained after exposing LSGF Gel to CH_3OH vapours (gas mixture from the reactor). Region between 1650 and 2550 cm^{-1}. The spectra are shifted for a better comprehension.

Both samples are scarcely active whit methyl alcohol (IR band at 2054 cm^{-1}), and only starting from 350°C they produce very small amounts of carbon monoxide (QMS data and IR band at 2143 cm^{-1}) and hydrogen (QMS). These products are consistent with the decomposition of methanol (1):

$$CH_3OH \rightleftharpoons 2H_2 + CO \qquad (1)$$

At the highest temperature (400°C), carbon dioxide can be detected (IR band at 2363 cm^{-1}) and traces of formic acid are also present (IR band at 1745 cm^{-1}).

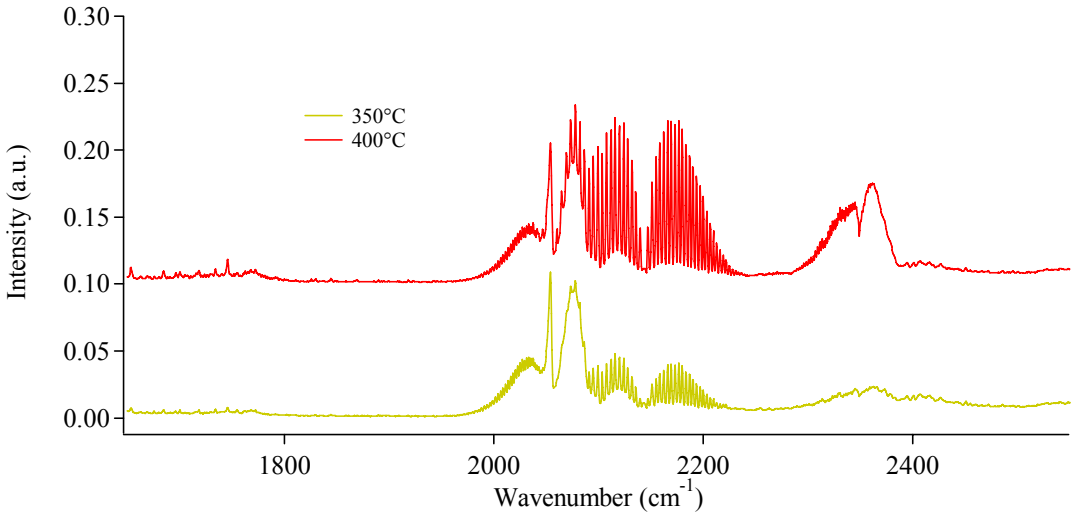

Figure 5.13. FTIR spectra obtained after exposing LSGF Pec to CH_3OH vapours (gas mixture from the reactor). Region between 1650 and 2550 cm^{-1}. The spectra are shifted for a better comprehension.

As reported in Chapter 2, perovskite-type materials exhibit great ability in the oxygen management. In detail, two kind of oxygen can be involved. At low temperature, the adsorbed oxygen is prevalent and its interaction with the reactants is assumed. At higher temperature lattice oxygen can become available. [54, 55] These observations suggest that formation of the more oxidised products, such as CO_2 and HCOOH, can involve lattice oxygen (equations 2, 3).

$$CO + O_P \rightleftharpoons CO_2 + O_V \quad (2)$$

$$CH_3OH + 2O_P \rightleftharpoons HCOOH + H_2O + 2O_V \quad (3)$$

(with O_P = perovskite oxygen and O_V = oxygen vacancy)

Finally, carbon dioxide can also arise from the Boudouard reaction [53] (4):

$$2CO \rightleftharpoons C + CO_2 \quad (4)$$

It is interesting to note that these catalysts, unlike LCC-type samples, never product methyl formate. It is reasonable that the active site involved in the LSGF catalysts allow a different mechanism for the methanol reactions. Furthermore, taking into account the

compositions of the samples, it is possible that the active sites are located on the B-cation (also see considerations in Chapters 3 and 4).

LSGF samples react with ethanol vapours starting from 300°C. At this temperature, beyond the characteristics signals from gaseous ethyl alcohol (1934, 2110 and 2272 cm^{-1}), only very small amounts of hydrogen (QMS data, figure 5.14) and acetaldehyde (figure 5.15 and 5.16, IR band centred at 1745 cm^{-1}) are evident. The increase of the temperature until 350 and 400°C favours the increase of the activity and a more relevant production of the same species. The observed chemicals are consistent with the dehydrogenation of ethanol (5):

$$CH_3CH_2OH \rightleftharpoons H_2 + CH_3CHO \qquad (5)$$

At 400°C traces of ethylene are also detected for both compounds; LSGF Pec, furthermore, produces a small amount of CO_2. Finally, IR spectra never show evidences for carbon monoxide presence. Anyway, it can be produced in very low amount. QMS trend for m/z = 28 can not help in the identification since this mass may also be ascribed to ethylene.

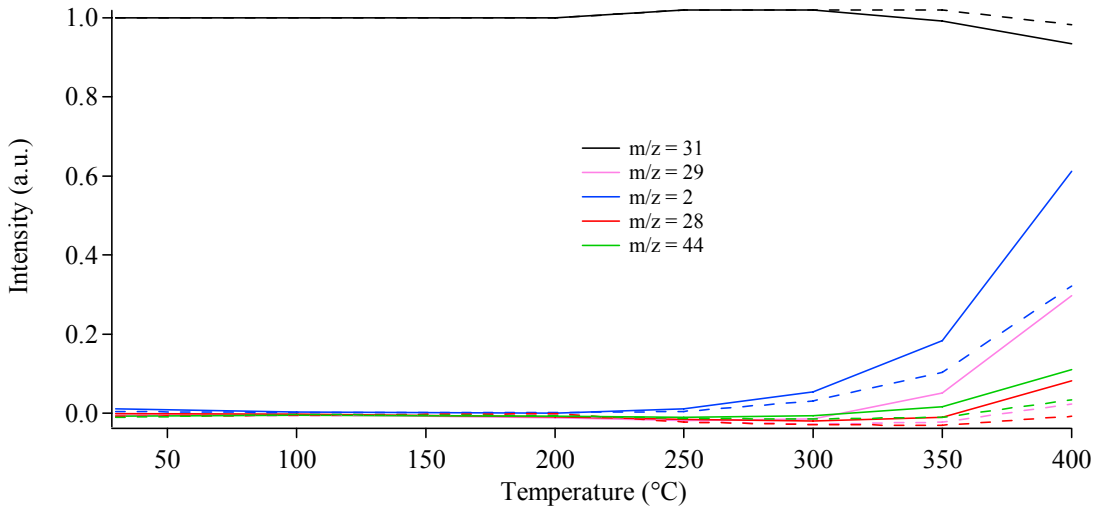

Figure 5.14. QMS data for m/z = 31 (ethanol), m/z = 29 (acetaldehyde) m/z = 2 (hydrogen), m/z = 44 (carbon dioxide) and m/z = 28 (carbon monoxide and ethylene) obtained at the investigated temperatures, in the test with pure CH_3CH_2OH vapours. The intensities of m/z = 2, 28, 29 and 44 are magnified 3 folds. Solid lines stand for LSGF Gel, dashed lines for LSGF Pec.

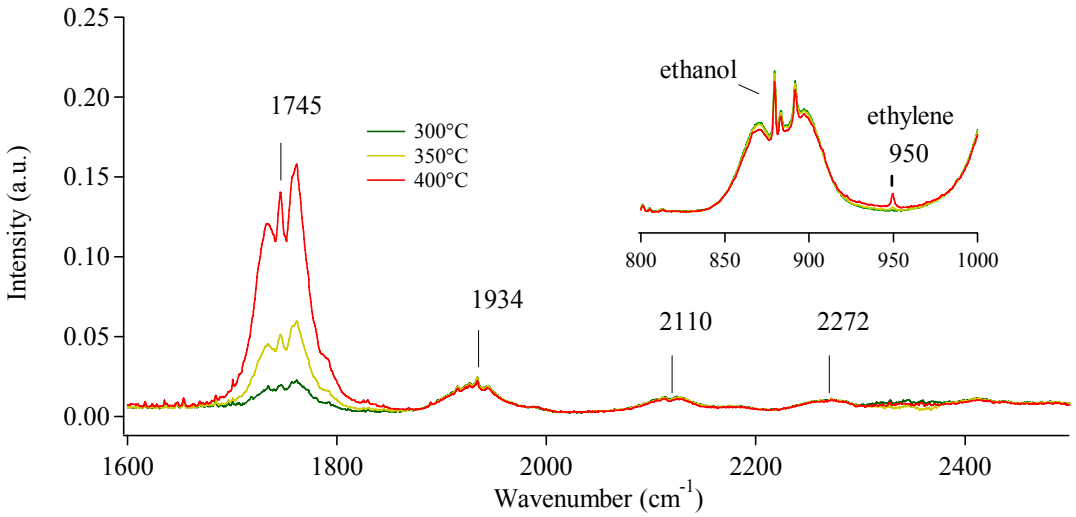

Figure 5.15. FTIR spectra obtained after exposing LSGF Gel to CH_3CH_2OH vapours at increasing temperatures (gas mixture from the reactor). Region between 1600 and 2500 cm^{-1}. Insert: region between 800 and 1000 cm^{-1}.

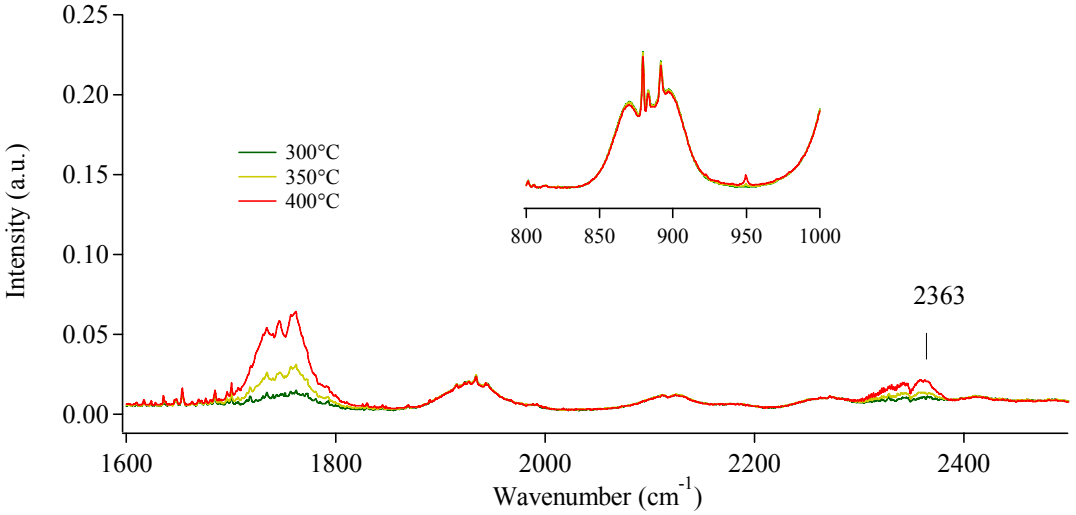

Figure 5.16. FTIR spectra obtained after exposing LSGF Pec to CH_3CH_2OH vapours at increasing temperatures (gas mixture from the reactor). Region between 1600 and 2500 cm^{-1}. Insert: region between 800 and 1000 cm^{-1}.

Table 5.8. Conversions of fuels and yields for products obtained at 400°C for LSGF Gel and LSGF Pec with respect to the reaction with pure methanol and ethanol vapours.

	CH_3OH		CH_3CH_2OH	
sample	conv (%)[a]	yield H_2 (%)[b]	conv (%)[a]	yield H_2 (%)[b]
LSGF Gel	2	1	5 [c]	6
LSGF Pec	7	2	2	3

Note:
[a] conversions determined by QMS (see appendixes A, B)
[b] yields by QMS (see appendixes A, B)
[c] medium value between QMS and IR conversions

Table 5.8 summarizes the conversions of methanol and ethanol, and the yields in hydrogen calculated in the experiments with pure alcohol vapours. In detail, the yields for H_2 are calculated considering the decomposition of methanol (1) and the dehydrogenation of ethanol (5).

As a general consideration, both catalysts appear scarcely active toward the reactants; furthermore, the evidences for the formation of minor products suggest that the stoichiometry of the reactions is not clearly defined. This can affects the values of the obtained yields and help to justify the mismatches between the conversions and the yields for LSGF Pec.

Methanol and Ethanol oxidation

LSGF Pec and Gel were investigated toward methanol oxidation. Figure 5.17 summarizes the QMS outcomes, while the figures 5.18 and 5.19 show the obtained IR spectra.

The results indicate that both samples are not active until 300°C. Starting from 350°C, signals arising from H_2 (QMS data), CO (QMS and IR band centred at 2143 cm^{-1}), CO_2 (QMS and IR spectra at 2363 cm^{-1}) and H_2O (QMS and IR vibro-rotational band centred at 1595 cm^{-1}) appear; traces of formic acid (band at 1755 cm^{-1}) can not be excluded. At the highest temperature (400°C) both catalysts increase their activity with a more evident production of the same species.

Looking at the obtained products, the considerable amounts of H_2 and CO, compared to H_2O and CO_2, suggest that the oxidation reaction (6) competes with the methanol decomposition (1).

$$CH_3OH + 3/2O_2 \rightleftharpoons 2H_2O + CO_2 \qquad (6)$$

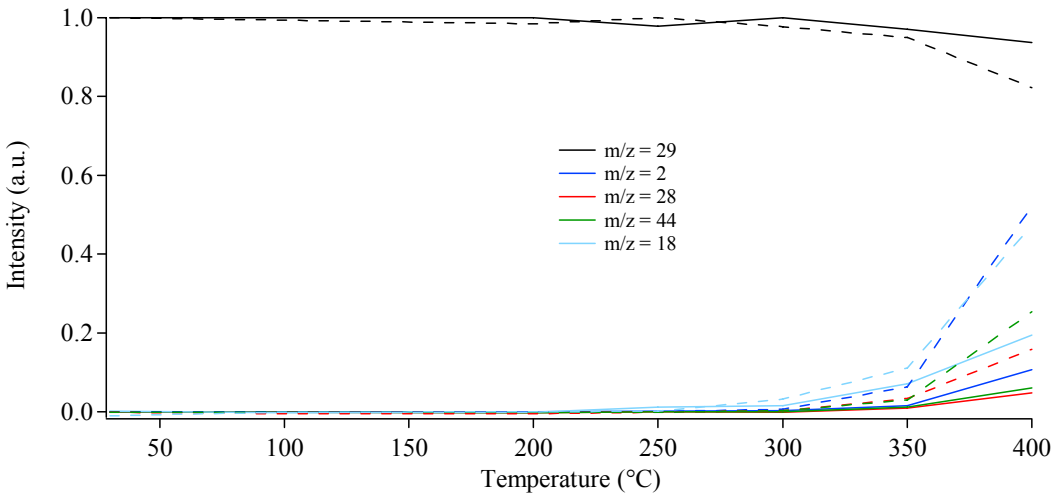

Figure 5.17. QMS data obtained for m/z = 29 (methanol), m/z = 2 (hydrogen), m/z = 28 (carbon monoxide), m/z = 44 (carbon dioxide) and m/z = 18 (water) in oxidizing conditions at the investigated temperatures. Solid lines stand for LSGF Gel, dashed lines for LSGF Pec.

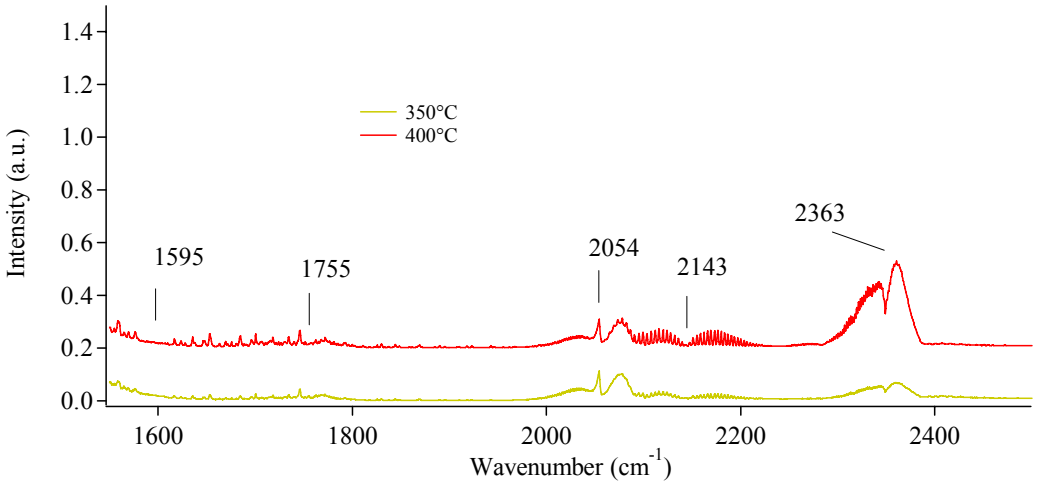

Figure 5.18. FTIR spectra obtained after exposing LSGF Gel to CH_3OH vapours O_2 enriched (gas mixture from the reactor). Region between 1600 and 2500 cm^{-1}.

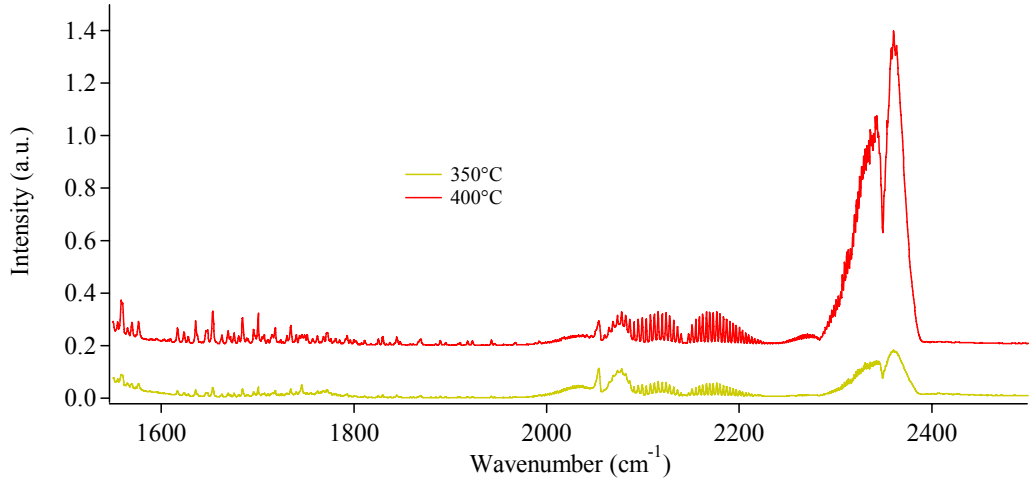

Figure 5.19. FTIR spectra obtained after exposing LSGF Pec to O_2 enriched CH_3OH vapours (gas mixture from the reactor). Region between 1600 and 2500 cm^{-1}.

LSGF catalysts were tested with respect to ethanol oxidation. They show no activity until 300°C: at this temperature small traces of hydrogen (figure 5.20, QMS data) and acetaldehyde (figures 5.21, 5.22, IR band centred at 1755 cm^{-1}) can be detected. At 350 and 400°C the amounts of these products increase and new QMS and IR signals ascribable to CO (band centred 2143 cm^{-1}), H_2O (1595 cm^{-1}) and CO_2 (2363 cm^{-1}) appear, suggesting a more relevant contribution from ethanol oxidation.

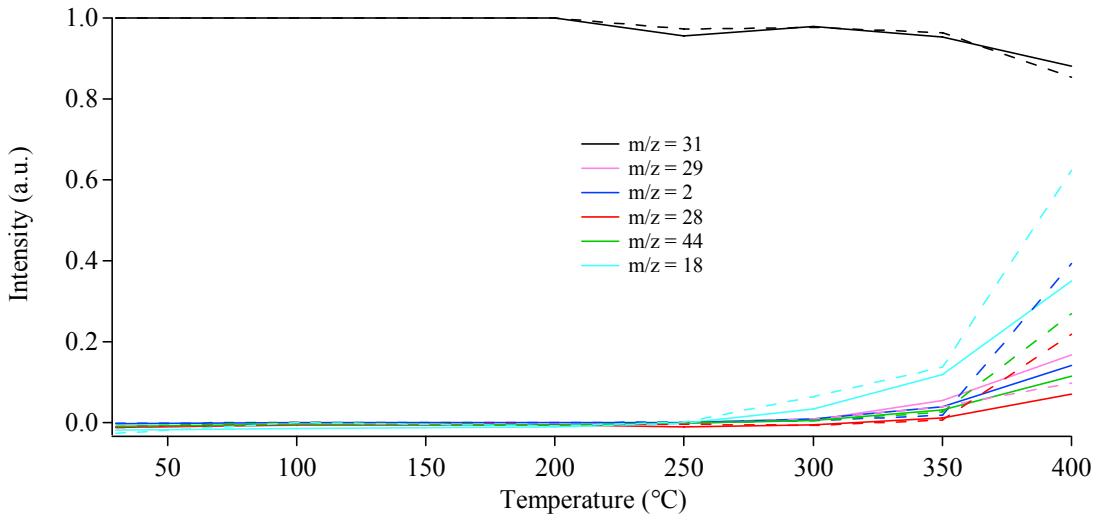

Figure 5.20. QMS data obtained for m/z = 31 (ethanol), m/z = 29 (acetaldehyde), m/z = 2 (hydrogen), m/z = 28 (carbon monoxide), m/z = 44 (carbon dioxide) and m/z = 18 (water) in oxidizing conditions. Solid lines stand for LSGF Gel, dashed lines for LSGF Pec.

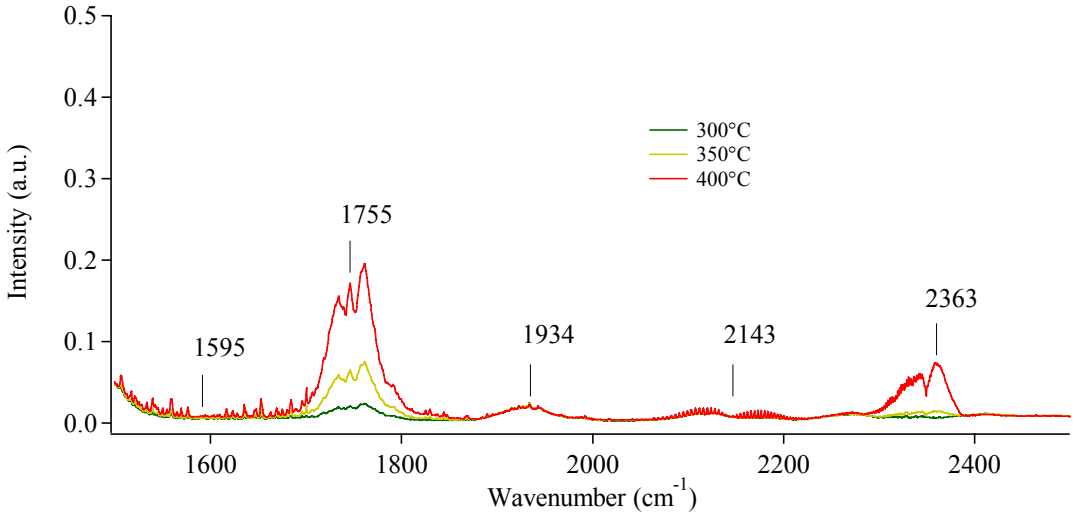

Figure 5.21. FTIR spectra obtained after exposing LSGF Gel to CH_3CH_2OH vapours O_2 enriched (gas mixture from the reactor). Region between 1500 and 2500 cm^{-1}.

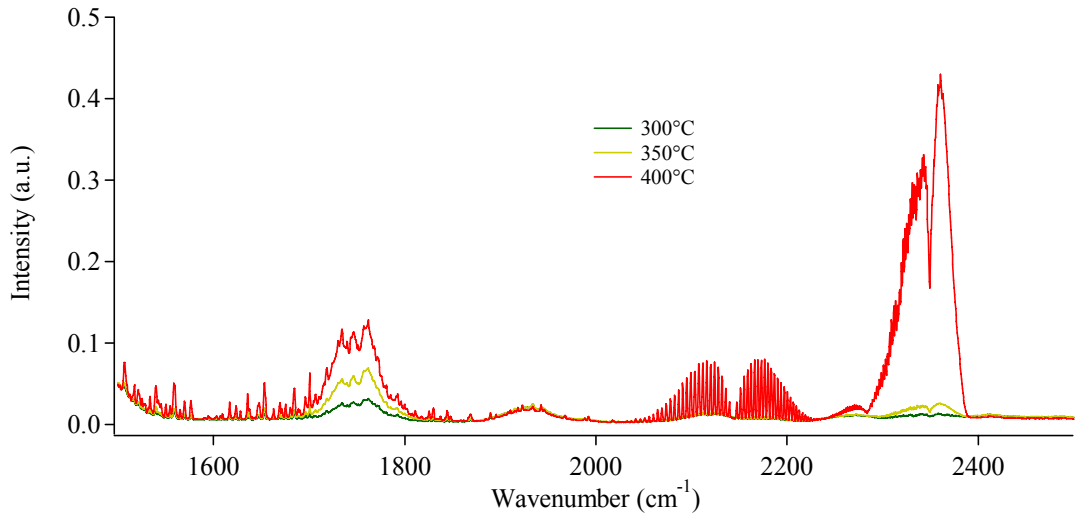

Figure 5.22. FTIR spectra obtained after exposing LSGF Pec to CH_3CH_2OH vapours O_2 enriched (gas mixture from the reactor). Region between 1500 and 2500 cm^{-1}.

Table 5.9. Conversions of fuels and yields for products obtained at 400°C for LSGF Gel and LSGF Pec with respect to methanol and ethanol oxidation.

	CH_3OH/O_2				CH_3CH_2OH/O_2			
sample	conv	yield H_2	yield CO	yield CO_2	conv	yield H_2	yield CO	yield CO_2
LSGF Gel	6	3	1	2	13	6	ND [a]	2
LSGF Pec	18	12	6	11	14	19	2	5

Note:
[a] not detectable
all data are in % and obtained by QMS (see appendixes A and B)

The values for fuels conversions (table 5.9) suggest that both catalysts show a poor reactivity toward the oxidation of the alcohols. It is now interesting to compare the behaviour of LSGF and LCC samples. In Chapters 3 and 4 a very good activity toward methanol and ethanol oxidation was observed for LCC-based catalysts. LSGF samples, otherwise, exhibit a general low activity, and the oxidation competes with the decomposition (for methanol) and the dehydrogenation (for ethanol). The large amounts of hydrogen as by-product confirm the hypothesis.

Methanol and Ethanol steam reforming

LSGF Pec and Gel start to convert methyl alcohol from 350°C in steam reforming conditions. The observed products are mainly H_2 (figure 5.23, QMS data), CO (QMS and IR band at 2143 cm^{-1}, figure 5.24 and 5.25) and CO_2 (QMS and IR band at 2363 cm^{-1}), which agree with the steam reforming of methanol (7).

$$CH_3OH + H_2O \rightleftharpoons 3H_2 + CO_2 \quad (7)$$

The presence of carbon monoxide is easily explained assuming the steam reforming reaction as the sum of the decomposition of methanol (1) followed by the water gas shift reaction (8): [53]

$$CH_3OH \rightleftharpoons 2H_2 + CO \quad (1)$$

$$CO + H_2O \rightleftharpoons CO_2 + H_2 \quad (8)$$

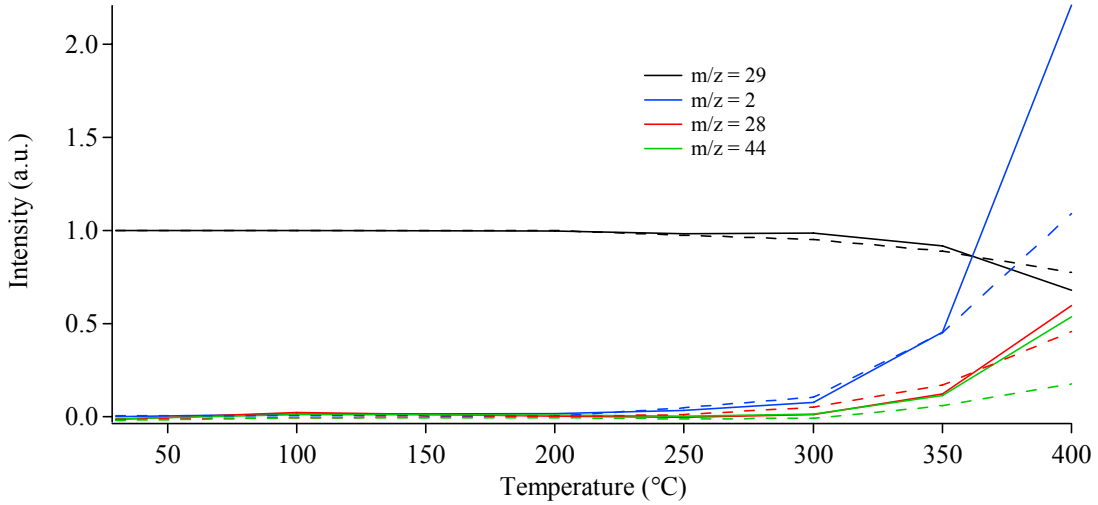

Figure 5.23. QMS data obtained for m/z = 29 (methanol), m/z = 2 (hydrogen), m/z = 28 (carbon monoxide), and m/z = 44 (carbon dioxide) in steam reforming conditions. Solid lines stand for LSGF Gel, dashed lines for LSGF Pec.

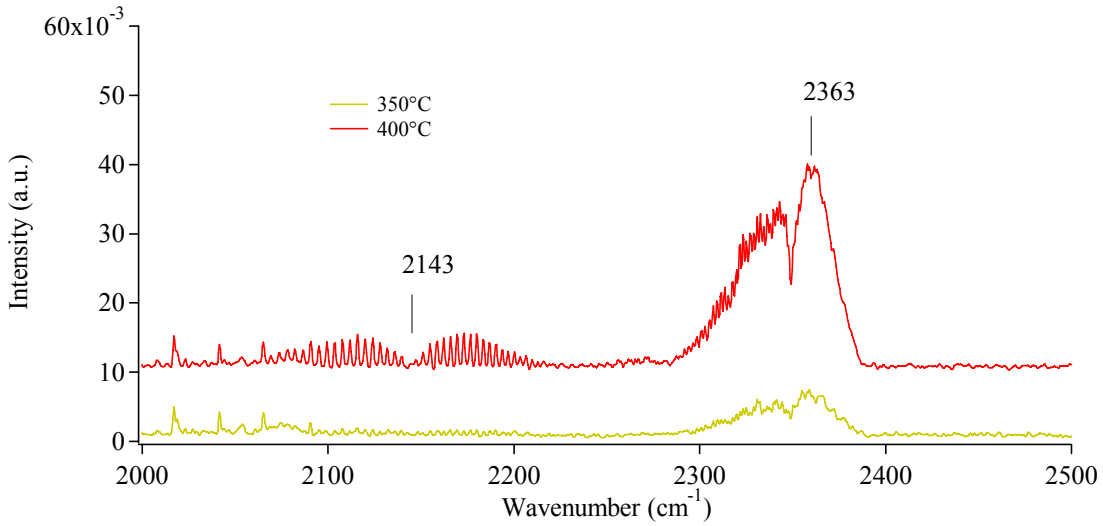

Figure 5.24. FTIR spectra obtained after exposing LSGF Gel to CH_3OH 1M vapours (gas mixture from the reactor). Region between 2000 and 2500 cm^{-1}. The spectra are shifted for a better comprehension.

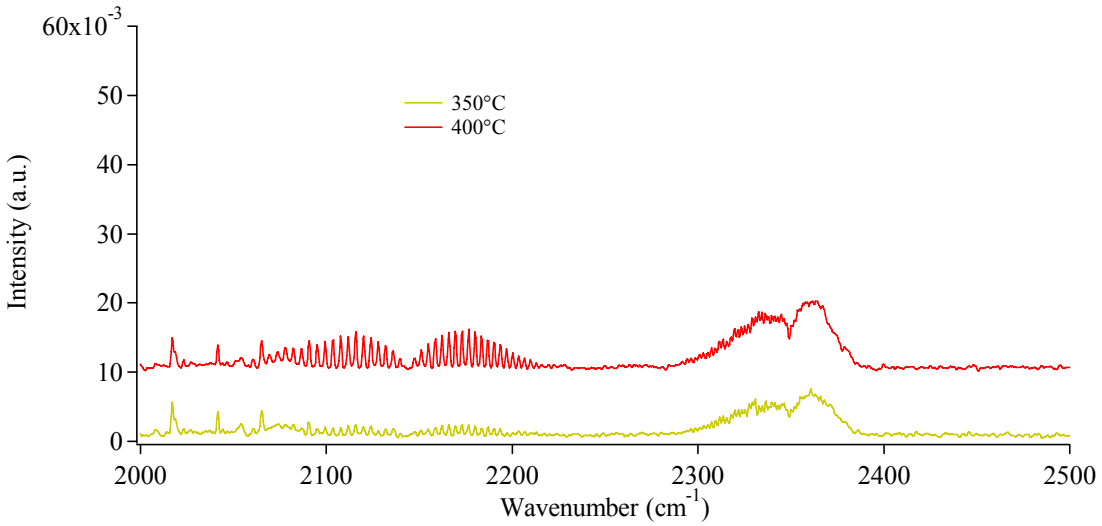

Figure 5.25. FTIR spectra obtained after exposing LSGF Pec to CH_3OH 1M vapours (gas mixture from the reactor). Region between 2000 and 2500 cm^{-1}. The spectra are shifted for a better comprehension.

LSGF catalysts become active toward ethanol steam reforming since 300°C, when only weak signals for m/z = 2 (hydrogen), m/z = 28 (carbon dioxide and ethylene) and m/z = 29 (acetaldehyde) are detected (figure 5.26). The increase of the temperature at 350 and 400°C emphasizes the activity with a larger production of H_2 and CO_2 (QMS data and IR band at 2363 cm^{-1}, figure 5.27 and 5.28). Unlike LSGF Pec, acetaldehyde is also present as product in the test with LSGF Gel. In both the catalysts, the QMS signals for m/z = 28 can arise from carbon monoxide and ethylene. The lack of the IR signals due to these species probably arises from the low sensitivity of this technique.

Quantitative values for the conversions of the alcohols and the yields of typical steam reforming products at 400°C are summarized in table 5.10. From these data it can be seen that both catalysts appear scarcely active toward the reforming of the fuels. Furthermore, a mismatch between the conversions values and the yields for hydrogen and the carbon-containing species is well evident. A very similar behaviour was already seen for LCC samples: in that case a large amount of carbonate species were retained on the catalysts surface. Taking into account the observations reported in Chapters 3 and 4, it is highly probable that the A-cations (Sr and La) strongly interact with the reaction products.

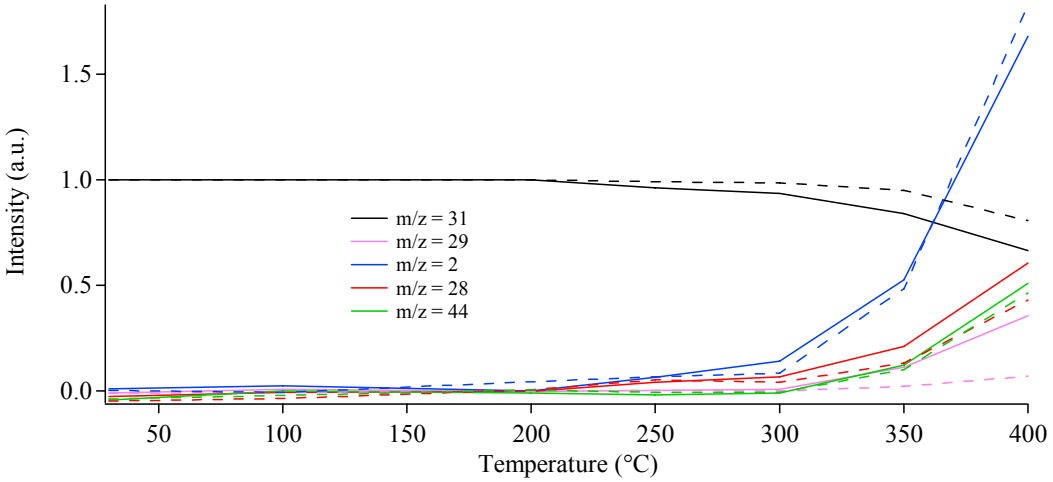

Figure 5.26. QMS data obtained for m/z = 31 (ethanol), m/z = 29 (acetaldehyde) m/z = 2 (hydrogen), m/z = 44 (carbon dioxide) and m/z = 28 (carbon monoxide and ethylene) in steam reforming conditions. Solid lines stand for LSGF Gel, dashed lines for LSGF Pec.

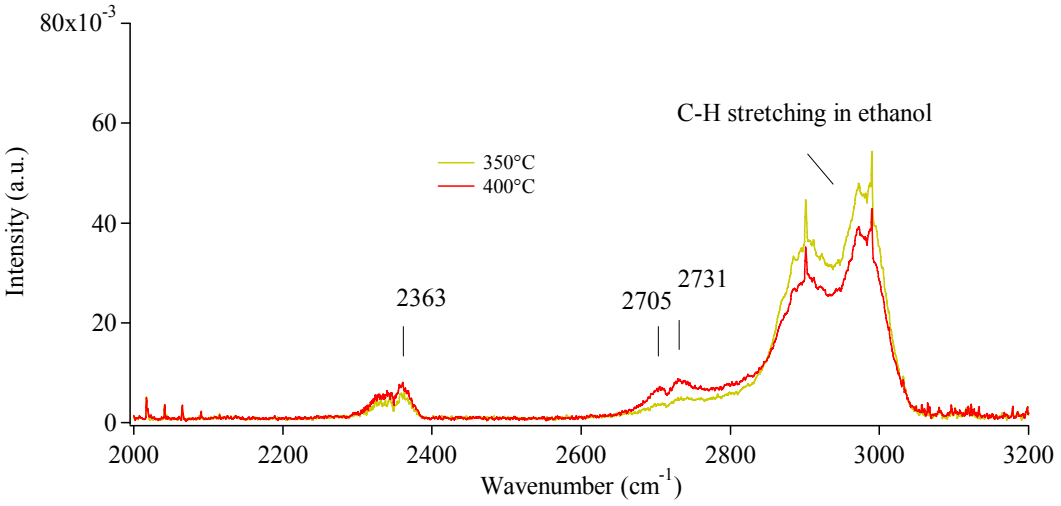

Figure 5.27. FTIR spectra obtained after exposing LSGF Gel to CH_3CH_2OH 1M vapours (gas mixture from the reactor). Region between 2000 and 3200 cm^{-1}.

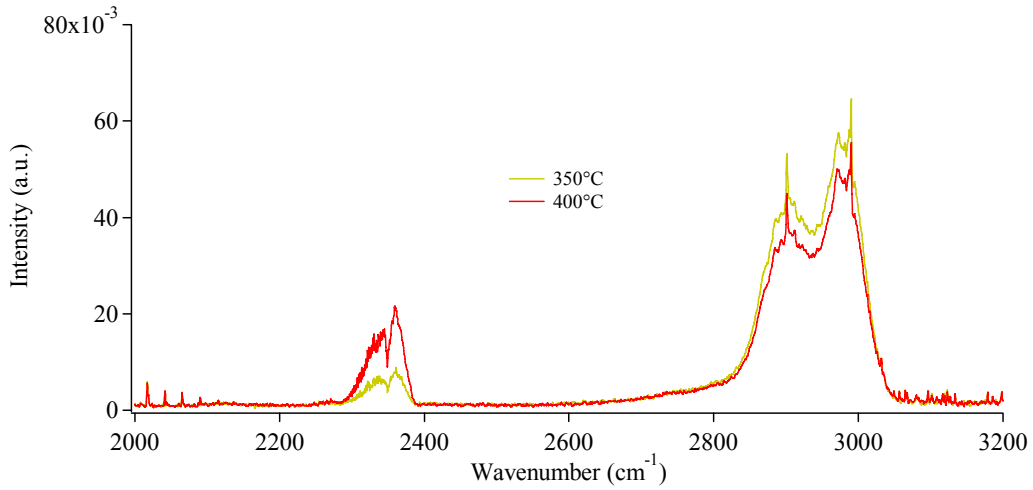

Figure 5.28. FTIR spectra obtained after exposing LSGF Pec to CH_3CH_2OH 1M vapours (gas mixture from the reactor). Region between 2000 and 3200 cm^{-1}.

Table 5.10. Conversions of fuels and yields for products at 400° for LSGF Gel and LSGF Pec with respect to methanol and ethanol steam reforming.

	CH_3OH 1M				CH_3CH_2OH 1M			
sample	conv	yield H_2	yield CO	yield CO_2	conv	yield H_2	yield CO	yield CO_2
LSGF Gel	32	5	ND [a]	ND	34	6	ND	ND
LSGF Pec	23	2	ND	ND	20	5	ND	ND

Note:
[a] not detectable
all data are in % and obtained by QMS (see appendixes A and B)

Chapter 6

$La_{0.8}Sr_{0.2}Ga_{0.8}Cu_{0.2}O_{3-\delta}$ (LSGC)

Synthesis

Strontium- and copper-doped lanthanum gallate was synthesized employing the Pechini and the Polyacrylamide Gel methods. These synthetic procedures are widely described in Chapter 2. As already seen for LCC- and LSGF-based materials, the desired compound $La_{0.8}Sr_{0.2}Ga_{0.8}Cu_{0.2}O_{3-\delta}$ was obtained by heating the gel-like intermediate products at 900°C for 5 h. The heating treatment is necessary to dehydrate and decompose the organic network and generate the perovskite phase. The samples were named LSGC Gel (obtained by Polyacrylamide Gel) and LSGC Pec (from Pechini method).

Characterization

XRD

The crystallographic compositions of LSGC Gel and LSGC Pec were investigated by means of X-Ray Diffraction. Figure 6.1 shows the obtained XRD patterns whereas table 6.1 summarizes the crystallographic phase identified for each sample.

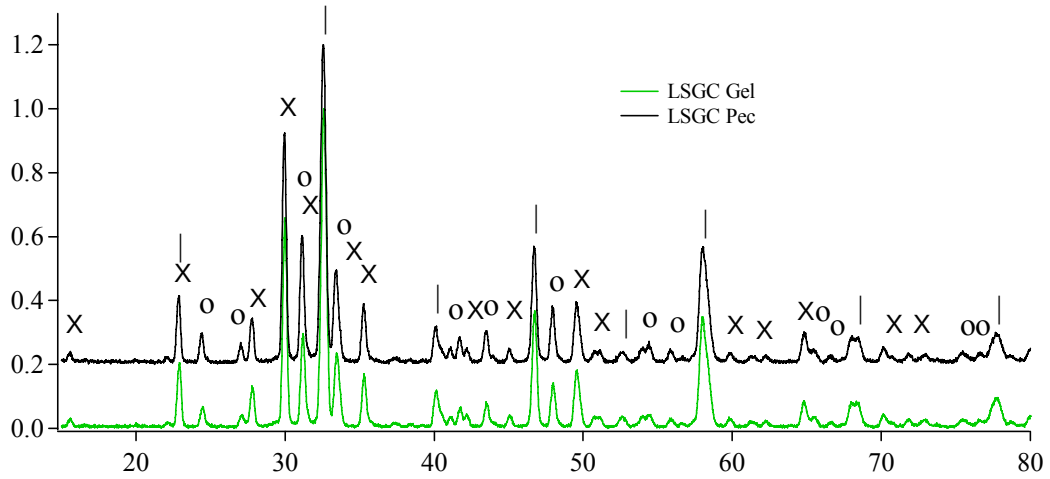

Figure 6.1. XRD patterns obtained for LSGC Pec (—) and LSGC Gel (—) after calcination at 900°C for 5 h. The markers stand for: $LaGaO_3$ (|), La_2CuO_4 (o), $SrLaGaO_7$ (x). The spectra are shifted for a better comprehension.

Table 6.1. XRD compositions obtained for LSGC Pec and LSGC Gel.

sample	*main phase*	*minor phases*	*crystallographic lattice*	*JCPDS number*
LSGC Gel and LSGC Pec	lanthanum gallate		orthorhombic	81-2300
		$SrLaGa_3O_7$	tetragonal	45-0637
		La_2CuO_4	orthorhombic	82-1661

By comparison with the JCPDS database, several crystallographic phases can be detected. As already seen for LSGF samples, literature does not give any references for the doped lanthanum gallate; [29, 83] this problem is even worst since LSGC compounds have never been studied before. The most intense signals are due to the expected phase (by comparison with JCPDS of $LaGaO_3$) however the possible reciprocal solubility of the phases has always to be considered. In fact, beside the main phase, characteristics peaks arising from $SrLaGa_3O_7$ and La_2CuO_4 are also detectable and no relevant differences are evident between the two synthetic procedures.

It is now interesting to compare the XRD outcomes obtained for LSGF (Chapter 5) and LSGC samples. The chemical compositions of the two compounds are very similar, and

the only difference is the replacement of iron with copper (even the relative amounts are the same). It's clearly evident (see XRD data for LSGF, Chapter 5, figure 5.1) that the patterns for the LSGC samples appear much more complicated.

It seems that the introduction of copper provokes a destabilization of the whole system un-favouring the formation of the desired phase. As reported in Chapter 5, the crystallographic equilibrium for the doped lanthanum gallate is affected by several factors; firstly, it depends on the nature and the amounts of the dopant elements. Kinetic causes can also interfere in some cases slowing down the equilibrium. [84, 85, 86]

It is evident that further investigations are needed to better understand the effects of the temperature and time (i. e. of kinetic factors) in the thermal treatments.

The LSGC Gel and Pec samples were completely characterized and tested with respect to methanol and ethanol in the present form. Nevertheless, it would be interesting to investigate the influence of minor phases.

XPS

LSGC samples were investigated by means of X-ray Photoelectron Spectroscopy; figure 6.2 shows the extended spectra, while the picture 6.3 shows the detailed photoelectronic peaks for La3d, Sr3d, Ga2p, Cu2p, O1s and C1s.

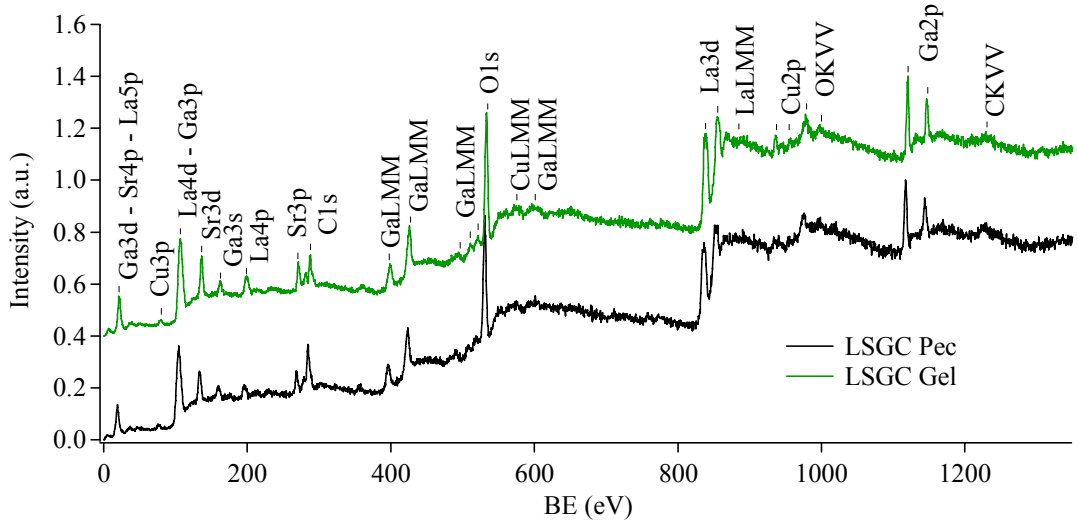

Figure 6.2. Extended XP spectra (surveys) obtained for LSGC Gel (—) and Pec (—). The spectra are normalized with respect to their maximum value and shifted for a better comprehension.

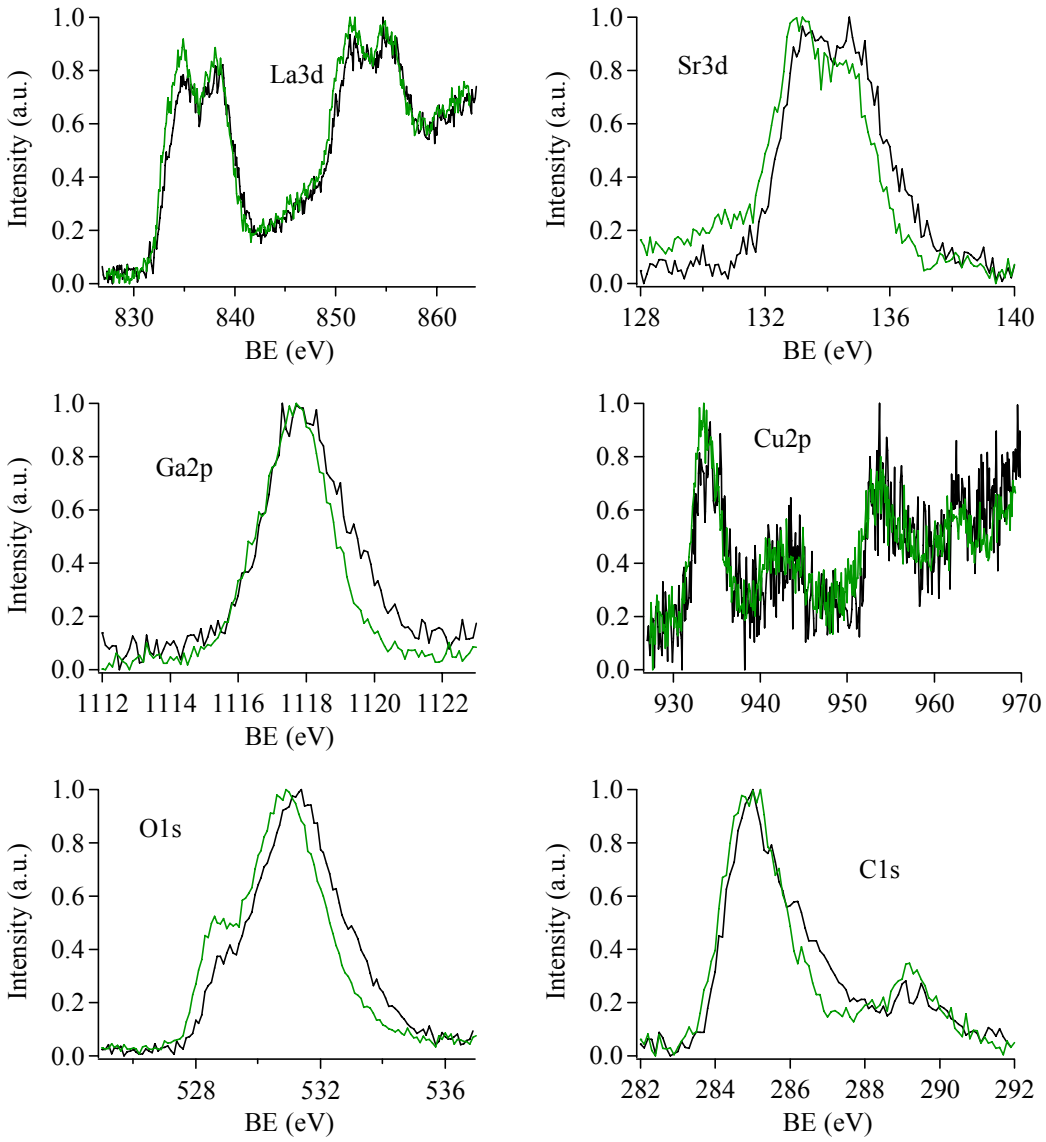

Figure 6.3. XP spectra obtained for La3d, Sr3d, Ga2p Cu2p, O1s and C1s for LSGC Pec (—) and Gel (—). All spectra are normalized with respect to their maximum value.

The extended spectra allow to state that no pollutants elements are present on the surface of the samples except adventitious carbon.

The La3d photoelectronic peak shapes agree with how expected for La(III) compounds. The observed binding energies are consistent with the values reported in literature for similar compounds (table 6.2) however, the presence of lanthanum hydroxide can not be excluded. Concerning Sr3d, the peak appears constituted by more components both in LSGC Gel and Pec. The relative intensities and the measured peak positions suggest that three overlapping doublets can constitute them. The one at lower binding energies (about 132.2 eV) is ascribable to Sr in the perovskite structure, the second one (about 133.3 eV) can arise from $SrCO_3$, [90, 92] while the last one, at about 134.0 eV can be due to strontium oxide. [87, 89]

$Ga2p_{3/2}$ peak in both samples agree with Ga(III) compounds. As mentioned in the Chapter 5 for the LSGF samples, XPS data for gallium-containing materials, nevertheless, appear with quite similar binding energies for all Ga(III) compounds.

Table 6.2. XPS peak positions (binding energy, eV) obtained for LSGC Gel and Pec. Literature data are also reported for comparison.

sample	ref	BE (eV) $La3d_{5/2}$ and $_{3/2}$		Sr3d	$Ga2p_{3/2}$	$Cu2p_{3/2}$	O1s (lattice)	O1s (OH/CO_3)
LSGC Pec		835.1	851.6	133.6 134.8	1117.9	934.2	529.0	531.4
LSGC Gel		834.9	520.0	133.2 134.5	1117.7	933.8	529.1	530.8
$La_{1.8}Sr_{0.2}CuO_4$	30					933.2		
$La_{0.8}Sr_{0.2}Co_{0.8}Fe_{0.2}O_3$	38	834.4		131.8 133.6 134.8			529.7	531.4
La_2O_3	42	833.7					530.1	
$La(OH)_3$	44	835.0						
Ga_2O_3	44				1117.8			
$La_{0.88}Sr_{0.12}Ga_{0.82}Mg_{0.12}O_3$	44	835.2		134.8	1117.8		529.9	531.9
La_2CuO_4	45	833.6						
CuO	45					933.6	529.6	
La_2CuO_4	45	833.6				932.6		
La_2CuO_4	46					933		
$La_{0.6}Sr_{0.4}CoO_3$	47	833.4		131.8 134.2				
$La_{0.7}Sr_{0.3}MnO_3$	48	833.7						
$SrCO_3$	63			133.5				
Ga_2O_3	63				1117.5			
$La_{0.3}Sr_{0.7}CoO_3$	87	834.6	851.4	132.3 133.0 134.5				
$La_{0.8}Sr_{0.2}CoO_3$	88			130.5 134.2				
SrO	89			134.0			530.6	
$SrCO_3$	90			133.3				
$La_{0.8}Sr_{0.2}Ga_{0.8}Mg_{0.2-x}Co_xO_3$	91	833.5		132.0 133.9	1116.8		528.9	531.6

The Cu2p region is characterized by a low signal to noise ratio because of the low amount of this element. Anyway, the peak positions and the well evident shake-up contributions at 943 and 962 eV suggest that copper is present as Cu(II). Furthermore, the measured binding energies suggest that copper tends to be present mainly as CuO.

O1s photoelectronic peak is constituted of three contributions both in LSGC Gel and LSGC Pec. The first, at about 529.0 eV is consistent with the lattice oxygen, while the contribution at about 531.4 eV in LSGC Pec and 530.8 eV in LSGC Gel can be attributed to hydroxyl and carbonate groups. A third component, at about 530.6 eV, can be due to the oxygen in SrO. [89]

Finally, in the C1s region two peaks are evident. Beside the signal due to hydrocarbon contamination (set at 285.0 eV), a minor peak at about 289.4 eV agreeing with carbonate species is evident.

Table 6.3. XPS and nominal compositions (atomic %) obtained for LSGC Gel and Pec.

sample	*LSGC Pec*		*LSGC Gel*		*nominal composition*	
					oxide	cations
element						
La	11	35	10	35	17	40
Sr	8	25	8	26	4	10
Ga	9	30	8	27	17	40
Cu	3	10	4	12	4	10
O	69		70		58	

Table 6.3 summarizes the XP and the nominal compositions (calculated taking into account the amounts of the precursors used during the synthesis) for LSGC Gel and Pec. The values clearly show an oxygen overabundance for both samples. This behaviour is easily explained taking into account the presence, on the surface, of hydroxyl and carbonate species. Concerning the amounts of the metal cations, both samples show a large enrichment in strontium, while lanthanum percentages appear slightly lower that the nominal values. Concerning the B-site cations, a depletion for gallium is observed; copper content, instead, agrees with the nominal composition.

It is worth to note that the comparison between nominal and XP concentrations can be particularly significant, since the XP data refer to the surface, while the nominal composition refers to the bulk. It can thus help to understand the tendency for an element to be surface segregated or to diffuse into the bulk.

It is clearly evident that Sr tends to be surface segregated, probably because of its basic properties, and the ability to react with atmospheric CO_2 to give carbonate species. Lanthanum shows a similar behaviour, but in a lower extend (for example, Tabata et al. [88] observed an enrichment in Sr for $La_{0.8}Sr_{0.2}CoO_3$).

DRIFT

Figure 6.4 shows the diffuse reflectance infrared spectra obtained for LSGC Gel and Pec. Both compounds exhibit an intense absorption at wavenumbers lower than 1000 cm^{-1}, due to the lattice vibration modes. Beyond these, the remaining parts of the spectra appear with no appreciable signals and no functional groups seem to be present.

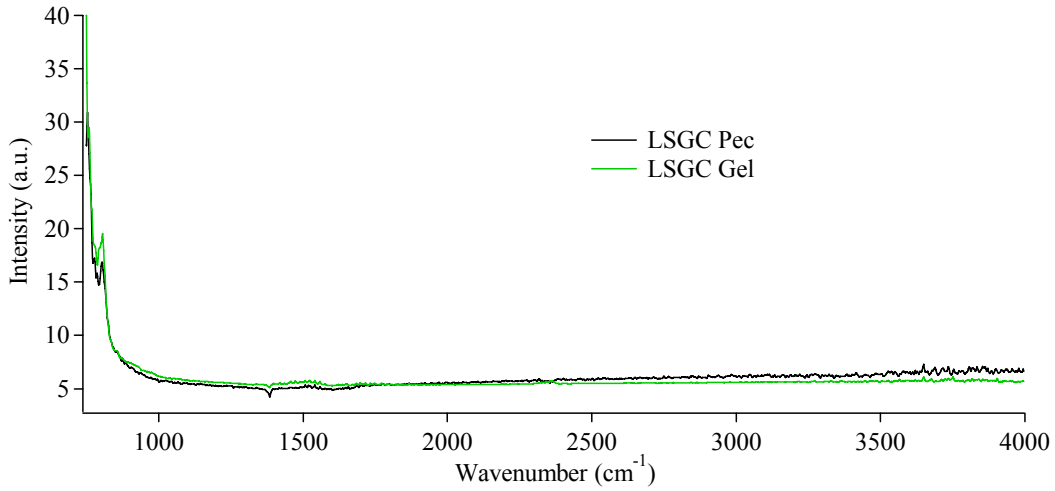

Figure 6.4. DRIFT spectra obtained at RT for LSGC Gel and Pec. Region between 750 and 4000 cm^{-1}.

Reactivity toward methanol and ethanol: chemisorption tests

DRIFT technique was used to investigate the interaction between the LSGC samples and pure vapours of methanol and ethanol at various temperatures between RT and 200°C. Figures 6.5 and 6.6 show the spectra obtained for LSGC Gel after exposure to methanol and ethanol, respectively. The spectra recorded after the successive evacuation of the DRIFT chamber with Ar (5 minutes at 80 $cm^3 \cdot min^{-1}$) are also shown.

The spectra obtained after the exposure to methanol always show the characteristics IR band of the gaseous alcohol at every investigated temperature. In fact, the vibro-rotational band centred at 1034 cm^{-1} (fig 6.5a) and the bands at 2850 and 2950 cm^{-1} (fig 6.5b) arise from C-O and C-H stretching (asymmetrical and symmetrical) respectively in methanol vapours.

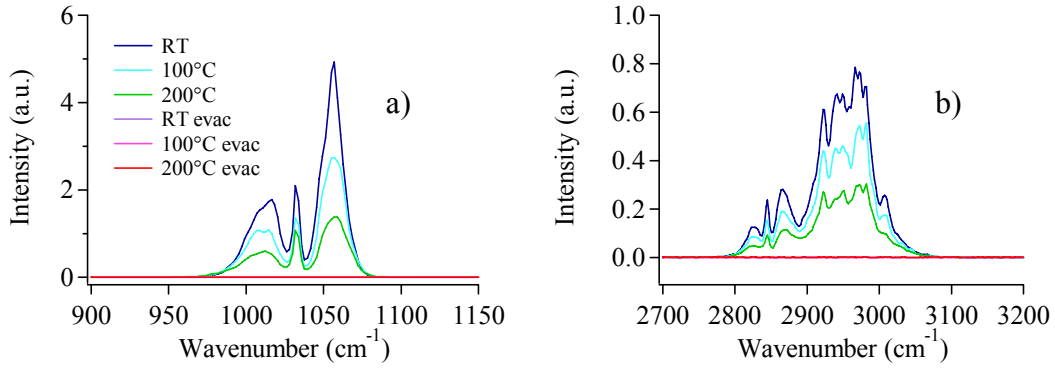

Figure 6.5. DRIFT spectra obtained for LSGC Pec exposed to methanol, at increasing temperatures, before and after evacuation with Ar flow; a) region between 900 and 1150 cm^{-1}, b) region between 2700 and 3200 cm^{-1}.

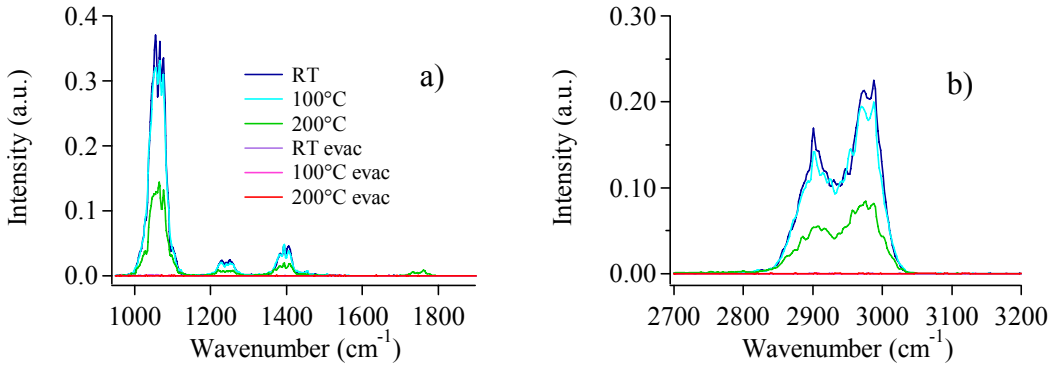

Figure 6.6. DRIFT spectra obtained for LSGC Gel exposed to ethanol vapours at increasing temperatures before and after evacuation with Ar; a) region between 950 and 1900 cm^{-1}, b) region between 2700 and 3200 cm^{-1}.

Signals arising from chemisorbed species were never observed. In fact, the spectra obtained after evacuation always appear with no appreciable bands.

In the tests performed with ethyl alcohol, no evidences from dissociative chemisorption are revealed. In the recorded spectra are clearly visible the typical IR signals of ethanol: the C-O stretching (1066 cm^{-1}), the C-H bending (1240 and 1394 cm^{-1}) and the C-H stretching (2900 and 2980 cm^{-1}). Only at 200°C a weak signal at 1755 cm^{-1} appears. It is consistent with the presence of acetaldehyde, probably due to the dehydrogenation of ethanol.

As in the case of methanol, no traces of chemisorbed species are evident after the evacuation of the DRIFT chamber.

Activity toward methanol and ethanol: catalytic tests

Methanol and ethanol vapours

The reactivity of the synthesized catalysts toward methanol and ethanol was investigated in several conditions.

The first types of experiments were carried out with respect to pure alcohol vapours. Figure 6.7 shows the QMS outcomes obtained, as a function of temperature, for LSGC Gel and Pec in the tests with methanol, while figures 6.8a and 6.8b show the IR spectra obtained at the corresponding temperatures.

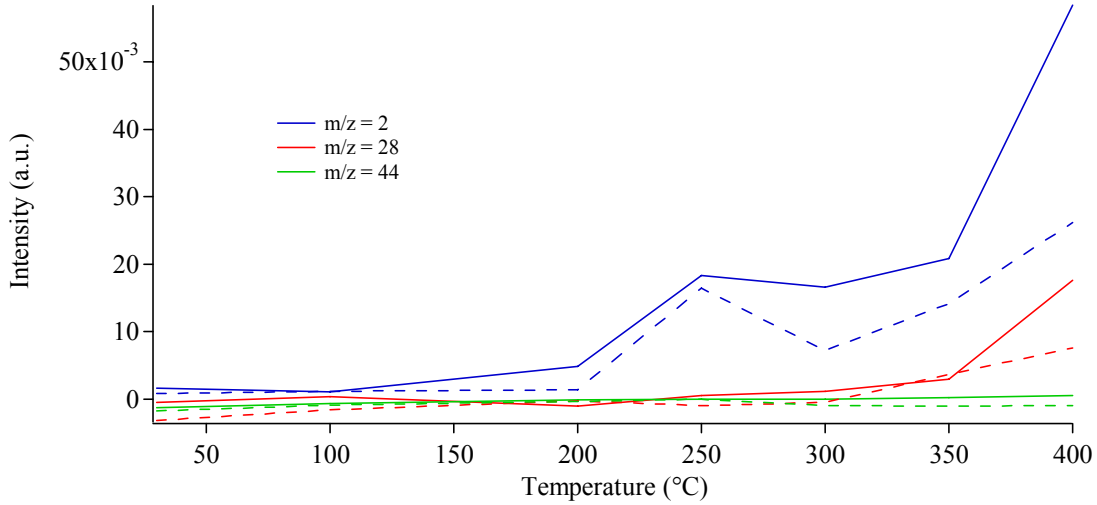

Figure 6.7. QMS data obtained for m/z = 2 (hydrogen), m/z = 28 (carbon monoxide) and m/z = 44 (carbon dioxide) at the investigated temperatures in the test with pure CH_3OH vapours. Solid lines stand for LSGC Gel, dashed lines for LSGC Pec.

The data suggest that both samples start to react with methanol vapours at 250°C, with the production of hydrogen (fig. 6.7) and methyl formate (figures 6.8a, 6.8b, signals around 1755 cm^{-1}), as summarized in equation 1:

$$2CH_3OH \rightleftharpoons HCOOCH_3 + 2H_2 \qquad (1)$$

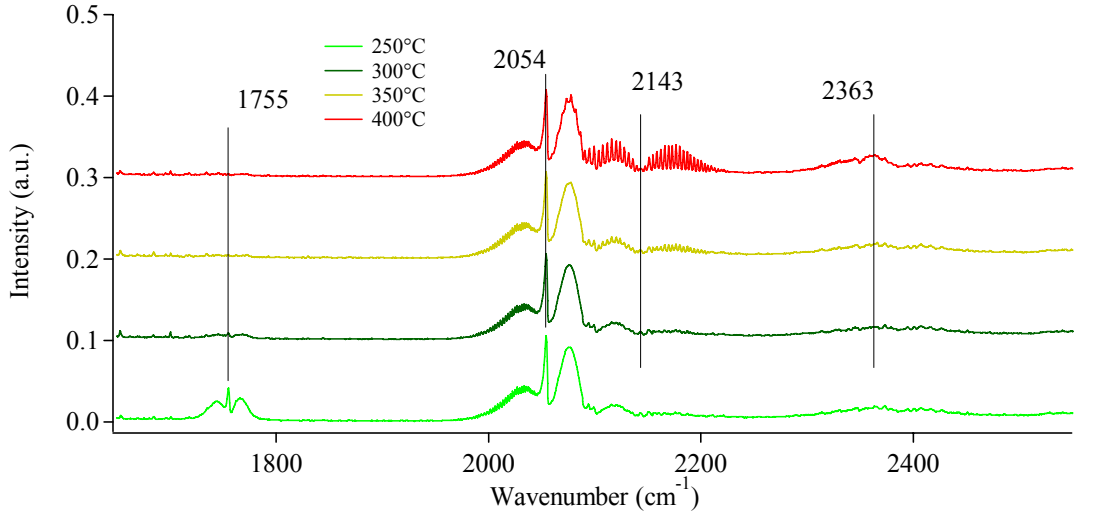

Figure 6.8a. FTIR spectra obtained after exposing LSGC Gel to CH_3OH vapours (gas mixture from the reactor). Region between 1650 and 2550 cm^{-1}. The spectra are shifted for a better comprehension.

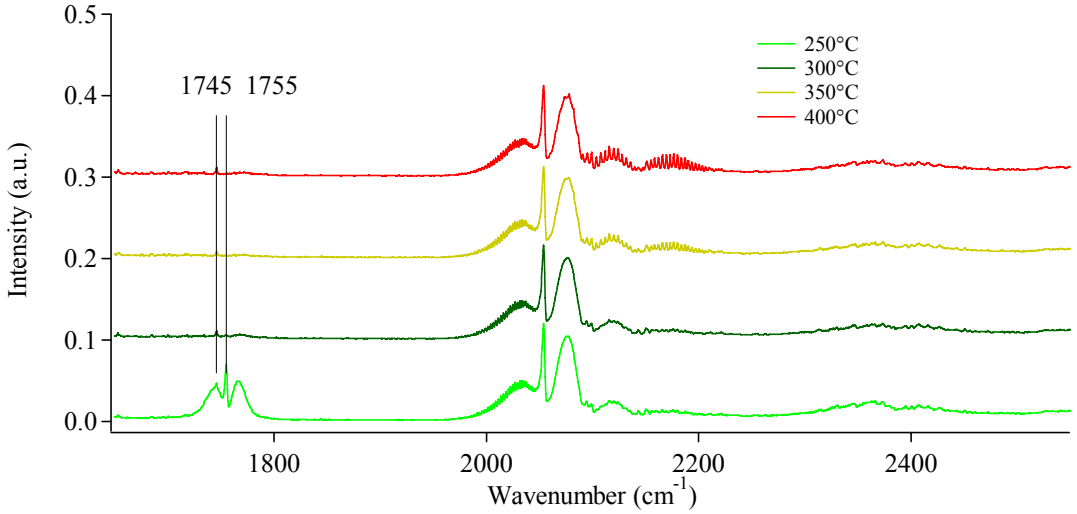

Figure 6.8b. FTIR spectra obtained after exposing LSGC Pec to CH_3OH vapours (gas mixture from the reactor). Region between 1650 and 2550 cm^{-1}. The spectra are shifted for a better comprehension.

Moreover, in the LSGC Pec sample, the shape of the IR band for methyl formate suggests a second contribution at about 1745 cm^{-1}, which is ascribable to formic acid (figure 6.9).

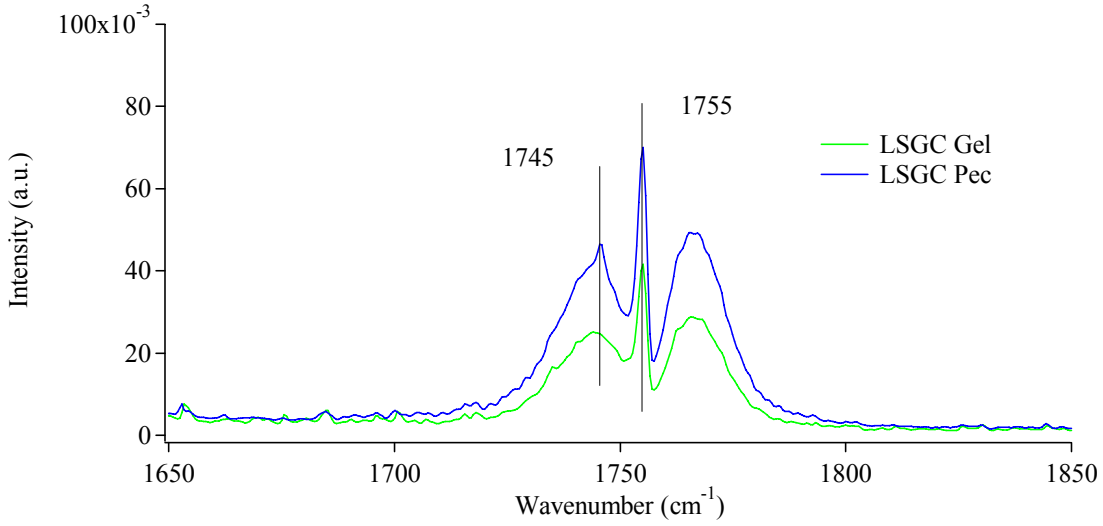

Figure 6.9. FTIR spectra obtained after exposing LSGC Gel and Pec to CH3OH vapours (gas mixture from the reactor) at 250°C. Detail of the methyl formate (1755 cm^{-1}) and formic acid (1745 cm^{-1}) contributions.

Literature indicates that methyl formate is formed on Cu-based catalysts with highest yield at about 200÷240°C, while at higher temperatures it decomposes toward CO and H_2. (equation 2) [51, 52] The results obtained after exposing LCC-compounds to methanol (Chapters 3 and 4) confirm these observations.

$$HCOOCH_3 \rightleftharpoons 2CO + 2H_2 \quad (2)$$

In the present case, the outcomes obtained for LSGC samples suggest that eq (1) occurs but with a less intensities at 300°C, since a decrease in m/z = 2 is observed and no clear traces of CO are evident.
Catalytic activity raises at 350 and 400°C again with a more relevant formation of hydrogen and carbon monoxide. In these conditions, methanol is mainly decomposed (3):

$$CH_3OH \rightleftharpoons 2H_2 + CO \quad (3)$$

Finally, only very small traces of carbon dioxide (figure 6.8, band at 2363 cm^{-1}) are evident for LSGC Gel sample. CO_2 formation can be explained by the Boudouard reaction (4): [53]

$$2CO \rightleftharpoons C + CO_2 \quad (4)$$

or taking into account the oxygen released by the perovskite structure (5): [54, 55]

$$CO + O_P \rightleftharpoons CO_2 + O_V \quad (5)$$

(with O_P = perovskite oxygen and O_V = oxygen vacancy).

LSGC samples were also investigated as a function of time. Figures 6.10 and 6.11 show the IR spectra obtained after 1, 2, 3, 4 and 20 minutes of exposure methanol vapours. The spectra indicate that both the samples activity decreases during the test (the trend is more evident for LSGC Pec), probably because of a poisoning due to un-desorbed species. Furthermore, figure 6.11 underline a detail not much clear in figure 6.8a and 6.8b: it is possible to see a contribution at 1745 cm^{-1} arising from a small amount of formic acid.

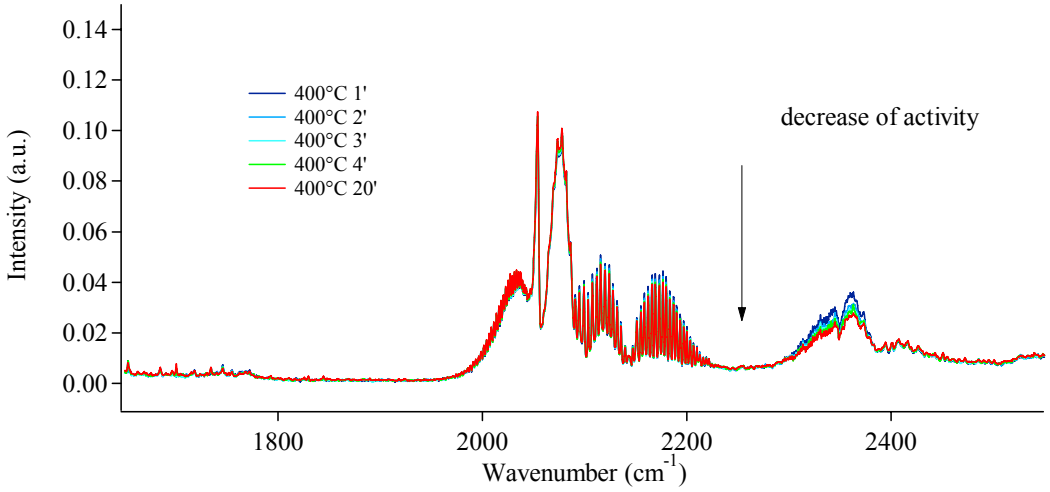

Figure 6.10. FTIR spectra obtained for LSGC Gel after exposure to CH_3OH vapours at increasing time (1, 2, 3, 4 minutes and at the end of the test, 20 minutes) at 400°C. Region between 1650 and 2500 cm^{-1}.

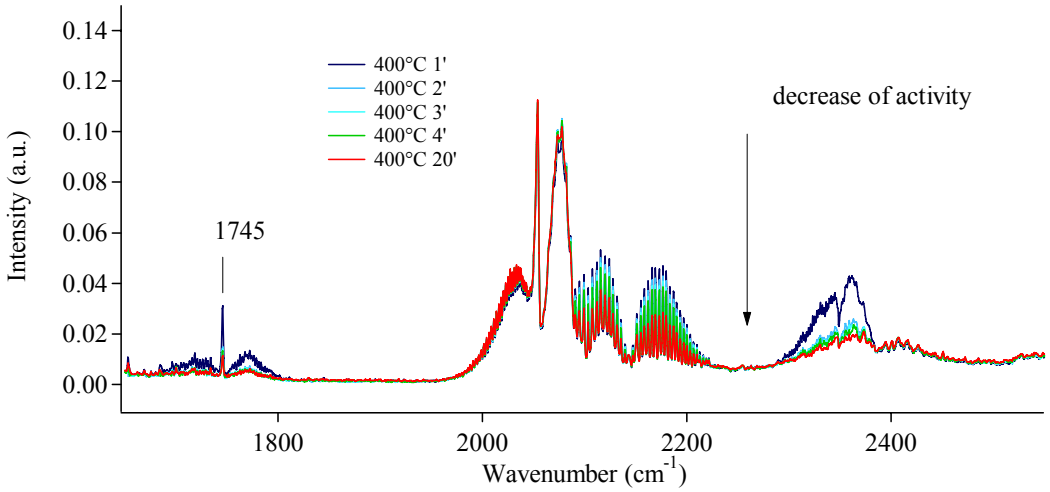

Figure 6.11. FTIR spectra obtained for LSGC Pec after exposure to CH_3OH vapours at increasing time (1, 2, 3, 4 minutes and at the end of the test, 20 minutes) at 400°C. Region between 1650 and 2500 cm^{-1}.

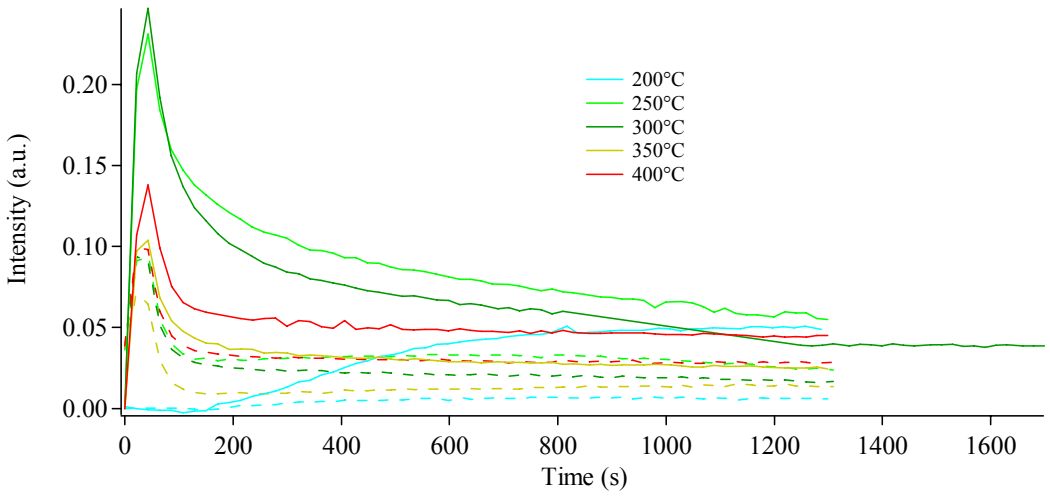

Figure 6.12. QMS data obtained for m/z = 2 (hydrogen) as a function of time for LSGC Gel (solid lines) and LSGC Pec (dashed lines) exposed to CH_3CH_2OH vapours at increasing temperatures.

LSGC compounds show an interesting activity toward ethanol. In fact, they start to convert the alcohol into acetaldehyde and hydrogen since 200°C (6).

$$CH_3CH_2OH \rightleftharpoons H_2 + CH_3CHO \qquad (6)$$

Figure 6.12 shows the trend obtained for m/z = 2 (hydrogen) as a function of time. The data indicate that at 200°C the reaction starts after few minutes and reaches a steady state after about 13 minutes for LSGC Gel and after about 6 minutes for LSGC Pec. However, at 200°C the formation of H_2 is a lot less evident when considering LSGC Pec. At higher temperatures, both samples show a peak at the beginning of each experiment. After this, the activity decreases until the steady state (or a less evident decrease) is reached. The trends can be explained considering that at 200°C the reaction starts on fresh active sites, while at higher temperatures the effect of poisoning un-desorbed species should be considered. Moreover, the heating processes (from 200 to 250°C, from 250 to 300°C…) can favour the desorption of the weak bound species (arising from the experiment at the previous temperature) and liberate some active sites. The IR spectra (figures 6.13 and 6.14) confirm the observed behaviour with respect to the temperature and underline that the dehydrogenation of the ethyl alcohol is the main reaction taking place (acetaldehyde band at 1745 cm^{-1}). Only at 400°C very small amounts of ethylene (from the dehydration of ethanol) can be detected.

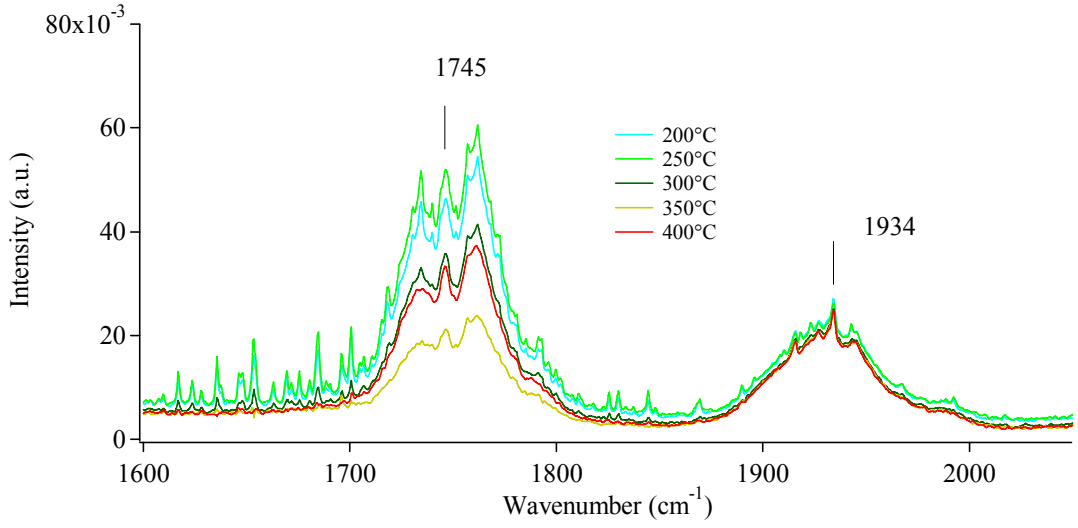

Figure 6.13. FTIR spectra obtained after exposing LSGC Gel to CH_3CH_2OH vapours at increasing temperatures (gas mixture from the reactor). Region between 1600 and 2050 cm^{-1}.

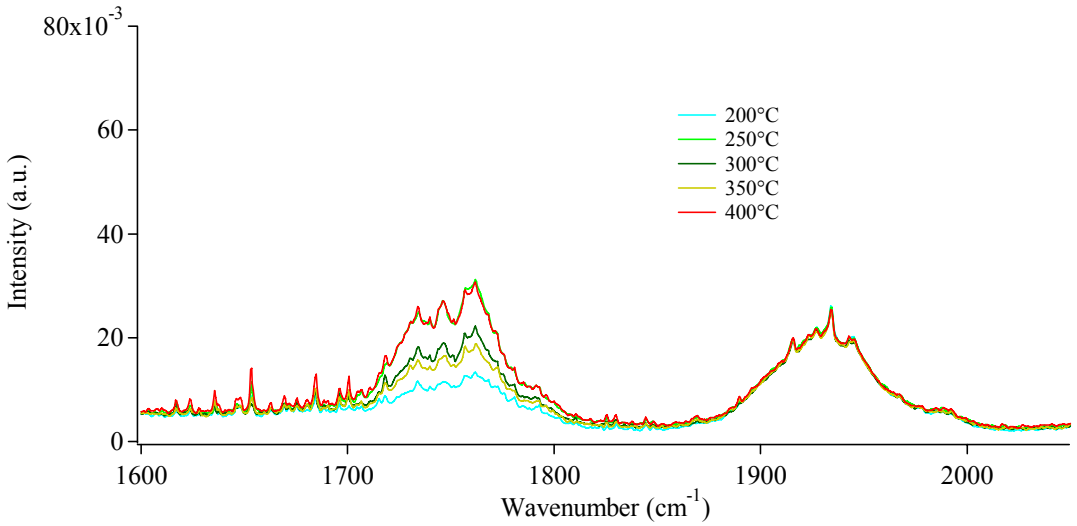

Figure 6.14. FTIR spectra obtained after exposing LSGC Pec to CH_3CH_2OH vapours at increasing temperatures (gas mixture from the reactor). Region between 1600 and 2050 cm^{-1}.

Table 6.4. Conversions of fuels and yields for products obtained for LSGC Gel and LSGC Pec with respect to the reaction with pure methanol and ethanol vapours.

	CH_3OH			CH_3CH_2OH		
sample	T max react (°C)	conv (%)[a]	yield H_2 (%)[b]	T max react (°C)	conv (%)[a]	yield H_2 (%)[b]
LSGC Gel	400	ND [c]	< 1	250	5	1
LSGC Pec	400	ND	< 1	250 and 400	1	ND

Note:
[a] conversions determined by QMS (see appendixes A, B)
[b] yield by QMS (see appendixes A, B)
[c] not detectable

Table 6.4 summarizes the obtained values for the conversions of the alcohols and the yields in hydrogen at the temperatures of maximum activity. Concerning the tests with methanol, both catalysts are scarcely active even at the highest temperature. The values appear slightly better when reacting with ethanol, although both samples are probably poisoned by un-desorbed species. It is worth to point out that the slightly better conversions obtained for ethanol can also be due to the minor WHSV used (see appendix B).

Methanol and Ethanol oxidation

A second type of experiment concerns the evaluation of the oxidation abilities with respect to methanol and ethanol. In these cases, the carrier gas was enriched with oxygen.

Figure 6.15 shows the QMS data obtained, as a function of temperature, for methanol oxidation, while the figures 6.16 and 6.17 show the corresponding IR spectra. The outcomes indicate that the catalysts are inert until 250°C. Starting from 300°C only small amounts of formic acid (1745 cm^{-1}), methyl formate (1755 cm^{-1}) and carbon dioxide (2363 cm^{-1}) are evident. At 350°C the activity increases, but only at 400°C the oxidation of ethanol takes place with a great formation of H_2O (QMS and IR band 1595 cm^{-1}) and CO_2 (equation 7). Hydrogen (QMS) and carbon monoxide (QMS and IR band at 2143 cm^{-1}) are also present probably because of the partial oxidation of methanol (8, 9).

$$CH_3OH + 3/2O_2 \rightleftharpoons 2H_2O + CO_2 \quad (7)$$

$$CH_3OH + 1/2O_2 \rightleftharpoons CO + H_2O \quad (8)$$

$$CH_3OH + 1/2O_2 \rightleftharpoons CO_2 + H_2 \quad (9)$$

The partial oxidation products can be due to a low selectivity of the catalysts or to inappropriate experimental conditions. Further investigations can be carried out to better understand if the amounts of partial oxidation products can be reduced employing different reaction conditions (i.e. minor value for WHSV, see appendix B).

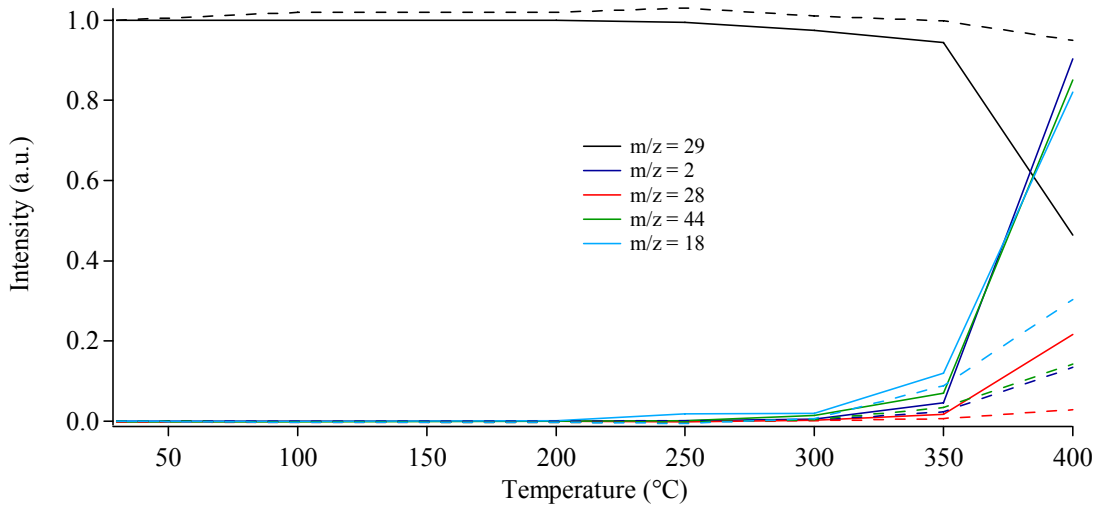

Figure 6.15. QMS data obtained for m/z = 29 (methanol), m/z = 2 (hydrogen), m/z = 28 (carbon monoxide), m/z = 44 (carbon dioxide) and m/z = 18 (water) in oxidizing conditions at the investigated temperatures. Solid lines stand for LSGC Gel, dashed lines for LSGC Pec.

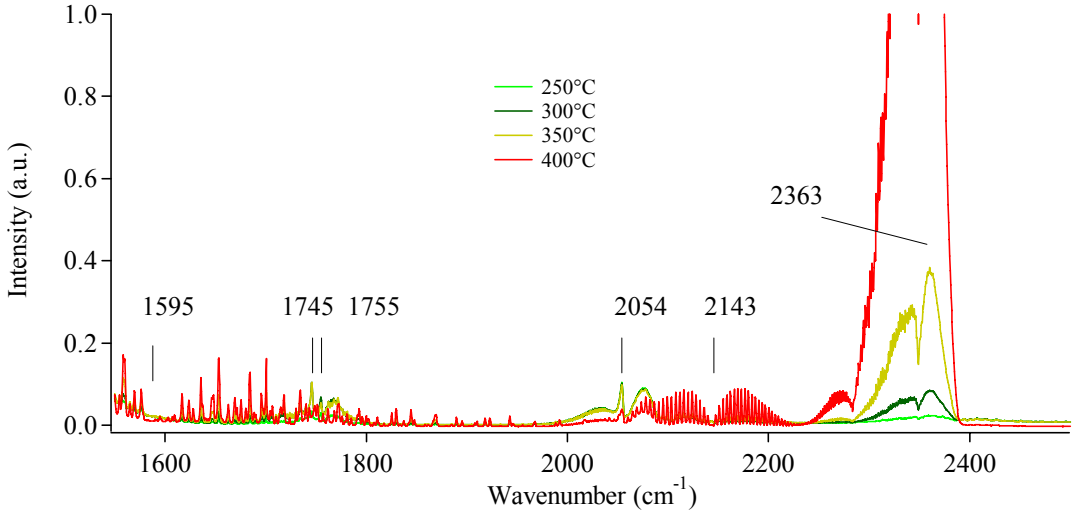

Figure 6.16. FTIR spectra obtained after exposing LSGFC Gel to CH_3OH vapours O_2 enriched (gas mixture from the reactor). Region between 1550 and 2500 cm^{-1}.

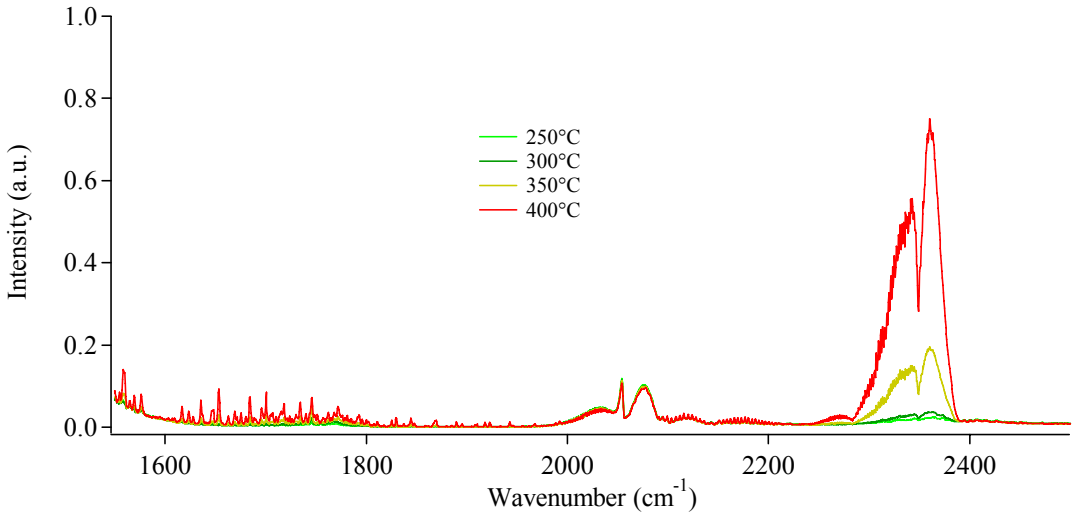

Figure 6.17. FTIR spectra obtained after exposing LSGC Pec to O_2 enriched CH_3OH vapours (gas mixture from the reactor). Region between 1550 and 2500 cm^{-1}.

Figure 6.18 shows the QMS outcomes obtained when investigating ethanol oxidation. The following figures 6.19 and 6.20 show the IR spectra collected after exposing LSGC Gel and Pec respectively, to ethanol under oxidizing conditions. The data suggest that at 300°C only small amounts of acetaldehyde (band at 1755 cm^{-1}) are produced. At 350 and 400°C both catalysts improve their performances with more considerable amounts of products arising from total and partial oxidation of ethanol. CO_2 (QMS and IR band at 2363 cm^{-1}) and H_2O (QMS and IR at 1595 cm^{-1}) seem to be the main products, although H_2 (QMS), CH_3CHO (QMS and IR at 1755 cm^{-1}) and CO (QMS and IR at 2143 cm^{-1}) are also present.

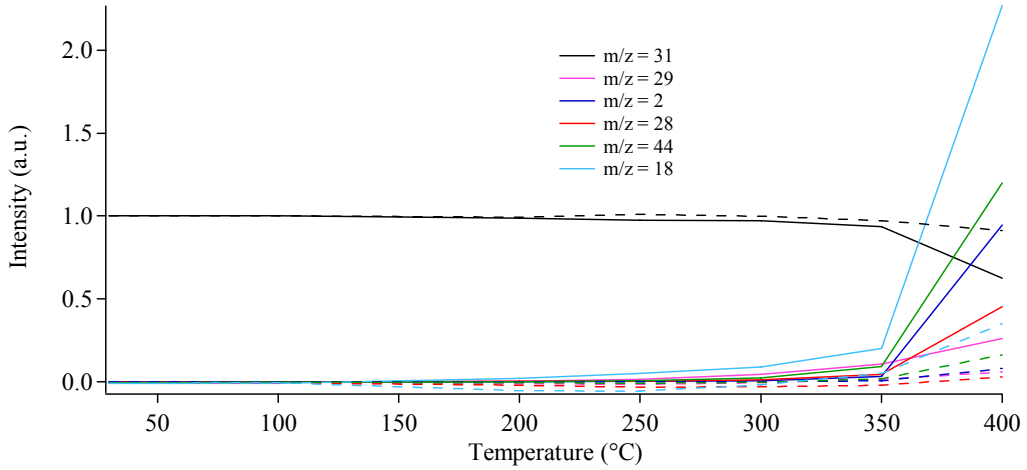

Figure 6.18. QMS data obtained for m/z = 31 (ethanol), m/z = 29 (acetaldehyde), m/z = 2 (hydrogen), m/z = 28 (carbon monoxide), m/z = 44 (carbon dioxide) and m/z = 18 (water) in oxidizing conditions. Solid lines stand for LSGC Gel, dashed lines for LSGC Pec.

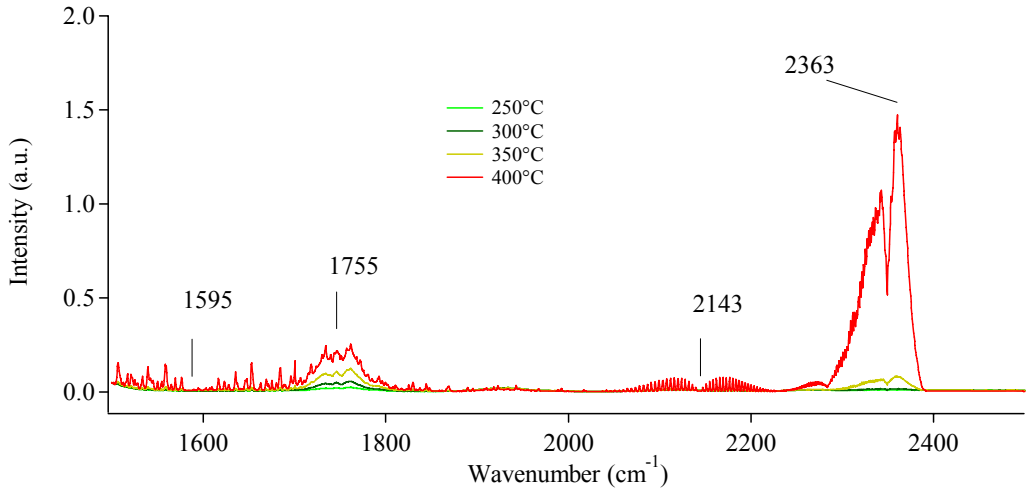

Figure 6.19. FTIR spectra obtained after exposing LSGC Gel to CH_3CH_2OH vapours O_2 enriched (gas mixture from the reactor). Region between 1500 and 2500 cm^{-1}.

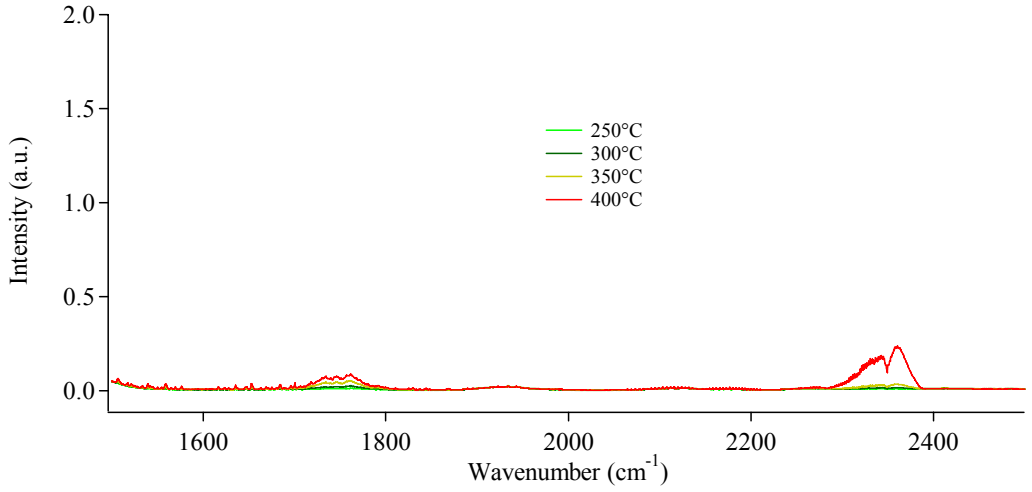

Figure 6.20. FTIR spectra obtained after exposing LSGC Pec to CH_3CH_2OH vapours O_2 enriched (gas mixture from the reactor). Region between 1500 and 2500 cm^{-1}.

Table 6.5. Conversions of fuels and yields for products obtained at 400°C for LSGC Gel and LSGC Pec with respect to methanol and ethanol oxidation.

	CH_3OH/O_2				CH_3CH_2OH/O_2			
sample	conv	yield H_2	yield CO	yield CO_2	conv	yield H_2	yield CO	yield CO_2
LSGC Gel	55	14	5	24	38	41	7	24
LSGC Pec	5	3	< 1	5	9	3	ND [a]	3

Note:
[a] not detectable
all data are in % and obtained by QMS (see appendixes A, B)

The values obtained for the conversions and the yields of the main products of methanol and ethanol oxidation at 400°C are summarized in table 6.5. From these, it can be seen that LSGC synthesized by polyacrylamide gel method always guarantees the best performances with both alcohols. A deeper analysis of the data can be done by comparing the conversions and yields. The high presence of hydrogen suggests that it is not easily burned into water. Furthermore, regarding methanol, the low yield in CO_2, compared to CH_3OH conversion, indicates that a certain amount of products remains adsorbed on the catalysts. Finally, concerning ethyl alcohol, the oxidation reaction always competes with the dehydrogenation, since IR spectra confirm the presence of acetaldehyde.

Methanol and Ethanol steam reforming

LSGC Gel and LSGC Pec were finally investigated with respect to the steam reforming of the fuels.

Figure 6.21 shows the QMS data obtained for LSGC samples at the investigated temperatures, when a methanol aqueous solution (1 M) is used as feed. FTIR spectra collected for LSGC Gel and Pec are shown in figures 6.22 and 6.23 respectively.

The methanol steam reforming occurs starting from 300°C with both catalysts. As a general consideration, the performances of the samples improve with temperature increase. In detail, both catalysts guarantee the best ability at the highest investigated temperature (400°C).

The main observed products agree with those assigned to the steam reforming reactions (equations 3, 10 and 11):

$$CH_3OH \rightleftharpoons 2H_2 + CO \quad (3)$$

$$CO + H_2O \rightleftharpoons CO_2 + H_2 \quad (10)$$

$$CH_3OH + H_2O \rightleftharpoons 3H_2 + CO_2 \quad (11)$$

It is worth to underline that the overall methanol steam reforming reaction (11) is the sum of two subsequent reactions: the decomposition (3) and the water gas shift reaction (10). [53]

The IR spectra confirm the QMS data, nevertheless, in the test with LSGC Gel at 400°C a new species appears. The new bands at 2766 and 2800 cm^{-1} can be ascribed to a small amount of formaldehyde, probably due to the dehydrogenation of CH_3OH (12):

$$CH_3OH \rightleftharpoons H_2 + HCOH \quad (12)$$

Unfortunately, the presence of HCOH can not be confirmed by the more significant C-O stretching band (at 1746 cm^{-1}) because of the overlapping with the more intense water vibro-rotational band.

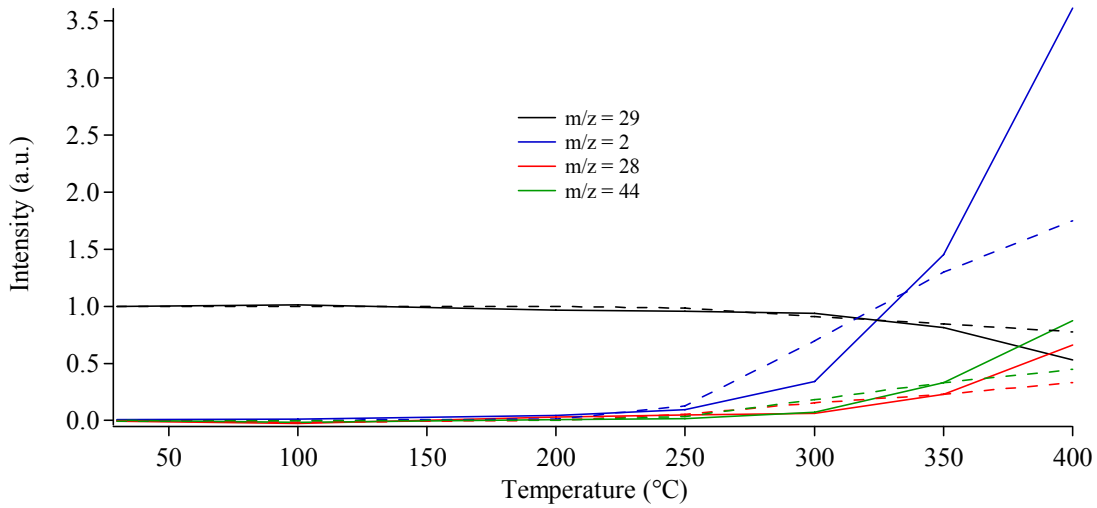

Figure 6.21. QMS data obtained for m/z = 29 (methanol), m/z = 2 (hydrogen), m/z = 28 (carbon monoxide), and m/z = 44 (carbon dioxide) in steam reforming conditions. Solid lines stand for LSGC Gel, dashed lines for LSGC Pec.

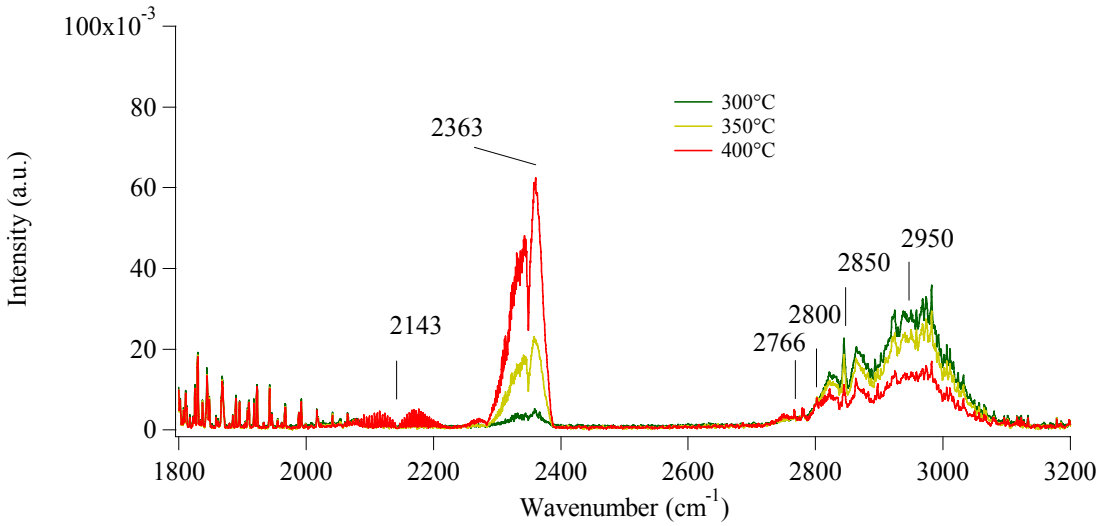

Figure 6.22. FTIR spectra obtained after exposing LSGC Gel to CH_3OH 1M vapours (gas mixture from the reactor). Region between 1800 and 3200 cm^{-1}.

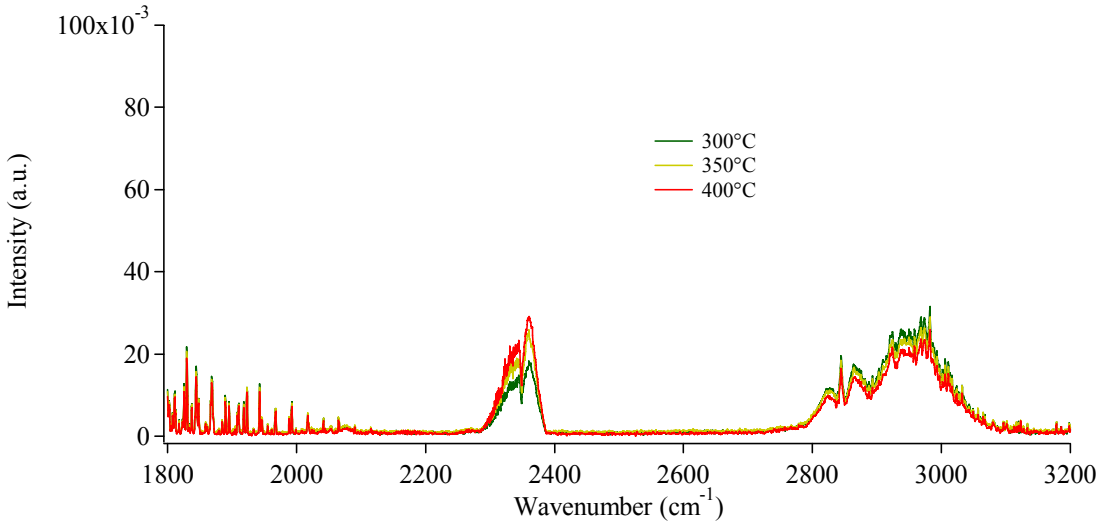

Figure 6.23. FTIR spectra obtained after exposing LSGC Pec to CH_3OH 1M vapours (gas mixture from the reactor). Region between 1800 and 3200 cm^{-1}.

The tests performed with the ethanol aqueous solution (1 M) show an irregular trend. Both catalysts give the best results at 300°C producing hydrogen (figure 6.24, QMS outcomes), acetaldehyde (QMS and IR bands at 2705 and 2731 cm^{-1} in the figures 6.25 and 6.26) and CO_2 (QMS and IR band at 2363 cm^{-1}). Furthermore, a remarkable contribution from m/z = 28 is observed. This signal can be due to carbon monoxide and ethylene; the first species is an intermediate in the steam reforming reaction, while the second one can derive from the dehydration of ethyl alcohol.

LSGC Pec sample shows worse performances compared to LSGC Gel. IR spectra only show the typical band assignable to C-H stretching in acetaldehyde, while the more

sensitive QMS evidences the presence of small amounts of H_2, CH_3CHO and a contribution from m/z = 28 (CO and CH_2CH_2).

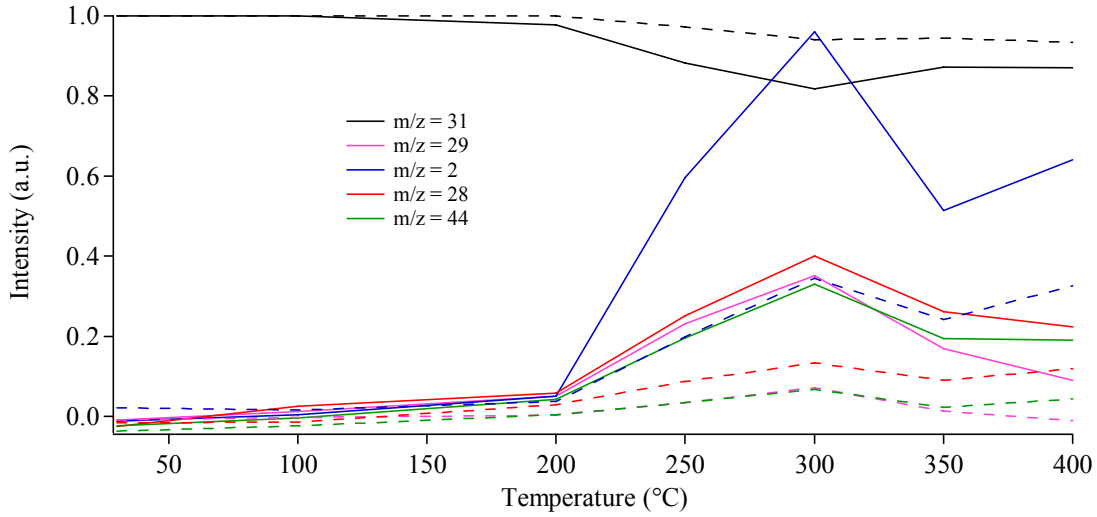

Figure 6.24. QMS data obtained for m/z = 31 (ethanol), m/z = 29 (acetaldehyde) m/z = 2 (hydrogen), m/z = 44 (carbon dioxide) and m/z = 28 (carbon monoxide and ethylene) in steam reforming conditions. Solid lines stand for LSGC Gel, dashed lines for LSGC Pec.

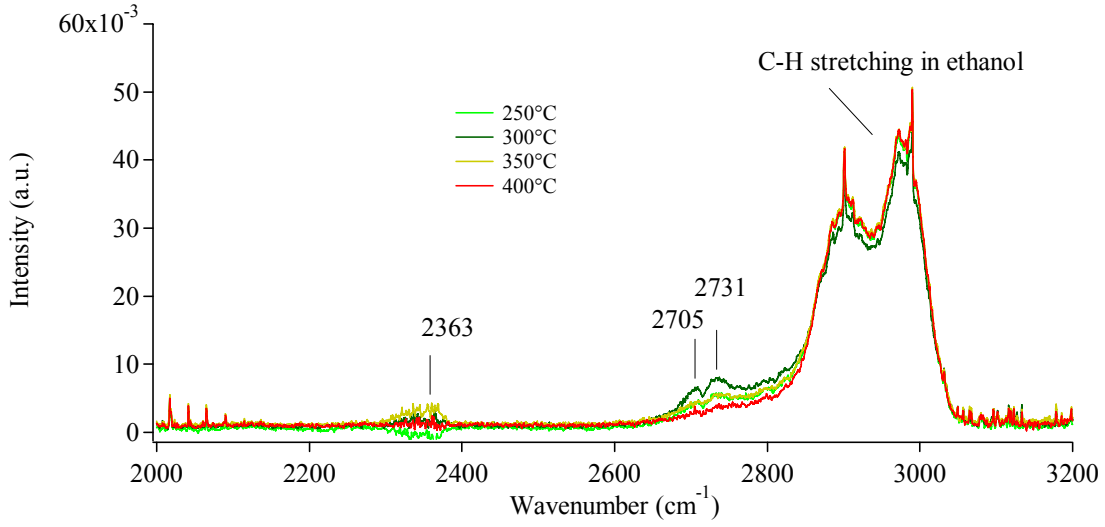

Figure 6.25. FTIR spectra obtained after exposing LSGC Gel to CH_3CH_2OH 1M vapours (gas mixture from the reactor). Region between 2000 and 3200 cm^{-1}.

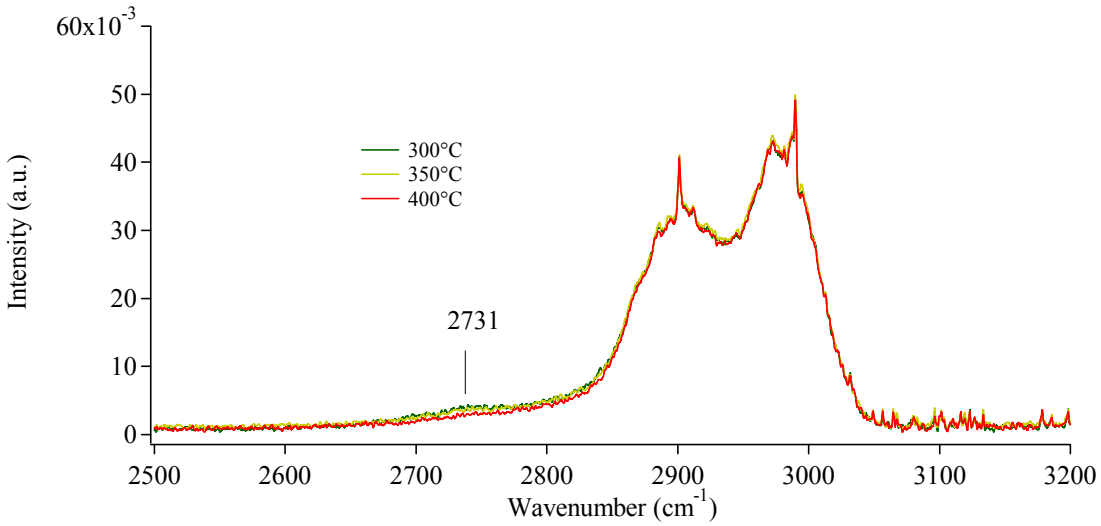

Figure 6.26. FTIR spectra obtained after exposing LSGC Pec to CH_3CH_2OH 1M vapours (gas mixture from the reactor). Region between 2500 and 3200 cm^{-1}.

Table 6.6. Conversions of fuels and yields for products obtained for LSGC Gel and LSGC Pec with respect to methanol and ethanol steam reforming at the temperature of maximum activity (400°C and 300°C respectively).

	CH_3OH 1M				CH_3CH_2OH 1M			
sample	conv	yield H_2	yield CO	yield CO_2	conv	yield H_2	yield CO	yield CO_2
LSGC Gel	47	11	ND [a]	2	19	< 1	ND	ND
LSGC Pec	23	4	ND	ND	6	ND	ND	ND

Note:
[a] not detectable
all data are in % and obtained by QMS (see appendixes A, B)

Table 6.6 summarizes the calculated values for the conversions of the alcohols and the yields for H_2, CO and CO_2 in steam reforming conditions. The obtained values suggest that both catalysts react better with methanol than with ethanol. Furthermore, looking at the conversions, LSGC Gel confirms its higher activity also as reforming catalyst. Nevertheless, the clear lacks in the carbon-containing species in the exit-gas, indicate that considerable amounts of products are retained on the catalysts.

It is worth to underline once again, that literature studies concerning the interactions between ethyl alcohol and perovskite-type materials are practically missing. Thus only data concerning metal oxides can be considered for comparison. Some important information can be obtained from the studies performed on various transition metal oxides and metals or noble metals supported by transition metal oxides. [66, 67, 68, 69, 70] From these papers it can be seen that the catalysts react with ethanol in several modes. Most of the Authors agree that ethanol firstly forms ethoxy species on the surface of the

catalysts, and then these species react producing various kinds of chemicals as a function of the catalyst. In particular, McCabe et al. [64] state that ethanol oxidation (with the formation of acetaldehyde and carbon dioxide) is promoted by basic catalysts such as hopcalite (CuO 20% - MnO_2 80%), Pt/Al_2O_3, $Cu/Cr/Al_2O_3$, Cu/Cr/MgO etc, while the dehydration (formation of diethyl ether and ethylene) seems to be promoted by acidic catalysts such as ZrO_2, Al_2O_3, W/ZrO_2 etc.

Another very important aspect concerns the stability of the ethoxy species (or the other adsorbed species, included molecular ethanol) on the catalysts surface. Yee et al., [68] for example, found different desorption temperatures for the reaction products in the tests between ethanol and CeO_2. This can also indicate that the un-desorbed products may affect the performances of the catalysts.

In the present case, the chemisorption tests never show the absorption of ethoxy species on the catalyst surfaces. Nevertheless, the activity tests clearly show that both catalysts become active since 250°C (the chemisorption test were carried out until 200°C) and their presence at higher temperatures can not be excluded.

Anodic activity: a brief summary

In the chapters 3, 4, 5 and 6 the reactivity of all the synthesized compounds was treated. In detail, the outcomes obtained with respect to the interaction and the activity toward methanol and ethanol vapours, the oxidation and the steam reforming of the same alcohols were described. All these data provide important information regarding the application of the analyzed compounds at the anode site of a solid oxide fuel cell. It is now opportune to resume the foremost outcomes.

Firstly, the chemisorption tests indicate that methanol and ethanol never interact by dissociative adsorption with the catalysts at least until 200°C. In fact, the obtained DRIFT spectra never give evidences for the formation of chemisorption products such as methoxy or ethoxy species. The spectra obtained after evacuation of the DRIFT chamber with argon confirm the inertia of the samples.

Concerning the activity tests toward the pure alcohol vapours, all the investigated catalysts show scarce tendencies toward the alcohol decompositions. Methanol is mainly decomposed into hydrogen and carbon monoxide, while small amounts of carbon dioxide are also detected. It is interesting to observe that traces of intermediate products such as methyl formate and formic acid were also detected as a function of the catalyst. Methyl formate is thought to derive from the interaction between carbon monoxide and methanol [51]

$$CO + CH_3OH \rightleftharpoons HCOOCH_3 \qquad (13)$$

The direct dehydrogenation reaction, in contrast:

$$2CH_3OH \rightleftharpoons 2H_2 + HCOOCH_3 \qquad (1)$$

is considered rather un-favourable. It was observed, however, that copper-containing catalysts promote the direct formation of methyl formate at 200÷300°C; this could also be the case of the LCC and LSGC samples investigated in the present work. As a matter of fact, in all cases, copper is present; moreover the active intervention of copper is evidenced by its reduction to Cu(I) observed (by means of XPS) on the worn-out catalyst. Methyl formate, in contrast, is not formed in the sample without copper

(LSGF). At higher temperature the formation of H_2 and CO (from the rapid decomposition of methyl formate) is favourite, as confirmed by literature data. [51, 52]

In all the samples, ethanol undergoes mainly dehydrogenation with the formation of acetaldehyde and hydrogen and no significant differences have been revealed between the catalysts. The activity of the copper-containing samples reaches its maximum at about 250÷300°C both with respect to methanol and ethanol, while LSGF compounds show a monotone trend until the highest investigated temperature (400°C). LSGC samples, moreover, seems to show an intermediate behaviour between LCC and LSGF compounds: it shows an activity peak at about 250°C and a new activity increase at 400°C. The positive influence of copper on ethanol dehydrogenation was already underlined by Velu et al. [75]

A significant point to be considered is the formation of traces of ethylene at about 400°C; this behaviour could be due to the formation of surface acidic sites as a consequence of temperature [64]

All the investigated compounds are poisoned by un-desorbed reaction products.

All the samples show rather low conversion values. It is worth to point out that the low activity of the catalysts toward pure alcohols should be seen as a positive property. In fact, taking into account the employment as anode in the solid oxide fuel cells, the fuel (such as ethanol or methanol) should not be decomposed by the anode materials, but electro-oxidised for the power generation.

The tests performed in oxidising conditions give very interesting results.

Copper-containing samples offer the best performances, in particular in the order LCC2 > LCC1 > LSGC (for the last compound the lower copper content should be considered). LCC samples, moreover, show incandescence at the highest temperature (400°C). Methanol is mainly fully oxidised to water and carbon dioxide, and only minor amounts of partial oxidation products such as hydrogen and carbon monoxide are present (probably as a consequence of the test conditions).

Ethanol oxidation seems to be slightly more difficult and acetaldehyde is always present as a by-product.

This kind of experiments does not reproduce exactly the conditions at the anode side of a fuel cell, but they allow to better understanding the behaviour of the compounds when oxygen is available for the oxidation reactions.

Finally, the catalysts were tested with respect to the steam reforming of the alcohols. This kind of experiments was carried out taking into account that most of direct alcohol

fuel cells are fed with aqueous solutions of the alcohols. The second important reason involves the great attention dedicated to the hydrogen production by means of steam reforming of the alcohols.

All the catalysts promote the formation of the steam reforming products (hydrogen and carbon dioxide); carbon monoxide is also present. The catalysts always show a monotone trend with respect to the temperature, reaching their best performances at the highest investigated temperature (400°C). Copper containing samples show, once again, the best results (good conversion and H_2 yields values).

An approximate mechanism for alcohol steam reforming consider as the first step, the dehydrogenation to the aldehyde followed by its successive decomposition to the final product as a consequence of the interaction with surface adsorbed hydroxyl groups and water molecules. The observed formation of the acetaldehyde could support this hypothesis.

It is necessary to underline that all samples undergo deep poisoning due to un-desorbed carbon-containing species such as reaction intermediates or reaction products. The characterization of the worn-out catalysts and the observed trend during the long term tests suggest that the adsorption of the carbonaceous species occur mainly on the basic sites, such as lanthanum and strontium as a consequence of the interaction with carbon dioxide to give carbonate species. The poisoning of the B-sites cations (copper, cobalt, gallium and iron) seems to be less evident, since the activity decrease appears quite low if compared to the amount of the retained carbonate. The observations of De Asha et al. [56] concerning the interactions between carbon dioxide and lanthanum layer deposited on a copper substrate, confirm obtained results.

Chapter 7

Oxygen permeability

Introduction

Fuel cells derive electric power by operating the electro-oxidation of the fuels. In detail, the overall combustion is obtained by carrying out the oxidation of the fuel at the anode site, and the reduction of the combustive agent (typically oxygen) at the cathode site.
The outcomes from various kinds of experiments were presented and discussed in the Chapters 3, 4, 5 and 6. All those tests can help to better understand the anodic capability of the synthesized samples.
On the other hand, this chapter is focused in clarifying the cathode abilities of the compounds.
The oxygen reduction can be summarized as in equation (1):

$$O_2 + 4e^- \rightleftharpoons 2O^{2-} \qquad (1)$$

Equation (1) appears as a simple half-reaction. Nevertheless, a lot of features affect the process. Adler, in his widely cited review, [19] summarizes the main ones.

Equation (1) appears as a simple half-reaction. Nevertheless, a lot of features affect the process. Adler, in his widely cited review, [19] summarizes the main ones.
The efficiency of a fuel cell depends on (among other elements) the internal losses in the cell, including the ohmic resistance of the electrolyte and the overpotential losses at the electrodes. While the first one is well understood today, the second one needs a deeper characterization. At the cathode site, in particular, the oxygen reduction is generally thought to be the most difficult reaction to activate in a SOFC. The mechanism appears rather elaborate and various aspects need to be considered.
Firstly, molecular O_2 need to be converted into some "electro-active" intermediate form via one or more processes. These reactions do not depend on the current (except in the limit of steady state) and they are driven by the chemical potential (depletion or surplus of the intermediate). The second important point concerns the diffusion of the intermediate species (mass transfer) through the electrode (to the electrolyte). Since electrochemical reactions and diffusion occur cooperatively over an active area, the overall rate is co-limited by both these processes.

Oxygen permeability

In this research project, the cathode reaction is investigated by means of unusual technique. In particular, the capability of the synthesized samples as cathode materials is studied by means of oxygen permeation measurements.
The information provided by this kind of experiments can be very useful in relation to the cathode activity. The oxygen permeation, in fact, is a selective phenomenon which allows separating oxygen from a mixture of gases. Figure 7.1 schematizes the permeation mechanism.

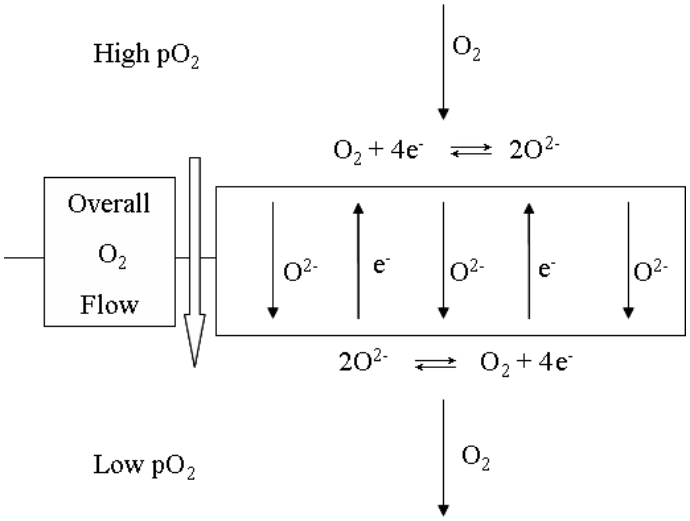

Figure 7.1. Schematic view of the oxygen permeation in a mixed electronic-ionic conductor.

As illustrated in the figure 7.1, oxygen undergoes reduction at the O_2-rich side, and then the oxide ions are transported through the membrane at the O_2-deficient side. The last step involves the re-oxidation of the oxide ions and the releases of molecular oxygen. As can be seen, the driving force of the overall process is the O_2 pressure gradient between the two sides of the membrane.

Summarizing, the permeation mechanism involves both the electrochemical and the transport properties of the investigated material.

It is now opportune to point out that the assumed mechanism can only be carried out by a mixed electronic-ionic conductor material (MIEC). In fact, electrons must be able to move to the O_2-rich side to reduce O_2 and the oxide ions (generated at the cathode site) need to reach the O_2-deficient side.

The last feature involved in the permeation mechanism concerns the chemical properties of the material with respect to the reduction and oxidation of oxygen.

From the statements above, a strong relationship between oxygen permeation properties and cathode activity is well evident. As pointed out in Chapter 1 when considering solid oxide fuel cells operation, the cathode site promotes the oxygen reduction and provides for carrying the oxide ions to the electrolyte.

As can be seen, the processes involved in oxygen permeation and in SOFCs cathode working, are very similar and the only difference concerns the last step (i.e. re-oxidation of oxide ions in the permeation process, compared to oxide ions transfer to the electrolyte in the SOFCs).

It should be evident that a high oxygen permeation rate can guarantees an overall fast operation when the material is employed as cathode in SOFCs.

Equations of electrochemical transport in a mixed conductor [102, 103, 104, 105, 106, 107, 108]

The permeation phenomena can be described taking into account the oxygen ions and the electrons diffusion through the membrane. In detail, picture 7.1 suggests that electrons and ions move in opposite directions in order to give a total current density equal to zero under steady state conditions (2):

$$j_t = j_e + j_{O^{2-}} = 0 \qquad (2)$$

Where j_t indicates the total current density, while j_e and j_{O2}- are the electronic and ionic partial currents respectively. All the currents are given in $C \cdot cm^{-2} \cdot s^{-1}$.
Starting from these considerations, the partial current density of oxygen ions can be given as follow (3):

$$j_{O^{2-}} = \frac{1}{4F} \frac{RT\sigma_e\sigma_i}{(\sigma_e + \sigma_i)t_m} \ln\left(\frac{P_h}{P_l}\right) \qquad (3)$$

With:
F = Faraday constant ($C \cdot mol^{-1}$)
R = universal gas constant ($J \cdot mol^{-1} \cdot K^{-1}$)
T = absolute temperature (K)
σ_e and σ_i = electronic and ionic conductivity ($S \cdot cm^{-1}$)
t_m = membrane thickness (cm)
P_h and P_l = oxygen partial pressure at the O_2-rich and O_2-deficient sides respectively (Pa)

The partial current density j_{O2}- can be conveniently turned in terms of oxygen flux J_{O2} (mol·cm^{-2}·s^{-1}). Equation (4) shows the conversion:

$$J_{O_2} = \frac{j_{O^{2-}}}{4F} \qquad (4)$$

Further considerations and simplifications can be carried out taking into account the values of σ_e and σ_i and then the opportunity to omit the less relevant term in the sum (σ_e + σ_i).

Oxygen permeation measurements: the permeation cell

The oxygen permeation measurements were carried out by means of a home made measurements cell. Literature references provide a wide number of papers regarding selective permeation of gases through thin membranes. The main applications concern the separation of oxygen from a mixture of gases (typically air) or the production of syngas by partial oxidation of methane. [108, 109, 110]

The employed devices for the described operation can be very different. The variations mainly involve the geometric features but also the heating systems as well as the temperature controls and the membrane fastening.

The permeation cell design emphasized many interesting points. Firstly, the device should be made up with a non porous material, just to avoid the permeation through the reactor walls. It must to obviously withstand the high temperatures (at least until 800°C) and has to be completely inert both with respect to the sample and to the oxidising conditions (oxidising and inert atmosphere).

A deep investigation suggests that the most suitable compound is a ceramic material known as macor® (Corning).

The second issue concerns the sealants. It is necessary that the constituent parts are well connected to avoid leakages. In this way, a proper kind of gaskets must be used.

Finally, it is indispensable to minimize the undesired permeation through the sealant glue (ceramic glue) used for pasting the membrane to the sample holder.

Taking into account both the hints from literature data and the properties and specifics for materials, gaskets and ceramic glues, a permeation cell was realized. Figure 7.2 shows a simplified model of the reactor, while figure 7.3 shows a section of the realized project.

Beyond the project details, it is worth to underline that the aim is realizing two distinct chambers, the first one (outer chamber) is O_2-riched (using a N_2-O_2 mixture 80-20%), while in the second one (inner chamber) an inert gas (argon) flows.

The analyzed compound, pressed as a pellet, acts as a semi-permeable wall for the selective permeation of oxygen. Finally, the exit gases (argon + permeated oxygen) reach the mass detector for the quantitative analysis. It is worth to point out that in the N_2-O_2 mixture, nitrogen can be used as internal standard to subtract the spurious permeation (for example from small leakages) to the overall permeated O_2.

The permeation cell is heated up by two electric heaters until 800°C; the temperature is checked by means of two thermocouples located at the both sides of the sample. Finally, to minimize the heat dissipations, the overall apparatus is totally shielded with an insulator cover.

Figure 7.4 shows the photographs of the realized permeation cell.

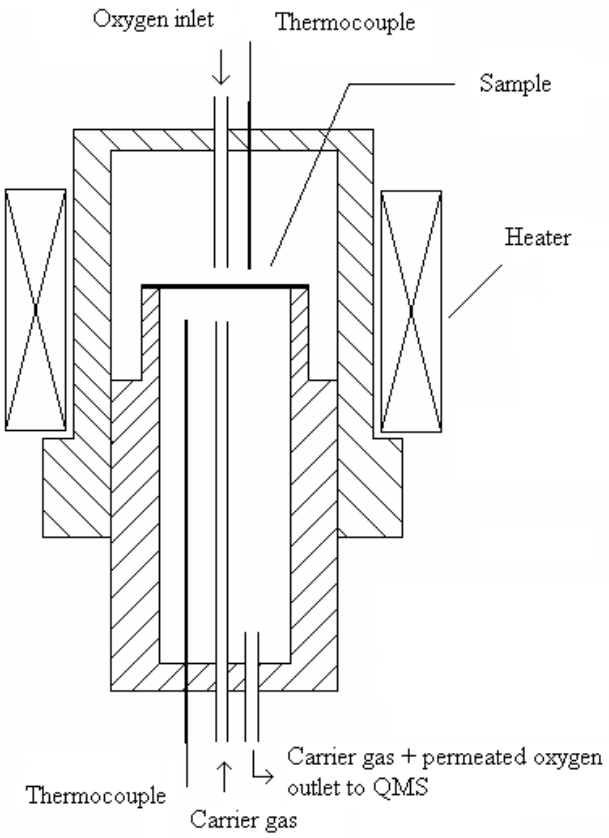

Figure 7.2. Simplified model of the permeation cell.

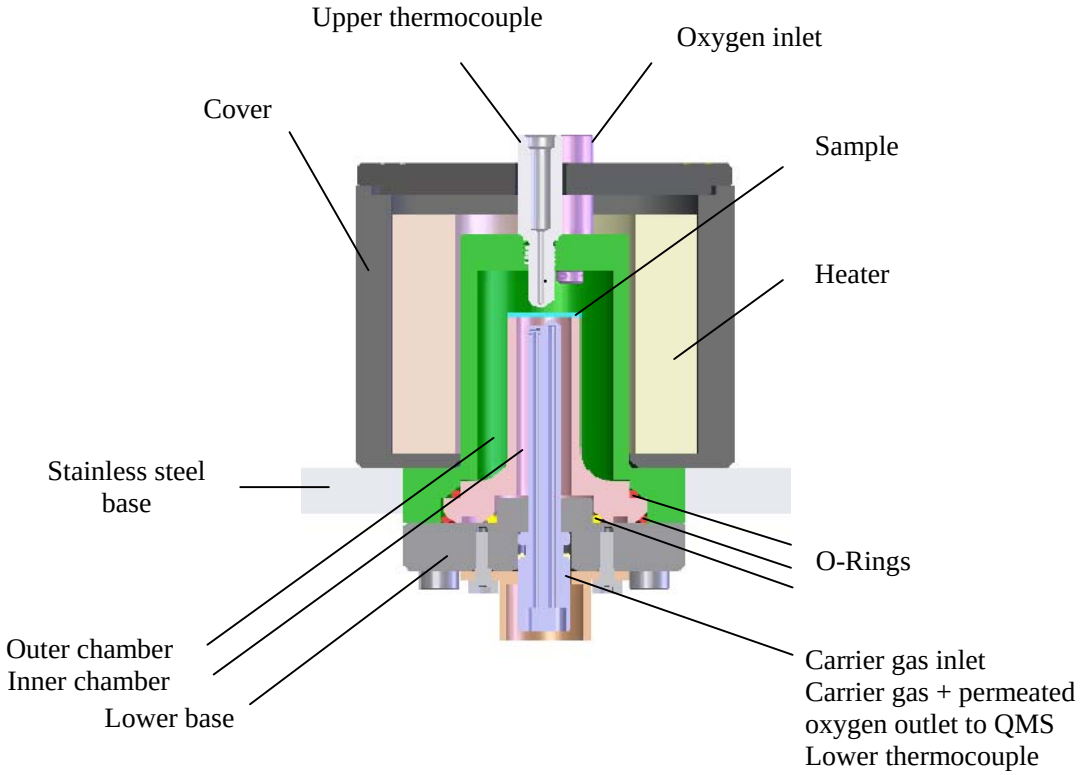

Figure 7.3. Schematic view of a vertical section of the permeation cell.

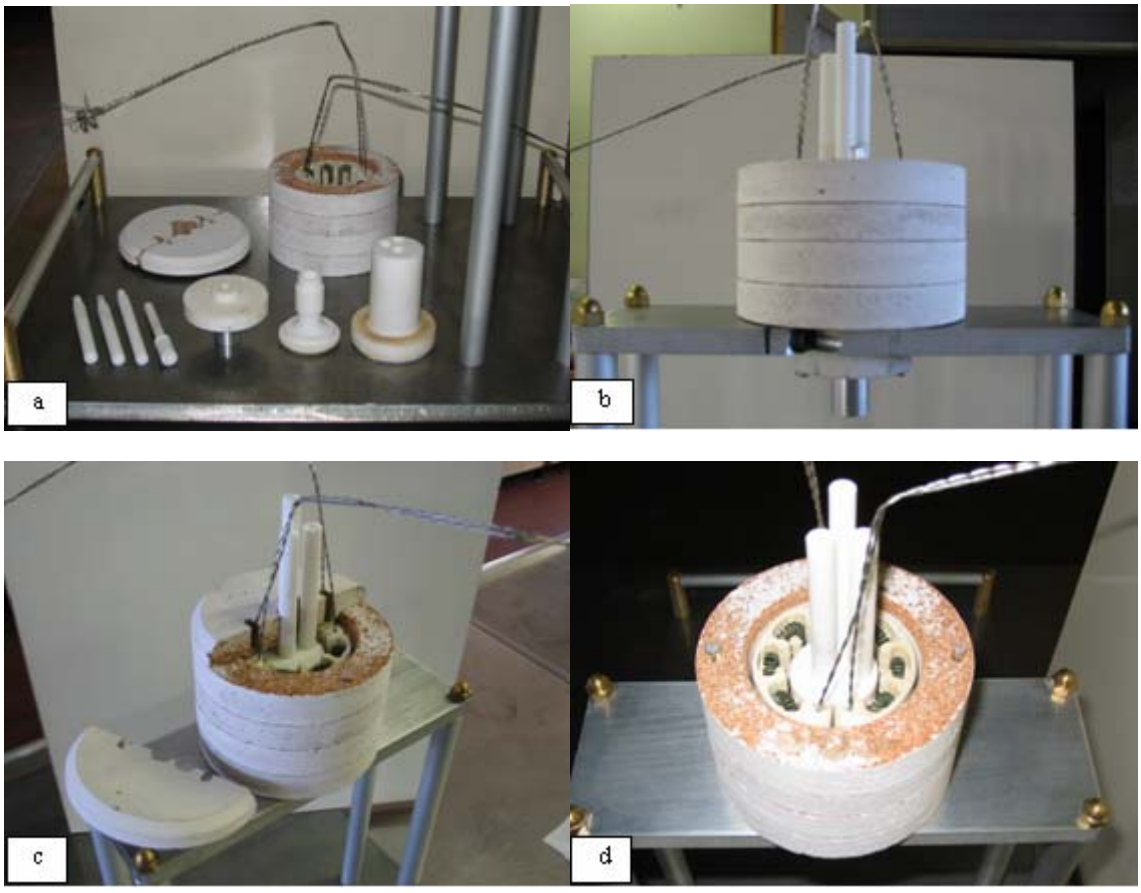

Figure 7.4. Photographs of the permeation cell. a) view of the single components of the reactor (in the foreground), of the heaters and the shield cover (background). Front (b) and upper views (c, d) of the assembled system.

In the performed tests, the oxygen permeation rate J_{O2} (ml·cm^{-2}·min^{-1}) is calculated from the experimental parameters taking into account the following equation (5):

$$J_{O_2} = \frac{TFR \cdot C_{O_2}}{S} \qquad (5)$$

With:

TFR = total flow rate (carrier + permeated oxygen) at the O_2-deficient side (ml·min^{-1})

C_{O2} = O_2 concentration in the exit gas (carrier + permeated oxygen) (%)

S = effective area of the membrane (cm^2)

Sample processing

The as prepared samples need a further preparation before the permeation test. Since all the synthesized compounds appear as a powder, the first step involves the preparation of the pellet.

An appropriate amount of powder was used to produce a discoid pellet with Ø = 13 mm and thickness 0.75 mm (the powder was pressed by means of a hydraulic press at 7.5 tons·cm^{-2} for 30 minutes). Finally, the obtained pellets were sintered at 900°C for 5 h in air.

It is interesting to point out that the samples obtained by polyacrylamide gel method never gave good quality pellets: they always tend to exfoliate with the consequent pellet breaking. Because of this, the permeation tests were carried out on the compounds obtained by Pechini process.

The second step consist in the pasting the pellet to the sample holder. This is a very important point, since, as stated above, the sample must be firmly fixed to the sample holder, and the fixing glue should not permit the permeation of gases.

A very large number of tests were carried out to find out the best way to do it. Finally, the pellets were pasted by means of several layers of ceramic glue, and a sintering process at 800°C for 5 h.

Permeation tests

The permeation tests were carried out by means of the described experimental reactor on the LCC2 Pec and LSGF Pec compounds.

In each test, the whole system was left to equilibrate for 2 h at RT in the operating atmospheres (N_2-O_2 mixture 80-20% in the O_2-rich side, Ar 100% in the O_2-deficient side), before starting the data acquisition. The composition of the exit gases was acquired for 1.5 h at each investigated temperature (RT, 600, 700 and 800°C); finally, the tests were repeated three times for both samples.

Figure 7.5 summarizes the obtained outcomes for the oxygen permeation through LCC2 Pec and LSGF Pec samples.

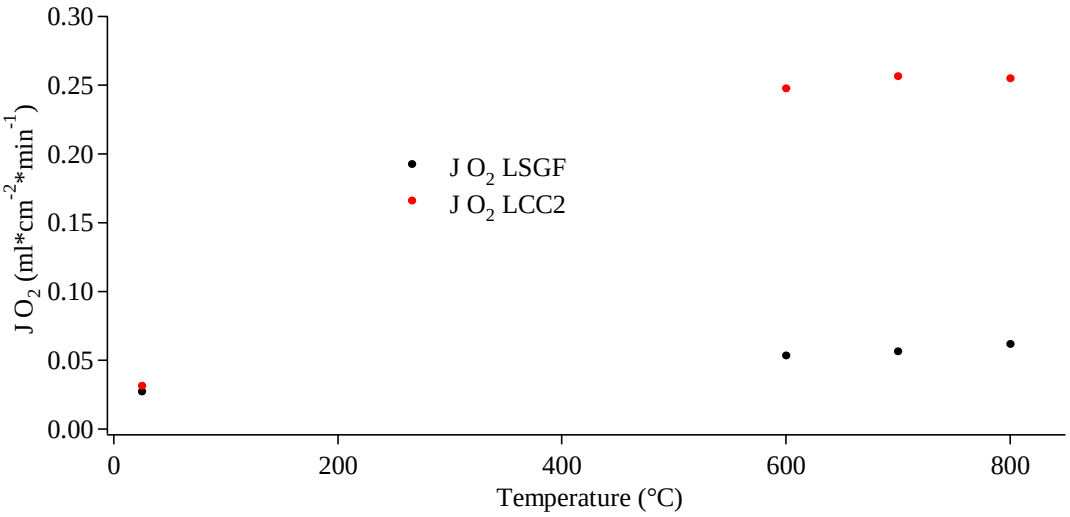

Figure 7.5. O_2 flux obtained in the permeation test for LSGF Pec (•) and LCC2 Pec (•).

The obtained data suggest that LCC2 Pec sample allows a better O_2 permeation than LSGF Pec. In fact, the O_2 flow appears about 4÷5 times higher with respect to that observed for LSGF Pec.

Literature data confirm the obtained values for LSGF Pec. [107, 108] Furthermore, the low O_2 permeation rate in LSGF seems to be due to a scarce redox activity in the reduction and re-oxidation of oxygen rather than a low diffusion rate through the membrane. Lee et al. [108] show that the covering with a more active material (such as $LaCoO_3$) greatly improves the permeation abilities of LSGF.

LCC2 sample, instead, shows a good oxygen permeation flow, which can suggest a good overall process. Nevertheless, no literature data are available for a better comparison.

It is worth to underline that, by equation (3), the permeated oxygen flow should increase with the temperature. Anyway, the obtained data suggest that J_{O2} reaches a plateau for LCC2 at about 700÷800°C. Since all the three tests show the same trend, a new rate determining step can cause the observed behaviour. Eq (3) indicates that several parameters influence the overall O_2 flow; since P_h and P_l were steady along the tests time, it is possible that a variation occur to the electrical properties of LCC2. In particular, σ_e (electronic conductivity) can cause the permeation drop.

As mentioned in Chapter 2 about the electric properties of perovskite materials, they can show metallic conductivity, semiconductor-like behaviour or act as an insulating material in relation to their composition.

Since no data are available regarding the electronic conductivity of LCC2 sample, it is possible that it reaches the highest value at 700÷800°C (metallic like behaviour). In this way new investigations are necessaries.

Conclusions

The aim of the present research project is to develop new advanced materials for applications in the intermediate temperature solid oxide fuel cells (IT-SOFCs). This almost new type of fuel cells operates at a slightly lower temperature (500÷700°C) than the common SOFCs (typically 800÷1100°C). The IT-SOFCs are particularly interesting due to longer term stability and the reduced costs thanks to the cheaper materials and procedures for the materials processing.
A reduction in working temperature, however, involves an improvement of the materials used as electrodes and electrolyte.
In the present study, several perovskite based oxide materials have been considered. These particular compounds show a wide range of interesting properties which can be tuned employing different constituting elements and different kinds and amounts of dopant elements.

Taking into account the literature suggestions, two kinds of compounds have been studied. The first type of compounds are lanthanum gallate doped with strontium and iron or copper ($La_{0.8}Sr_{0.2}Ga_{0.8}Fe_{0.2}O_{3-\delta}$, named LSGF and $La_{0.8}Sr_{0.2}Ga_{0.8}Cu_{0.2}O_{3-\delta}$, named LSGC), while the second type derives from lanthanum cuprate ($LaCu_{0.8}Co_{0.2}O_{3-\delta}$, named LCC1 and $La_2Cu_{0.8}Co_{0.2}O_{4-\delta}$, named LCC2):

All the compounds have been synthesized employing two synthetic procedures: the Pechini process and the Polyacrylamide Gel method. In both procedures, the precursors of the elements (usually the metal oxides mineralized with HNO_3) are incorporated in an organic polymer network (polyester citric acid–ethylene glycol for Pechini process,

polyacrylamide in the other case). At high temperatures the organic network decomposes favouring the formation of the perovskite phase.

The obtained catalysts have been fully characterized by means of X-Ray Diffraction (to investigate the crystallographic structure), X-ray Photoelectron Spectroscopy (for an accurate surface characterization) and Diffuse Reflectance Infrared Fourier Transformed spectroscopy (to study the functional groups).
In all cases but LCC1, XRD data reveal the presence, beside the desired one, of minor phases whose amount and typology is influenced by the composition and doping. In the case of LCC1, in contrast, a mixture of $La_2Cu_{0.8}Co_{0.2}O_{4-\delta}$ and CuO was obtained instead of $LaCu_{0.8}Co_{0.2}O_{3-\delta}$. XPS investigation testifies the surface segregation of Sr as carbonate and oxide in LSGF and LSGC and La segregation as oxide and hydroxide. As a general consideration the presence of carbonate species and hydroxyl groups is mainly a surface phenomenon, since DRIFT technique never reveals traces of these functional groups in the bulk material.

The activity of the materials has been investigated in several conditions at various temperatures between RT and 400°C, employing a continuous flow reactor and monitoring the exit stream by IR and QMS. The reaction conditions have been selected to reach a better comprehension of the catalyst reactivity in alcohols oxidation.
The synthesized compounds have firstly investigated with respect to the pure methanol and ethanol vapours. The outcomes suggest that methanol is mainly decomposed into hydrogen and carbon monoxide, while small amounts of carbon dioxide are also detected. It is interesting to observe that minor amounts of intermediate products such as methyl formate and formic acid are also detected as a function of the catalyst and temperature. The copper-containing catalysts (LCC and LSGC samples) promote the formation of methyl formate at 200÷300°C, while at higher temperature the formation of H_2 and CO (from the rapid decomposition of methyl formate) is favourite.
Ethyl alcohol, instead, undergoes mainly dehydrogenation with the formation of acetaldehyde and hydrogen.
The obtained conversion data suggest that the overall decomposition reactions occur only in small amount for all the catalysts.
The second type of catalytic tests have been performed by adding an over stoichometric amount of oxygen to the methanol and ethanol vapours. These conditions are realized to

investigate the ability of the catalysts with respect to the oxidation of the fuel. To be true, the employed conditions do not exactly reproduce the anodic site of a fuel cell, but they allow to better understand the behaviour of the compounds when oxygen is available for the oxidation reactions.

The outcomes clearly indicate that the copper-containing catalysts (LCC and LSGC) show the best performances for the full oxidation of the alcohols; moreover, LCC1 and LCC2 sample show incandescence when investigated at the highest temperature (400°C). Methanol is mainly oxidised to water and carbon dioxide, while minor amounts of partial oxidation products such as hydrogen and carbon monoxide are also present (maybe depending on the test conditions). Ethanol oxidation seems to be slightly more difficult and acetaldehyde is always present as by-product.

Finally, the catalysts have been investigated under steam reforming conditions, by employing an aqueous solution (1 mole·l^{-1}) of the alcohols. These experiments have been performed since most of the direct alcohol fuel cells are fed with aqueous solutions of the fuel. A second important reason concerns the hydrogen production by means of steam reforming of alcohol and hydrocarbons.

All the catalysts promotes the formation of the steam reforming products (hydrogen and carbon dioxide), while carbon monoxide is also present as intermediate product. The catalysts always show a monotone trend with respect to the temperature, reaching their best performances at the highest investigated temperature (400°C). Copper containing samples show, once again, the best activity; LSGF also shows good conversion and H_2 yields values.

Nevertheless, it is necessary to underline that all samples undergo deep poisoning due to un-desorbed carbon-containing species such as reaction intermediates or reaction products.

It is worth to point out that significant differences have been observed between the samples obtained by means of the two different preparation procedures: the results, as a whole, indicate that the samples obtained by Gel procedure show higher activity. This could be related to a wider surface area but further investigations are needed to reach a better comprehension.

The cathodic activity has been investigated by measuring the oxygen permeability throughout the materials pressed as a pellet. The permeation mechanism is specific for O_2 and provides useful information concerning both redox and transport properties (for oxide anions) of the investigated material.
Permeability measurements were carried out employing a home made reactor. This is expressly conceived, realized and optimized during the PhD term. A detailed study concerning the materials (ceramic macor) and fittings has been done (paying particular attention to the pasting of the samples on the ceramic support). The tests have been monitored by means of QMS.
The analysis have been performed at 600, 700 and 800°C on LSGF and LCC2 samples obtained by Pechini method (the samples from the gel method show several disadvantages concerning the realization of the pellets). The obtained outcomes suggest that LCC2 sample is the best material as cathode catalyst.

Summarizing, all the investigated materials show interesting characteristics and significant reactivity. Nevertheless, LCC2 ($La_2Cu_{0.8}Co_{0.2}O_{4-\delta}$) gives the best results both as anode and cathode material whereas LSGF and LSGC seem particularly promising as buffer inter-layers.

Appendix A

Analytical techniques, instruments and data processing

The aim of the work is to develop (synthesize and investigate) new perovskite-like materials for applications as anodes and cathodes in the Intermediate Temperature Solid Oxide Fuel Cells (IT-SOFCs).

To better understand the whole characteristics of the prepared compounds, all the catalysts were investigated by means of the most suitable analytical techniques. In particular, the X-Ray Diffraction (XRD), X-ray Photoelectron Spectroscopy (XPS), Infrared and Diffuse Reflectance Infrared Fourier Transform spectroscopy (IR and DRIFT) and Quadrupolar Mass Spectrometry (QMS) were employed.

Furthermore, the particular behaviour observed for LSGF samples, required a deeper investigation with Mössbauer Spectroscopy, UV-Vis spectroscopy and Temperature Programmed Desorption (TPD).

X-Ray Diffraction (XRD) [111]

Since most of the properties of the perovskite-like compounds are related to their crystal lattice, it is very important to investigate the structure of the synthesized samples. XRD analysis provides qualitative and quantitative information about the crystallographic order in relation to the composition of the sample, the cell parameters and the average size of the crystallites.

Diffraction occurs when a radiation interacts with an object (obstacle) in its path; the phenomenon occurs with any kind of waves (electromagnetic but also sound waves, water waves…). The diffraction is based on the scattering of the waves by an ordered means and its effects are well evident when the distances between the scattering centres are of the same order of magnitude as the wavelength of the radiation. In the case of a crystal lattice, X-rays are required.

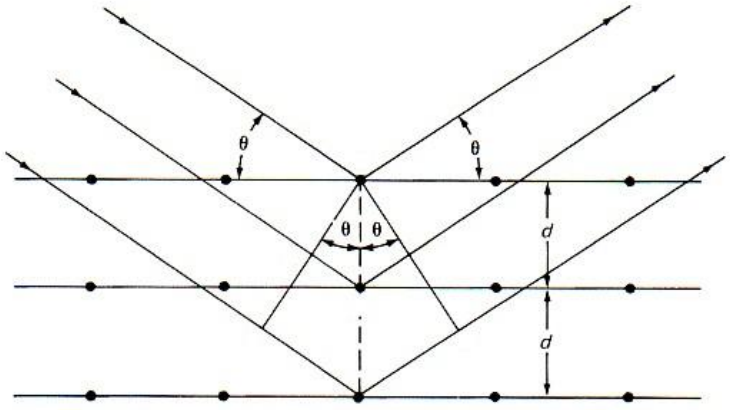

Figure A.1. Diffraction of X-rays by a crystal lattice.

The figure A.1 summarizes the diffraction of the X-rays by a crystal lattice; it can be seen that the X-rays are scattered by the atoms in the lattice. The scattered rays interact and the interactions can be destructive or constructive. The Bragg's law (1) explains the diffraction taking into account the geometric relations for the scattered rays:

$$2dsen\theta = n\lambda \qquad (1)$$

with:

d = distance between the crystallographic planes

θ = angle of incidence

n = diffraction order
λ = X-rays wavelength

The scattered rays can give constructive interaction only if their paths differ for an integer number of wavelengths.

Concerning the LSGF samples the phase compositions and the crystallite sizes of the powders were determined with great accuracy by Rietveld's powder structure refinement analysis of XRD data, by using the MAUD (Material Analysis Using Diffraction) software. [112] The required crystallographic data were taken from ICSD (Inorganic Crystal Structure Database, v. 2007, Fachinformationszentrum, Karlsruhe, Germany).

A typical XRD spectrum shows the intensities of the diffraction signals versus the angle 2θ. The identification of a particular crystallographic phase is carried out by comparison between the obtained spectrum and a reference (in this case from JCPDS: Joint Committee on Powder Diffraction Standards).
The analysis were performed by means of a Bruker D8 Advance diffractometer with Bragg-Brentano geometry using a Cu Kα radiation (40 V, 40 mA, λ = 0.154 nm).

X-ray Photoelectron Spectroscopy (XPS)

X-ray Photoelectron Spectroscopy (XPS), belongs to the wide family of the surface characterization methods based on the detailed energy studies of the electrons emitted from a sample surface into ultra-high vacuum environment. XPS is a highly surface specific technique which provides important information in relation to the chemical state of the elements (valence state and type of chemical surround) and the composition (relative composition) of the surface.
XPS is known to be a surface specific spectroscopic technique due to the escape depth of the emitted photoelectron. Although X-Rays can penetrate the sample for several mm, the measured photoelectron signal originates from a surface depth not more than ~50Å, due to the inelastic scattering of the emitted electrons within the sample.

The XPS analyses are very important since the characteristics of the surface can heavily differ from the bulk. In this work, furthermore, the prepared compounds are employed as heterogeneous catalysts for the oxidation of the methanol and ethanol and the reduction of oxygen. It is well known that the surfaces of a heterogeneous catalyst play a key role, and then, their investigation can help the explanation of the reaction mechanisms.

This spectroscopy is based on the photoelectric effect discovered by Hertz in 1887 [113] and mathematically justified by Einstein in 1905 [114]: when a material is hit by photons with an energy greater than the binding energy of the electrons, there is a certain probability that a photon is absorbed and an electron is expelled (figure A.2).

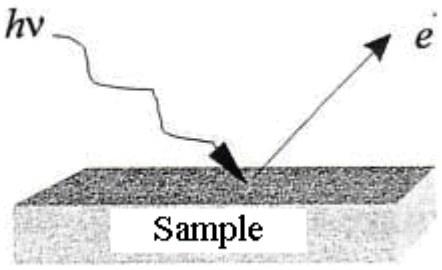

Figure A.2. Schematic view of the photoemission process.

For an atom in gas phase, the kinetic energy (*KE*) of the emitted photoelectron is given, in the monoelectronic approximation, by the Einstein equation (2):

$$KE = h\nu - BE \qquad (2)$$

where hυ is the energy of the incident photon, *BE* the binding energy of the electron, referred to the vacuum level, and *KE* the kinetic energy of the expelled electron. A schematic description of the process is reported in figure A.2. As already noted, in gas-phase spectroscopy *BE* is equal to the ionisation energy (Koopmans' approximation), whereas in solid-phase it is more convenient to refer to the Fermi level and the energetic balance become (3):

$$KE = h\nu - BE - \phi \qquad (3)$$

where Φ is a correcting factor representing the work function. In this case the work function takes into account not only the energy necessary to remove an electron from the highest occupied energy level in the solid (the "Fermi level"), to the "vacuum level" but also the electrostatic environment in which the electron is generated and measured and some instrumental correction factors.

The work function characteristic of the materials can be altered by changes in the chemistry and composition of the surface.

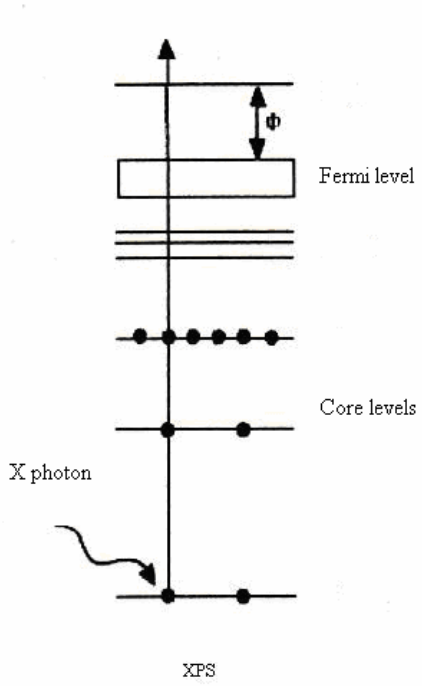

Figure A.3. Schematic view of the XPS process.

Figure A.3 shows a schematic view of the XPS process. Since each energy level is quantized, there is a characteristic binding energy associated with each core orbital for each element. This important statement allows to associate a particular XPS peak to a well defined element. Furthermore, the intensity of the peak is related to the concentration of the element in the sample surface.

It is interesting to underline that the observed binding energies also depend on the oxidation state and on the chemical environment. Changes in these aspects give rise to small shifts in the peak position (the so-called chemical shifts).

During the photoionization process, holes are formed in the core levels. They can decay through a recombination with an electron coming from higher energy states according to two distinct and competitive processes (figure A.4): Auger emission, in which the

excess energy is released to an electron (Auger electron), which is emitted (non radiative decay, figure A.4a) or X-ray fluorescence, in which the excess energy is emitted as photons (radiative decay, figure A.4b).

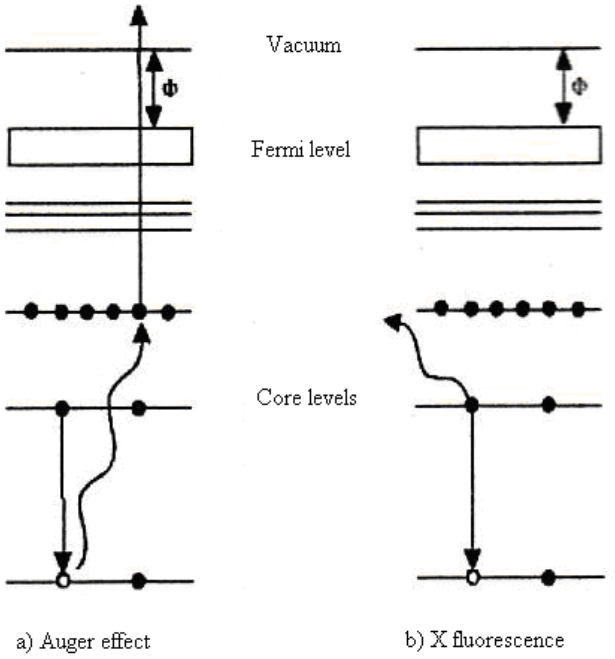

Figure A.4. Decay processes for a hole (white circles) created in a core level. a) Auger effect, b) X fluorescence.

Noteworthy, the KE of the Auger electrons only depend on the energies of the involved levels (characteristics for each element and for the valence state); this allows to distinguish Auger electrons from photoelectrons because of the independence of their kinetic energy upon the photon energy.

Description of the XP spectra

A typical XP spectrum appears as a graph showing the intensities of the XP peaks versus the binding energies (figure A.5). The background increases because of the inelastic scattering of the photoelectrons.

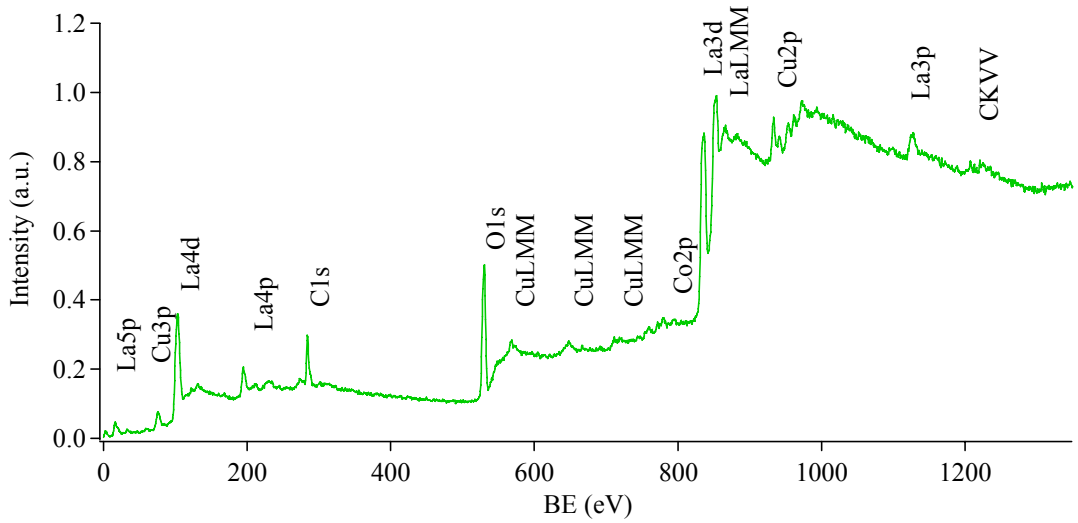

Figure A.5. Example for a typical extended XP spectrum.

In the spectrum are well evident the peaks due to the photoelectrons from the core levels (La5p, Cu3p, C1s…) and the Auger peaks (CuLMM, CKVV…): the so-called "primary structure" of the spectrum. The photoelectron peaks are labelled taking into account the level occupied by the ejected electron, while for the Auger electrons, the levels involved in the decay are mentioned. Beside the primary structure, more detailed information can be obtained by means of a deeper investigation of the positions and the shapes of the photoelectronic peaks. The "secondary structure" involves the less intense peaks arising from X-ray source (satellite peaks or ghost peaks, due to the non monochromaticity of the source or to its contamination, respectively) or from multi-electronic processes such as shake-up, shake-off peaks or peaks from multiplet splitting. Shake-up and shake-off peaks arise from the interaction of the photoelectron with the valence shell electrons, while multiplet splitting occurs when unpaired electrons are present.

It is worth to underline that charging effects can affect the measurements. Insulating materials acquire a surface charge, under X-ray bombardment. The positive charge causes the electrons emitted from the sample to lose kinetic energy and to appear at higher binding energies. Since carbon is the most commonly detected element in contamination layers and its 1s photoelectrons have a known binding energy of 285.0 eV, it is used for referencing purposes. The difference between the measured position of C1s photoelectrons in the energy spectrum and the above value gives the charging value.

Finally, an XPS analyses allows to determinate the relative amounts of the elements present in the surface of the sample.

In general, beside the sample specific features (composition, differential cross-section, probability for no-loss escape) the photoelectron peak intensity depends on several instrumental characteristics (X-ray flux, acceptance solid angle of electron analyzer, instrumental detction efficiency) and thus only relative intensity measurements are significant. [115]

The XPS investigations in this work were carried out with a Perkin Elmer Φ 5600ci Multi Technique System with a double anode as X-ray source (Mg – Al).
The instrument is shown schematically in figure A.6. It consists of an X-ray source with magnesium and aluminium anodes, a sample chamber, a detection system (hemispherical analyzer), an ion source for sputtering and a pumping system.

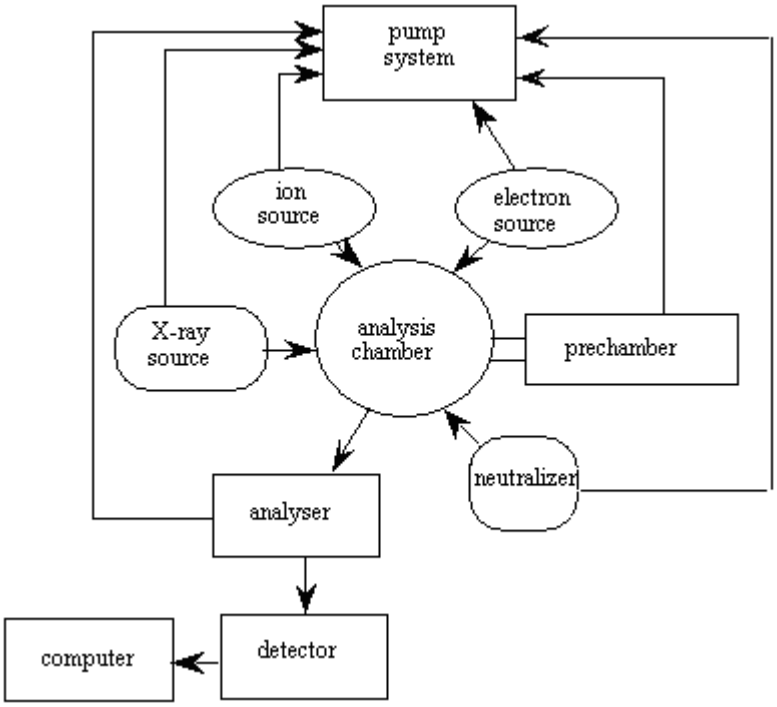

Figure A.6. Perkin Elmer Φ 5600ci Multi Technique System.

It is worth to underline that every instrument device is connected to the vacuum pump system. The XPS analysis must be performed under Ultra High Vacuum (UHV) for two reasons. Firstly, the photoelectrons mean free path has to be sufficiently long to minimize the inelastic scattering. For this purpose a vacuum of $10^{-1} \div 10^{-2}$ Pa is sufficient. The requirement for an ultra high vacuum level arises from the nature of the technique itself, which is very sensitive to surface contamination. This condition is fulfilled at $10^{-6} \div 10^{-7}$ Pa.

The spectrometer was calibrated by assuming the binding energy (BE) of the Au $4f_{7/2}$ line to be 84.0 eV with respect to the Fermi level. Extended spectra (survey) were collected (187.85 eV pass energy, 0.4 eV·step^{-1}, 0.05 s·step^{-1}). Detailed spectra were also recorded (11.75 eV pass energy, 0.1 eV·step^{-1}, 0.1 s·step^{-1}). The standard deviation in the BE values of the XPS line is 0.10 eV. The atomic percentage, after a Shirley type background subtraction, [116] was evaluated by using the PHI sensitivity factors. [63]
Fitting procedures were carried out by means of Voight functions.

Infrared and Diffuse Reflectance Infrared Fourier Transform spectroscopy (IR and DRIFT) [111, 117, 118]

Spectroscopic analysis carried out by means of infrared radiation provides important information about chemical bonds and geometric properties of the investigated molecules.
IR measurements on solid samples are usually carried out by means of dispersing agents such as nujol or KBr pellets. Nevertheless, these common ways are unusable for the investigation of the activity of the samples with respect to probe molecules (methanol and ethanol for example).
The Diffuse Reflectance Infrared Fourier Transform (DRIFT) spectroscopy can usefully be employed for the study of the catalytic activity of the synthesized samples. With this technique, the compound can be directly analyzed as a powder, without further treatments which can modify its surface (and then its reactivity).
In the DRIFT technique the intensity of the reflected radiation by the sample is measured. The incident radiation can be reflected in a mirror-like way (the reflection angle is equal to the incidence angle) or diffuse in many directions as shown in figure A.7. The diffusion of the radiation prevails if the dimensions of the particles are of the same order of magnitude as the wavelength of the incident radiation. Otherwise, the specular reflection is preferred.

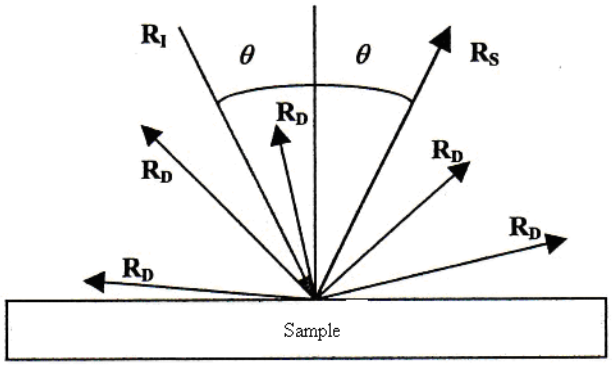

Figure A.7. Schematic representation of the specular and diffuse reflectance by a solid sample. R_I identifies the incident radiation, R_S the specular reflected radiation, and R_D the diffused radiation.

The interpretation of the signals obtained in these kinds of measurements is based on the Kubelka-Munk theory. The Kubelka-Munk (K-M) function, $f(R\infty)$, is defined as:

$$f(R_\infty) = \frac{(1-R_\infty)^2}{2R_\infty} = \frac{k}{s}$$

Where R_∞ is the reflectance of a layer with infinite thickness. The K-M function is proportional to the absorption coefficient, k ($k = 2.303 \cdot \varepsilon \cdot c$ with ε molar absorption coefficient and c molar concentration), and inversely proportional to the scattering factor, s.

The IR spectra were collected in a Bruker Tensor 27 spectrophotometer (with a Globar source and DTGS detector) accumulating 32 scans at a resolution of 4 cm^{-1} for the measurements in reflectance mode, and 32 scans at a resolution of 1 cm^{-1} for the measurements in trasmittance mode.

Quadrupolar Mass Spectrometry (QMS) [111]

Mass spectrometry is a powerful analytical technique widely employed in many areas. A mass analysis provides important information about qualitative and quantitative composition of samples, structures of molecules and isotopic ratios. A mass spectrometer converts the sample (gases, liquids or solids) into gaseous ions and then separates them with respect to their mass/charge ratios.

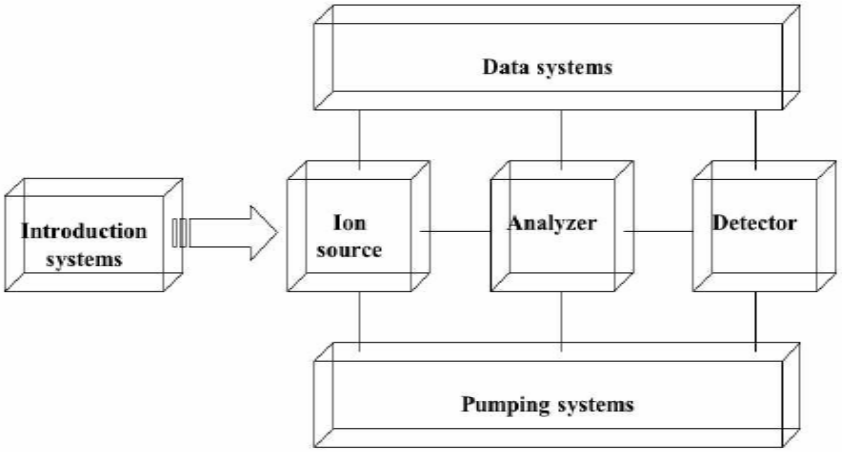

Figure A.8. Schematic view of the components of a typical mass spectrometer.

Figure A.8 shows a simplified scheme of the components for a typical mass spectrometer. The analyzed sample is introduced in the instrument by an introduction chamber and then it is converted into gaseous ion. In the present case a quadrupolar mass spectrometer is used and thus gases are investigated.

The ionization procedures can be various and depend on the analyzed samples. A common ionization technique is the EI (electronic impact): an electronic beam hits the sample producing various kinds of charge fragments. The produced ions pass through the mass analyzer where they are separated with respect to their mass/charge (m/z) ratios. The mass analyzer is a very important constituent of the mass spectrometer since its characteristics affect the resolution (ability to separate fragments with similar m/z) of the whole instrument. Quadrupolar mass filter is a common and useful mass analyzer. In this device, the fragments are deviated by a variable electric field generated by four polarized bars. In this manner, only the fragments with a suitable m/z reach the mass detector. The mass detector is a device which converts the signals from ion current into electric current and it usually is an electrons multiplier or a Faraday cup.

It is interesting to point out that the ion source, the analyzer and the detector are in a high vacuum environment. This is necessary to obtain good resolutions, since residual gaseous molecules into the analytical chamber could interfere with the analyzed samples.

QMS data were obtained by means of a System Genesys I 200D by European Spectrometry Systems equipped with a electronic impact source, a quadrupolar filter and a dual detector with a Faraday cup and electronic multiplier.

QMS data processing

In this work, the mass spectrometry is employed to analyze the gaseous mixture from the reactor. The reaction products and the un-reacted reactants are simultaneously analyzed by FTIR and QMS to better identify their composition.
It is now necessary to point out that the fragmentation pattern for a specific compound strongly depends on the used instrument. In order to obtain the fragmentation patterns for the employed substances, each compound was analyzed separately. This operation allows to identify the most intense fragment for each compound and to employ it for a more accurate quantitative analyses. Another very important aspect is related to the possible interferences, for a same fragment, from various compounds. For example, the fragment with m/z = 16 can arise from O_2 but also from CH_4 or H_2O etc. The accurate knowledge of the fragmentation patterns allows to calculate the correct contribution for a specific mass and avoid an overestimation of the analyzed compound.
Consistently, the following fragments have been monitored to better understand the composition of the reaction products: 2, 14, 15, 16, 17, 18, 20, 27, 28, 29, 31, 32, 40, 44, 45, 46 and 60.
In order to quantify the main reaction products in the activity tests, pure CO, CO_2 and 5% H_2/Ar were employed to create the calibration curves. Taking into account the instrument characteristics and the operative conditions, the uncertainty for the determined values for conversions and yields can be assumed to be 1%.

The row QMS data, obtained from the activity tests, were carefully analyzed in order to eliminate the multi-contributions from each fragment. The intensities of the "cleaned" fragments were employed for the quantitative determination of the conversions of the reactants and the yields of the main products (H_2, CO and CO_2).
Furthermore, only for a qualitative illustration of the data and for a better comparison, the intensities of the analyzed fragments were normalized with respect to the intensity of the fuel (methanol or ethanol).
It is worth to point out that the amount of the fuel affects the appearance of the data. In detail, the trends observed for the tests can be directly compared only if the amount if the fuel is about the same (table B.2, appendix B). For this reason, the outcomes from the activity tests with methanol and methanol/O_2 can be compared for the various catalysts, and so those from the tests with ethanol and ethanol/O_2. The trends observed

for the tests in steam reforming conditions show more intense signals for the reaction products because the less amount of fuel (the denominator in the normalization procedure) in the feed stream.

Mössbauer spectroscopy, [119] UV-Vis spectroscopy and Thermal Programmed Desorption

Mössbauer, UV-Vis spectroscopy and Thermal programmed desorption (TPD) were employed as additional techniques in the study of the LSGF sample (Chapter 5). Since their use is limited, they are here only briefly described.

Mössbauer-Effect Spectroscopy, commonly called Mössbauer Spectroscopy, is a very powerful nuclear technique based on the Mössbauer Effect, which is the resonant absorption, by a certain nucleus called absorber, of γ-rays emitted without recoil from another nucleus called emitter. The technique is isotope specific and the effect arises from a certain isotope of a particular element; the most suitable isotope for the Mössbauer spectroscopy is ^{57}Fe. A Mössbauer analyses provides information about the interaction of the nucleus and its environment, thus information about the electron density, the symmetry of the examined nucleus are easily accessible.

In a transmission experiment, the gamma radiation passes through the absorber, where they are partially absorbed, and then enter into the detector. As the electron density at the nucleus affects the energy levels of the emitting and absorbing nuclei, it is necessary to modulate the γ-rays energy to have a resonant absorption. This is usually accomplished by moving the source relative to a stationary absorber giving the γ-rays an energy shift as a result of the first-order Doppler effect. The resulting Mössbauer spectrum consists in a plot of gamma ray relative absorption (or transmission, or counts) against the velocity of the source with respect to the absorber.

Mössbauer spectroscopy analyses (MS) were performed on a conventional constant-acceleration spectrometer, with a room temperature Rh matrix ^{57}Co source (nominal strength 1850 MBq). The hyperfine parameters isomer shift (δ), quadrupole splitting (Δ) or quadrupole shift when magnetic splitting occurred (ε), full linewidth at half maximum (Γ), expressed in mm/s, were obtained by means of standard least-squares minimization techniques. The spectra were fitted to Lorentzian line shapes with the minimum number of sextets and doublets. It was assumed that, in all the spectra, each

hyperfine parameter was affected by the same error, postulated as the maximum error over all measurements. The hyperfine field distribution emphasizes relaxation processes and particle size and/or crystallinity effects. A deviance of ± 0.03 mm/s from the obtained value was assigned to δ, Δ and Γ. and ± 5 % to A. Isomer shift is quoted relative to metallic iron at room temperature. Low-temperature spectra were collected by an ARS® closed circuit cryostat. The spectra were collected between 298K (RT) and 11K.

In a Temperature Programmed Desorption, the residual gas present in the UHV chamber is analysed by means of a Quadrupolar Mass Spectrometer, while the sample is heated up. As the temperature rises, the thermal energy given to the system will stimulate the desorption of absorbed species that will be detected as an increase in partial pressure for a certain mass. This results in a peak in the mass versus temperature plot. The temperature of the peak maximum provides information on the binding energy of the bound species. The peak area gives an indication on the amount of species desorbed.

The TPD analyses were performed with HIDEN HAL 301 PIC mass detector installed in a home made UHV chamber. The samples were supported on a copper sample holder and heated at $1.5°C \cdot s^{-1}$.

UV-Vis spectroscopy is a well note technique and will not be further explained here. The measurements were performed with a CARY 5E UV-Vis-NIR spectrophotometer by Varian in reflectance mode. The spectra were collected from 200 to 800 nm.

Appendix B

Experimental set-up and catalytic test conditions

The activity tests were always performed under strictly controlled conditions; this allows to compare the outcomes from the investigated catalysts and to calculate the conversions of the reactants and the yields for the main reaction products.

Chemisorption tests

The chemisorption tests were performed by means of DRIFT spectroscopy.
Prior to each experiment, ca. 50 mg of the sample was loaded in the sample cup of a low-temperature reaction chamber (CHC) installed in the Praying Mantis accessory for diffuse reflectance infrared spectroscopy (Harrick Scientific Corporation) and fitted with ZnSe windows (figure B.1). The temperature of the powder was checked by means of a thermocouple inserted into the sample holder directly in contact with the powder. Before measurements, the powder was kept in Argon flow to eliminate water traces until a stable IR spectrum was obtained (about 2 h).

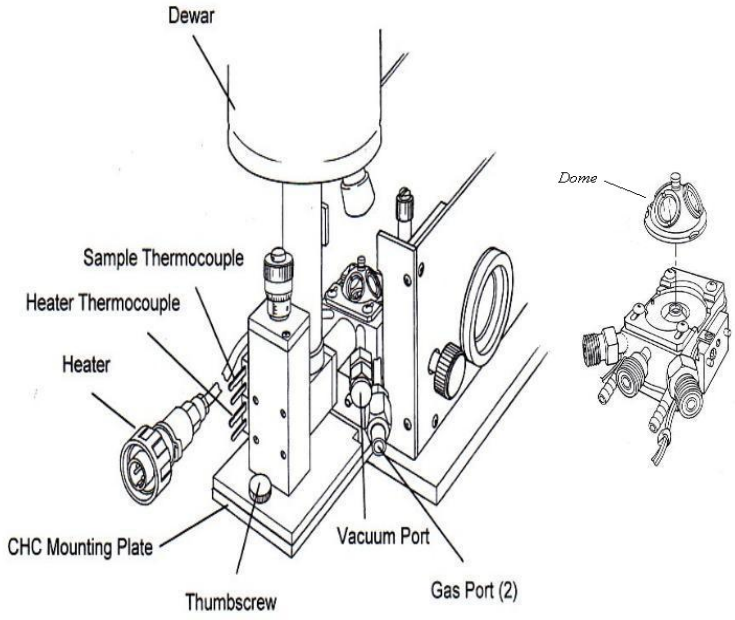

Figure B.1. Representation of the CHC chamber. On the right a detail of the analytical chamber.

The reactive species (methanol and ethanol vapours) were carried into the CHC chamber by means of an Argon flow (50 $cm^3 \cdot min^{-1}$). For each measurement, methanol or ethanol vapours were left to flow (carried by Ar) for 1 minute, then the IR spectrum was collected. Finally, the CHC chamber was evacuated for 5 minutes with pure Ar and a new spectrum was collected.

Activity tests

The activity tests were performed by means of a home made reactor and monitored by FTIR and QMS. Figure B.2 schematizes the experimental set-up.

In each test, vapours of pure methanol, ethanol or 1M solution of the alcohols were carried by a gas (pure argon or mixture argon/oxygen) from the bubbler to the tubular glass reactor. The bubbler temperature was set at 15°C. The reaction products and the un-reacted reactants reached then the FTIR and QMS for the analysis. The carrier flow was controlled by a MKS-mass flow controller (table B.1 summarizes the carrier flows for each test condition). Repeated measures were carried out at each temperature to confirm the observed results. Moreover, at each temperature (RT, 100, 200, 250, 300, 350 and 400°C), the reaction was followed as a function of time.

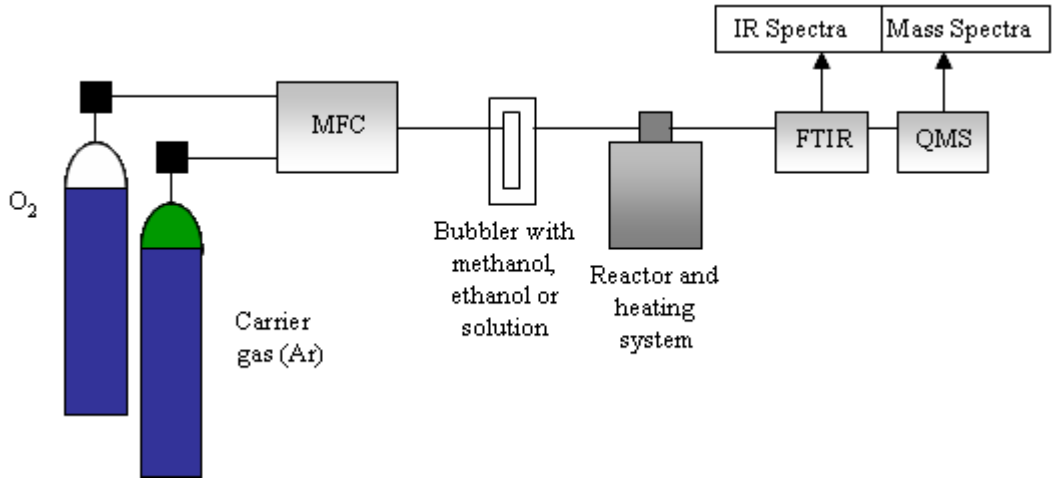

Figure B.2. Simplified scheme of the experimental set-up employed in the activity tests (MFC = mass flow controller).

Table B.1. Gas flows employed in the activity tests.

Test conditions →	methanol/ethanol	methanol/O_2	ethanol/O_2	methanol/ethanol 1M
Flows ($cm^3 \cdot min^{-1}$)				
Argon	65	65	64	130
Oxygen	-	10	11	-

The described conditions allow to determinate the characteristics of the feed streams. The amounts of the reactants were calculated taking into account the Weight Hourly Space Velocity (WHSV), which is defined as (1):

$$WHSV = (amount\ of\ reactant) \cdot (amount\ of\ catalyst)^{-1} \cdot h^{-1} \quad (1)$$

The amount of the catalyst was always 40 mg. Table B.2 summarizes the feed stream conditions.

Table B.2. Weight Hourly Space Velocity (WHSV) values employed in the catalytic tests.

Test conditions	WHSV (h^{-1})
pure methanol	20
methanol/O_2	21
methanol 1M	2
pure ethanol	13
ethanol/O_2	14
ethanol 1M	2

It is worth to point out that the determination of the conversion and yields values is affected by the WHSV. The conversions of reactants and the yields of the products are

calculated (taking into account the equation 2), as shown in the following equations (3) and (4):

$$n_a A \rightarrow n_b B \tag{2}$$

$$Conversion_A = \frac{a_0 - a_f}{a_0} \cdot 100 \tag{3}$$

$$Yield_B = \frac{\frac{n_a}{n_b} \cdot \left(b_f - b_0\right)}{a_0} \cdot 100 \tag{4}$$

Where:

A, B = reactant, product

n_a, n_b = stoichiometric coefficients

a_0, a_f = number of moles of A at the beginning and at the end of the reaction

b_0, b_f = number of moles of B at the beginning and at the end of the reaction

From the equations (3) and (4), it is clear that the conversion and the yield appear lower if higher amount of reactant is used and an equal number of b_f are produced.

Table B.3 summarizes the characteristics of the reactants, gases and gas mixtures employed in the catalytic tests.

Table B.3. Specifics of the reactants, gases and gas mixtures used in the catalytic tests.

Reactant	Purity (%)	Supplier
methyl alcohol anhydrous		Carlo Erba
ethyl alcohol absolute anhydrous		Carlo Erba
Gases and gas mixtures		
Argon Alphagaz 2	99.9999	Air Liquide
Oxygen Alphagaz 2	99.9999	Air Liquide
Carbon monoxide	99.97	Air Liquide
Carbon dioxide	99.998	Air Liquide
Nitrogen (80%)-Oxygen (20%)	99.999	Air Liquide
Hydrogen (5%)-Argon (95%)	99.9999	Air Liquide

References:

[1] K. Weissermel, H.J. Arpe industrial organic chemistry III Ed. VCH, **1997**

[2] Ullmann's Encyclopaedia of the Chemical Technology V Ed, VCH, Weinheim, **1998**

[3] Carrette, L., Friedrich, K.A., Stimming, U.; *ChemPhysChem*, **2000**, 1, 162

[4] Haile, S.M.; Acta Mater., **2003**, 51, 5981

[5] Weber, A., Ivers-Tiffée, E.; *J. Power Sources*, **2004**, 127, 273

[6] Steele, B.C.H.; *Solid State Ionics*, **2000**, 134, 3

[7] Ni, M., Leung, M.K.H., Leung, D.Y.C., Sumathy, k.; *Renew. Sust. Energ. Rev.*, **2007**, 11, 401

[8] Aroutiounian, V.M., Arakelyan, V.M., Shahnazaryan, G.E.; *Sol. Energy*, **2005**, 78, 581

[9] Mor, G.K., Varghese, O.K., Paulose, M., Shankar, K., Grimes, C.A.; *Sol. Energy Mater. Sol. Cells*, **2006**, 90, 2011

[10] Esper, B., Badura, A., Rogner, M.; *Trend in plant science*, **2006**, 11, 543

[11] Rupprecht, J., Hankamer, B., Mussgnug, J.H., Ananyev, G., Dismukes, C., Kruse, O.; *Appl. Microbiol. Biotechnol.*, **2006**, 72, 442

[12] Palo, D.R., Dagle, R.A., Holladay, J.D.; *Chem. Rev.*, **2007**, 107, 3992

[13] McIntosh, S., Gorte, R.; *Chem. Rev.*, **2004**, 104, 4845

[14] Dilara, P.A., Vohs, J.M.; *J. Phys. Chem.*, **1993**, 97, 1919

[15] Winter, M.; Brodd, R.J.; *Chem. Rev.*, **2004**, 104, 4245

[16] Liu, J., Madsen B.D., Ji, Z., Barnett, S.A.; *Electrochem Solid-State Lett.*, **2002**, 5, A122

[17] Murray, E.P., Tsai, T., Barnett, S.A.; *Nature*, **1999**, 400, 649

[18] Liu, J., Barnett, S.A.; *Solid State Ionics*, **2003**, 158, 11

[19] Adler, S.B.; *Chem. Rew.*, **2004**, 104, 4791

[20] Maffei, N., Pelletier, L., McFarlan, A.; *J. Power Sources*, **2004**, 136, 24

[21] Stover, D., Buchkremer, H.P., Uhlenbruck, S.; *Ceram. Int.*, **2004**, 30, 1107

[22] Hrovat, M., Ahmad-Khanlou, A., Samardzija, Z., Hole, J.; *Mat. Res. Bull.*, **1999**, 34, 2027

[23] Bi, Z., Yi, B., Wang, Z., Dong, Y., Wu, H., She, Y, Cheng, M.; *J. Electrochem. Soc.*, **2004**, 7, A105

[24] Kharton, V.V., Marques, F.M.B., Atkinson A.; *Solid State Ionics*, **2004**, 174, 135

[25] Yamaji, K., Horita, T., Ishikawa, M., Sakai, N., Yokokawa, H.; *Solid State Ionics*, **1998**, 108, 415

[26] Huang, K., Goodenough, J.B.; *J. Alloy Compd.*, **2000**, 303, 454

[27] Fierro, J.L.G., Pena, M.A.; *Chem. Rev.*, **2001**, 101, 1981

[28] Zheng, F., Bordia, R.K., Pederson, L.R.; *Mat. Res. Bull.*, **2004**, 39, 141

[29] Ishihara, T., Yamada, T., Arikawa, H., Nishiguchi, H., Takita, Y.; *Solid State Ionics*, **2000**, 135, 631

[30] Raghuveer, V., Ravindranathan Thampi K., Xanthopoulos, N., Mathieu, H.J., Viswanathan, B.; *Solid State Ionics*, **2001**, 140, 263

[31] Raghuveer, V., Viswanathan, B.; *Fuel*, **2002**, 81, 2191

[32] Yu, H.C., Fung, K.Z., Guo, T.C., Chang, W.L.; *Electrochim. Acta*, **2004**, 50, 811

[33] Sin, A., Oldier, P.; *Adv. Mat.*, **2000**, 12, 649

[34] Malavasi, L; Mozzati, M.C.; Polizzi, S.; Azzoni, C.B.; Flor, G.; *Chem. Mater.*, **2003**, 15, 5036

[35] Douy, A. Int. J. *Inorg. Mater.*, **2001**, 3, 699

[36] Huang, K.; Goodenough, J.B.; *J. Solid State Chem.*, **1998**, 136, 274

[37] Jin, W.; Li, S.; Huang, P.; Xu, N., Shi, J.; *J. Membr. Sci.*, **2000**, 170, 9

[38] Galenda, A., Natile, M.M., Krishnan, V., Bertagnolli, H., Glisenti, A.; *Chem. Mater.*, **2007**, 19, 2796

[39] Karppinen, M., Yamauchi, H., Suematsu, H., Isawa, K., Nagano, M., Itti, R., Fukunaga, O.; *J. Solid State Chem.*, **1997**, 130, 213

[40] Falcon, H., Martinez-Lope, M.J., Alonso, J.A., Fierro, J.L.G., *Appl. Cat., B*, **2000**, 26, 131

[41] Darracq, S., Kang, S.G., Choy, J.H., Demazeau, G.; *J. Solid State Chem.*, **1995**, 114, 88

[42] http://srdata.nist.gov

[43] McIntyre, N.S., Cook, M.G.; *Anal. Chem.*, **1975**, 47, 2208

[44] Shkerin, S.N., Kuznetsov, M.V., Kalashnikova, N.A.; *Russ. J. Electrochem.*, **2003**, 39, 591

[45] Zhu, Y., Tan, R., Yi, T., Gao, S., Yan, C., Cao, L.; *J. Alloy Comp.*, **2000**, 311, 16

[46] Dai, H.X., Ng, C.F., Au, C.T.; *J. Catal.*, **2001**, 197, 251

[47] Bocquet, A.E., Chalker, P., Dobson, J.F., Healy, P.C., Myhra, S., Thompson, J.G.; *Physica C*, **1989**, 160, 252

[48] Saitoh, T., Mizokawa, T., Bocquet, A.E., Namatame, H., Fujimori, A., Takeda, T., Takano, M.; *Surf. Sci. Spectra*, **1999**, 6, 294

[49] Bernal, S., Botana, F.J., Garcia, R., Rodriguez-Izquierdo, J.M.; *Reactivity of Solids*, **1987**, 4, 23

[50] Milt, V.G., Spretz, R., Ulla, M.A., Lombardo, E.A., Fierro, J.L.G.; *Catal. Lett.*, **1996**, 42, 57

[51] Yang, R., Zhang, Y., Iwama, Y., Tsubaki, N.; *Appl. Catal., A*, **2005**, 288, 126

[52] Rodriguez-Ramos, I., Guerrero-Ruiz, A., Rojas, M.L., Fierro, J.L.G.; *Appl. Catal.*, **1991**, 68, 217

[53] Laosiripojana, N., Assabumrungrat, S.; *Chem. Eng. Sci.*, **2006**, 61, 2540

[54] Royer, S., Berubè, F., Kiliaguine, S.; *Appl. Catal., A*, **2005**, 282, 273

[55] Lisi, L., Bagnasco, G., Ciambelli, P., De Rossi, S., Porta, P., Russo, G., Turco, M., *J. Solid State Chem*, **1999**, 146, 176

[56] De Asha, A.M., Nix, R.M.; *J Chem Soc Faraday Trans.*, **1995**, 91, 3611

[57] Auroux, A.; Gervasini, A. *J. Phys. Chem.* **1990**, 9*4*, 6371

[58] Rethwisch, D. G.; Dumesic, J. A. *Langmuir* **1986**, 1-2, 73

[59] Lavalley, J. C. *Trends Phys. Chem.* **1991**, 2, 305

[60] Martin, D.; Duprez, D. J. Mol. Catal. A: Chem. **1997**, 118, 113

[61] Lombardo, E.A., Tanaka, K., Toyoshima, I.; J. Catal., **1983**, 80, 340

[62] Wagner, C.D. In *Practical Surface Analysis*; Briggs, D., Seah, M. P., Eds.; Wiley: New York, **1983**

[63] Moulder, J.F., Stickle, W.F., Sobol, P.E., Bomben, K.D.; *Handbook of X-ray Photoelectron Spectroscopy*; Chastain, J., Ed.; Physical Electronics: Eden Prairie, MN, 1992.

[64] McCabe, R.W., Mitchell, P.J.; *Ind. Eng. Chem. Prod. Res. Dev.*, **1984**, 23, 196

[65] Domok, M., Tòth, M., Rasko, J., Erdohelyi, A.; *Appl. Catal., B*, **2007**, 69, 262

[66] Erdohelyi, A., Rasko, J., Kecsk[s, T., Tòth, M., Domok, M., Baàn, K.; *Catal. Today*, **2006**, 116, 367

[67] Laosiripojana, N., Assabumrungrat, S.; *J. Power Sources*, **2007**, 163, 943

[68] Yee, A., Morrison, S.J., Idriss, H.; *J. Catal.*, **1999**, 186, 279

[69] Golay, S., Doepper, R., Renken, A.; *Appl. Catal., A*, **1998**, 172, 97

[70] Rasko, J., Hancz, A., Erdohelyi, A.; *Appl. Catal. A*, **2004**, 269, 13

[71] Morpurgo, F.; tesi di laurea, *Effetto del drogaggio sulla reattività del manganato di lantanio nell'ossidazione dell'etanolo*, Università degli Studi di Padova, A.A. 2006-07, Relatore Dr. Antonella Glisenti

[72] Zecchina, A., Scarano, D., Bordiga, S., Spoto, G.; Advances in Catalisys, **2001**, 46, 265 and references therein.

[73] Jiang, C.J., Trimm, D.L., Wainwright, M.S., Cant, N.W.; *Appl. Catal., A,* **1993**, 97, 145

[74] Llorca, J., Homs, N., Ramirez de la Piscina, P.; *J. Catal.*, **2004**, 227, 556

[75] Velu S., Suzuki, K., Vijayaray, M., Barman, S., Gopinath, C.; *Appl. Catal., B,* **2005**, 55, 287

[76] Collins, S.E., Baltanas, M.A:, Bonivardi, A.L.; *J. Phys. Chem. B,* **2006**, 110, 5498

[77] Bolis, V., Magnacca, G., Cerrato, G., Morterra, C.; *Thermochim. Acta*, **2001**, 379, 147

[78] Manoilova, O.V., Podkolzin, S.G., Tope, B., Lercher, J., Stangland, E.E., Goupil, J.M., Weckhuysen, B.M. *J. Phys. Chem. B,* **2004**, 108, 15770

[79] van der Heijden, A.W.A.M., Belliere, V., Alonso, L.E., Daturi, M., Manoilova, O.V., Weckhuysen, B.M.; *J. Phys. Chem. B,* **2005**, 109, 23993

[80] Ferri, D., Forni, L.; *Appl. Catal. B,* **1998**, 16, 119

[81] Royer, S., Duprez, D., Kaliaguine, S.; *J. Catal.*, **2005**, 234, 364

[82] Fadley, C.S.; *Progress in Surface Science*, **1984**, 16, 275

[83] Tsuruta, Y., Todaka, T., Nisiguchi, H., Ishihara, T., Takita, Y.; *J. Electrochem. Soc.*, **2001**, 4, E13

[84] Yuenyongchaiwat, J., Tantayanon, S., Lou, J., Ma, Y.H.; *J. Mater. Sci.*, **2004**, 39, 7067

[85] Leonidov, I.A., Kozhevnikov, V.L., Mitberg, E.B., Patrakeev, M.V., Kharton, V.V., Marques, F.M.B.; *J. Mater Chem.*, **2001**, 11, 1201

[86] Kharton V.V., Shaulo, A.L., Viskup, A.P., Avdeev, M., Kurbakov, A.I., Naumovich, E.N., Marques, F.M.B.; *Solid State Ionics*, **2002**, 150, 229

[87] Kozhukharov, V. Machkova, M., Ivanov, P., Bouwmeester, H. J. M., van Doorn, R.; *J. Mater. Sci. Lett.*, **1996**, 15, 1727

[88] Tabata, K, Kohiki, S.; *J. Mater. Sci. Lett.*, **1987**, 9, 1030

[89] van Doveren, H., Verhoeven, J.A.T.; *J. Electron Spectrosc. Relat. Phenom.*, **1980**, 21, 265

[90] Measures carry out in our laboratory on a $SrCO_3$ powder (Aldrich 99.9+%)

[91] Polini, R., Falsetti, A., Traversa, E., Schaf, O., Knauth, P.; *J. Eur. Cer. Soc.*, **2007,** 27, 4291

[92] Galenda, A., Natile, M.M., Glisenti, A.; *Surf. Sci. Spectra*, **2006**, 13, 31

[93] Tsyganenko, A.A., Filimonov, V.N.; *J. Mol. Struct.*, **1973**, 19, 579

[94] Chen, W, Wen, T., Nie, H., Zheng, R.; *Mat. Res. Bull.*, **2003**, 38, 1319

[95] Ciambelli, P., Cimino, S., Lisi, L., Faticanti, M., Minelli, G., Pettiti, I., Porta, P.; *Appl. Catal., B*, **2001**, 33, 193

[96] Capek, L., Kreibich, V., Dedecek, J., Grygar, T., Wichterlova, B., Sobalik, Z., Martens, J.A., Brosius, R., Tokarova, V.; *Microporous Mesoporous Mater.*, **2005**, 80, 279

[97] Perez-Ramirez, J., Kumar, M.S., Bruckner, A.; *J. Mater. Chem.*, **2004**, 223, 13

[98] Jitianu, A., Crisan, M., Meghea, A., Rau, I., Zaharescu, M.; *J. Mater. Chem.*, **2002**, 12, 1401

[99] Pedersen, T., Saadi, S., Nielsen, K.H., Mørup, S., Kammer, K.; *Solid State Ionics*, **2005**, 176, 1555

[100] Russo, U.; Long, G.J. *Mössbauer Spectroscopy Studies Of The High Oxidation State Of Iron in Mössbauer Spectroscopy Applied To Inorganic Chemistry*, Vol 3, Long, G.J.; Grandjean, F., Ed.; Plenum Press, NY **1989**

[101] Saorin, A., tesi di laurea, *Studio dell'influenza dei droganti sulla distribuzione di siti attivi nelle perovskiti*, Università degli Studi di Padova, A.A. 2005-06, Relatore Dr. Antonella Glisenti

[102] Itoh, N., Kato, T., Uccida, K., Haraya, K.; *J. Membr. Sci.*, **1994**, 92, 239

[103] Ishihara, T., Ishikawa, S., Furuno, T., Yu, C., Ando, M., Nishiguchi, H., Takita, Y.; *Solid State Ionics*, **2004**, 175, 367

[104] Ishihara, T., Tsuruta, Y., Chunying, Y., Tokada, T., Nishiguchi, H., Takita, Y.; *J. Electrochem. Soc.*, **2003**, 150, E17

[105] Tablet, C., Grubert, G., Wang, H., Schiestel, T., Schroeder, M., Langanke, B., Caro, J.; *Catal. Today*, **2005**, 104, 126

[106] Teraoka, Y., Honbe, Y., Ishii, J., Furukawa, H., Moriguchi, I.; *Solid State Ionics*, **2002**, 152-153, 681

[107] Lee, S., Lee, K.S., Woo, S.K., Kim, J.W., Ishihara, T., Kim, D.K.; *Solid State Ionics*, **2003**, 158, 287

[108] Lee, K.S., Lee, S., Kim, J.W., Woo, S.K.; *Desalination*, **2002**, 147, 439

[109] Shao, Z., Yang, W., Cong, Y., Dong, H., Tong, J., Xiong, G.; *J. Membr. Sci.*, **2000**, 172, 177

[110] Tong, J., Yang, W., Cai, R., Zhu, B., Lin, L.; *Catal. Lett.*, **2002**, 78, 129

[111] Skoog, D.A.; Leary, J.J.; *Chimica Analitica Strumentale*, EdiSES, Napoli, **1995**

[112] http://www.ing.unitn.it/~luttero/maud/

[113] Hertz, H.; *Ann. Physik*, **1887**, 31, 983

[114] Einstein, A.; *Ann. Physik*, **1905**, 17,132

[115] C.S. Fadley in *Electron Spectroscopy: theory, techniques and Applications* vol 2 C.R. Brundle and A.D. Baker Eds Academic Press **1978** Chapter 1

[116] Shirley, D. A.; *Phys. Rev. B* **1972**, 5, 4709

[117] Little, L.H.; *Infrared Spectra of Adsorbed Species*, Academic Press, Press and N.Y. **1996**

[118] Weckhuysen, B.M., Schoonheydt, R.A.; *Catal. Today*, **1999**, 49, 441

[119] Dickson, D.P.E., Berry, F.J.; *Mössbauer spectroscopy*, Cambridge University Press, London **1986**

Acknowledgments:

Questa è la conclusione di un periodo veramente interessante della mia vita. Durante questi tre anni ho imparato molte cose grazie soprattutto alle persone che mi sono state accanto.
Però, dopo quasi duecento pagine in inglese, vorrei poter ringraziare chi mi ha sostenuto nella mia lingua natia…

Il più sincero dei ringraziamenti va alla dottoressa Antonella Glisenti, la quale mi ha permesso di sviluppare autonomamente le mie idee. Grazie per i suggerimenti che ha saputo dare per migliorare l'intero lavoro.
Grazie alla dottoressa Marta Maria Natile per l'insostituibile aiuto nella discussione dei dati e per l'accuratezza con la quale ha sempre contribuito al lavoro.

Un sentito ringraziamento va al Chiar.mo Prof. Eugenio Tondello per aver fornito fondamentali spunti di discussione che hanno permesso di intraprendere nuove e proficue vie di ricerca.

Grazie anche a tutti coloro i quali hanno collaborato fornendo preziose informazioni attraverso le loro competenze. Grazie, dunque al Prof. Umberto Russo e al Dott. Luca Nodari per le misure Mossbauer. Grazie al Prof. Gian Andrea Rizzi per le analisi TPD.
Grazie al Dott. Davide Barreca per l'aiuto nelle misure XRD e UV-Vis.

Un doveroso ringraziamento va al Sig. Stefano Girardi per l'aiuto nella realizzazione della camera di permeazione.

A conclusione di tutto, desidero ringraziare con la classica " pacca sulle spalle", tipica della vera amicizia, tutti gli amici che mi fanno star bene… Beppe, Massimo, Marcel, Silvia, Alessia, "il Volto" e tutta la "bat…"

Special thanks to… mamma e papà, Laura e tutta la mia famiglia.
Senza dimenticare l'insostituibile d.Max e tutto il suo "seguito".